Stellingen behorende bij het proefschrift:

THE USE OF SATELLITES IN GRAVITY FIELD DETERMINATION AND MODEL ADJUSTMENT

door

Petrus Nicolaas Anna Maria Visser

10 september 1992

De toenemende nauwkeurigheid waarmee satellietbanen kunnen worden berekend maakt de toepassing van analytische lineaire baanverstoringstheoriën, bijvoorbeeld de Lagrange lineaire baanverstoringstheorie, in het aanpassen en uitbreiden van bestaande modellen voor het zwaartekrachtveld weer concurrerend met numerieke integratietechnieken.

Het gebruik van radar-hoogtemeter kruispuntverschillen in de geïntegreerde benadering, waarin gelijktijdig een bestaand model voor het zwaartekrachtveld wordt aangepast en een model voor de grootschalige oceaanstromingen wordt geschat uit satelliet radar-hoogtemetingen, leidt tot een betere scheiding en daarmede een meer stabiele aanpassing en schatting van deze twee modellen. Het feit dat kruispuntverschillen geen informatie leveren over de geografisch gecorreleerde baanfout is onvoldoende reden om deze waarnemingen niet te gebruiken in de geïntegreerde benadering.

De betekenis van de huidige hoogtemeter-satellieten (ERS-1 en TOPEX/Poseidon) en toekomstige hoogtemeter-satellieten voor de oceanografie, geofysica en geodesie zal aanzienlijk toenemen indien de ARISTOTELES missie daadwerkelijk doorgang vindt.

Het oorspronkelijk voor militaire doeleinden ontworpen satelliet-navigatiesysteem GPS ("Global Positioning System") zal uiteindelijk meer civiele dan militaire gebruikers kennen.

De voltooiing van de complete GPS configuratie (24 satellieten) opent de mogelijkheid de baan van een satelliet die uitgerust is met een kwalitatief goede GPS ontvanger te bepalen met ongeëvenaarde nauwkeurigheid en continuïteit.

De doelstellingen van de ARISTOTELES missie op het gebied van het modelleren van het zwaartekrachtveld kunnen alleen worden gehaald indien deze satelliet wordt uitgerust met zowel een zeer goede GPS ontvanger als een gradiometer. De grote mogelijkheden die de implementatie van een GPS ontvanger aan boord van ARISTOTELES leveren, mogen echter niet tot de misvatting leiden dat de metingen van deze GPS ontvanger alleen voldoende zijn om de missie-doelstellingen te realiseren.

De brandstof benodigd voor het wijzigen van de baan-inclinatie van ARISTOTELES van 96° naar 92°, met als doel waarnemingen boven de poolkappen te verkrijgen, kan beter worden aangewend voor een verlenging van de ARISTOTELES gravitatiemissie in de baan met een inclinatie van 96°.

Het is niet reëel een exacte voorspelling te willen geven van de wetenschappelijke opbrengst van een toekomstige satelliet-missie. De resultaten die zijn behaald met bijvoorbeeld de hoogtemeter-satellieten SEASAT en GEOSAT op het gebied van de geofysica en de oceanografie overtroffen alle verwachtingen. Alleen al dit feit zou een enorme stimulans moeten zijn voor het realiseren van de ARISTOTELES missie.

Bij het toekennen van budgetten aan ruimtevaart-projecten speelt het prestige veelal een grotere rol dan de mogelijke wetenschappelijke en maatschappelijke opbrengst. Als voorbeeld moge dienen het feit dat grote budgetten worden gereserveerd voor de ontwikkeling van bemande ruimtevaart, terwijl er grote moeilijkheden zijn bij het financieren van een relatief goedkope en veelbelovende missie als ARISTOTELES.

De kans op een computerstoring neemt meer dan recht evenredig toe met het aantal gebruikers.

De aanschaf van steeds krachtiger computers vermindert de stimulans bij de gebruikers tot het maken van efficiënte software.

De verkoop van Fokker aan DASA zal leiden tot een verdergaande afkalving van het Nederlandse industrieel en technologisch potentieel, en mogelijk tot afkalving van het wetenschappelijk potentieel.

De korting op het salaris van de assistent-in-opleiding (AIO) heeft niet alleen negatieve consequenties voor de financiële draagkracht van de betreffende persoon, maar brengt ook het gevaar van een uitholling van zijn/haar status en motivatie met zich mee.

THE USE OF SATELLITES IN GRAVITY FIELD DETERMINATION AND MODEL ADJUSTMENT

THE USE OF SATELLITES IN GRAVITY FIELD DETERMINATION AND MODEL ADJUSTMENT

PROEFSCHRIFT

Ter verkrijging van de graad van doctor
aan de Technische Universiteit Delft,
op gezag van de Rector Magnificus, Prof. Drs. P.A. Schenck,
in het openbaar te verdedigen ten overstaan van een
commissie aangewezen door het College van Dekanen
op 10 september 1992 te 10.00 uur

door

PETRUS NICOLAAS ANNA MARIA VISSER

Geboren te De Goorn
Vliegtuigbouwkundig Ingenieur

Delft University Press / 1992

Dit proefschrift is goedgekeurd door de promotor
prof. ir. K.F. Wakker

ISBN 90-6275-802-9/CIP

Contents

Part II. Application of LPT to real satellite observations

Part III. Gravity field recovery and adjustment from satellite-to-satellite tracking and gradiometry

Part IV. Conclusions, bibliography, appendices

Samenvatting

Titel: Het gebruik van satellieten bij het bepalen van het gravitatieveld en het aanpassen van gravitatiemodellen

Dit proefschrift beschrijft het onderzoek van de auteur verricht in het kader van de postdoctorale 4-jarige AIO-opleiding. Doel van dit onderzoek was het ontwikkelen en verbeteren van methoden op het gebied van de modellering van het aardse gravitatieveld. Dit aardse gravitatieveld speelt een belangrijke rol in de beschrijving en bepaling van satellietbanen, in de geodesie, oceanografie, geofysica, etc.

De nadruk van dit proefschrift ligt op het bepalen en/of verbeteren van gravitatieveldmodellen met behulp van waarnemingen verricht door of naar satellieten. De onderzochte waarnemingstypen zijn satelliet radar hoogtemetingen ("satellite altimetry"), satelliet laser afstandsmetingen (SLR) tussen een station op de aarde en een satelliet, metingen van de afstand en/of afstandsveranderingen tussen twee satellieten ("satellite-to-satellite tracking") en metingen van de zogenaamde gravitatietensor ("satellite gradiometry"). Deze waarnemingen waren beschikbaar, ofwel als aktuele metingen ofwel in gesimuleerde vorm. Met name de laser afstandsmetingen en de radar hoogtemetingen waren in ruime mate bij de Technische Universiteit Delft voorhanden. In de studies beschreven in dit proefschrift is voornamelijk gebruik gemaakt van laser afstandsmetingen en radar hoogtemetingen van de SEASAT- en GEOSAT-missies. De andere waarnemingstypen, "satellite-to-satellite tracking" en "satellite gradiometry", waren in gesimuleerde vorm door de auteur gegenereerd.

Dit proefschrift bestaat uit vier delen. In het eerste deel wordt beschreven hoe het aardse gravitatieveld kan worden gemodelleerd. Bovendien wordt een analytische theorie, de "Lagrange Linear Perturbation Theory", gepresenteerd, die het verband geeft tussen het model voor het het aardse gravitatieveld en de verstoringen van een satellietbaan. Aangetoond wordt dat deze analytische theorie de baanverstoringen zeer goed kan beschrijven.

In het tweede deel wordt beschreven hoe deze analytische baanverstorings-theorie werd toegepast op echte satelliet waarnemingen en wordt beschreven hoe een bestaand gravitatieveldmodel kon worden aangepast met behulp van deze waarnemingen. Aangetoond wordt dat deze aanpassing leidt tot een aanzienlijke verbetering in de beschrijving van de satellietbaan (in dit geval van de SEASAT-baan). Allereerst werd een experiment tot verbetering van een bestaand gravitatieveldmodel uitgevoerd met behulp van SEASAT laser afstandsmetingen en radar hoogtemetingen. Deze aanpassing werd vergeleken met een aanpassing berekend met gebruikmaking van een numeriek baanberekenings- en parameter-schattingsprogramma ("GEODYN").

Daarna werd een uitgebreid onderzoek gedaan naar een totale aanpassing van een bestaand gravitatieveldmodel met behulp van GEOSAT radar hoogtemetingen. Dit leidde tot een zodanige nauwkeurigheid in de beschrijving van het aardse gravitatieveld, en daarmede tot een dermate nauwkeurige bepaling van de satellietbaan, dat

het mogelijk bleek gelijktijdig een model te genereren voor de beschrijving van de grote oceaanstromingen. Aangezien twee jaar van GEOSAT radar hoogtemetingen beschikbaar waren, werd tevens een onderzoek verricht naar veranderingen in deze oceaanstromingen. Hierbij kon duidelijk een jaarlijkse cyclus worden onderscheiden, hetgeen de grote mogelijkheden aangeeft van satelliet-missies als ERS-1 (1991) en TOPEX/Poseidon (1992) op het gebied van de fysische oceanografie en klimatologie.

Het derde deel van dit proefschrift beschrijft de resultaten van simulatiestudies in het kader van de toekomstige geodetische satelliet ARISTOTELES (1997). Deze satelliet zal worden uitgerust met zowel een zogenaamde GPS ontvanger ("satellite-to-satellite tracking") als een "gradiometer". De GPS ontvanger maakt het mogelijk dat kontinu simultane afstands- en doppler-metingen naar 6-8 satellieten van het Amerikaanse Global Positioning System (GPS) worden verkregen. Gezien de enorme hoeveelheid waarnemingen die deze instrumenten op de satelliet zullen leveren, werd in eerste instantie gekozen voor een simulatie waarin alleen lokaal (West-Europa) het gravitatieveld werd bepaald. Indien echter sprake is van een speciale geometrie van de waarnemingen, dan kunnen bepaalde vereenvoudigingen worden toegepast, waardoor het mogelijk wordt ook simulaties uit te voeren voor het bepalen van het gravitatieveld voor de hele aarde. Hierdoor kon worden aangetoond dat het mogelijk zal zijn om uit de door ARISTOTELES vergaarde GPS en gradiometer signalen het aardse gravitatieveld met grote nauwkeurigheid en met hoge resolutie te modelleren. Ook zal het met een dergelijke missie mogelijk worden om de mariene geoide, die een representatie van het aardse zwaartekrachtveld boven zee is, en het gemiddelde zeeoppervlak, dat uit radar hoogtemetingen vanuit satellieten kan worden bepaald, te scheiden. Hierdoor kunnen de radar hoogtemetingen worden gebruikt om allerlei grootschalige oceaan-stromingen in detail te bepalen.

Het laatste deel van dit proefschrift geeft een samenvatting van de onderzoeksresultaten en conclusies. Bovendien omvat dit deel een literatuuroverzicht en aanvullende achtergrondinformatie.

Gesteld kan worden dat reeds met bestaande satellietwaarnemingen zeer waardevolle resultaten kunnen worden behaald op het gebied van de baanberekening van satellieten, gravitatieveldmodellering en oceanografie. Bovendien is door de beschreven simulatie studies geverifiëerd dat met de ontwikkeling en toenemende toepassing van "satellite-to-satellite tracking" (GPS), de toekomstige implementatie van een GPS ontvanger en gradiometer op ARISTOTELES (1997) en de lanceringen van de ERS-1 (1991) en TOPEX/Poseidon (1992), onze kennis en begrip van de planeet aarde aanzienlijk zullen kunnen worden verbeterd en uitgebreid.

Curriculum Vitae

Pieter Visser was born on Thursday 16th of December 1965 in De Goorn (The Netherlands), where he visited primary school. He visited secondary school from 1977 to 1983 at the Werenfridus Lyceum in Hoorn.

In 1983, at the age of 17, he started his study at the Faculty of Aerospace Engineering of Delft University of Technology. During the first two and a half years, the emphasis of the study was laid on obtaining a firm mathematical and physical background, in addition to courses in the field of airplane aerodynamics, constructions and mechanics, and introductory courses in aerospace engineering. After this period, he decided to specialize in space technology and a two-months training period was spent at the Dutch aerospace company Fokker Space & Systems, Amsterdam, on the subject of modeling a solar panel with finite elements for strength computations. After this, he joined the Section Orbital Mechanics of Delft Univerity's Faculty of Aerospace Engineering and graduated on the subject of "Rendezvous and Docking of Spacecraft".

After receiving his Master's degree on February 8, 1988, he accepted a job as an "AIO", a 4-year post-doctoral research position. In these four years he performed studies in the field of gravity field determination, satellite orbit errors and oceanography, partly in the framework of contract studies for the European Space Agency (ESA). Contributions were made to several articles and scientific reports and the study results were presented at several international congresses and symposia.

Acknowledgments

The author wishes to express his gratitude to the many people who have made it possible to do the work described in this thesis. Special thanks go to Prof. K.F. Wakker, head of the Section Orbital Mechanics, Faculty of Aerospace Engineering, Delft University of Technology (DUT/FAE/SOM), for his support and stimulating enthusiasm. The author also wishes to thank Prof. R. Rummel and Ernst Schrama, from the Faculty of Geodetic Engineering of Delft University of Technology.

The author further wishes to thank Rene Zandbergen, who left DUT/FAE/SOM and now has a position at the European Space Operations Center (ESOC) in Germany, Boudewijn Ambrosius, Ron Noomen, Hans Leenman, Ernst Hesper, Remko Scharroo, Marc Naeije and other colleagues at DUT/FAE/SOM, for the many useful discussions.

Special thanks go to my parents, for their constant support and advice.

Part of the work described in this thesis was sponsored by the European Space Agency (ESA).

List of abbreviations

cpr	cycles per (orbital) revolution
rms	root-mean-square (square root of mean of squares)
rss	root-sum-square (square root of sum of squares)
AIAA	American Institute for Aeronautics and Astronautics
CIGAR	Consortium for the Investigation of Gravity Anomaly Recovery
CSR	Center for Space Research
DGFI	Deutsches Geodätisches Forschungs-Institut
DUT	Delft University of Technology
ERS	European Remote-Sensing satellite
ESA	European Space Agency
ESOC	European Space Operations Center
FAE	Faculty of Aerospace Engineering
GEM	Goddard Earth Model
GRGS	Groupe Recherches de Géodésie Spatiale
GSFC	Goddard Space Flight Center
GPS	Global Positioning System
HE	Hill Equations
JGR	Journal of Geophysical Research
JPL	Jet Propulsion Laboratory
LEO	Low Earth Orbiting
LPT	Linear Perturbation Theory
NASA	National Aeronautics and Space Administration
OSU	Ohio State University
PGS	Preliminary Gravity Solution
PDOP	Position-Dilution-of-Precision
SAO	Smithsonian Astrophysical Observatory
SE	Standard Earth model
SGG	Satellite Gravity Gradiometry
SLR	Satellite Laser Range
SOM	Section Orbital Mechanics
SST	Satellite-to-Satellite Tracking; Sea Surface Topography
SWH	Significant Wave Height
TEG	TOPEX Earth Gravity field
TUM	Technische Universität München

List of symbols

This list gives an overview of the symbols used in the main text and most of the symbols used in the appendices.

a	semi-major axis; state-vector term
$\bar{a}$	acceleration
a_e	mean equatorial radius of the Earth
b	state-vector term
e	eccentricity
e_0	total night-time electron content
e_1	amplitude of daily variation of total electron content
f	frequency
f_{lmp}	frequency of gravity field perturbation
f_c	Coriolis parameter
$\bar{g}$	gravity force vector
h	sea height
h_g	geoid undulation
h_0	height of ionospheric layer
i	inclination
k_l	variance of geopotential for degree l
l	degree of spherical harmonic
$lmax$	maximum degree of gravity field expansion
$lsst$	maximum degree of dynamic sea surface topography expansion
m	order of spherical harmonic
n	orbital angular velocity
nr	number or nodal orbital revolutions per day
$nday$	number of nodal days of repeat period
$nobs$	number of observations
$nrev$	number of nodal orbital revolutions in repeat period
r	radius of satellite orbit
$\ddot{r}$	radial acceleration
s	surface element of a sphere
t	time
t_{loc}	local solar time
u	argument of latitude; radial orbit perturbation

u_g	north-south geostrophic current
v	along-track orbit perturbation
v_g	east-west geostrophic current
w	cross-track orbit perturbation; orbital angular velocity; weight factor
x	vector of unknowns
z	90°-elevation
A	design matrix (left-hand side of observation equations)
$\bar{C}_{lm}, \bar{S}_{lm}$	normalized harmonic coefficients
C	covariance matrix
C_{tt}	covariance matrix for t
C_{tx}	row of correlations between t and x
$C(0)_t$	variance of t
C_i	"computed" measurement at time t_i
D	diagonal noise-variance matrix
$\ddot{E}W$	acceleration in longitude direction
F	observation model
F_{lmp}	function of inclination i
G	inverse of gravity field covariance matrix
$G(T)$	gravity tensor
G_{lpq}	function of eccentricity e
H_{lmp}	radial orbit error amplitude factor
$K(U(P),U(Q))$	covariance function of the geopotential for points P and Q
L^i	functional of the gravity potential
M	mean anomaly
N	normal matrix; geoid undulation
$\ddot{N}S$	acceleration in latitude direction
O_i	observation at time t_i
P_{lm}	(associated) Legendre polynomial
R	vector of observation residuals
S	inverse of covariance matrix of the state-vector
S_{lmpq}	part of spherical harmonic in orbital elements
S^*_{lmpq}	primitive of S_{lmpq}
$S(r,\psi)$	Stokes' kernel
T	disturbing gravity field potential
U	gravitational field potential
V_A	a priori covariance matrix
W	gravity field potential
$Xover$	crossover difference

α	regularization parameter
β	frequency in cycles per nodal orbital revolution
γ	normal gravity acceleration
δ	declination
ε	noise
θ	Greenwich sidereal angle
λ	longitude
μ	gravity parameter of the Earth
ρ	range; correlation
σ	standard deviation
ϕ	latitude
ψ	spherical distance; argument of S_{lmpq}
ω	argument of perigee
ω_e	rotation rate of the Earth
Δc	cross-track orbit perturbation
Δg	gravity anomaly
Δh	geoid height
Δr	radial orbit perturbation
Δt	measurement time interval
$\Delta\tau$	along-track orbit perturbation
Δ	Laplace operator
Γ	gravity gradient, tensor
Ω	right ascension of ascending node
$\bullet$	scalar product

Subscripts, superscripts

a	atmosphere; a priori; ascending node
asc	ascending track
cal	calibrated
des	descending track
e	Earth
g	gravity field
i	instrument
i,j,k,p,q	summation indices
l	degree of spherical harmonic

m	order of spherical harmonic
o	ocean topography
ref	reference
rw	real-world
s	significant wave height; state-vector
sg	spacecraft geometry
$state$	state-vector
st	ground station
t	tides
u	radial
v	along-track
w	cross-track
x	along-track
y	cross-track
z	radial
SST	dynamic sea surface topography
T	transpose
-1	inverse
ξ	dynamic sea surface topography
—	normalized (bar)
.	time derivative (dot)

Introduction

Since the launch of the first artificial satellite, the Soviet "Sputnik" in 1957, much attention has been paid to extracting gravity field information of the Earth from satellite observations. Although already a huge amount of (accurate) satellite ground-tracking data are available, current models for the Earth's gravity field are not accurate enough to fully exploit the information content of satellite observations acquired in a number of geodetic, geophysical and oceanographic satellite missions. Examples of these missions are the geodetic LAGEOS satellite and the ERS-1 and TOPEX/Poseidon altimetric missions. Both types of missions require very precise orbits, and this requires the availability of accurate gravity field models. In addition, altimetry satellites also require the availability of a precise geoid which is an equipotential surface for the Earth's gravity field potential.

Although current gravity field models can still be improved by reprocessing the available satellite tracking data, the accuracy and resolution of these models is limited because of the non-global coverage of this data set. However, with the advent of future satellite missions like the solid Earth satellite ARISTOTELES (Rummel, 1989a and 1989b) and Gravity Probe B (Smith et al., 1988) and the ongoing deployment of the Global Positioning System (GPS), it will be possible to obtain a data set of satellite observations with high accuracy and almost perfect global coverage. With such a data set it will be possible to improve and enlarge current gravity field models drastically, especially for short-wavelength gravity field variations. These models are expected to have an unprecedented accuracy and resolution. With these new models it seems possible to answer many questions in the field of geophysics, oceanography, geodesy and orbit determination and prediction.

In this thesis, methods will be proposed and discussed to improve gravity field models with the presently available data of satellite observations and with observations coming from future satellites. Essentially, a distinction will be made into three categories of satellite observations. The first category consists of observations between a fixed station on the surface of the Earth and an orbiting satellite. Examples of this category are satellite laser range (SLR) measurements, doppler observations and camera optical observations. Although observations of this category can be, and in many cases are, very accurate, they generally do not provide a fine global data set due to the non-global coverage of the ground stations.

Observations acquired by Earth remote-sensing satellites belong to the second category of satellite observations. The most important example of this category are the satellite altimeter measurements, which are produced by an orbiting satellite that measures its height above the ocean's surface. In principle, observations of this type can cover two-thirds of the Earth. However, these observations do not really have the capability of improving current gravity field models dramatically, because they do not only provide information about the Earth's geoid and radial orbit perturbations, but they also provide information about oceanographic phenomena. In other words, in the description of an altimeter measurement both the gravity field and ocean dynamics play a role and parts of these features behave the same mathematically. This means

that a separation of these features requires sophisticated mathematical methods and is not always possible, and the latter implies that oceanic features will be aliased into a gravity field solution if these measurements are used to determine the gravity field. Huge amounts of altimeter observations of the GEOS-3 (1975-1978), SEASAT (1978) and GEOSAT (1985-1990) are available, and have been the subject of many studies.

The third and last category of satellite observations is defined as satellite-to-satellite tracking (SST) and satellite gravity gradiometry (SGG). The first concept produces observations of the range or range-rate between two orbiting satellites. Although today small data sets of SST observations are available from e.g. ATS-6/GEOS-3 (Schmid et al., 1975), ATS-6/Apollo (Vonbun et al., 1980) and Landsat-5/GPS (Bertiger et al., 1986), these observations have not yet contributed significantly to the development of gravity field models. However, with the ongoing deployment of the GPS system and the future launch of TOPEX/Poseidon and low Earth satellites, like ARISTOTELES and Gravity Probe B, that will be equipped with a GPS receiver, the importance of this category of observations in gravity field determination will grow. Moreover, because of the spatial distribution of the GPS-satellites a perfect global coverage of satellite observations will be possible.

Satellite gradiometry is based on the measurement of the differences of the acceleration experienced by a number of test masses which are placed very close together (on the order of a few meters) and thus delivering information about the second derivative of the Earth's gravity potential, i.e. the gravity tensor. In other words, because the masses are so close together, the difference between their accelerations divided by their distance is very close to the local gradient of the gravity field force. A gradiometer will be implemented on the ARISTOTELES satellite. This satellite, which will encircle the Earth in a low-altitude (about 200 km) almost polar orbit, will be capable of providing a global data set of observations for the entire spectrum of gravity field variations over the Earth up to a resolution of about 100 km because of its low altitude (Visser et al., 1990).

This thesis is concerned with the question of how to use all the different types of satellite observations in gravity field adjustment and improvement. In principle, all types of satellite observations mentioned give information of the satellite orbit perturbations and in conjunction the Earth's gravity field, because the satellite orbits are affected most by the Earth's gravity field. Therefore, the first part of this thesis consists of two subjects: representation forms of the gravity field of the Earth and the theory of satellite orbit perturbations. An analytical orbit perturbation theory is presented and shown to be sufficiently accurate for describing satellite orbit perturbations if certain conditions are fulfilled.

In the second part of this thesis, gravity field adjustment experiments using the analytical orbit perturbation theory are discussed using real satellite observations. These observations consisted of SEASAT laser range measurements and crossover differences, and of GEOSAT altimeter measurements and crossover differences. A crossover difference is the difference between two altimeter measurements made at the same geographical position, one when the satellite orbit was ascending and one when the satellite orbit was descending. The treatment of the GEOSAT radar altimeter height measurements required special attention, because this type of measurements

does not only deliver information about the gravity field and satellite orbit perturbations but also about other phenomena, like ocean currents. The gravity field adjustment experiments with the GEOSAT observations will show the possibility of determining a long-wavelength stationary ocean circulation model and of adjusting a gravity field model simultaneously. With this integrated approach, satellite altimetry can be used to really improve gravity field models, while providing an attractive by-product.

The third part of this thesis is more or less a look into the future. This part is mainly related to the question of the possible impact of future satellite missions on gravity field modeling. Studies are presented which investigate the possibility of gravity field model adjustment and enlargement using observations of the third category, i.e. SST observations and gradiometer measurements. These studies are for the larger part related to the ARISTOTELES mission. Because the instruments on board of the ARISTOTELES satellite are assumed to deliver a very dense set of observations with high accuracy and perfect global distribution, it is expected that the gravity field can be determined to a high resolution and with a high accuracy.

The determination of a high-resolution and high-accuracy global gravity field model requires the determination of a huge amount of (unknown) gravity field coefficients. Therefore, first a local approach of gravity field determination was investigated. In this way, the number of gravity field unknowns could be kept within limits. This analysis consisted of two parts: a covariance analysis based on least-squares collocation and a deterministic gravity field recovery from simulated ARISTOTELES gradiometer and GPS SST observations.

However, if certain simplifications are made and certain conditions are met, it is possible to extend this type of analysis and to study also global gravity field recovery experiments from large amounts of satellite observations. The results from this study will be compared with the results from the local experiments. It will be demonstrated that the ARISTOTELES mission can contribute to a major improvement in gravity field modeling and to a better understanding of a number of topics in the field of geodesy, geophysics and oceanography.

Finally, in part IV of this thesis all results obtained in the first three parts will be summarized and conclusions will be drawn.

Part I. Theory of gravity field modeling and orbit perturbations

1. The representation of the Earth's gravity field

1.1 Introduction

The Earth's gravity field can be represented in many ways. However, not all of these representations are suitable for gravity field recovery and adjustment from satellite observations. Therefore, a selection of representations will be made: only those representations are described that will be used in the gravity field recovery and adjustment experiments and simulations in parts II and III of this thesis.

In this Chapter, first a description of the selected gravity field representations is presented. In the following, these representations will be called gravity field models. This will be followed by a discussion of the current (i.e. 1991) status of gravity field modeling.

1.2 Mathematical formulation of gravity field models

This Section will give an overview of the types of Earth gravity field models to be used in this thesis. A distinction will be made between global and local gravity field models.

As a starting point in describing the gravity field of the Earth may serve the well-known equation of Laplace (Kaula, 1966). The potential U of the Earth's gravitational field is known to satisfy this equation, that reads for a position "in vacuo" for a rectangular coordinate frame x, y and z:

$$\Delta U = \frac{\partial^2 U}{\partial x^2}+\frac{\partial^2 U}{\partial y^2}+\frac{\partial^2 U}{\partial z^2} = 0 \,. \tag{1.1}$$

The solution of this equation can be represented by an infinite series of so-called spherical harmonics, which reads:

$$U = \frac{\mu}{r}\left\{1+\sum_{l=2}^{\infty}\sum_{m=0}^{l}\left[\frac{a_e}{r}\right]^l (\bar{C}_{lm}\cos m\lambda+\bar{S}_{lm}\sin m\lambda)\bar{P}_{lm}(\sin\phi)\right\} \tag{1.2}$$

In this equation μ denotes the gravity parameter of the Earth, a_e the mean equatorial radius of the Earth, $\bar{P}_{lm}$ the fully normalized Legendre polynomial of degree l and

order m, $\bar{C}_{lm}$ and $\bar{S}_{lm}$ denote the fully normalized gravity field harmonic coefficients. The position in a geocentric coordinate frame is denoted by the radius r, the longitude λ and the geocentric latitude ϕ. The constituents of the solution can be divided into three groups:

1- zonals: m=0. The zonal harmonics divide the Earth's sphere into zones. These harmonics change sign l times from the North (ϕ= 90°) to the South pole (ϕ=-90°);

2- sectorials: $l=m\neq 0$. The sectorials divide the Earth's sphere into sectors. They change sign $2m$ times for $0\leq\lambda<360°$;

3- tesserals: $l\neq m\neq 0$. The tesseral harmonics divide the Earth's sphere into compartments (blocks) and change sign l-m times for $-90° \leq \phi < 90°$ and $2m$ times for $0\leq\lambda<360°$.

Global gravity field models used in this thesis are of this form and consist of values for the normalized harmonic coefficients $\bar{C}_{lm}$ and $\bar{S}_{lm}$. In practice, the series of harmonic coefficients are truncated at a certain degree l. This truncation can be justified by several effects. Firstly, the effect of these coefficients on the total potential U decreases with increasing l. In (Kaula, 1966), it is shown that this decrease can roughly be written as:

$$\bar{C}_{lm},\bar{S}_{lm} + \frac{10^{-5}}{l^2} . \tag{1.3}$$

This equation is called Kaula's rule of thumb. Secondly, the term $(a_e/r)^l$ in equation (1.2) decreases with increasing l (for satellite orbits $r > a_e$). The latter explains the choice of the low altitude for the future ARISTOTELES orbit. One of the objectives of this satellite is to determine a high-degree gravity field model (Rummel, 1986a and 1989a). The latter effect and Kaula's rule of thumb indicate that for a high degree l, the corresponding terms of the gravitational potential have a very small effect on the satellite orbit. This means that their signals are not detectable from satellite tracking data. Finally, the truncation is justified by the fact that the data sets of observations used to determine current gravity field models have a poor global coverage. For example, satellite tracking observations are only made in the vicinity of ground stations and the Earth is generally not covered completely with such stations. For such a data set of observations, the resolution, which means the maximum degree l of the gravity field harmonic expansion, is limited.

The field of the potential U is called the *gravitational field.* If the potential of the centrifugal force, caused by the Earth's rotation rate ω_e, is added to this potential, the *gravity field potential* is obtained (Moritz, 1980):

$$W = U + \frac{1}{2}\omega_e{}^2 r^2 \cos^2\phi . \tag{1.4}$$

The surfaces, for which W=constant, are called equipotential surfaces. One of these

surfaces, which gives a best approximation of the average surface of the oceans, is called the geoid. This surface plays an important role in the processing of altimeter measurements (Chapters 4, 5 and 6).

In comparison to global gravity field models, local gravity field models are in the form of point values or mean values over a certain surface on the Earth of functionals of the gravity field potential W. Examples are gravity anomalies Δg and geoid undulations N. Values for these functionals are most often computed by using a so-called disturbing potential T. This is a residual potential after subtracting a reference gravity field potential W_{ref} from the potential W ($T=W-W_{ref}$). In most cases, the reference potential is defined as the gravity field potential with a best-fitting ellipsoid as an equipotential surface, which includes a mass distribution with a mass equal to the mass of the Earth (including the atmosphere). Then, a geoid undulation is defined as the height of the geoid above this ellipse and a gravity anomaly as the difference between the norms of the gravity force vector on the geoid and on the surface of this ellipse, where the gravity force vector is defined as:

$$\bar{g} = (\text{grad } W) \, . \tag{1.5}$$

It has been found that gravity anomalies and geoid heights can be approximated very well by the following equations (Moritz, 1980):

$$\Delta g = -\frac{\partial T}{\partial r} - 2\frac{T}{r} \tag{1.6}$$

$$N = \frac{T}{\gamma} \, . \tag{1.7}$$

In this equation, γ represents the norm of the gravity force on the reference ellipsoid mentioned above, and the disturbing potential T can be written as:

$$T = \frac{\mu}{r} \sum_{l=2}^{\infty} \sum_{m=0}^{l} \left(\frac{a_e}{r} \right)^l (\Delta \bar{C}_{lm} \cos m\lambda + \Delta \bar{S}_{lm} \sin m\lambda) \bar{P}_{lm}(\sin\phi) \, . \tag{1.8}$$

This thesis will describe methods to adjust or determine harmonic coefficients in global gravity field recovery experiments or values of gravity anomalies and geoid undulations in local gravity field recovery experiments.

1.3 Status of Earth gravity field models

Before the launch of the Soviet "Sputnik" in 1957, Earth gravity field models were based on measurements on the surface of the Earth (Wakker et al., 1987a). Because this data set of measurements had a poor global coverage - most measurements were made in the more readily accessible land areas - spherical harmonic representations of the gravity field consisted of only very low degree and order terms. Even these terms were determined with a low accuracy compared to the accuracy of these terms of

recently determined gravity field models.

However, with the launch of more and more Earth orbiting satellites and the development and deployment of satellite tracking systems, like camera, doppler, and satellite laser range (SLR) measurement systems, it became possible to determine the orbits and the orbit perturbations of these satellites. These data have been used by many researchers to determine series of gravity field models with increasing accuracy and resolution. For example, the Smithonian Astrophysical Observatory (SAO) produced a series of models referred to as Standard Earth models followed by a number (SE-models). In the determination of these models, use was made of analytical representations of the perturbed satellite motion. However, for high-precision orbits, these analytical representations became unmanageable complex and therefore the last SE-model was produced around 1978.

In Europe, the Groupe de Recherches de Géodésie Spatiale (GRGS) and the Deutsches Geodätisches Forschungs-Institut (DGFI) were involved in the determination of a series of gravity field models indicated by the acronym GRIM and a number. In the development of these models, an alternative approach was used. In this approach, the satellite equations of motion were solved by numerical integration. This approach is still applied and the most recent model available at Delft University of Technology (DUT), Faculty of Aerospace Engineering (FAE), is GRIM4S1, complete to degree and order 50 (private comm., DGFI, Munich, FRG).

The same approach was used by the NASA Goddard Space Flight Center (GSFC). This center has produced a series of gravity field models called Goddard Earth models (GEM). These models have been used many times at DUT/FAE. The most recent GEM-model available at our University is the PGS4591 model, complete to degree and order 50 (private comm., GSFC, Greenbelt, USA). This model is a preliminary GEM-T3 model. The GEM-T-series are computed to be used in the determination of the TOPEX satellite orbit.

Other series of gravity field models that have to be mentioned are the TEG-series (TOPEX Earth gravity field models) computed at the University of Texas, Austin, and the OSU-series at the Ohio State University, Columbus. Although the preceding overview is not complete, it will be obvious that at the moment many global gravity field models are available. These models can be divided into three types: satellite-only, so-called combined models, and geoid models.

The satellite-only models are computed from satellite tracking data only. These observations consist of laser range, doppler and camera measurements and deliver information about the satellite orbit perturbations. For example, the models computed from these observations are used in satellite orbit determination and prediction. Because of the presence of the factor $(a_e/r)^l$ in equation (1.2) and with in mind Kaula's rule of thumb (equation (1.3)), the maximum degree of gravity terms that can be modeled is limited. Another reason for this limitation, is the amount of computing time necessary for a precise orbit determination. For example, if the maximum degree of a gravity field model is doubled, it takes about four times as much computing time (CPU-time) to compute the gravity field force at a certain geographical location. At the moment this maximum degree is equal to 36-50 for the latest models developed at GFSC, e.g. the the GEM-T1 and GEM-T2 models (Marsh, 1988 and 1989a). The

resolution on the surface of the Earth of a gravity field model complete to degree and order 50 is equal to about 400 km. Together with the determination of GEM-T1 and GEM-T2, their accuracy has been estimated. For example, GEOSAT orbits (about 800 km altitude) computed with the GEM-T2 model are claimed to have a gravity field induced radial orbit error of about 20 cm for the radial position (Haines et al., 1990). For the future TOPEX/Poseidon satellite orbit this precision is claimed to be about 10 cm (Marsh et al., 1989a). The maximum degree of satellite-only models is limited by the spatial distribution of the observations that are used in the determination of these models and by the altitude of the satellites that have been tracked. Therefore, it is not expected that these models can be improved or enlarged significantly any further from existing sets of "satellite-only" observations.

The so-called combined models use in addition to satellite tracking observations also satellite altimeter measurements and gravimetric measurements made on the surface on the Earth. Also these models are used in the computation and determination of high-precision satellite orbits, and also the maximum degree at the moment is equal to 36-50. Thus, the difference between these models and the satellite-only models is the incorporation of non-tracking data. Because the altimeter measurements are affected to a great extent by oceanic phenomena and also by the gravity field, mostly ocean height models are computed simultaneously with gravity field models from these measurements. Despite the better global coverage of the Earth with altimeter data, this approach may have the disadvantage of aliasing oceanic phenomena in the gravity fields models and vice-versa. However, this approach has led to gravity field models complete to degree and order 50 and long-wavelength dynamic sea surface topography models complete to degree and order 10 that look very promising (Nerem et al., 1988; Engelis and Knudsen, 1989; Denker and Rapp, 1990; Marsh et al., 1990). The errors made in satellite orbit determination when using these models are claimed to be somewhat less than those of the satellite-only models. For example, a preliminary GEM-T3 model is a model computed from both tracking, gravimetric measurements and altimeter observations and has a predicted accuracy of about 8 cm for the radial position of the TOPEX/Poseidon satellite orbit (Marsh, 1988).

The availability of huge amounts of altimeter measurements offers the possibility of determining a gravity field model with a much finer resolution than the 400 km of models complete to degree and order 50. Available satellite altimeter data cover two-thirds of the surface of the Earth with a resolution much smaller than 400 km. Therefore, gravity field models have been developed up to degree and order 360. However, instead of using these models in precise orbit determinations, these models are especially used in computing high-resolution geoids (i.e. with a resolution of about 50 km for a model complete to degree and order 360) that fit best to the ocean surface and therefore will be referred to as geoid models. An example of such a model is the OSU89b model complete to degree and order 360 (Rapp and Pavlis, 1990). This model is claimed to have an accuracy of about 65 cm over the oceans. The geoid models are not used for orbit determination and prediction because of their size (leading to very time-consuming computer runs) and because of their aliasing of various non-gravity phenomena (e.g. oceanic features) in the gravity field terms. Especially the aliasing of long-wavelength oceanic features might lead to satellite orbit errors when using these

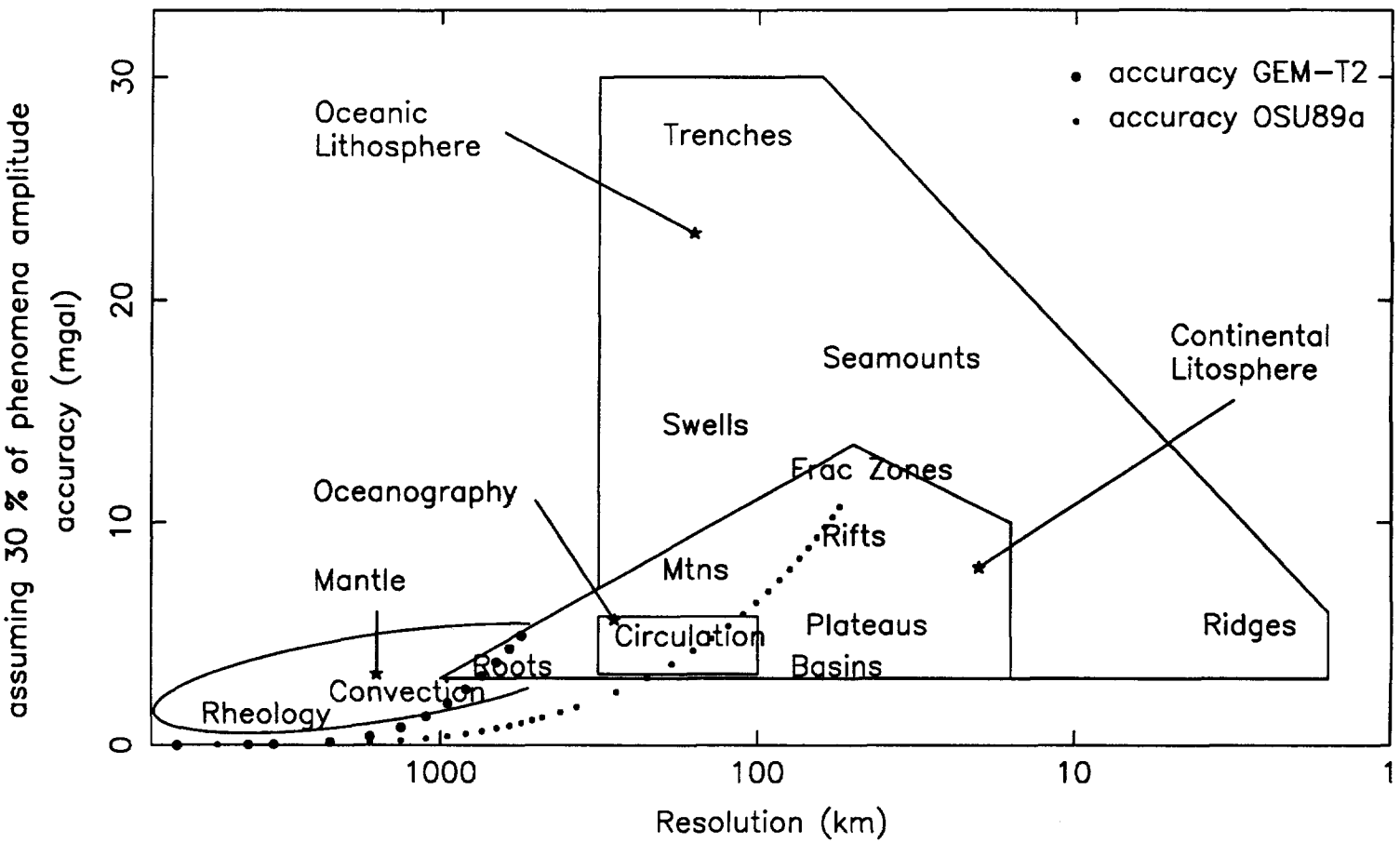

Figure 1.1 Summary of requirements for gravity measurement accuracy as a function of the spatial resolution compared to gravity model accuracy (Gravity Workshop,1987)

models.

The accuracy of current gravity field models can be compared with the accuracy required for the recovery of important phenomena in geophysics, oceanography and geodesy. In Figure 1.1, the gravity signal (in the form of gravity anomalies) of various features of different spatial scales is sketched (Gravity Workshop, 1987). Also indicated is the cumulative error of two recent gravity field models, the GEM-T2 and OSU89a gravity field models. The cumulative errors of these models have been computed from available error estimates of the several terms of these models (Marsh et al., 1989a; Rapp and Pavlis, 1990). It will be obvious that recent models have to be improved significantly before they can be used to study these phenomena. This is particularly true, since the errors indicated in Figure 1.1 for the OSU89a model are probably too optimistic, because oceanographic signals are aliased into this model.

2. Satellite orbit linear perturbation theory

2.1 Introduction

Many types of satellite observations, e.g. satellite ground tracking observations, deliver information about the satellite orbit perturbations, i.e. the changes in satellite position and velocity relative to a reference Kepler orbit. Therefore, in order to be able to process these observations their relation to orbit perturbations must be known. For the greater part, these variations are caused by the gravity field of the Earth.

In this Chapter a theory is presented, the so-called Lagrange linear perturbation theory (LPT), that gives relations between terms of the Earth's gravity field potential and satellite orbit perturbations. Two methods to derive these relations will be discussed. These two methods consist of a method based on equations derived by Kaula (Kaula, 1966) and a method originating from the Hill equations (Dunning, 1973). These two methods yield the same numerical results.

2.2 Kaula solution

In (Kaula, 1966) relations are derived for the satellite orbital element variations caused by a disturbing potential T of the gravity field of the Earth. These elements, the Kepler elements, are the satellite's orbital semi-major axis a, eccentricity e, argument of perigee ω, inclination i, right ascension of ascending node Ω and the mean anomaly M. The first step in deriving these relations was the establishment of the Lagrange planetary equations (Kaula, 1966):

$$\frac{da}{dt} = \frac{2}{na}\frac{\partial T}{\partial M} \tag{2.1a}$$

$$\frac{de}{dt} = \frac{1-e^2}{na^2e}\frac{\partial T}{\partial M} - \frac{(1-e^2)^{1/2}}{na^2e}\frac{\partial T}{\partial \omega} \tag{2.1b}$$

$$\frac{d\omega}{dt} = -\frac{\cos i}{na^2(1-e^2)^{1/2}\sin i}\frac{\partial T}{\partial i} + \frac{(1-e^2)^{1/2}}{na^2e}\frac{\partial T}{\partial e} \tag{2.1c}$$

$$\frac{di}{dt} = \frac{\cos i}{na^2(1-e^2)^{1/2}\sin i}\frac{\partial T}{\partial \omega} - \frac{1}{na^2(1-e^2)^{1/2}\sin i}\frac{\partial T}{\partial \Omega} \tag{2.1d}$$

$$\frac{d\Omega}{dt} = \frac{1}{na^2(1-e^2)^{1/2}\sin i}\frac{\partial T}{\partial i} \tag{2.1e}$$

$$\frac{dM}{dt} = -\frac{1-e^2}{na^2 e}\frac{\partial T}{\partial e} - \frac{2}{na}\frac{\partial T}{\partial a} \tag{2.1f}$$

where n is the orbital angular velocity.

In order to be able to solve these equations with the Earth's disturbing potential T as input (equation (1.8)), this potential was rewritten as a function of orbital elements (Kaula, 1966):

$$T = \sum_{l=2}^{\infty}\sum_{m=0}^{l}\sum_{p=0}^{l}\sum_{q=-\infty}^{\infty}\frac{\mu a_e^{\,l}}{r^{l+1}}F_{lmp}G_{lpq}S(\omega,M,\Omega,\theta)_{lmpq} \tag{2.2a}$$

where F_{lmp} is a function depending only on the satellite's orbital inclination i, in the following referred to as inclination function, G_{lpq} is a function depending only on the eccentricity e, in the following referred to as eccentricity function, p and q are summation indices, θ is the Greenwhich sidereal angle of the Earth's rotation, and S_{lmpq} satisfies:

$$S_{lmpq} = \begin{bmatrix}\Delta\bar{C}_{lm}\\ -\Delta\bar{S}_{lm}\end{bmatrix}\begin{matrix}l-m\ even\\ l-m\ odd\end{matrix}\cos\psi \tag{2.2b}$$

$$+\begin{bmatrix}\Delta\bar{S}_{lm}\\ \Delta\bar{C}_{lm}\end{bmatrix}\begin{matrix}l-m\ even\\ l-m\ odd\end{matrix}\sin\psi\ .$$

The argument ψ is defined as:

$$\psi = (l-2p)(\omega+M)+m(\Omega-\theta)+qM = f_{lmp}u+m\lambda_a+qM \tag{2.2c}$$

where u is the argument of latitude, λ_a is the longitude at an ascending node passage, and,

$$f_{lmp} = l-2p-m\frac{\lambda_a-\Omega+\theta}{\omega+M} = l-2p-\frac{m}{nr}\ . \tag{2.2d}$$

where nr is the number of satellite orbital revolutions per day. It can be shown that the eccentricity functions G_{lpq} are of order $O(e^{|q|})$ (Kaula, 1966). This characteristic will be used explicitly in the following.

Inserting the disturbing potential (equations (2.2a)-(2.2d)) in the Lagrange Planetary Equations (equations (2.1a)-(2.1f)), the linearized solution for the perturbations of the Kepler elements due to one term *lmpq* of the disturbing potential (equation (2.2a)) reads:

$$\Delta a_{lmpq} = 2a\left[\frac{a_e}{a}\right]^l F_{lmp}G_{lpq}(l-2p+q)\frac{n}{\dot{\psi}}S_{lmpq} \tag{2.3a}$$

$$\Delta e_{lmpq} = \frac{(1-e^2)^{1/2}}{e}\left[\frac{a_e}{a}\right]^l F_{lmp} G_{lpq}\left[(1-e^2)^{1/2}(l-2p+q)-(l-2p)\right]\frac{n}{\dot{\psi}} S_{lmpq} \quad (2.3b)$$

$$\Delta\omega_{lmpq} = \left[\frac{a_e}{a}\right]^l\left[(1-e^2)^{1/2} F_{lmp}\frac{G'_{lpq}}{e} - \frac{\cot i F'_{lmp} G_{lpq}}{(1-e^2)^{1/2}}\right]\frac{n}{\dot{\psi}} S^*_{lmpq} \quad (2.3c)$$

$$\Delta i_{lmpq} = \frac{1}{\sin i\,(1-e^2)^{1/2}}\left[\frac{a_e}{a}\right]^l F_{lmp} G_{lpq}\left[(l-2p)\cos i - m\right]\frac{n}{\dot{\psi}} S_{lmpq} \quad (2.3d)$$

$$\Delta\Omega_{lmpq} = \left[\frac{a_e}{a}\right]^l F'_{lmp} G_{lpq}\frac{1}{\sin i\,(1-e^2)^{1/2}}\frac{n}{\dot{\psi}} S^*_{lmpq} \quad (2.3e)$$

$$\Delta M_{lmpq} = \left[\frac{a_e}{a}\right]^l F_{lmp}\left[2(l+1)G_{lpq} - \frac{1-e^2}{e}G'_{lpq} - 3G_{lpq}(l-2p+q)\frac{n}{\dot{\psi}}\right]\frac{n}{\dot{\psi}} S^*_{lmpq} \quad (2.3f)$$

where

$$F' = \frac{\partial F}{\partial i} \quad (2.3g)$$

$$G' = \frac{\partial G}{\partial e} \quad (2.3h)$$

$$\dot{\psi} = \frac{d\psi}{dt} \quad (2.3i)$$

and

$$S^*_{lmpq} = \begin{bmatrix}\Delta\bar{C}_{lm}\\ -\Delta\bar{S}_{lm}\end{bmatrix}\begin{matrix}l-m\ even\\ l-m\ odd\end{matrix}\ \sin\psi \quad (2.3j)$$

$$-\begin{bmatrix}\Delta\bar{S}_{lm}\\ \Delta\bar{C}_{lm}\end{bmatrix}\begin{matrix}l-m\ even\\ l-m\ odd\end{matrix}\ \cos\psi\ .$$

All the satellites that will be considered in this thesis have near-circular orbits, i.e. the eccentricity e is almost equal to zero. To calculate the first-order perturbations for such orbits only eccentricity functions for q=-1,0,+1 have to be calculated. As can be seen from the solution of the Lagrange planetary equations, the eccentricity e is only present until first order in the denominator, thus only eccentricity functions that behave as $O(e^q)$ with $-2<q<2$ will introduce significant orbital element variations for an eccentricity close to zero. It can be shown that (Schrama, 1986a):

$$G_{lp0} = 1 \quad (2.4a)$$

$$G_{lp-1} = (-l+4p+1)\frac{e}{2} + O(e^2) \quad (2.4b)$$

$$G_{lp+1} = (3l-4p+1)\frac{e}{2}+O(e^2). \tag{2.4c}$$

Often satellite observations deliver information about the position and/or velocity perturbations that are a combination of perturbations in the direction along the vector connecting the Earth's geocenter with the satellite (radial direction), in the direction perpendicular to this direction but in the satellite's orbital plane (along-track direction) and in the direction perpendicular to this plane (cross-track direction). Therefore, it is convenient to transform the satellite orbital element variations into perturbations in the satellite radial (upward), along-track (in the direction of the satellite's velocity vector) and cross-track (completing a right-hand coordinate system) directions for a circular reference orbit.

For near-circular satellite orbits, the radial, along-track and cross-track perturbations can be written as a function of Kepler element perturbations (Rosborough, 1986):

$$\Delta r = \Delta a - a\,\Delta e\cos M + ae\,\Delta M\sin M \tag{2.5a}$$

$$\Delta\tau = a(\Delta\omega+\Delta\Omega\cos i+\Delta M+2\sin M\,\Delta e+2e\cos M\,\Delta M) \tag{2.5b}$$

$$\Delta c = a(\Delta i\sin(\omega+M)-\Delta\Omega\sin i\cos(\omega+M)). \tag{2.5c}$$

Relations for the radial (r), along-track (τ), and cross-track (c), orbit perturbations for near-circular orbits are now found by combining the equations (2.3), (2.4) and (2.5) and neglecting all terms of O(e). In this case, the summation over the index q reduces to only one term and only summations over the degree l, order m and index p remain. For one combination of l, m, and p, the solution reads:

$$\Delta r_{lmp} = a\left[\frac{a_e}{a}\right]^l F_{lmp}\left[\frac{2(l-2p)}{f_{lmp}}+\frac{4p-3l-1}{2(f_{lmp}+1)}+\frac{4p-l+1}{2(f_{lmp}-1)}\right]S_{lmp0} \tag{2.6a}$$

$$\Delta\tau_{lmp} = a\left[\frac{a_e}{a}\right]^l F_{lmp}\left[\frac{2(l+1)-3(l-2p)\dfrac{1}{f_{lmp}}}{f_{lmp}}+\frac{4p-3l-1}{f_{lmp}+1}+\frac{l-4p-1}{f_{lmp}-1}\right]S^*_{lmp0} \tag{2.6b}$$

$$\Delta c_{lmp} = \frac{1}{2}a\left[\frac{a_e}{a}\right]^l\frac{1}{f_{lmp}}\left[\left[\frac{F_{lmp}}{\sin i}((l-2p)\cos i-m)-F'_{lmp}\right]S^*_{(l+1)mp0}\right. \tag{2.6c}$$

$$\left.-\left[\frac{F_{lmp}}{\sin i}((l-2p)\cos i-m)+F'_{lmp}\right]S^*_{(l-1)mp0}\right].$$

It must be noted that the equations (2.6a)-(2.6c) are not valid for $f_{lmp} = 0$ or ±1 (resonance). In that case, some denominators in the equations (2.6a)-(2.6c) become equal to zero. This may occur for certain combinations of the order m and degree l, but

certainly will occur for so-called zonal orbit perturbations (order $m = 0$). Further attention to these cases will be paid in the next Section.

2.3 Hill equations

Equivalent mathematical relations for the satellite orbit perturbations can be derived by using the Hill equations (Dunning, 1973). The Hill equations (HE) were derived to describe the perturbations of the Moon's orbit around the Earth with the gravity field potential of the Sun as disturbing potential. However, these equations can also be applied to determine the linearized satellite orbit perturbations caused by the Earth's gravity field variations relative to a near-circular reference orbit. The orbit perturbations are computed in a local orthogonal coordinate system with the *u*-, *v*- and *w*- axes in respectively the satellite radial, along-track and cross-track directions. With the Earth's disturbing potential, represented by T, these equations are (Schrama, 1989):

$$\ddot{u} - 2n\dot{v} - 3n^2 u = f_u = \frac{\partial T}{\partial u} \tag{2.7a}$$

$$\ddot{v} + 2n\dot{u} = f_v = \frac{\partial T}{\partial v} \tag{2.7b}$$

$$\ddot{w} + n^2 w = f_w = \frac{\partial T}{\partial w} . \tag{2.7c}$$

In these equations, the terms f_u, f_v and f_w denote the disturbing gravity force vector. The *w*-equation (cross-track direction) is uncoupled from the others and can therefore be treated independently. This equation describes the well-known mass-spring system oscillating at frequency n.

To enable the solution of the equations (2.7a)-(2.7c) the disturbing forces f_u, f_v, f_w must be known. The disturbing potential T can be expressed as a function of orbit parameters (equation (2.2a)). Therefore, the partial derivatives of this potential with respect to u, v and w may be translated to partial derivatives with respect to the orbit parameters. With the equations (2.5a)-(2.5c), the following relations can be derived for circular reference orbits ($e = 0$), with the radius r of the satellite orbit equal to the semi-major axis a:

$$\Delta u = \Delta r \tag{2.10a}$$

$$\Delta v = \Delta \tau = r(\Delta(\omega + M) + \Delta\Omega \cos i) \tag{2.10b}$$

$$\Delta w = \Delta c = r(\Delta i \sin(\omega + M) - \Delta\Omega \sin i \cos(\omega + M)) . \tag{2.10c}$$

For a circular reference orbit, two independent sets of orbital elements can be chosen: a set consisting of r, $(\omega+M)$ and Ω, and a set consisting of r, $(\omega+M)$ and i (Schrama, 1990). Using the first set, i.e. with the inclination i kept constant, the disturbing forces

become:

$$\frac{\partial T}{\partial u} = \frac{\partial T}{\partial r} \tag{2.9a}$$

$$\frac{\partial T}{\partial v} = \frac{1}{r}\frac{\partial T}{\partial(\omega+M)} \tag{2.9b}$$

$$\frac{\partial T}{\partial w} = \frac{1}{r\cos(\omega+M)\sin i}\left\{\frac{\partial T}{\partial(\omega+M)}\cos i - \frac{\partial T}{\partial \Omega}\right\}. \tag{2.9c}$$

Using the second set, i.e. with the right ascension of ascending node Ω kept constant, equation (2.9c) must be replaced by:

$$\frac{\partial T}{\partial w} = \frac{1}{r\sin(\omega+M)}\frac{\partial T}{\partial i}. \tag{2.9d}$$

The equations (2.9c) and (2.9d) are singular at arguments of latitudes of respectively 90° and 0°. In order to overcome these singularities, these equations are combined into:

$$\frac{\partial T}{\partial w} = \left[\cos^2(\omega+M)+\sin^2(\omega+M)\right]\frac{\partial T}{\partial w} = \tag{2.9e}$$

$$\frac{\cos(\omega+M)}{r\sin i}\left\{\frac{\partial T}{\partial(\omega+M)}\cos i - \frac{\partial T}{\partial \Omega}\right\} + \sin(\omega+M)\frac{\partial T}{r\,\partial i}.$$

For circular reference orbits the combination of the equations (2.2a)- (2.2b) and (2.9a)-(2.9e) yields:

$$f_{u,lmp} = \frac{\mu a_e{}^l}{r^{l+2}}(-l-1)F_{lmp}S_{lmp\,0} \tag{2.10a}$$

$$f_{v,lmp} = -\frac{\mu a_e{}^l}{r^{l+2}}(l-2p)F_{lmp}S^*_{lmp\,0} \tag{2.10b}$$

$$f_{w,lmp} = -\frac{1}{2}\frac{\mu a_e{}^l}{r^{l+2}}\left[\left[\frac{F_{lmp}}{\sin i}((l-2p)\cos i - m) - F'_{lmp}\right]S^*_{(l+1)mp\,0}\right.$$

$$\left.+\left[\frac{F_{lmp}}{\sin i}((l-2p)\cos i - m) + F'_{lmp}\right]S^*_{(l-1)mp\,0}\right] \tag{2.10c}$$

Inserting the equations (2.10a)-(2.10c) in the Hill equations and applying the Laplace transformation, expressions can be derived which describe the radial, along-track and cross-track perturbations (Schrama, 1989). These formula's can be split into a particular and a homogeneous solution. For perturbations in the radial and along-track direction, the particular solution is equal to the formula's derived in Section 2.2 (equations (2.6a)-(2.6b)) for non-resonance gravity field perturbations. For perturbations in the cross-track solution, the particular solution of equation (2.7c) reads:

$$\Delta c_{lmp} = \frac{1}{2} r \left[\frac{a_e}{r}\right]^l \left[\frac{1}{f_{lmp}(f_{lmp}+2)} \left[\frac{F_{lmp}}{\sin i}((l-2p)\cos i - m) - F'_{lmp}\right] S^*_{(l+1)mp\,0}\right.$$

$$\left. + \frac{1}{f_{lmp}(f_{lmp}-2)} \left[\frac{F_{lmp}}{\sin i}((l-2p)\cos i - m) + F'_{lmp}\right] S^*_{(l-1)mp\,0}\right] . \qquad (2.11)$$

The equations (2.6c) and (2.11) have been tested numerically and equivalent results were obtained if the total perturbation of one harmonic coefficient (summation over p) was computed. The homogeneous solution represents the orbit perturbations caused by epoch-vector errors (or errors in the initial conditions) and is of the form (Schrama, 1989):

$$u = (a_u^0 + a_u^1 t)\cos nt + (b_u^0 + b_u^1 t)\sin nt + c_u^0 \qquad (2.12a)$$

$$v = (a_v^0 + a_v^1 t)\cos nt + (b_v^0 + b_v^1 t)\sin nt + (c_v^0 + c_v^1 t) \qquad (2.12b)$$

$$w = a_w^0 \cos nt + b_w^0 \sin nt \qquad (2.12c)$$

For resonance gravity field perturbations the solution takes a different form. This resonance occurs when $f_{lmp} = 0$ or ± 1 and this is always the case for part of the zonal gravity field perturbations. In (Schrama, 1989) expressions have been derived for resonance orbit perturbations. As an example, the resonance radial orbit perturbations caused by zonal constituents for which $f_{lmp} = 0$ or ± 1 can be found by inserting these constituents in those expressions. This procedure yields:

$$l\ even: u_{l0l/2} = \frac{\Delta \bar{C}_{l0}}{n^2} \frac{(l+1)\mu a_e^{\,l}}{r^{l+2}} F_{l0l/2}(\cos nt - 1) \qquad (2.13a)$$

$$l\ odd: u_{l0(l\pm1)/2} = \Delta \bar{C}_{l0} \frac{\mu a_e^{\,l}}{r^{l+2}} \left[F_{l0(l-1)/2} - F_{l0(l+1)/2}\right] \frac{l-1}{2n} \left(t\cos nt - \frac{1}{n}\sin nt\right) \qquad (2.13b)$$

Comparing the equations (2.12a) and (2.13a)-(2.13b), it can be seen that the resonance perturbations can be "absorbed" by the homogeneous solution. In other words, orbit perturbations caused by resonance zonal terms can be "absorbed" by adjusting the satellite epoch-vector. This statement is, of course, only true as long as the orbit perturbations are small and in addition to this, the linearization of the orbit perturbation equations is justified.

In the next Chapter attention will be paid to the accuracy of the orbit perturbations derived by the linearized theories described in this Chapter.

3. Comparison between the linear perturbation theory and numerical orbit integration

3.1 Introduction

Considering the accuracy of recent gravity field models, it becomes possible to compute high-precision satellite orbits. This has as a result that the orbit perturbations caused by gravity field model errors become very small. Therefore, in order to model these perturbations, it will be justified to linearize the equations of motion relative to the high-precision orbits and the errors due to this linearization will be small. In that case, the linear perturbation theory described in the previous Chapter can be used to model satellite orbit perturbations caused by gravity field model errors. In order to support this statement, a test was performed in which the results of a numerical orbit integration were compared with the results of the linear perturbation theory, as described in Chapter 2.

The test started with the computation of a satellite orbit with two different gravity field models by numerical integration. The differences between the satellite orbits that were obtained in this way were compared with the differences predicted by the application of the linear perturbation theory. In the latter case, the differences between the coefficients of the two gravity field models were used in the LPT to model the orbit differences.

The two selected gravity field models were GEM-T1 and GEM-T2, truncated at degree and order 36. The selected orbit was an ERS-1 like satellite orbit, with an inclination of 98.5162° and a semi-major axis of 7158741.2 m. The application of these orbit parameters led to a repeat period of 3 days, comprising 43 orbital revolutions. A repeat orbit is defined as a satellite orbit that repeats exactly after an integer number of orbital revolutions, i.e. after this number of revolutions the satellite is at the same geographical position. For the test, the orbit was integrated over a period of 6 days, i.e. two repeat periods, centered at the epoch for which the orbital elements were assumed to be known. So, the orbit was integrated 3 days backward in time and 3 days forward in time. Using this procedure, the orbit differences in the center of the 6-day orbit were equal to zero.

Having a satellite orbit with a repeat period has one very specific advantage over "ordinary" satellite orbits: the orbit perturbations as predicted by the LPT (equations (2.6a)-(2.6c)) become true Fourier series. In that case, the amplitudes of the orbit perturbations predicted by the LPT can be compared with the amplitudes computed by applying a discrete Fourier transformation on the orbit differences derived from numerically integrated orbits. To be able to use the discrete Fourier transformation, orbit differences with a constant sampling interval are necessary for an integer number of repeat periods (Colombo, 1984). Fourier series were computed from the orbit differences computed from the numerically integrated satellite orbits and were

predicted by the LPT. This means that the orbit differences were represented as:

$$\Delta orbit = \sum_{i=1}^{nmax} a_i \cos(iu/nrev) + b_i \sin(iu/nrev) \qquad (3.1)$$

where a_i and b_i are the Fourier amplitudes, and u the argument of latitude.

In the first part of this Chapter, the computation of orbit differences by subtracting two numerically integrated orbits is described. After this, the modeling of these orbit differences by the LPT is discussed, followed by a comparison between the orbit differences computed by both techniques.

3.2 Orbit differences by numerical orbit integration

In order to be able to numerically integrate satellite orbits with high accuracy and stability, an Adams-Moulton integrator was developed and applied (Boyce and DiPrima, 1986). The characteristics of this integrator are described in Appendix F. The order of this integrator can be chosen freely. For the computations to be presented in this Chapter this order was taken equal to 10. The time step used was taken equal to 75 s. The selection of this time step was based on the following arguments. The gravity fields used are complete to degree and order 36. This means that the resolution of the gravity field variations, defined as half the smallest wavelength of a gravity field model, was equal to 5°. The satellite traverses an orbital arc of about 5° in 75 s. Therefore with an integration step of 75 s the gravity field variations modeled can be "followed", leading to a stable orbit integration. In order to support the preceding assumption, 3-day ERS-1 orbits were computed with time steps equal to 150 s, 75 s and 37.5 s with the integration order equal to 10 using the GEM-T1 gravity field model. The integration took place in an inertial rectangular coordinate frame, with its origin coinciding with the Earth's geocenter. It was found that the rms of the orbit differences between the orbits computed with a time step of 150 s and 75 s were on the order of 10^7 m in orbital position and 10^4 m/s in orbital velocity. The rms of these orbit differences were on the same order of magnitude for the orbits computed with time steps equal to 150 s and 37.5 s. In contrast, the rms of these orbit differences were on the order of 1 m in position and 1 mm/s in velocity for the orbits computed with time steps equal to 75 and 37.5 s. In order to justify the choice of 10 for the integration order, 3-day ERS-1 orbits were computed with this order equal to 9, 10 and 11 with the time step equal to 75 s, again with the GEM-T1 gravity field model. The increase of the integration order from 9 to 10 resulted in an rms of orbit differences equal to about 10 m in position, and 1 cm/s in velocity. For an increase of this order from 10 to 11, the rms of orbit differences was equal to about 1 m in position and 1 mm/s in velocity. Therefore, it is concluded that with an integration order equal to 10 and a time step of 75 s, the numerical orbit integration has an accuracy of about 1 m in orbital position and 1 mm/s in orbital velocity.

After this, ERS-1-like satellite orbits were computed with the GEM-T1 and GEM-T2 (truncated at degree 36) models for a 6-day period. The resulting GEM-T1 and

GEM-T2 orbit ephemerides were transformed into orbit differences in the satellite radial, cross-track and along-track directions. The rms of these differences was respectively equal to 3.49 m, 3.02 m and 97.76 m for the radial, cross-track and along-track directions. The mean of these differences was equal to respectively -0.41 m, -7.80 m and 0.02 m for the radial, along-track and cross-track directions.

In order to be able to perform a discrete Fourier transformation on the orbit differences, non-periodic and resonant orbit differences were filtered out by estimating epoch state-vector terms of the form indicated by the equations (2.12a)-(2.12c). Subtracting these terms from the orbit differences, new orbit differences were formed. These were found to have an rms of respectively 1.90 m, 1.90 m and 7.86 m for the radial, cross-track and along-track direction. By estimating the epoch state-vector terms, the orbit computed with GEM-T2 was "fitted" to the orbit computed with GEM-T1.

After this, a discrete Fourier transformation was applied to these new orbit differences. This resulted in spectra displayed in the top of the Figures 3.1, 3.2 and 3.3. As can be seen, the larger part of the orbit differences is concentrated at 0 and 1 cpr. This concentration can be explained by considering the equations (2.6a)-(2.6c). The denominator of these equations becomes zero for orbit perturbations with a frequency equal to 0 and/or 1 cpr (resonance). Thus, for orbit perturbations with a frequency close to 0 or 1 cpr, the amplitudes of the Fourier spectra will be relatively large.

3.3 Orbit differences predicted by linear perturbation theory

The orbit differences in the radial, cross-track and along-track directions caused by the GEM-T1 and GEM-T2 coefficient differences were also computed with the LPT described in the previous Chapter. As indicated in Section 3.1, the orbit perturbations can be represented by a Fourier series for a repeat period, and by epoch state-vector terms. As explained in the previous Section, the state-vector terms have been filtered out of the orbit differences of the numerically integrated orbits. Therefore only attention will be paid to the Fourier series. The application of the LPT to the GEM-T1/GEM-T2 coefficient differences led to frequency spectra displayed in the middle of the Figures 3.1, 3.2 and 3.3. The power of these spectra, which is defined as the rss (root-sum-square) of the amplitudes of these spectra divided by the square root of 2, was equal to respectively 1.94 m, 1.89 m and 7.62 m for the radial, cross-track and along-track directions. These values compare very well with the rms-values of the orbit differences of the previous Section (after the subtraction of the epoch state-vector and resonance terms). As can be seen from the Figures, again the greater part of the orbit differences is concentrated at 0 and 1 cpr.

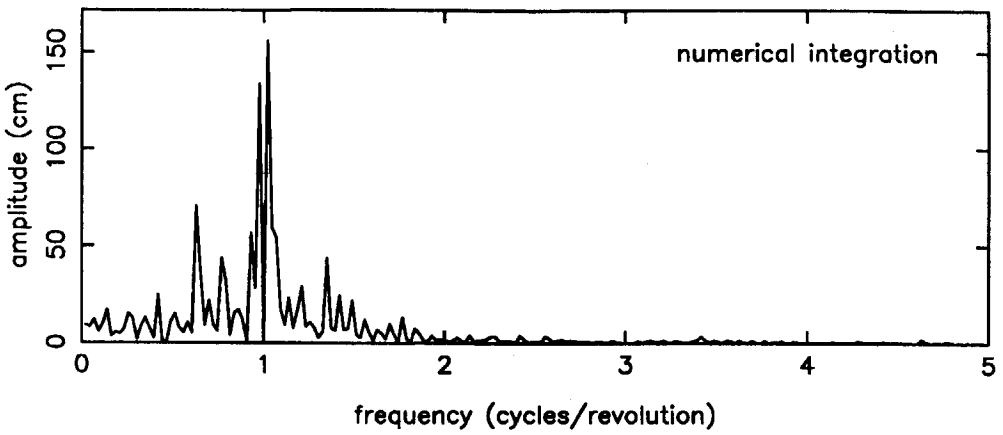

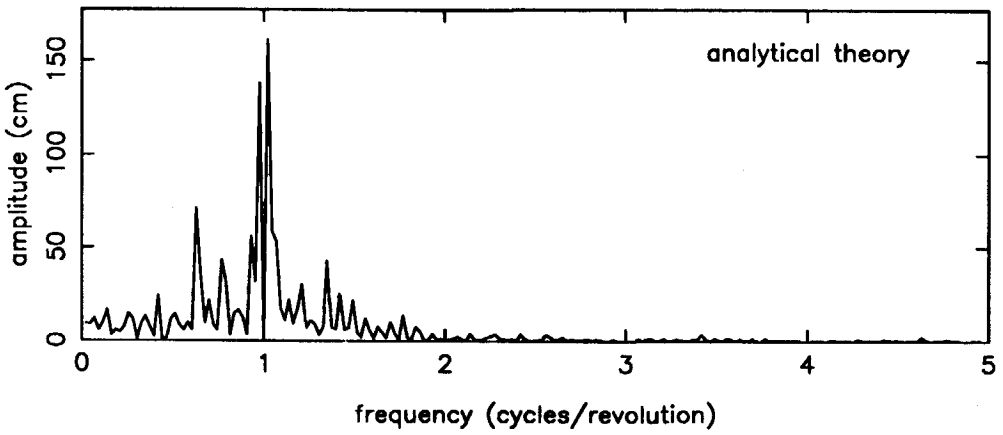

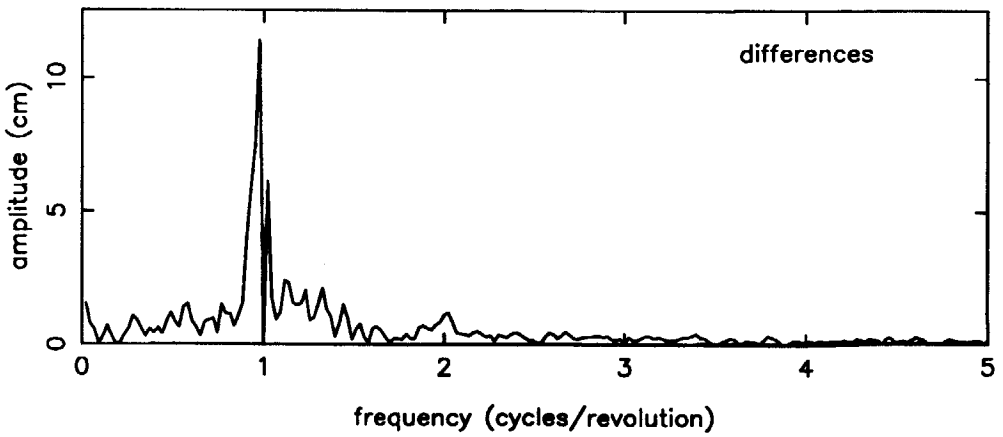

Figure 3.1 Radial orbit perturbations for the ERS−1 satellite from GEM−T1 and GEM−T2 coefficient differences

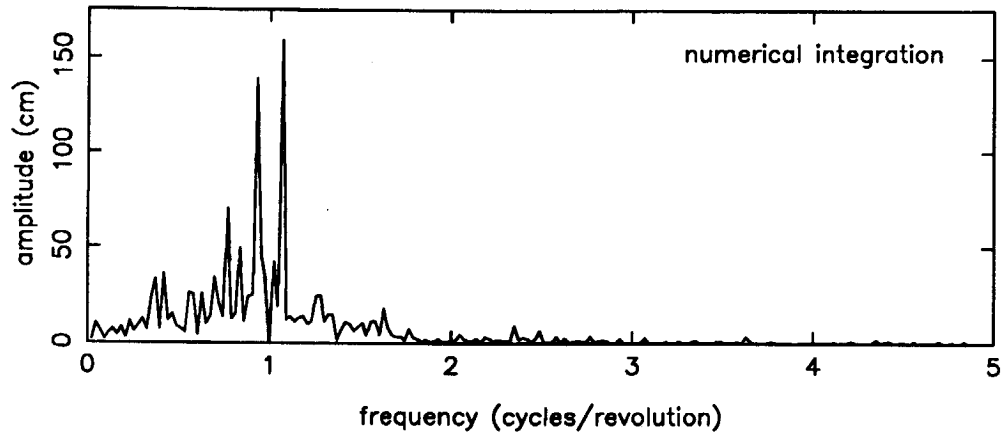

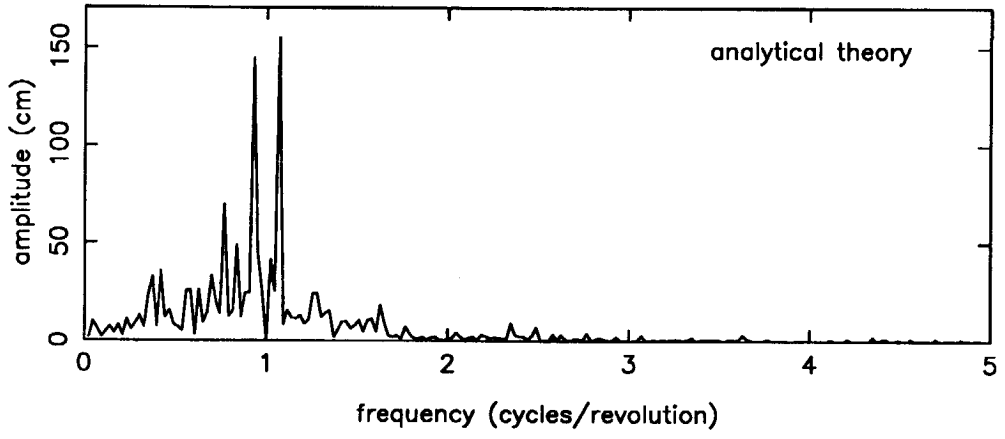

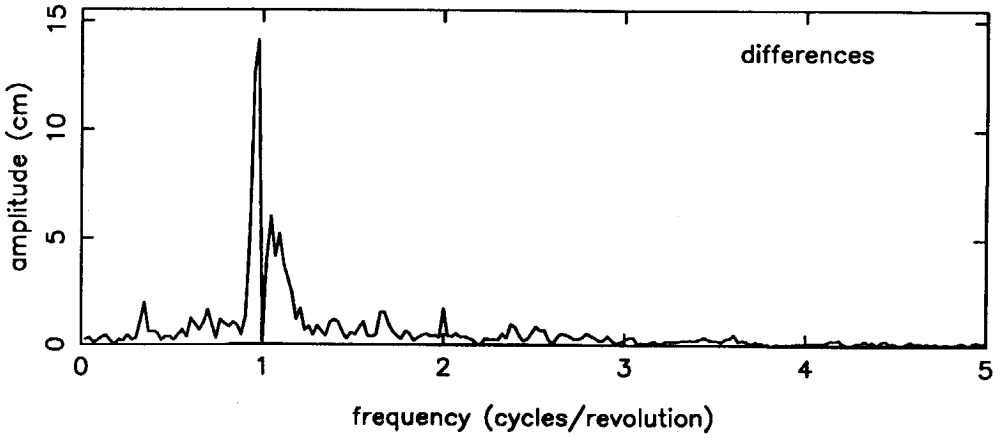

Figure 3.2 Cross track orbit perturbations for the ERS–1 satellite from GEM–T1 and GEM–T2 coefficient differences

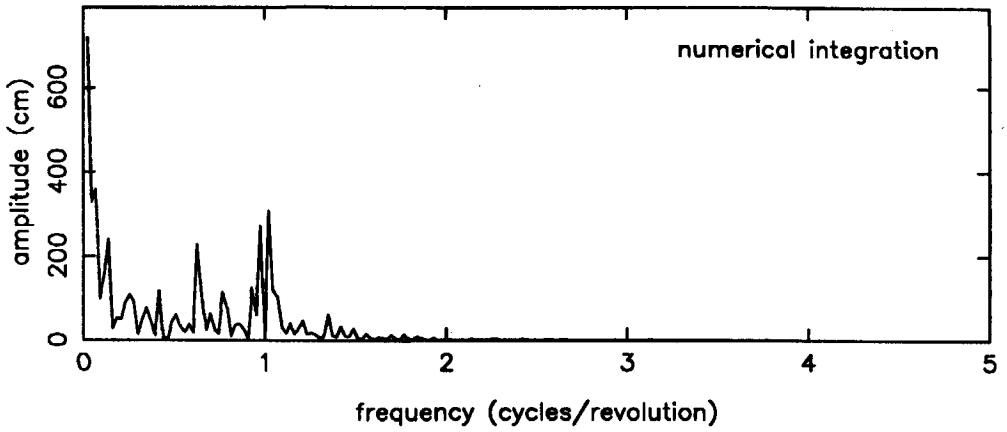

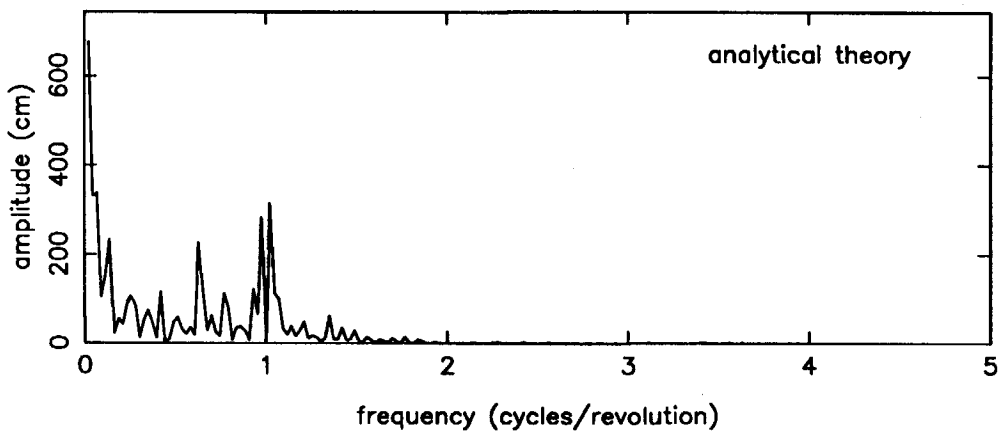

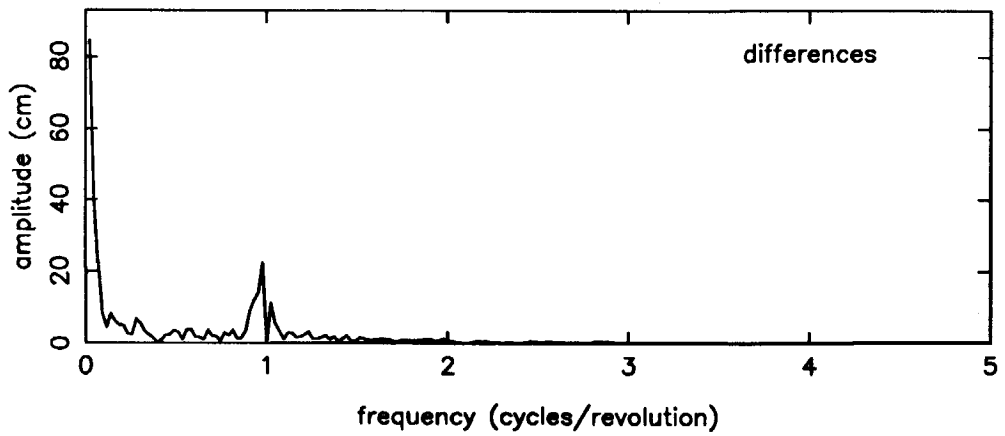

Figure 3.3 Along track orbit perturbations for the ERS–1 satellite from GEM–T1 and GEM–T2 coefficient differences

3.4 Comparison between numerical orbit integration and LPT

The frequency spectra obtained with the two techniques described above, were compared by subtracting the coefficients a_i and b_i (equation (3.1)), which resulted in "difference" frequency spectra. These spectra are displayed at the bottom of the Figures 3.1, 3.2 and 3.3. The power of these spectra was respectively 0.19 m, 0.24 m and 1.05 m for the radial, cross-track and along-track directions. These power values are only a fraction (~ 10 %) of the power values of the orbit differences of the numerically integrated orbits (Section 3.2). Therefore, it can be concluded that the LPT is an appropriate tool for modeling orbit errors. Moreover, it must be noted that the GEM-T1 and GEM-T2 models are known to behave relatively poorly for the chosen orbital inclination of about 98° (Marsh et al., 1986 and 1989a). This means that for other orbital inclinations the differences between the orbit differences computed by numerical orbit integration and by the LPT are expected to be smaller.

Part II. Application of LPT to real satellite observations

4. The satellite altimeter measurement

4.1 Introduction

In part II of this thesis the LPT will be used in the analysis of real satellite observations. The observations used in this analysis consisted of satellite laser range measurements and satellite altimeter measurements of the altimeter satellites SEASAT and GEOSAT. This Chapter will give a description of the satellite altimeter measurement together with error sources that affect such a measurement. An assessment of the magnitude of these error sources for the SEASAT and GEOSAT altimeter measurements will be included. This description will be the basis for the analysis and the mathematical modeling of these measurements. This Chapter will conclude with the description of a special type of difference between two altimeter measurements, the so-called crossover difference.

4.2 The altimeter measurement

In the ideal case, a satellite altimeter measurement is equal to the instantaneous distance between the satellite's geocenter and the ocean surface. However, an altimeter measurement is subject to many disturbances which have to be accounted for (Figure 4.1). An altimeter measurement may be written in the following form (Tapley et al., 1982):

$$h^* = h+h_{sg}+h_i+h_a+h_s+h_g+h_t+h_0+\epsilon \qquad (4.1)$$

All the individual terms will be explained briefly, together with an accuracy assessment for the SEASAT and GEOSAT altimeter measurements (a more extensive analysis of these terms is given in (Tapley et al., 1982) and (Zandbergen, 1990)). The left-hand side h^* represents the distance between the satellite's geocenter and a chosen reference ellipsoid and is a result of a precise orbit computation. For example, using the GEM-T2 gravity field model, the error of this term for GEOSAT is approximately 40 cm compared to a value for h^* of about 800 km (Haines et al., 1990). Because SEASAT is in a comparable orbit, the error of this term for SEASAT will be of the same order of magnitude (in Chapter 5 it will be shown that this is the case). The actual measurement is represented by h, with a value of about 800 km and a

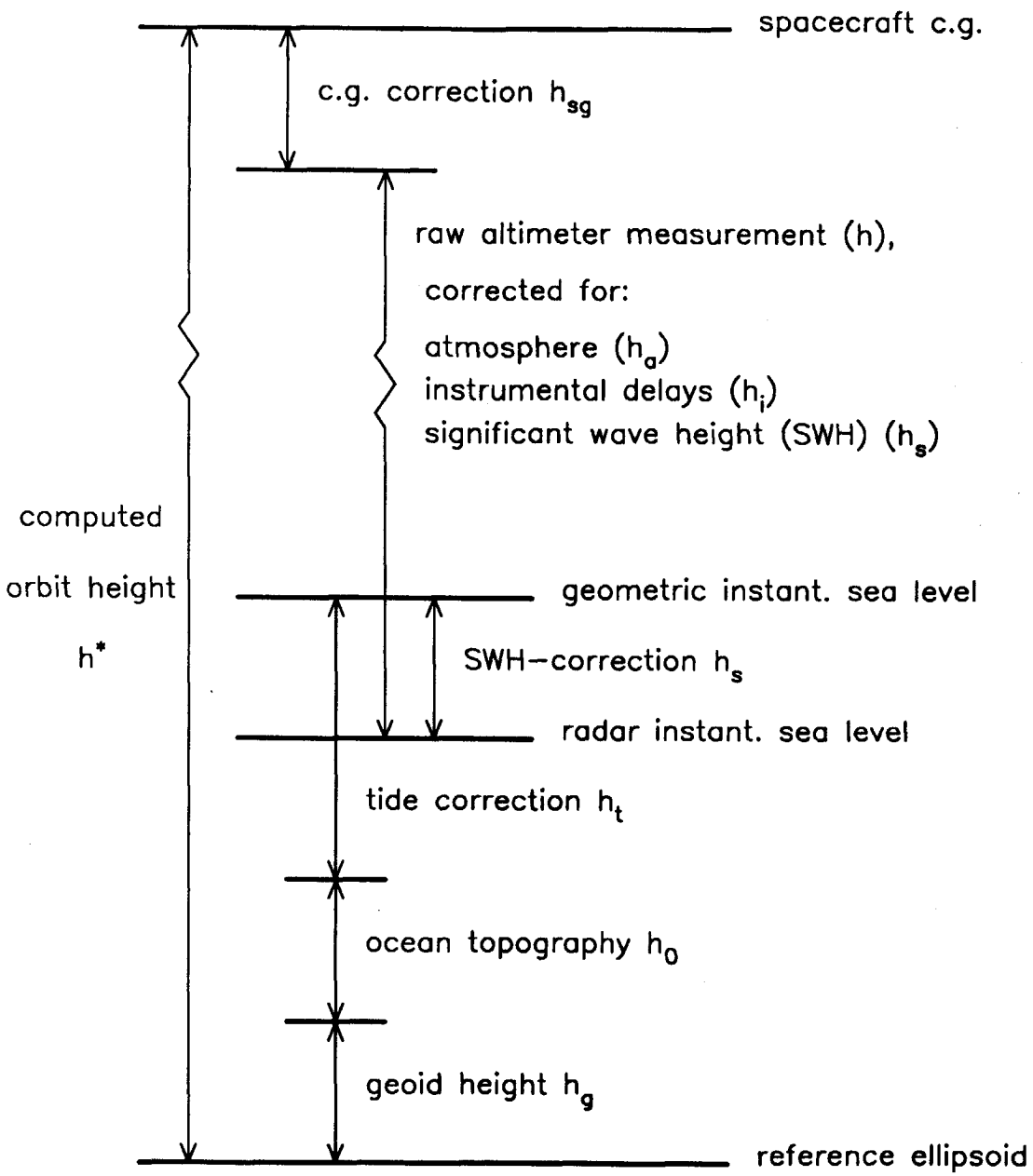

Figure 4.1 Altimeter measurement geometry

measurement noise ε of 2-5 cm. The measurements have to be corrected for the position offset of the altimeter instrument from the satellite's geocenter: h_{sg}. This value can be determined very accurately before launch. Furthermore, corrections have to be applied to account for instrumental delays: h_i. These corrections are on the order of a few decimeters with subdecimeter accuracy. The correction term h_a represents atmospheric path length delays, i.e. the altimeter measurement has to be reduced by this correction. This term can be divided into a tropospheric correction, on the order of 2.5 m with an error of 3-6 cm, and an ionospheric correction, on the order of 30 cm with an error of 2-3 cm. An additional instrument correction, h_s, has to be applied to account for the interaction between the radar pulse and the ocean surface. This correction is mostly a few percent of the so-called significant wave height (SWH). This SWH is on the order of a few meter, but in extreme circumstances this SWH may be as big as 20 m. The error of this correction is 1-2 % of the SWH, i.e. 1-40 cm. However, on the average the SWH will be below 4 m, thus the error below 4-8 cm.

The geoid height and the height induced by the solid Earth and ocean tides are represented by respectively h_g and h_t. For the long-wavelength part of the geoid, i.e. for wavelengths above 4000 km, the error of recent gravity field models is on the order of 50 cm. For example, the error in the long-wavelength geoid computed with GEM-T2 is expected to have a magnitude of 52 cm using the GEM-T2 gravity field model. This is the so-called geoid commission error of the GEM-T2 gravity field. This commission error was found by taking into account the error estimates of the GEM-T2 coefficients (Marsh et al., 1989a). The errors in modeling of solid-Earth and ocean tides are typically about 2 and 10 cm respectively for the large ocean basins. Finally, h_0 represents the ocean surface topography. This topography is the elevation of the surface of the ocean above the geoid caused by ocean dynamics. This ocean topography consists of a permanent and a variable part. The permanent part is defined as the dynamic sea surface topography. This topography has an rms of about 65 cm. In Chapter 6, it will be described how a long-wavelength dynamic sea surface topography model is determined together with a gravity field model adjustment. The variable part of the ocean surface topography is known to have an rms of about 15 cm.

If all corrections have been applied and the reference models have been used, the result is the so-called sea height residual. This sea height residual can be represented as:

$$\Delta h = \Delta h_g - \Delta r + h_{SST} + \sigma \qquad (4.2)$$

The right-hand side of this equation consists of the geoid error Δh_g, the radial orbit error Δr, the dynamic sea surface topography h_{SST} and a term σ representing the errors in all corrections, ocean surface variability and measurement noise. This σ has an rms-value of about 21 cm, which has been obtained by taking the rss of the error terms and ocean surface variability described above.

4.3 The crossover difference

Considering all the different phenomena that affect an altimeter measurement, it will be obvious that it is hazardous to use the altimeter measurement in the original form (equation (4.1)) as satellite tracking data in a precise orbit determination. In addition, it will also be difficult to use these observations in a gravity field model adjustment. In Chapter 6, it will be shown that for the use of these measurements in gravity field modeling, special procedures must be followed. For example, errors in the geoid h_g and the ocean topography h_o are completely correlated with the radial position of the satellite, i.e. these errors can be completely compensated by a radial orbit error, and in addition, errors in the modeling of the ocean topography can be compensated by a geoid error. However, a special type of tracking observation can be formed in which most of these errors are canceled. This measurement is defined as the satellite altimeter height crossover difference, in the following referred to as crossover difference. A crossover difference is formed by subtracting two altimeter measurements made at the same geographical location, one of these measurements being made when the satellite was in a descending (southbound) pass, and the other being made when the satellite was in an ascending (northbound) pass (Zandbergen, 1990). A residual crossover difference is formed by subtracting the respective sea height residuals at these locations. In this way, all permanent components, like the geoid and permanent ocean topography, are canceled and with them errors in modeling these components. It can be shown that a crossover difference is for the greater part a representation of radial orbit differences and a residual crossover difference of the difference in radial orbit errors along the descending and ascending passes (Wakker et al., 1987a). It must be mentioned that, by forming a (residual) crossover difference, part of the information of the radial orbit differences (errors) gets lost. This is the part of the orbit difference (error) that is equal both for the ascending and descending pass and is referred to as the geographically correlated orbit difference (error). However, in Chapter 5, it will be shown that crossover differences can contribute to a precise orbit determination and gravity field modeling in a straightforward way.

Chapter 5. Gravity field recovery experiments with SEASAT

5.1 Introduction

The objective of the experiments described in this Chapter is to show and justify the application of the LPT in processing real satellite observations to adjust gravity field models. It will be demonstrated that the LPT is a powerful tool both for gravity field adjustment from satellite observations and for a quantitative analysis of the impact of future missions in this field. Much attention to these subjects will be paid in Chapter 6 and Part III of this thesis. The satellite observations used in the experiments described in this Chapter consisted of laser range measurements and crossover differences of the SEASAT satellite (1978). These observations were first used as input to the GEODYN program (Martin et al., 1980) together with suitable a priori models to compute the orbit of this satellite in such a way that this orbit fitted the observations best in a least-squares way. In fact, this means that the rms of differences between the real and modeled observations, the so-called observation residuals, was minimized. From the information content of these residuals, the gravity field model was to be adjusted.

The first part of this Chapter describes the concept of gravity field tailoring. Tailoring of a gravity field model means that only a certain amount of selected gravity field harmonic coefficients is adjusted. The gravity field adjustment process is a so-called least-squares adjustment, which basically comes down to the formation of the so-called observation equations and solution of the related normal equations. The concepts of least-squares and observation equations are explained in the second part of this Chapter.

Finally, gravity field tailoring experiments are described using the SEASAT satellite observations. These experiments included both gravity field adjustments by numerical integration and by implementing the LPT.

5.2 Concept of gravity field tailoring

From the LPT and the Figures 3.1 to 3.3, it may be concluded that the major part of the orbit perturbations are concentrated at frequencies below 2 cpr. It can also be shown that gravity field induced orbit errors can be modeled for the larger part by orders m of the geopotential running from 1 to the number of satellite orbital revolutions per day incremented with one (Rosborough, 1987b). From equation (2.2d), it follows that for every order m, 4 frequencies in the 0-2 cpr band are possible. For example, these frequencies are *-1-(5/nr),-(5/nr),1-(5/nr)* and *2-(5/nr)* for $m = 5$. Therefore, for each order m, 8 harmonic coefficients must be selected to model orbit errors. In addition, it has been shown in Chapter 2 that the linearized orbit perturbations in the

cross-track direction are decoupled from the perturbations in the radial and along-track directions. With the preceding statements, it seems possible to model orbit errors by adjusting the following number of gravity field harmonic coefficients:

$$d \bullet n \bullet p \bullet c \tag{5.1}$$

where,

d=2, because of the decoupling cross-track and radial-along-track;
n=number of revolutions per day + 1 (15 for SEASAT);
p=4 frequencies for each order m, take 4 degrees l;
c=2 harmonic coefficients per order m and degree l.

For the SEASAT orbit, with 14 1/3 orbital revolutions per day, the application of equation (5.1) means the adjustment of 240 harmonic coefficients. However, because the greater part of the satellite observations that will be used in the gravity field tailoring experiments (Section 5.5), the altimeter crossover differences, deliver only information about the radial orbit perturbations, only half of this number (the cross-track direction has not to be accounted for), i.e. 120 harmonic coefficients, will be adjusted.

The advantage of the concept of gravity field tailoring is that by this procedure the necessary computer time is limited. In addition to this, only a relatively small set of SEASAT observations will be used (Section 5.5). With such a small data set, there is not enough information for the adjustment of a complete gravity field model.

5.3 Least-squares parameter adjustment

In the first part of this Section, the concept of the least-squares solution of so-called observation equations is described. Added to this solution may be a priori information of the quality of the parameters that are adjusted in the least-squares solution. The second part of this Section describes the inclusion of this information, leading to a so-called minimum-variance solution with a priori information or Bayesian least-squares.

Assume an a priori model for the satellite observations, so that each observation O_i can be modeled as C_i:

$$C_i = F(X_s \cdots \dot{X}_s, \bar{C}_{lm} \cdots \bar{S}_{lm}, P_1 \cdots P_m, t_i) \tag{5.2}$$

where the elements X are orbit epoch state-vector elements, $\bar{C}_{lm}$ and $\bar{S}_{lm}$ are gravity field harmonic coefficients and P are several other model parameters, e.g. ground tracking station coordinates, non-conservative force model parameters, etc. The variable t_i represents the time at which the observation was made.

In the least-squares method the residual is modeled by a first-order Taylor-series expansion of equation (5.2):

$$O_i - C_i = \left[\frac{\partial F}{\partial X_s}\right]_{t_i} \Delta X_s \cdots + \left[\frac{\partial F}{\partial \bar{C}_{lm}}\right]_{t_i} \Delta \bar{C}_{lm} \cdots + \left[\frac{\partial F}{\partial P_i}\right]_{t_i} \Delta P_i \cdots \tag{5.3}$$

If i is summed over all observations, equation (5.3) reads in matrix notation:

$$A\,\Delta X = R \tag{5.4}$$

where,

$$A = \begin{bmatrix} \left[\frac{\partial F}{\partial X_s}\right]_{t_1} & \cdots & \left[\frac{\partial F}{\partial \bar{C}_{lm}}\right]_{t_1} & \cdots \\ \vdots & \cdots & \vdots & \cdots \\ \vdots & \cdots & \vdots & \cdots \\ \left[\frac{\partial F}{\partial X_s}\right]_{t_i} & \cdots & \left[\frac{\partial F}{\partial \bar{C}_{lm}}\right]_{t_i} & \cdots \\ \vdots & \cdots & \vdots & \cdots \\ \vdots & \cdots & \vdots & \cdots \end{bmatrix} \tag{5.5}$$

$$\Delta X = (\Delta X_s \cdots, \Delta \bar{C}_{lm}, \cdots, \Delta P_i, \cdots)^T \text{ and} \tag{5.6}$$

$$R = \begin{bmatrix} O_1 - C_1 \\ \vdots \\ O_i - C_i \\ \vdots \end{bmatrix}. \tag{5.7}$$

In general, more observations than parameters to be adjusted are available so that the system (5.4) is overdetermined, provided that the observations are not linearly dependent. The least-squares solution is obtained by minimizing:

$$\varepsilon^T \varepsilon = (R - A\,\Delta X)^T (R - A\,\Delta X). \tag{5.8}$$

The solution of this minimization is:

$$\Delta X = (A^T A)^{-1} A^T R \tag{5.9}$$

where $(A^T A)^{-1} = V$ is called the (formal) variance-covariance matrix of the solution for the parameters ΔX for uncorrelated observation errors, if all observations would have a variance $\sigma^2 = 1$. Otherwise, this matrix must be multiplied with this variance. The formal standard deviations σ_i of and correlations ρ_{ij} between different adjusted parameters can be calculated from this matrix V:

$$\sigma_i = \sqrt{V_{ii}} \tag{5.10}$$

$$\rho_{ij} = \frac{V_{ij}}{\sigma_i \sigma_j} \tag{5.11}$$

In addition to the observation equations (5.4), information may be available about

the (co-)variances of parameters of the a priori models that were used in the computation of the C_i. This information is most often represented by a (calibrated) covariance matrix V_A. Also information of the accuracy of the observations may be available. In that case, the contribution of each observation equation is scaled by this accuracy. This is equivalent to multiplying the matrix A and vector of residuals R with a weight matrix W. In this case the so-called minimum-variance solution with a priori information is obtained by minimizing (Kendal and Alan, 1961):

$$Q = (WR - WA\,\Delta X)^T (WR - WA\,\Delta X) + \Delta X^T V_A^{-1} \Delta X \tag{5.12}$$

The solution of this minimization leads to:

$$\Delta X = (A^T W^T WA + V_A^{-1})^{-1} (A^T W^T WR) \tag{5.13}$$

In this case the matrix $(A^T W^T WA + V_A^{-1})^{-1}$ represents the a posteriori covariance matrix of the solution. It can readily be seen that in the case of uniform data weights ($W=I$) and no a priori information about the quality of the a priori parameter values ($V_A^{-1} = 0$), equation (5.13) reduces to (5.9).

5.4 Observation equations

As mentioned in the previous Section, the observation residuals are modeled by a first-order Taylor-series expansion (i.e. by linearization). This leads to the so-called observation equations (5.4)-(5.7), which are solved by the least-squares method. In order to be able to compute the observation equations, the partial derivatives of the function F, that models the relation between the observations and the parameters to be adjusted, must be known. This Section describes the derivation of the partial derivatives of SEASAT altimeter crossover differences and laser range measurements to gravity field harmonic coefficients by applying the LPT.

As explained in Section 4.3, a residual crossover difference is for the greater part caused by radial orbit errors. In that case, a residual crossover difference can be modeled by subtracting the radial orbit error of the sea heigh residual (equation (4.2) of the descending pass from the radial orbit error of the sea height residual of the ascending pass. If these orbit errors are caused by gravity field modeling errors, a residual crossover difference $\Delta Xover$ can be modeled by using equation (2.6a):

$$\Delta Xover = \sum_{l=2}^{lmax} \sum_{m=0}^{l} \sum_{p=0}^{l} \left\{ (\Delta r_{lmp})_{asc} - (\Delta r_{lmp})_{des} \right\} \tag{5.14}$$

The partial derivative of this residual crossover difference to a gravity field harmonic coefficient is easily found by inserting the equations (2.2b) and (2.6a) in equation (5.14).

For satellite laser range measurements the derivation of the partial derivatives to gravity field harmonic coefficients is more complicated. This kind of measurement gives the instantaneous range between the orbiting satellite and a ground station. Laser

range residuals are formed by subtracting the laser range measurements computed with a priori models from the real laser range measurements. Assuming that these residuals are the result of orbit errors (in general the position of ground stations is known with high precision), orbit errors in the radial, along-track and cross-track direction must be considered. The partial derivatives of laser range measurements to gravity field harmonic coefficients by applying the LPT are then found by taking the partial derivative of a combination of the equations (2.6a)-(2.6c) to the harmonic coefficients. The computation of this partial derivative is quite laborious. The procedure to compute this partial derivative is described in Appendix B.

5.5 Gravity field tailoring experiments

Gravity field tailoring experiments were performed using SEASAT residual crossover differences and laser range residuals from 4 three-day periods (from 15th of September to 28th of September 1978). These observations were first processed by the GEODYN software package (Martin et al., 1980). This means that with a priori force models the SEASAT orbit was integrated numerically in such a way that the rms of the observation residuals (obtained by subtracting the computed observations along the computed SEASAT orbit from the real observations) was minimized. In other words, the SEASAT orbit parameters were determined by the method of least-squares adjustment. The same set of observations was used in (Zandbergen, 1990). The a priori gravity field model consisted of the GEM-T1 gravity field model complete to degree and order 36. In addition to this gravity model, other a priori models were used. An overview of these models is given in Table 5.1 (Zandbergen, 1990). The most important models listed in this Table may be summarized as follows. Solid-Earth tides were taken into account in the force modeling, but also in the displacement of the position of the laser stations. The laser station coordinates were taken from the general-purpose UT/CSR 8402 global station coordinates set. The atmospheric drag was modeled using the MSIS atmospheric model (Hedin et al., 1977) with daily estimated drag coefficients. In addition, a solar radiation parameter was estimated for each 3-day period to model the radiation pressure. Thus, for each 3-day period a number of 10 state-vector parameters had to be estimated, 3 daily drag parameters, 1 solar radiation parameter and 6 orbit epoch state-vector parameters consisting of the 6 Kepler elements. The orbit parameters of the SEASAT orbit are listed in Table 5.2. This Table shows that the SEASAT orbit is a so-called repeat one: the orbit repeats after 3.01 solar days or 3 satellite nodal days (called an arc), or 43 orbital revolutions.

The GEODYN computations led to SEASAT reference orbits and computed laser range measurements and crossover differences. These computed measurements were subtracted from the real measurements to form measurement residuals. In the computations, measurements for which the residual was greater than 3.5 times the rms of all residuals were edited out. This was done automatically by GEODYN to exclude spurious measurements. This procedure was repeated until convergence. It was found that

Table 5.1 Summary of the main a priori models and other parameters used in the computation of the SEASAT orbits with GEODYN.

Gravity model	GEM-T1 complete to degree and order 36
Other modeling information	MSIS (1983) atmospheric drag, daily drag parameters Solar radiation pressure, 3-day parameters Area tables for drag and solar radiation Ocean tides: none Luni-solar attraction, JPL DE-96 ephemerides Wahr solid Earth tides, station tidal displacements Precession, nutation, polar motion, UT1 Indirect moon-J2 effect
Constants	a_e=6,378,137 m; flattening=298.257 gravity parameter=398600.436 km^3/s^2 speed of light=299792.5 m/s; SEASAT mass=2213.6 kg
Integration	11-th order Cowell integration, step size 75 s

Table 5.2 SEASAT orbit characteristics.

Semi-major axis (km)	7172.3
Eccentricity	0.0008
Inclination (deg)	108.0
Mean altitude (km)	797
Nodal period (min)	100.8
Ground track repetition period (day)	3.01
Equatorial spacing successive tracks (km)	2796
Spacing adjacent tracks the equator (km)	932
Rotation rate of the right ascension of ascending node (deg/day)	2.044

1.3 % of the measurements were edited out. The statistics of the so-obtained measurement residuals are listed in Table 5.3. The GEODYN computations led to 893 laser range residuals with an rms of 56 cm and 2806 residual crossover differences with an rms of 62 cm. The larger part of the residuals was assumed to be caused by geopotential mismodeling, i.e. by errors in the harmonic coefficients of the GEM-T1 model. The rms-value of the residual crossover differences indicates that the SEASAT reference orbits have an accuracy of about 45 cm in the radial position. This value was obtained by dividing the rms of the residual crossover differences by the square root of 2. However, as discussed in Section 4.3 of the preceding Chapter, a residual crossover difference only gives information of the non-geographically correlated orbit error. In (Rosborough, 1986 and 1988) it has been shown that this non-geographically correlated orbit error is of the same order of magnitude as the geographically correlated orbit error for orbit errors caused by geopotential mismodeling. In (Zandbergen, 1990) the most reliable estimate for the radial orbit accuracy for the SEASAT orbits using GEM-T1 was about 55 cm. However, this value was obtained for the case in which the SEASAT reference orbits were determined from only laser range measurements. The incorporation of crossover differences as tracking data may explain this poorer accuracy of 55 cm compared to the accuracy of 45 cm obtained above for the SEASAT reference orbits.

The laser range residuals and residual crossover differences were used in a GEM-T1 tailoring experiment. As discussed in Section 5.2, 120 harmonic coefficients will be selected, 8 harmonic coefficients for each order m from 1 to 15. Therefore, for each order m, 4 degrees l have been chosen. The selected harmonic coefficients are listed in Table 5.4. The choice of the 4 degrees for each order m was rather arbitrary, but it will be shown that very satisfactory results were obtained with this set of harmonic coefficients. Moreover, the most important objective of the tailoring experiments was to serve as a test bed for the LPT in gravity field adjustment compared to numerical integration, not to determine the most optimal set of 4 degrees l for each order m. The selected harmonic coefficients were estimated in a least-squares adjustment process as explained in Section 5.3. This estimation was done by computing the partial derivatives of the measurement residuals to the selected harmonic coefficients both by using the LPT and by numerical integration (GEODYN). In this way, two sets of 120 harmonic coefficient adjustments were obtained. By adding these adjustments to the a priori GEM-T1 coefficients, new tailored GEM-T1 models were obtained. With these new models, new SEASAT orbits and in conjunction new computed measurements, leading to new measurement residuals were computed with GEODYN. When the partial derivatives were computed by numerical integration, the rms of the residual crossover differences was reduced from an initial value of 62 cm (Table 5.3) to 43 cm (Table 5.5). Almost the same reduction was obtained when using the LPT in the computation of the partial derivatives. In this case, the rms of the residual crossover differences was reduced to 40 cm (Table 5.6, page 42). For the first case, the rms of the laser range residuals was reduced from 56 cm (Table 5.3) to 36 cm (Table 5.5). However, for the latter case, this value was reduced only to 50 cm (Table 5.6). This may be explained by the fact that in the GEODYN gravity field tailoring also a 10-element state-vector (see above) was estimated, together with the 120 selected

Table 5.3 Statistics of the laser range residuals and residual crossover differences for the reference SEASAT orbits.

	laser range res.		residual crossover diff.	
	number	rms (cm)	number	rms (cm)
arc1	208	65	736	63
arc2	242	47	701	62
arc3	232	49	643	59
arc4	211	62	726	62
total	893	56	2806	62

Table 5.4 Set of 120 harmonic coefficients selected for the gravity field model adjustment.

order	degree	number of coef.
1,2,3,4,5	5,6,7,8	40
6,7,8,9,10	10,11,12,13	40
11	12,13,14,15	8
12	13,14,15,16	8
13,14	14,15,16,17	16
15	15,16,17,18	8

Table 5.5 Improvement in the statistics of the laser range residuals and residual crossover differences of the SEASAT reference orbits by adjusting 120 harmonic coefficients by numerical integration.

	laser range res.		residual crossover diff.	
	number	rms (cm)	number	rms (cm)
arc1	207	49	735	48
arc2	241	34	698	43
arc3	231	36	634	39
arc4	210	41	724	41
total	889	36	2791	43

harmonic coefficients. This state-vector was not estimated in the LPT-technique. Especially the daily drag parameters can absorb a significant part of along-track orbit errors and thus reduce the laser range residuals. When the harmonic coefficients were adjusted with the LPT-technique, the state-vector terms were not taken into account. The harmonic coefficient adjustments with GEODYN and with the LPT-technique have been compared and the results are shown in the Figures 5.1-5.3 (page 43). Both methods led to harmonic coefficient adjustments that were of comparable and realistic magnitude (only a fraction of the magnitude indicated by Kaula's rule of thumb, equation (1.3)). Moreover, the spectra of the harmonic coefficient adjustments as a function of the order m were of the same form (Figures 5.1 and 5.2).

In Figure 5.3, the rms of harmonic coefficient adjustment differences between the two solutions are displayed as a function of the order m. These differences may have been caused by the included state-vector adjustments in the GEODYN computations and the exclusion of these adjustments in the LPT-technique. Especially, the differences between the harmonic coefficient adjustments of orders m close to 14 can be explained by aliasing of resonant state-vector terms in the LPT solution, because the SEASAT satellite makes about 14 orbital revolutions per day. The latter has as a result that the SEASAT orbit is in near-resonance with gravity field terms with the order m close to 14. In the GEODYN solution, the state-vector adjustments may have absorbed the resonance effects.

In addition to the preceding reflections, it may be argued that the greater part of the observation residuals, i.e. the crossover residuals, only deliver information of the radial orbit error. Therefore, there may be not enough information of the along-track and cross-track orbit errors to sufficiently constrain state-vector terms and 120 harmonic coefficients. Therefore, it is expected that the two solutions behave the same for modeling the radial orbit error, but may behave differently for modeling errors in the along-track and cross-track directions. In order to support this, the LPT was applied to compute frequency spectra for orbit perturbations in the radial, along-track and cross-track directions with the two solved sets of 120 harmonic coefficients, and the correlations between these spectra was computed. As can be seen in Table 5.7, the correlation for the radial direction is 0.71 and the correlation for the other two directions are negative, supporting the preceding reflections. Also the values for the power of the spectra for the radial direction, 44 cm for the LPT-solution and 54 cm for the GEODYN solution, are in agreement with the reduction of the apriori rms of the crossover residuals from 62 cm to approximately 40 cm. The high values for the power of the frequency spectra for the along-track and cross-track direction are caused by high values of the amplitudes close to the 0 and 1 cpr frequency. Perturbations with a frequency close to 0 and 1 cpr can be absorbed for a great part by state-vector terms.

It is concluded that tailoring the GEM-T1 gravity field model by using the LPT and by using GEODYN both led to new tailored GEM-T1 gravity field models that behave better in modeling the laser range measurements and crossover differences. Both methods led to harmonic coefficient adjustments of comparable magnitude and led to comparable reductions of the measurement residuals. It is therefore concluded that the LPT can serve as an appropriate tool in gravity field adjustments using satellite observations.

Table 5.6 Improvement in the statistics of the laser range residuals and residual cross-over differences of the SEASAT reference orbits by adjusting 120 harmonic coefficients by the LPT.

	laser range res.		residual crossover diff.	
	number	rms (cm)	number	rms (cm)
arc1	203	56	735	41
arc2	241	41	699	40
arc3	232	48	640	38
arc4	209	54	723	39
total	885	50	2797	40

Table 5.7 Frequency analysis of SEASAT orbit perturbations using the coefficient adjustments of both techniques.

direction	LPT solution power (cm)	GEODYN solution power (cm)	correlation
radial	44	54	0.71
along-track	449	407	-0.61
cross-track	91	66	-0.08

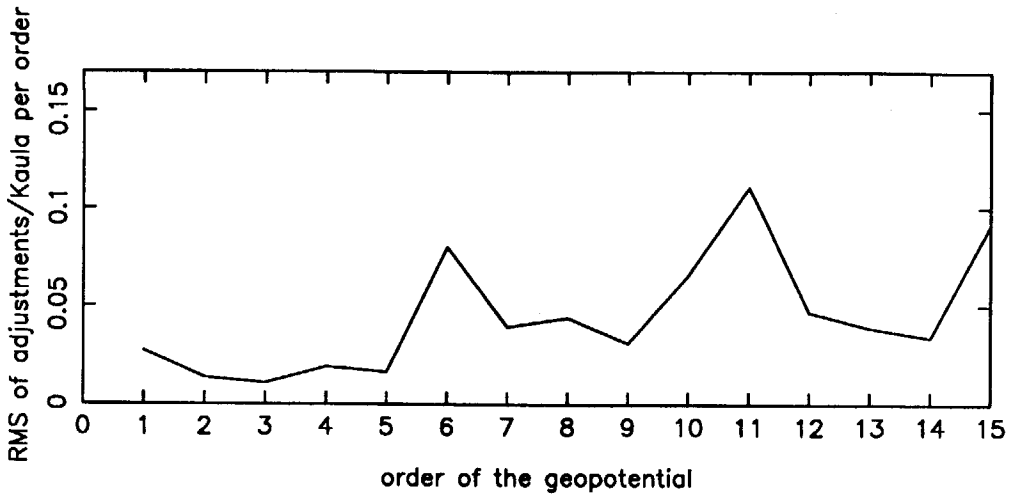

Figure 5.1. Coefficient adjustments by numerical integration (GEODYN)

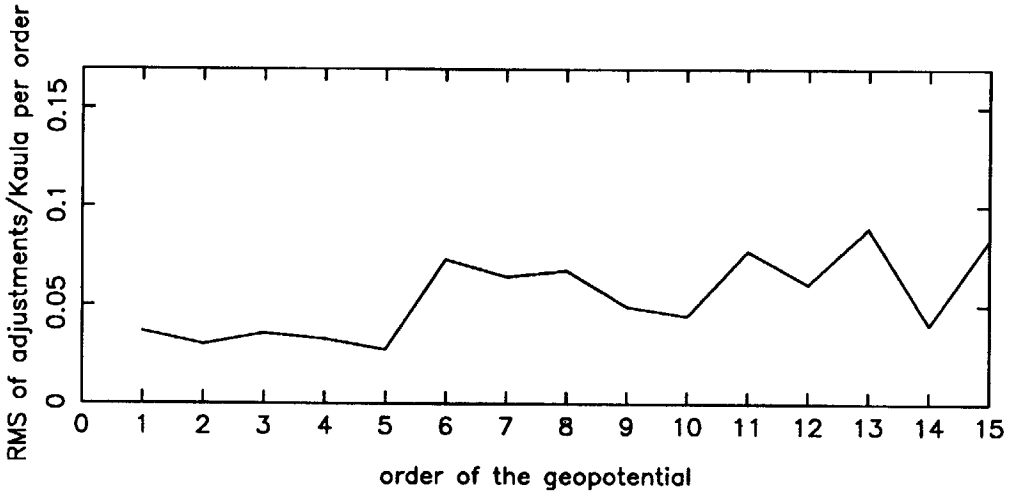

Figure 5.2. Coefficient adjustments by LPT

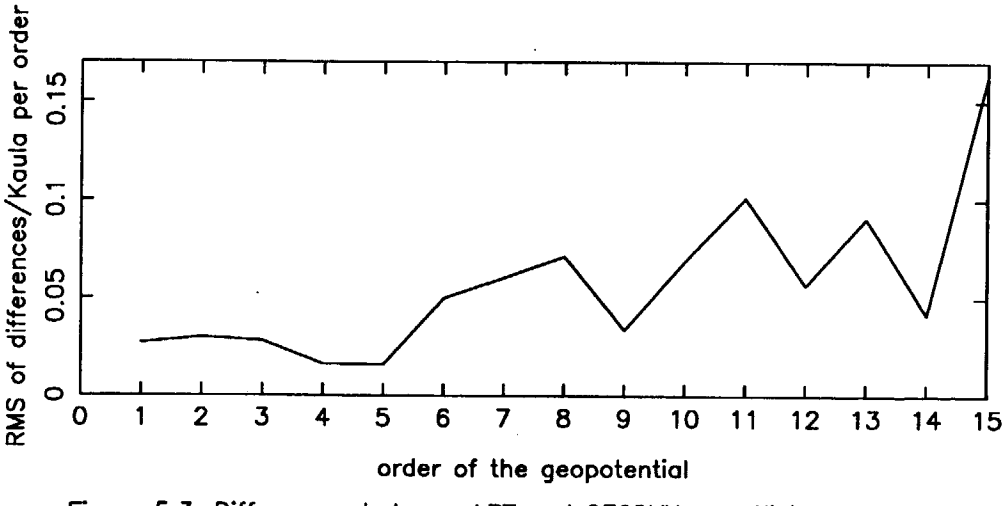

Figure 5.3. Differences between LPT and GEODYN ccoefficient adjustments

6. Simultaneous adjustment of the gravity field and determination of the dynamic sea surface topography from satellite altimetry

6.1 Introduction

The GEOSAT satellite has delivered a huge data set of satellite altimeter measurements with a high measurement precision. The continuous improvement in the accuracy of gravity field models has led to the possibility of computing GEOSAT satellite orbits with a radial accuracy of approximately 40 cm. This accuracy is achieved using the GEM-T2 gravity field model (Haines et al., 1990). This model has been used at the NASA Goddard Space Flight Center in the computation of GEOSAT orbits for the period from November 8, 1986, to November 7, 1988, i.e. a period of two years. These orbits will be used in the analysis of GEOSAT altimeter measurements, which is described in this Chapter. An accuracy of 40 cm in the radial position of the GEOSAT altimeter satellite offers the possibility to separate the signals of the dynamic sea surface topography, i.e. the permanent ocean topography produced by ocean currents, and of the gravity field. This is especially true since the main features of the dynamic sea surface topography are of a long-wavelength nature and the errors in the GEM-T2 geoid for these wavelengths are claimed to be very small, in any case smaller than the long-wavelength signals of the dynamic sea surface topography. For example, the dynamic sea surface topography is assumed to have an rms of approximately 65 cm for wavelengths greater than 4000 km (Engelis, 1987). From the calibrated GEM-T2 covariance matrix (Marsh et al., 1989a), it can be computed that the geoid error of this model for wavelengths longer than 4000 km has an rms-value of 52 cm for the geoid along the GEOSAT ground track, if the covariances of the complete GEM-T2 model are propagated. This is smaller than the rms-value of the dynamic sea surface topography. However, for smaller wavelengths down to 500 km the GEM-T2 geoid has an error of more than 114 cm and improvements can be made using satellite altimetry. It is emphasized that in this thesis the GEM-T2 gravity field model, and not a more recent model, will be used to model the long-wavelength geoid. The reason is that GEM-T2 is a so-called satellite only model (see Section 1.3), that has been constructed from satellite tracking data only. In the development of many other gravity field models, altimeter measurements have been used which means that oceanographic signals may be aliased into the geoid computed with such gravity field models.

In the following, the simultaneous adjustment of a gravity field model and the determination of a long-wavelength model for the dynamic sea surface topography from satellite altimetry will be referred to as the integrated approach. This integrated approach is a least-squares adjustment process. This integrated approach was also discussed and applied to altimeter measurements in (Nerem et al., 1988; Marsh et al., 1989b and 1990; Denker and Rapp, 1990; Engelis and Knudsen, 1989). In (Nerem et al., 1988) and (Marsh et al., 1989b and 1990) use was made of numerical integration

techniques to determine a high-precision GEOSAT orbit together with the adjustment of a gravity field model and the determination of a model for the long-wavelength dynamic sea surface topography. In (Engelis and Knudsen, 1989; Denker and Rapp, 1990) use was made of analytical techniques. The latter technique is in close agreement with the technique to be described in this Chapter.

This Chapter starts with a description of the mathematical modeling of sea height residuals, based on the description of the altimeter measurement given in Section 4.2, and the set-up of the measurement equations for sea height residuals and residual crossover differences. This is followed by a simulation study to show the possibilities and limits of the integrated approach based on the theory of formal error estimates of harmonic coefficients, both of the gravity field and the semi-permanent dynamic sea surface topography (Appendix D). After this, the principles and consecutive steps of the integrated approach are presented. This part includes the identification of problems related to forming the observation equations and computing a least-squares solution, the description of methods to solve these problems, the development of methods to test the accuracy of the newly obtained models for the gravity field and dynamic sea surface topography, and the implementation of these methods.

The integrated approach was applied to two 17-day repeat periods of real GEOSAT altimeter measurements combined with GEM-T2 orbits, computed at the NASA Goddard Space Flight Center, resulting in an adjusted GEM-T2 gravity field model and a model for the large-scale dynamic sea surface topography. The accuracy of these new models is tested by several methods and a comparison of these new models with other published models is presented.

Finally, the adjusted gravity field model and the new model for the dynamic sea surface topography were used to correct two years of GEOSAT altimeter residual sea heights. The resulting data set of two years of corrected altimeter data was used in the determination of the variability of the long-wavelength dynamic ocean surface topography. It is shown that this variability displays a clear annual cycle.

6.2 Mathematical model

The objective of the investigations described in this Chapter was to determine a new model for the dynamic sea surface topography as well as to adjust the gravity field to absorb the greater part of the long-wavelength radial orbit and geoid errors from the sea height residuals. A sea height residual can be represented by equation (4.2) (Section 4.2). The term σ in this equation is relatively small compared to the other terms in this equation and has a predominantly high-frequency signature (Zandbergen, 1990). Therefore, this σ-term will not be modeled.

To establish the observation equations for the unknowns of the dynamic sea surface topography model and for the gravity field coefficients, representation forms for the radial orbit and geoid errors, as well as for the dynamic sea surface topography are

required. Use will be made of spherical harmonic expansions. It must be noted that alternative representations are possible, e.g. based on functions orthogonal over the oceans (Hwang, 1991), but the investigation of these functions is outside the scope of this thesis.

The dynamic sea surface topography h_{SST} will be represented by a spherical harmonic expansion complete to degree and order *lsst* (Engelis and Knudsen, 1989):

$$h_{SST} = a_e \sum_{l=1}^{lsst} \sum_{m=0}^{l} \left\{ \bar{C}^{\xi}_{lm} \cos m\lambda + \bar{S}^{\xi}_{lm} \sin m\lambda \right\} \bar{P}_{lm}(\sin\phi) \tag{6.1}$$

where the superscript ξ denotes dynamic sea surface topography. The zero degree term, i.e. a constant, is not included in this expansion. The reason for this is that a constant will be included in the estimation of a state-vector. This will be shown in the following (equation (6.11)). The GEOSAT satellite is in a near-circular orbit. For such an orbit, this expansion can be rewritten as (Schrama, 1989):

$$h_{SST} = a_e \sum_{l=1}^{lsst} \sum_{m=0}^{l} \sum_{p=0}^{l} F_{lmp} S^{\xi}_{lmp} \tag{6.2}$$

where

$$S^{\xi}_{lmp} = \begin{bmatrix} \bar{C}^{\xi}_{lm} \\ -\bar{S}^{\xi}_{lm} \end{bmatrix} \cos\psi + \begin{bmatrix} \bar{S}^{\xi}_{lm} \\ \bar{C}^{\xi}_{lm} \end{bmatrix} \sin\psi \quad \begin{matrix} l-m \text{ even} \\ l-m \text{ odd} \end{matrix} . \tag{6.3}$$

Both the radial orbit error Δr and the geoid error Δh_g are functions of the disturbing potential T of the gravity field. This disturbing potential can also be represented by a spherical harmonic expansion (see equation (1.8)):

$$T = \frac{\mu}{a_e} \sum_{l=2}^{lmax} \sum_{m=0}^{l} \left[\frac{a_e}{r} \right]^{l+1} \left[\Delta\bar{C}_{lm} \cos m\lambda + \Delta\bar{S}_{lm} \sin m\lambda \right] \bar{P}_{lm}(\sin\phi) \tag{6.4}$$

where *lmax* represents the maximum degree of the spherical harmonic expansion used to model the disturbing potential T. For a spherical approximation for the Earth's shape, the normal gravity γ can be written as:

$$\gamma = \frac{\mu}{a_e^2} . \tag{6.5}$$

Combining the equations (1.7), (6.4) and (6.5) yields the following representation for the geoid error Δh_g:

$$\Delta h_g = a_e \sum_{l=2}^{lmax} \sum_{m=0}^{l} \left[\frac{a_e}{r} \right]^{l+1} \left[\Delta\bar{C}_{lm} \cos m\lambda + \Delta\bar{S}_{lm} \sin m\lambda \right] \bar{P}_{lm}(\sin\phi) . \tag{6.6}$$

For a circular orbit, a similar expression as for the dynamic sea surface topography can be obtained:

$$\Delta h_g = a_e \sum_{l=2}^{lmax} \sum_{m=0}^{l} \sum_{p=0}^{l} F_{lmp} S_{lmp} \tag{6.7}$$

The equations (6.4) and (6.7) show that the geoid error and permanent part of the

ocean surface are represented by similar mathematical expressions and therefore are unseparable from altimeter measurements, unless additional information is available. However, at long wavelengths, the error in the geoid is claimed to be smaller than the signal of the dynamic sea surface topography, if current accurate gravity field models are used. Moreover, the disturbing potential T also causes radial orbit errors, which may have another signature than h_{SST} and therefore decorrelate the gravity field signal and the dynamic sea surface topography. It must be noted that in the mathematical modeling it was assumed that the gravity force of the dynamic sea surface topography, which represents a certain amount of water, on the satellite orbit could be neglected. The same approach was followed in (Engelis and Knudsen, 1989).

The radial orbit errors can be modeled with great precision by the LPT for circular reference orbits as shown in Chapter 3. The GEOSAT satellite is in such an orbit. For these orbits, the radial orbit errors can be written as a function of the disturbing potential T. After manipulating equation (2.6a), the following relation has been derived for the non-resonant orbit errors (Schrama, 1989):

$$\Delta r = \sum_{l=2}^{lmax} \sum_{m=0}^{l} \sum_{p=0}^{l} H_{lmp} S_{lmp} \tag{6.8}$$

where

$$H_{lmp} = a \left[\frac{a_e}{a} \right]^l F_{lmp} \left[\frac{\beta(l+1)-2(l-2p)}{\beta(\beta^2-1)} \right] \tag{6.9}$$

$$\beta = l-2p-m \frac{nday}{nrev} . \tag{6.10}$$

The term *nday* is the number of nodal satellite days that is necessary for the satellite to make *nrev* nodal orbital revolutions. For an exact repeat mission (ERM), and GEOSAT has been in an exact repeat mission, *nrev* and *nday* are the smallest integer numbers possible. For the GEOSAT ERM, *nday* and *nrev* are equal to 17 and 244, respectively. The term β is the term f_{lmp} (equation (2.2d)) for repeat orbits. It is noted that for an ERM the series in equation (6.8) become true Fourier series: only perturbations with frequencies equal to a multiple of (1/*nrev*) cpr occur (equation (6.10)).

The equations (6.8)-(6.10) are only valid for $\beta \neq 0$ and $\beta \neq \pm 1$. For $\beta = 0$ or $\beta = \pm 1$ (resonance), which only occurs for zonals (provided *nrev*>*lmax*, equation (6.10)), the radial orbit error for a certain resonance zonal term can be written as described in Section 2.3 (equations (2.13a) and (2.13b)).

The radial orbit errors represented by equation (6.8) are only the particular solution of the LPT for the radial direction. The homogeneous solution (equation (2.12a)) must be added to these radial orbit errors. To this homogeneous solution is added an extra term representing the interaction of this homogeneous solution with the relatively large $\bar{C}_{20}$-coefficient (Engelis and Knudsen, 1989). The combination of this term and the homogeneous solution will be referred to as the state-vector radial orbit error Δr_s:

$$\Delta r_s = a_0+a_1\cos wt+b_1\sin wt+a_2 wt\cos wt+b_2 wt\sin wt+a_3\sin 2wt . \tag{6.11}$$

The state-vector can also absorb radial epoch state-vector uncertainties (i.e. the uncertainty of the radial position and velocity of the satellite at a certain epoch).

Now, the observation equations for sea height residuals can be established by combining the equations (6.2), (6.7), (6.8), (6.11) and (2.13a)-(2.13b):

$$\Delta h = \sum_{l=1}^{lsst}\sum_{m=0}^{l}\sum_{p=0}^{l} a_e F_{lmp}(i) S^{\xi}_{lmp} + \sum_{l=2}^{lmax}\sum_{m=0}^{l}\sum_{p=0}^{l}\left[a_e F_{lmp}(i) - H_{lmp}\right] S_{lmp}$$

$$+\Delta r_s + resonance\ terms \qquad (6.12)$$

In this equation the *resonance terms* are given by the equations (2.13a)-(2.13b).

A residual crossover difference is nothing else than the difference between two sea height residuals at the same geographical location, one for an ascending and one for a descending orbital track. Therefore, the geographical constant terms, i.e. the dynamic sea surface topography Δh_{SST} and the geoid error Δh_g, vanish in the observation equations for the residual crossover differences. Therefore, the only terms that remain in the modeling of a residual crossover difference are the non-resonant radial orbit error Δr, the state-vector term Δr_s and the *resonance terms*, all evaluated both for the ascending (*asc*) and descending (*des*) pass. This results in the following equation for a residual crossover difference $\Delta Xover$ (see also: equation (5.14)):

$$\Delta Xover = \Delta h_{asc} - \Delta h_{des} = \sum_{l=2}^{lmax}\sum_{m=0}^{l}\sum_{p=0}^{l} H_{lmp}\left[(S_{lmp})_{asc} - (S_{lmp})_{des}\right]$$

$$+(\Delta r_s)_{asc} - (\Delta r_s)_{des} + resonance\ terms\ (asc - des) \qquad (6.13)$$

For the dynamic sea surface topography the maximum degree *lsst* is taken equal to 10 and for the gravity field *lmax* equal to 36. In (Nerem et al., 1988; Engelis and Knudsen, 1989; Marsh et al., 1989b and 1990; Denker and Rapp, 1990) it was shown that the choice of 10 for the maximum degree of spherical harmonic expansion of the dynamic sea surface topography can be justified. For higher degrees, it is expected that the error in the determined geoid will be larger than the signal of the dynamic sea surface topography for these degrees. In (Nerem et al., 1988) this was the case for degrees beyond 9, and in (Marsh et al., 1989b and 1990) for degrees beyond 7. The truncation of the spherical harmonic expansion for the disturbing potential entails the introduction of omission errors in the observation equations. However, with a gravity field model complete to degree and order 36, a geoid with a resolution of about 500 km can be modeled. Therefore, omission errors with a wavelength smaller than 500 km are not expected to be aliased seriously in the dynamic sea surface topography, because of the abundance of observations over the oceanic regions which cover two-thirds of the Earth's surface. Moreover, the models that will be used to compute the geoid (Section 6.5) are expected to have small errors for the long wavelengths. Moreover, it can be shown that the effect of gravity terms above degree 36 on the GEOSAT radial orbit perturbations decreases rapidly.

The equation (6.12) will be used in the next Section in a simulation study to show the principles and problems associated with the integrated approach. After this, the equations (6.12) and (6.13) will be used to process real GEOSAT measurements and will be implemented in the integrated approach.

6.3 Formal harmonic coefficient error estimates in the integrated approach

A simulation study was performed to gain insight in the concept of the integrated approach. The starting point in this study was the assumption that the GEOSAT altimeter could deliver measurements with a constant measurement interval along its orbit. The first question that arose was whether it would be possible to solve for the coefficients of a gravity field complete to degree and order 36 and for the coefficients of a model for the dynamic sea surface topography complete to degree and order 10 from these measurements simultaneously. It will be shown that this is not a trivial problem. After this, a second assumption was made: the availability of satellite tracking observations from which it is possible to determine the GEOSAT satellite orbit accurately in the radial, cross-track and along-track directions, again with a constant measurement interval along the complete orbit. The question that had to be answered was whether with the addition of such a data set the earlier mentioned problems could be overcome.

With a constant measurement interval along a satellite orbit, the data set of measurements will satisfy the conditions for the estimation of formal errors of harmonic coefficients of the gravity field and dynamic sea surface topography models from the theory developed by O.L. Colombo if the satellite is at least in a repeat orbit. This theory of formal error estimates has been developed by O.L. Colombo for gravity field recovery from satellite-to-satellite tracking between two low Earth orbiting satellites (Colombo, 1984 and 1990; Schrama, 1990). The principles are explained in Appendix D. In this appendix, it is explained that in the simulations that are described in this Section an actual recovery of gravity field coefficients and coefficients for the dynamic sea surface topography does not take place, but that formal error estimates for these coefficients are produced if they are to be determined from the previously described special geometry of observations.

In the simulation study described in this Section, orbit parameters of the GEOSAT satellite were used, leading to a repeat period of 17 days in which the satellite makes 244 orbital revolutions. The inclination was equal to 108° and the semi-major axis equal to 7166376.2 m (about 800 km altitude). It was assumed that one repeat period of altimeter measurements was available. The sampling rate was taken equal to 20 s (equal to the batch interval for the computation of altimeter normal point measurements, see Section 6.5) and the globe was assumed to be completely covered by oceans. The standard deviation of the altimeter measurement was taken equal to 50 cm, which represents that part of the measurement errors in the modeling of these measurements that will not be corrected in the integrated approach (for the greater part high-frequency errors, see Section 6.2). In this way, a data set satisfying the special geometry described in Appendix D was obtained, i.e. a data set of observations covering the whole Earth along the GEOSAT ground tracks (thus for latitudes above 72° S and below 72° N).

For these observations, normal equations were derived analytically for a gravity field model complete from degree 2 to 36 and a model for the dynamic sea surface topography complete to degree and order 10. The normal matrix was computed using the

equation (6.12) without the resonance terms and the equations (D.1)-(D.7) of Appendix D.

The inverse of the so obtained block-diagonal matrix should deliver the formal error estimates of the harmonic coefficients. However, the normal matrix was singular, indicating that even for a perfect coverage of the Earth along the GEOSAT ground tracks with altimeter measurements, the gravity field and dynamic sea surface topography cannot be determined separately. This is in agreement with the discussion of Section 6.2. In order to overcome the singularity problem, additional information is necessary.

Because it was assumed that the GEOSAT satellite orbit can be computed from tracking observations very accurately (as indicated in Section 4.2, the GEOSAT orbit could be computed with a radial accuracy of about 40 cm using GEM-T2, and the ground tracking observations deliver also information of the along-track and cross-track perturbations), it was assumed that this additional information consisted of satellite position components in the radial, along-track and cross-track directions with the same sampling-rate and standard deviation as the altimeter measurements. In other words, it was assumed that it is possible to compute the GEOSAT orbit with an accuracy of 50 cm in all three directions. Also for these components, block-diagonal normal matrices were computed, however only for gravity field harmonic coefficients. It was assumed that the satellite tracking observations do not deliver information of the dynamic sea surface topography and therefore nothing was added to that part of the normal equations associated with the dynamic sea surface topography coefficients. The normal equations for the 3 position components were added to the normal equations of the altimeter measurements.

The inverse of these combined normal equations led to formal error estimates as displayed in the Figures 6.1 and 6.2. The standard deviations of the gravity field harmonic coefficients (solid line, Figure 6.1) were well below Kaula's rule of thumb. The standard deviations of the coefficients of the dynamic sea surface topography were on the order of a few cm (solid line, Figure 6.2). The rss of the coefficient errors of the dynamic sea surface topography solution was 14.6 cm. Also indicated in Figure 6.2 is the formal geoid error computed with the formal error estimates of the gravity field coefficients (dotted line). It can be seen in Figure 6.2 that this geoid error is smaller than the formal error of the dynamic sea surface topography for degrees up to 7. For degrees from 8 up to 10 this geoid error is almost equal to the formal dynamic sea surface topography error. This justifies the choice of 10 for the maximum degree of the spherical harmonic expansion of the dynamic sea surface topography. A remarkable characteristic in the Figures 6.1 and 6.2 is the saw-tooth pattern. This may be explained by the decoupling of formal error estimates for coefficients of even and odd degrees (Appendix D). The formal error estimates for a certain odd degree are a little bit smaller than the error estimates of the even degrees next to this odd degree. The maximum errors of the gravity field coefficients are found for degrees close to 25. This can be explained by the fact that non-zero correlations exist between the gravity field coefficients and coefficients for the dynamic sea surface topography. Although only coefficients of the dynamic sea surface topography for degrees below 10 were considered, they did have an effect on the error estimates for gravity field coefficients of degrees above 10. This can be explained by the fact that, besides correlations between

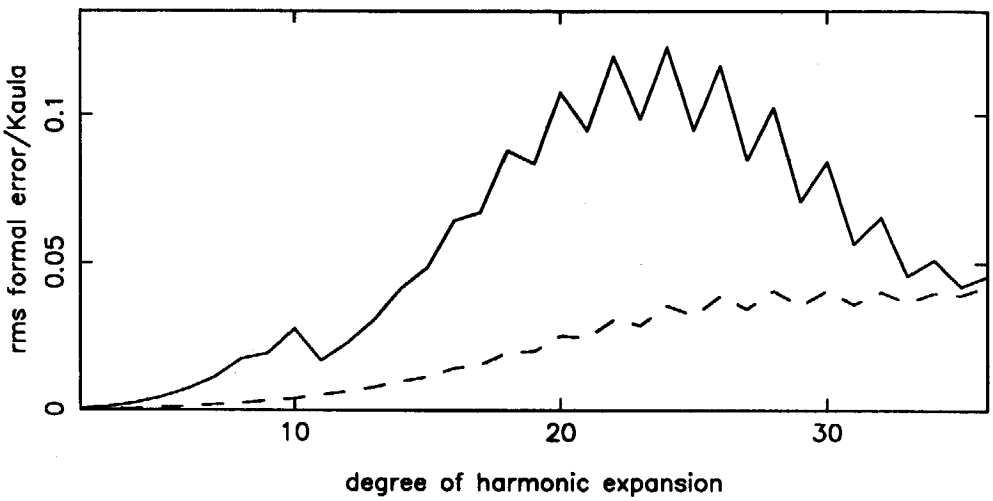

Figure 6.1 Formal gravity harmonic coefficient error estimates in an integrated approach covariance analysis (solid line: correlations included, dashed line: correlations not included)

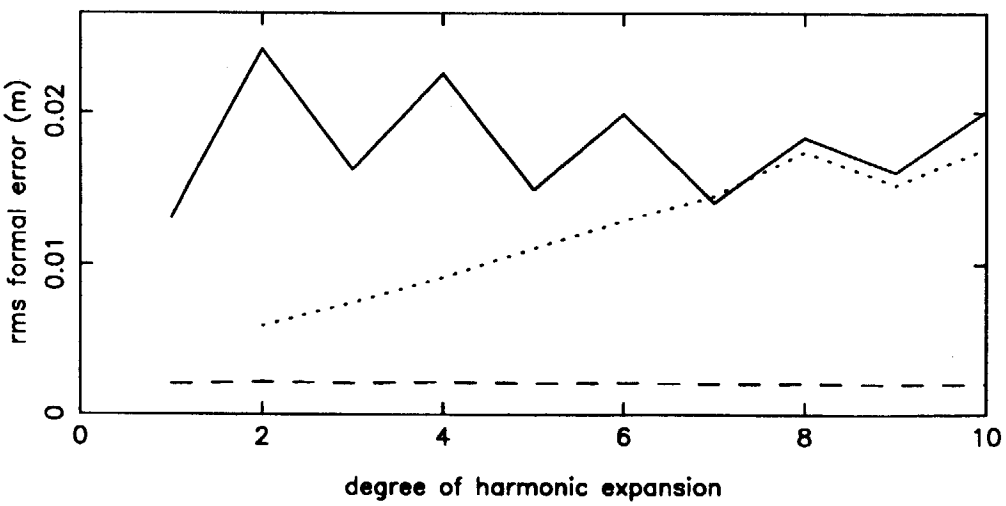

Figure 6.2 Formal SST harmonic coefficient error estimates in an integrated approach covariance analysis (solid line: correlations included, dashed line: correlations not included, dotted line: formal geoid error)

dynamic sea surface topography coefficients and gravity field coefficients below degree 10, also correlations exist between dynamic sea surface topography coefficients below degree 10 and gravity field coefficients above 10. In addition, the correlations between the dynamic sea surface topography coefficients and gravity field coefficients below degree 10 have an indirect effect on the formal error estimates of gravity field coefficients above degree 10, because of the correlations between gravity field coefficients of degrees below and above 10. Correlations between gravity field coefficients above degree 25 and dynamic sea surface topography coefficients below degree 10 become very small. For these degrees, the formal error estimates of gravity field coefficients become close to the case in which the gravity field coefficients are thought to be estimated separately from the dynamic sea surface topography coefficients, i.e. if the correlations between the dynamic sea surface topography coefficients and gravity field coefficients are made equal to zero. The latter case is indicated by the dashed lines in the Figures 6.1 and 6.2. In this case, the rss of the coefficient errors of the dynamic sea surface topography solution was found to be equal to 1.7 cm. Thus, if in theory the gravity field would be known exactly and would not have to be adjusted, a very high-accuracy dynamic sea surface topography model to degree and order 10 could be obtained, given the described geometry of satellite measurements. Unfortunately, at this moment, this is not the case.

In agreement with the discussion in Section 6.3, the results of this Section indicate that it is impossible to simultaneously adjust a gravity field model and determine a model of the dynamic sea surface topography from satellite altimetry alone, especially since in reality the effect of no measurements over land areas must also be accounted for. This will further destabilize the normal equations. However, if additional information is available, e.g. satellite tracking data from which the satellite's position may be computed with an accuracy of about 50 cm (which is certainly feasible nowadays) or an equivalent information source like a quality gravity field model together with a calibrated covariance matrix, very good results may be obtained. Therefore, with the current knowledge in gravity field modeling (the additional information) the investigation of applying the integrated approach to GEOSAT altimetry is certainly justified.

6.4 Solution strategy

In general, many more observations are available than coefficients to be determined or adjusted. If these observations do not form a linearly dependent system, an overdetermined system of observation equations has to be solved. A method to solve such an overdetermined system of observation equations is the concept of least-squares. In other words, the observation equations are solved by the method of least-squares parameter adjustment: the observation equations are transformed to normal equations. This has been explained in Chapter 5.

Considering the observation equation (6.12) for sea height residuals, it is obvious

that problems will occur: some coefficients to be determined or adjusted have the same signal characteristics for altimeter measurements and are therefore unseparable if no other information is available. For example, the zero-degree term $\bar{C}^{\xi}_{00}$ of the dynamic sea surface topography spherical harmonic expansion and the term a_0 of the state-vector (equation (6.11)), and $\bar{C}^{\xi}_{10}$ and a_1, b_1 are unseparable, or linearly dependent. Moreover, the spherical harmonic functions are only orthogonal for a global set of observations. However, altimeter measurements only cover the oceans below a latitude determined by the satellite orbital inclination and only over the oceans. These restrictions and correlations result in an instable set of normal equations.

A better separation of the gravity field and the dynamic sea surface topography solution is expected if normal equations for residual crossover differences are added to the normal equations for sea height residuals. In principle, residual crossover differences deliver no information of the semi-permanent dynamic sea surface topography and therefore the inclusion of this type of residuals leads to a better separation of the gravity field adjustment and the solution for the dynamic sea surface topography.

However, the addition of the normal equations for the residual crossover differences does not completely overcome the problem of instability of the normal equations. Only measurements made by one satellite altimeter instrument are used, which implies that information for the radial orbit perturbations and geoid errors for only one orbital inclination is used. In addition, as mentioned before, only measurements over the ocean's surface are available. Such a set of measurements leaves a high degree of freedom in a gravity field solution if a model complete to degree and order 36 is to be adjusted. Moreover, after the addition of normal equations for residual crossover differences, high correlations will still exist between coefficients of the gravity field and of the dynamic sea surface topography, and state-vector terms and coefficients of the dynamic sea surface topography are still unseparable.

The solution of the instability problem of the normal equations is to include a priori information. The state-vector terms may be constrained by using the covariance matrix of the state-vector, obtained in the orbit determination process. Also information of the accuracy of the gravity field coefficients is available and can be included in the solution. This information consists of a calibrated covariance matrix, computed along with the determination of the gravity field model. In this study, the calibrated GEM-T2 covariance matrix (Marsh et al, 1989a) was used, because the GEM-T2 gravity field model was used in the computation of the GEOSAT orbits and the long-wavelength geoid (for wavelengths longer than 1000 km). Finally, from spectral analysis, the magnitude of the coefficients of the dynamic sea surface topography as a function of the degree of the spherical harmonic expansion can be estimated and used as constraints. This spectral analysis can be summarized by the following formula (Marsh et al., 1989b and 1990):

$$\sigma^{\xi}_{lm} = -0.01344*l+0.13959 \quad (m) \tag{6.14}$$

The a priori information is used in a minimum-variance analysis which consists of the minimization of (see also: Section 5.3):

$$(Ax-r)^T(Ax-r)+w_{cal}x_g{}^T Gx_g$$

$$+w_{SST}\sum\sum\frac{\bar{C}^{\xi 2}_{lm}+\bar{S}^{\xi 2}_{lm}}{\sigma^{\xi 2}_{lm}}+w_{state}x_{state}{}^{T}Sx_{state}\ . \qquad (6.15)$$

In this equation, w_{cal}, w_{SST} and w_{state} denote the weight of the calibrated gravity field matrix G (i.e. inverse of the covariance matrix), the weight of the signal constraints of the dynamic sea surface topography, and the weight of the inverse S of the covariance matrix of the state-vector x_{state} respectively. The vector x represents all unknowns to be determined, which includes the vector x_g, which is the subset of gravity field harmonic coefficients to be adjusted, the state-vector x_{state} and the unknowns for the dynamic sea surface topography $\bar{S}^{\xi}_{lm}$ and $\bar{C}^{\xi}_{lm}$.

The solution of equation (6.15) is:

$$x = (A^{T}A+V_{A}{}^{-1})^{-1}A^{T}r =$$

$$\begin{bmatrix} A_{ss}{}^{T}A_{ss}+w_{state}S & A_{gs}{}^{T}A_{gs} & A_{\xi s}{}^{T}A_{\xi s} \\ A_{sg}{}^{T}A_{sg} & A_{gg}{}^{T}A_{gg}+w_{cal}G & A_{\xi g}{}^{T}A_{\xi g} \\ A_{s\xi}{}^{T}A_{s\xi} & A_{g\xi}{}^{T}A_{g\xi} & A_{\xi\xi}{}^{T}A_{\xi\xi}+w_{SST}D \end{bmatrix}^{-1} A^{T}r$$

$$= N^{-1}A^{T}r \qquad (6.16)$$

where $V_{A}{}^{-1}$ represents the a priori information. The matrix D is a diagonal variance matrix, with elements equal to $(1/\sigma^{\xi}_{lm})^2$. These elements are computed with equation (6.14). In the following, the normal matrix $(A^{T}A+V_{A}{}^{-1})$ will be referred to as N. This matrix has been divided in sub-matrices indicated by the indices s, denoting state-vector, g, denoting gravity field, and ξ, denoting dynamic sea surface topography. For example the sub-matrix $(A^{T}A_{gg}+w_{cal}G)$ represents the part of the normal equations for the gravity field coefficients to be adjusted.

An important question then is: what values must be assigned to the weight factors w_{state}, w_{cal} and w_{SST} ? In the first place, these factors must be chosen such that the adjustments of the gravity field unknowns are below the 3σ-level as indicated by the variances in the a priori information, i.e. the calibrated covariance matrix of the gravity field model used. Moreover, the rms of the coefficient values of the dynamic sea surface topography solution per degree must be below the 3σ-level indicated by the signal variances of equation (6.14).

The correctness of the selected values for the weight factors can be tested by the following procedure: using the inverse of the normal matrix N in equation (6.16), relations can be derived for the standard deviation of (sub)sets of the unknowns x and for the correlation between (sub)sets of the unknowns. These standard deviations are in the same unit as the observations (e.g. cm) and are valid for the set of observations (altimeter measurements) used. For the subset ξ (dynamic sea surface topography), the standard deviation $\sigma(h_{SST})$ becomes (Appendix C):

$$\sigma(h_{SST}) = \left\{ w_{cal}\sum_{i}\sum_{j}\left[N^{-1}{}_{\xi\xi}A_{\xi\xi}{}^{T}A_{\xi\xi}\right]_{ij}\right\}^{1/2} /\sqrt{nobs} \qquad (6.17)$$

In this equation, *nobs* is the number of observations used in the least-squares

adjustment process. The multiplication by w_{cal} is necessary, provided a proper calibration of the matrix G has taken place, i.e. the inverse of the calibrated GEM-T2 covariance matrix (Lerch, 1989). This can be explained as follows: if the observations are weighted properly, they can be added directly to the calibrated covariance matrix. In that case, the value w_{cal} in equation (6.16) must be equal to 1. However, the weight for all observations was taken equal to 1. As discussed in Section 5.3, these observations must be scaled by their accuracy and by their information content (for example, two identical measurements deliver the same information and in that case a scale factor of 1/2 is necessary). This scaling is realized by the factor w_{cal}. For the subset g (gravity field unknowns) a similar formula for the standard deviation can be derived:

$$\sigma(gravity) = \left\{ w_{cal} \sum_i \sum_j \left[N^{-1}{}_{gg} A_{gg}{}^T A_{gg} \right]_{ij} \right\}^{1/2} / \sqrt{nobs} \quad . \tag{6.18}$$

The equations (6.17) and (6.18) thus represent the standard deviation in observation units (cm for altimeter measurements) of the complete solution of the dynamic sea surface topography and of the complete solution of the gravity field averaged over all observations, respectively. The values $\sigma(h_{SST})$ and $\sigma(gravity)$ give an indication of the quality of the solution and the correctness of the weight factors. Also the correlation between the subsets g and ξ is a measure of the quality of the solution:

$$corr_{g\xi} = \frac{w_{cal} \sum_i \sum_j \left[N^{-1}{}_{g\xi} A_{g\xi}{}^T A_{g\xi} \right]_{ij}}{nobs\, \sigma(h_{SST}) \sigma(gravity)} \quad . \tag{6.19}$$

For a stable solution, it is desired to separate the gravity field adjustments and the solution for the dynamic sea surface topography coefficients as much as possible. A low absolute value for the correlation indicates a good separation.

The choice of the weight factors can further be tested by subtracting the radial orbit and geoid corrections and the dynamic sea surface topography, implied by the gravity field coefficient adjustments and coefficient solutions of the dynamic sea surface topography, from the original sea height residuals and residual crossover differences. The extent to which the sea height residuals or residual crossover differences are reduced by subtracting the radial orbit and geoid corrections or the dynamic sea heights must agree with the power of the coefficient adjustments and solutions. For example, if the dynamic sea surface topography solution has an rms-value of 65 cm over the oceans, the rms of the sea height residuals must be reduced accordingly if the dynamic sea heights are subtracted. Of course, this must also be valid for the corrections implied by the gravity field adjustments.

6.5 Processing of GEOSAT altimeter observations

The integrated approach has been applied to 34 days of GEOSAT altimeter

observations, when the GEOSAT satellite was in the Exact Repeat Mission (ERM), i.e. two 17-day repeat periods of observations were used to adjust a gravity field model complete to degree and order 36 and a model for the dynamic sea surface topography complete to degree and order 10. This 34-day period extended from November 25 to December 28, 1986. The combination of these two 17-day periods of altimeter measurements gathered by GEOSAT showed very few data gaps. This means that a better coverage of the oceans with GEOSAT altimeter measurements is hardly possible by extending the 34-day period.

After the subtraction of the height of the orbit with respect to the reference ellipsoid (semi-major axis = 6,378,137 m, flattening = 1/298.257), altimeter normal points were computed. This computation consisted of fitting a third-order polynomial through successive batches of 20 seconds of observations. In 20 seconds, the GEOSAT ground track traverses an arc with a length of about 130 km. This means that the third-order polynomial gives a smoothed representation of the altimeter measurement variations for such an arc. By taking a third-order polynomial, a great part of variations with a wavelength smaller than half this arc-length, i.e. 65 km, are filtered out. This 65 km corresponds to the resolution of the OSU89b model (Rapp and Pavlis, 1990) that will be used to model the geoid above degree 36. This will be discussed in the second part of this Section. Observations with a difference between its value and the value indicated by the third-order polynomial greater than three times the rms (root-mean-square) of fit were eliminated until convergence. After this, the third-order polynomial was evaluated in the middle of each batch, if the rms of fit of the polynomial was better than 20 cm (the power of σ in equation (4.2)) and if more than 15 observations were left for the polynomial fit. This procedure led to 32,980 normal points for the first 17-day period and 33,529 for the second period. The rms of fit was equal to about 5.5 cm. Thus, in the normal point computation, a signal with an rms of 5.5 cm could not be modeled by the third-order polynomial. This signal consists partly of measurement noise and will be for the greater part of a very high-frequency nature. Thus, by this normal point computation, the problem of aliasing very high-frequency signals in the dynamic sea surface topography solution and gravity field adjustments is partly prevented. Moreover, with this concept spurious observations were eliminated.

Sea height residuals were computed by subtracting all corrections described in Section 4.2 from the normal point values. The geoid was computed with the GEM-T2 gravity field model, which was also used in the orbit computation at the NASA Goddard Space Flight Center (Haines et al., 1990). Although this model has values for coefficients above degree 36, the geoid was computed using only GEM-T2 coefficients complete to degree and order 36. The remaining GEM-T2 coefficients are coefficients that absorbed part of resonance satellite orbit perturbations. These coefficients behave badly in geoid computations. In addition, a high-frequency geoid was subtracted from the normal point values to reduce the possible aliasing of these signals in the dynamic sea surface topography solution and gravity field adjustments. This geoid was computed with the OSU89b gravity field model from degree 37 to 360. The advantage of using the GEM-T2 model to compute the geoid for the lower degrees (up to 36) is that in this model no altimetry is aliased: it is a so-called satellite-only model in contrast to the OSU89b model. This combination of two different types of geoids is allowable

since the dynamic sea surface topography is determined only for the lower degrees.

Part of the so obtained sea height residuals were edited out by applying three criteria. Firstly, if the observations were made at a geodetic latitude above 70° North or below 70° South, the observations were edited out to prevent assigning too high a weight to the polar regions (this means that only a band of maximally 2 degrees of observations was eliminated: the orbital inclination of GEOSAT is 108°). Second, if the sea height residuals had an absolute value above 450 cm, the observations were edited out. This is a sort of 3σ-level criterion, because the rms of the residual sea heights was on the order of 150 cm, as will be shown. Finally, if the values for the high-frequency geoid corrections (OSU89b geoid for degrees greater than 36) were greater than 3.5 m, the observations were edited out to prevent using observations in geoid trench areas. In these trench areas, the accuracy of the OSU89b geoid deteriorates rapidly and because of this, high-frequency geoid errors are introduced. It must be prevented that these high-frequency errors are aliased in the long-wavelength dynamic sea surface topography and gravity field. The result of the normal point computations and the editing criteria was a data set consisting of 64,831 sea height residuals with an rms value of 146 cm (Table 6.1).

In addition to this data set, residual crossover differences were computed. This computation was performed by a procedure that can be summarized by the following. The original set of GEOSAT altimeter measurements was used, the same set that was used in the normal point computation, however without the altimeter measurements eliminated in this normal point computation. The geographical location of a crossover difference was determined by computing the intersection point of the ground track of an ascending and descending GEOSAT pass. The crossover difference was computed by a linear interpolation of two altimeter measurements on both passes closest to the intersection point. The crossover differences computed with this procedure were compared with crossover differences used in (Wakker et al., 1990a). It was found that these crossover differences compared very well with the crossover differences computed with the procedure described above (the agreement was always better than 1 cm). This procedure led to a data set of 35,907 observations with an rms-value of 51 cm (Table 6.1). The first two editing criteria were applied for residual crossover differences. The rms-value indicated a radial orbit error on the order of 35-40 cm. The rms of the residual crossover differences as a function of geographical location is displayed in Figure 6.3. These rms-values are relatively small for certain regions. This can be explained by considering the tracking network of ground stations that delivered the tracking data used to compute the GEOSAT orbits. The rms-values will be low for areas covered by these ground stations (Haines et al., 1990).

6.6 Results

Normal equations were computed for each 17-day period of sea height residuals and

Table 6.1 Statistics of a priori sea height residuals and residual crossover differences and corrections applied to them.

nobs	ERM	observation type	a priori rms (cm)	-grav (cm)	-SST (cm)	-grav-SST (cm)	-all (cm)
32174	2	sea heights	144.59	102.13	135.68	86.34	33.73
17735	2	crossovers	55.12	46.55			25.73
32657	3	sea heights	148.42	107.92	135.57	86.65	33.73
18172	3	crossovers	47.45	37.28			22.80

Explanation of columns:

(1) nobs : number of observations
(2) -grav : rms after subtraction of gravity field corrections
(3) -SST : rms after subtraction of dynamic sea heights
(4) -grav-SST : rms after subtraction of both gravity field corrections and dynamic sea heights
(5) -all : rms after subtraction of all corrections including state-vector corrections

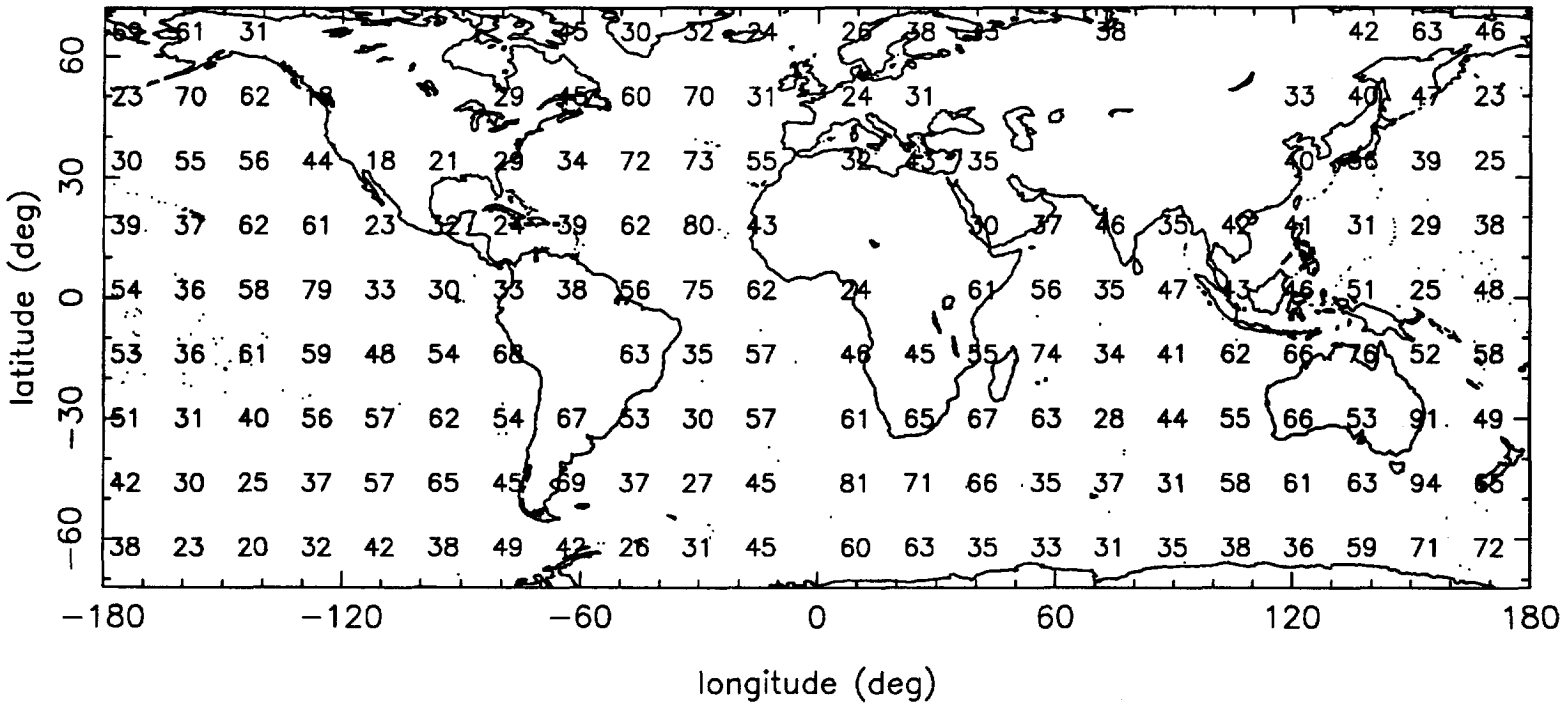

Figure 6.3 RMS of GEOSAT residual crossover differences (cm)
for ERM-2 and ERM-3 as a function of the location

residual crossover differences. The set of unknowns consisted of 1,365 gravity field parameters and 120 coefficients for the dynamic sea surface topography plus one set of 6 state-vector parameters for each 17-day period. The normal equations were combined by the method of partitioning to account for the state-vector parameters.

This Section describes the choice of and weights assigned to the a priori information included in the solution of the normal equations, the application of the theory described in Section 6.4 to test these weights, the comparison of the solved-for gravity field adjustments and dynamic sea surface topography with results from the literature, and the discussion and graphical representations of the dynamic sea surface topography solution.

For the state-vector parameter adjustments, simple constraints were applied: only the amplitudes a_1 and b_1 (1 cpr radial orbit error, equation (6.11)) were constrained by adding a constant to the corresponding diagonal elements of the normal equations. These constants were chosen such that these amplitudes were constrained to about 40 cm, i.e. the predicted radial orbit error for GEOSAT using the GEM-T2 gravity field model. The necessity of constraining a_1 and b_1 lies in the 100 % correlation with the $\bar{C}^{\xi}_{10}$ term.

The values for w_{cal} and w_{SST} (equation (6.15)) were chosen equal to 5.0 and 30.0 respectively. These values were found by applying the theory described in Section 6.4. Using these values, all criteria described in that Section were met. Firstly, the rms of the gravity parameter adjustments divided by the a priori sigmas of the calibrated GEM-T2 covariance matrix was equal to 0.84, with minimum and maximum values of -2.66 and 3.61 respectively. For the coefficient solutions of the dynamic sea surface topography (listed in Table 6.2), these values were respectively 0.57 (rms for complete solution), -3.72 and 2.59 (rms per degree). Thus, most of the adjustments and coefficient solutions were below the a priori 3σ-level.

Secondly, using the equations (6.17)-(6.19), it was found that the sum of the remaining gravity field induced errors for sea height residuals and residual crossover differences has a standard deviation of 20 cm for the ocean areas (equation (6.17)). For the dynamic sea surface topography solution a standard deviation of 9 cm was found (equation (6.18)). The correlation between the gravity field adjustments and dynamic sea surface topography solution was equal to -0.18 (equation (6.19)). These standard deviations were compared with the a priori standard deviations implied by the a priori information. Using the calibrated GEM-T2 covariance matrix and the degree variances of equation (6.14), the standard deviations for the sum of the radial orbit and geoid errors, $\sigma(\Delta h_g + \Delta r)$, and for the dynamic sea heights are respectively 124 and 64 cm. Thus, these a priori standard deviations were reduced significantly. A remaining question is the significance of the correlation of -0.18 between the gravity field and dynamic sea surface topography solution. An answer to this question was found by solving separately for the gravity field and dynamic sea surface topography, i.e. the off-diagonal matrices in equation (6.16) were set to zero. The gravity field solution obtained in this way led to a geoid differing 37 cm globally (rms-wise) from the original solution. For the dynamic sea surface topography this value was 23 cm. These numbers show that a significant aliasing of dynamic sea surface topography in the gravity field solution takes place if the dynamic sea surface topography would not have

Table 6.2. Coefficients of the new dynamic sea surface topography model (in cm).

l	m	$a_e\bar{C}_{lm}$	$a_e\bar{S}_{lm}$	l	m	$a_e\bar{C}_{lm}$	$a_e\bar{S}_{lm}$
1	0	0.70		7	6	-0.24	1.41
1	1	-8.61	-3.89	7	7	0.96	-0.55
2	0	-41.97		8	0	3.21	
2	1	-4.41	10.36	8	1	-4.17	-1.73
2	2	2.99	3.14	8	2	-0.33	-0.62
3	0	25.74		8	3	1.47	0.22
3	1	8.29	2.95	8	4	0.57	0.20
3	2	1.19	-4.37	8	5	-1.61	-0.39
3	3	-3.20	-1.15	8	6	-0.76	0.82
4	0	-10.97		8	7	-0.74	0.17
4	1	0.25	4.05	8	8	-0.40	0.54
4	2	-3.17	2.49	9	0	-1.54	
4	3	3.15	-0.81	9	1	0.66	0.63
4	4	-0.07	-3.79	9	2	-0.29	0.14
5	0	4.58		9	3	-0.87	0.21
5	1	-1.08	-2.78	9	4	0.52	0.58
5	2	-0.60	3.57	9	5	0.45	-0.71
5	3	-0.62	0.73	9	6	-0.46	0.33
5	4	-4.88	2.71	9	7	0.01	-0.11
5	5	-0.34	-0.82	9	8	0.28	0.22
6	0	7.80		9	9	0.39	-0.08
6	1	-5.21	1.33	10	0	0.05	
6	2	-3.42	0.97	10	1	0.13	-0.04
6	3	1.48	-1.73	10	2	-0.03	0.01
6	4	-1.93	-1.14	10	3	0.05	0.05
6	5	-0.72	0.12	10	4	-0.02	-0.05
6	6	-1.59	-1.55	10	5	-0.08	-0.07
7	0	-4.26		10	6	-0.06	0.02
7	1	3.21	0.06	10	7	0.02	0.05
7	2	2.53	2.26	10	8	-0.04	0.05
7	3	0.39	-2.54	10	9	-0.04	0.02
7	4	0.54	-0.59	10	10	0.01	-0.01
7	5	0.55	-1.23				

been included in the solution, indicating the strength of the integrated approach.

Thirdly, the radial orbit and geoid corrections implied by the gravity field parameter adjustments and the dynamic sea heights implied by the dynamic sea surface topography solution were subtracted from the residual sea heights. It was found that the dynamic sea surface topography solution had an rms-value of 65 cm over the oceans. As can be seen from Table 6.1, this solution reduced the rms of the residual sea heights for the two ERM's from respectively 145 and 148 cm to 136 and 136 cm, meaning a decrease of 50 and 60 cm rms-wise, respectively. These values indicate that indeed the rms of the residual sea heights were reduced by a value that is in good agreement with the rms-value of the solution. A similar procedure was performed for the gravity field sea height corrections: the predicted rms-value of the adjustments was 99 cm for the geoid plus orbit error corrections. This value was obtained by computing the Fourier series of the corrections by combining the equation (6.12) and the gravity field harmonic coefficient adjustments. The value of 99 cm equals the rss of the amplitudes of this series divided by the square root of 2 (the so-called power). The rms of the sea height residuals was reduced from 145 to 102 cm and from 148 to 108 cm for ERM's 2 and 3, respectively. These values are equivalent to a decrease of respectively 102 and 102 cm, rms-wise, values comparing quite well with the predicted value of 99 cm. Finally, for residual crossover differences the predicted reduction in radial orbit error using the gravity field adjustments has an rms-value of 27 cm. This value was obtained in the same way as for the residual sea height corrections, but in this case for the radial orbit corrections multiplied by the square root of 2, because a crossover difference has two (radial orbit error) constituents. These residual crossover differences were reduced rms-wise by respectively 30 and 30 cm for ERM's 2 and 3, which is in good agreement with the predicted value.

One final conclusion can be made from Table 6.1: the state-vector parameter adjustments had a significant effect on reducing the radial orbit errors. The term a_0 in equation (6.11) was equal to about 55 cm. If this term is attributed to an error in the semi-major axis of the reference ellipsoid (a priori value equal to 6,378,137 m), a new value for this axis is obtained: 6,378,136.45 m. This value is in good agreement with the value obtained in (Rapp and Pavlis, 1990).

The implementation of all corrections reduced the rms of the a priori sea height residuals and residual crossover differences from initial values of 146 and 51 cm to 34 and 24 cm, respectively. In the analysis described in (Nerem et al., 1988), a gravity field model complete to degree and order 50 was determined together with a model for the dynamic sea surface topography complete to degree and order 15, from 30 days of SEASAT altimeter data (7/28-8/15, 9/15-9/27, 1978) and 54 days of GEOSAT altimeter data (11/17/86-12/4/86, 12/21/86-1/24/87). The rms of the a posteriori GEOSAT residual crossover differences and sea height residuals was equal to about 20 cm and about 30 cm respectively, values comparing very well with the values mentioned above, whereas in (Nerem et al., 1988) many more gravity field coefficients (about 2500) and dynamic sea surface topography coefficients (255) were estimated. In (Marsh et al., 1989b and 1990), a gravity field model complete to degree and order 50 (PGS-3337) was determined together with a model for the dynamic sea surface topography complete to degree and order 10. In this analysis use was made of three months

of SEASAT altimeter data (7/27-10/10, 1978). Both the rms of the a posteriori SEASAT residual crossover differences and for sea height residuals was equal to about 30 cm. It may be concluded that, although in (Nerem et al., 1988) and (Marsh et al., 1989b and 1990) use was made of numerical integration techniques, reductions in the residual crossover differences and sea height residuals were obtained that were of comparable magnitude with the reductions obtained by using the analytical technique described in this Chapter. In (Engelis and Knudsen, 1989) a gravity field model complete to degree and order 36 and a model for the dynamic sea surface topography complete to degree and order 10 were determined, from 17 days of SEASAT altimeter measurements (7/26-8/13,1978). The rms-values of the a posteriori residual crossover differences and sea height residuals were about 20 cm. In this analysis, the 17-day period was divided into 4 arcs, and for each arc a 6-element state-vector (equation (6.11)) was estimated. This may explain the lower rms-value obtained for the sea height residuals and the slightly lower rms-value for the residual crossover differences. Residual crossover differences were not included in the computation of the normal equations. In (Denker and Rapp, 1990), also a gravity field model complete to degree and order 36, however with selected terms above degree 36 to model resonance orbit perturbations, and a dynamic sea surface topography model complete to degree and order 10 was estimated, from one year of GEOSAT altimeter data (11/8/86-11/10/1987). The rms-values of the a posteriori residual crossover differences and sea height residuals were about 22 cm and 37 cm respectively, comparing very well with the values displayed in Table 6.1. In this analysis, a state-vector including, besides the terms displayed in equation (6.11), also quadratic terms, was estimated for each 6-day arc. Residual crossover differences were not used in the computation of the normal equations.

The adjusted GEM-T2 gravity field model and the model for the dynamic sea surface topography were compared with other published models. Firstly, the geoid computed with the GEM-T2 model and with the adjusted GEM-T2 model (truncated at degree 36) were compared with the geoid computed with the OSU89b model (truncated at degree 36). This OSU89b geoid is expected to model the geoid in the oceanic regions better than the GEM-T2 geoid, also for terms with a degree below 37 (Rapp and Pavlis, 1990) although oceanic features may be aliased in this model. The rms of differences between the GEM-T2 geoid and the OSU89b geoid was found to be 119 cm. This value decreased to 65 cm when taking the differences between the adjusted GEM-T2 geoid and the OSU89b geoid. This is an improvement of 99 cm rms-wise, a value that compared very well with the global rms of the geoid adjustments which was found to be equal to 103 cm. Secondly, the dynamic sea surface topography model was compared with models computed by (Marsh et al., 1989b and 1990) from SEASAT altimetry and by (Engelis, 1987) from Levitus hydrography. These models are available at Delft University of Technology. It must be noted that for the comparison with the Engelis model, the $\bar{C}^{\xi}_{20}$ coefficient had to be corrected for the permanent zero frequency tides (Denker and Rapp, 1990):

$$\bar{C}^{\xi}_{20,adj} = \bar{C}^{\xi}_{20} + 10.52\ (cm) \tag{6.20}$$

Over the oceans, the rms of differences between the model described in this thesis (color plate I) and the models published in (Marsh et al., 1989b; color plate II) and

(Engelis, 1987) are respectively 25 and 34 cm. Compared to an rms-value for the dynamic sea heights of about 65 cm, the new model for the dynamic sea surface topography is in good agreement with the models published in (Marsh et al., 1989b and 1990) and (Engelis, 1987). This agreement is also clearly shown in the Color Plates I and II. Moreover, Engelis computed his model from several decades of hydrographic data and the model described in this thesis was computed from only 34 days of data in the year 1986. In (Marsh et al., 1989b and 1990) use was made of 3 months of SEASAT data in the year 1978. Thus, part of the differences may be explained by changes in the ocean currents and by the application of differences in time scales and periods. It must also be noted that the standard deviations of the dynamic sea heights computed with the model described in this thesis are equal to about 10 cm. Therefore, it is concluded that the differences between the new model and the earlier published models are on the order of 2σ to 3σ. Therefore, it is concluded that the new model is a meaningful representation of the long-wavelength dynamic sea surface topography.

It has been shown that an adjusted gravity field model has been determined with which it is possible to reduce geoid and radial orbit errors for the GEOSAT altimeter observations. However, so far, it has only been shown that this is the case for the selected 34-day period. In Section 6.7, it will be shown that by using the adjusted gravity field model and model for the dynamic sea surface topography also a significant reduction in the sea height residuals and residual crossover differences for a two-year period can be obtained, although these models are "tailored" to a 34-day period.

In addition to the numerical experiments, it was analyzed how well the GEM-T2 calibrated covariance matrix and the covariance matrix of the adjusted GEM-T2 gravity field model (i.e. $w_{cal}N^{-1}$), equation (6.16)) predicted the radial orbit error (combining the equations (6.8) and (C.10), Appendix C) and the residual crossover differences (equations (6.13) and (C.10)). In this prediction, no state-vector errors and secular effects were taken into account. The results are displayed in the Figures 6.4-6.9. The Figures 6.4 and 6.5 show the rms of the radial orbit errors as a function of the order, summed over all degrees, of the gravity field harmonic expansion for the GEM-T2 and the adjusted GEM-T2 gravity field. A clear peak can be distinguished at order 43 in Figure 6.4. The GEOSAT satellite makes approximately 14 1/3 orbital revolutions per day and 43 is an exact multiple of this. Therefore, this peak is a near-resonance peak, after each orbital revolution the satellite "senses" the same gravity field disturbing force. With a closer look to the Figures 6.4 and 6.5 the same phenomena can be distinguished at the orders 14-15 and 28-29, although less pronounced. The Figures clearly reveal that the radial orbit errors of the GEM-T2 gravity field were reduced significantly after the adjustment. The Figures 6.6 and 6.7 corroborate this statement and show that the orbit errors are concentrated around the 1 cpr frequency. Also this can be explained by the concept of near-resonance (see also: equation (2.6a)).

The Figures 6.8 and 6.9 show the crossover difference errors as a function of the geographical location. Again it is clear that radial orbit errors were reduced significantly. This is especially the case for the ocean areas, which could be expected by the fact that only observations over the oceans were used in the gravity field adjustment. Comparing the predicted GEM-T2 crossover difference errors (Figure 6.8) with

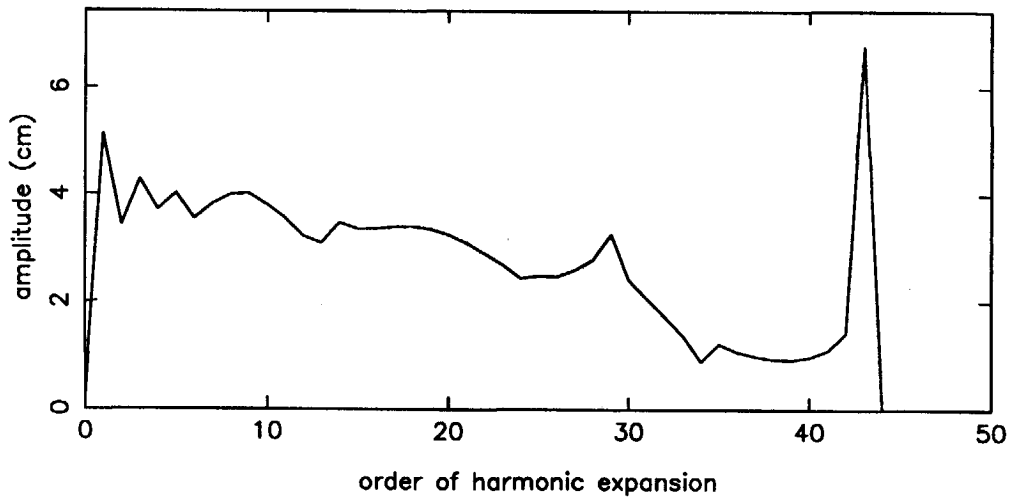

Figure 6.4 GEOSAT radial orbit error with the GEM–T2 calibrated covariance matrix

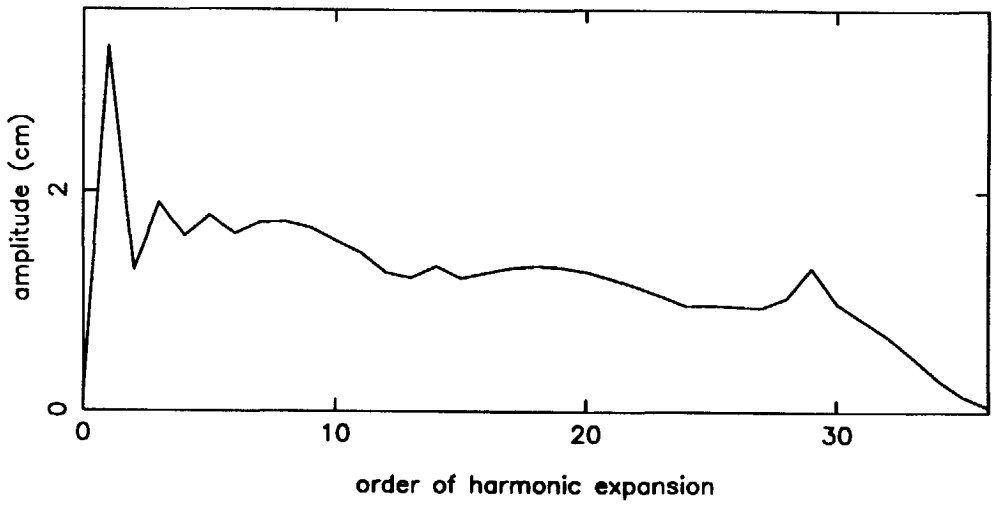

Figure 6.5 GEOSAT radial orbit error with the covariance matrix of the integrated approach

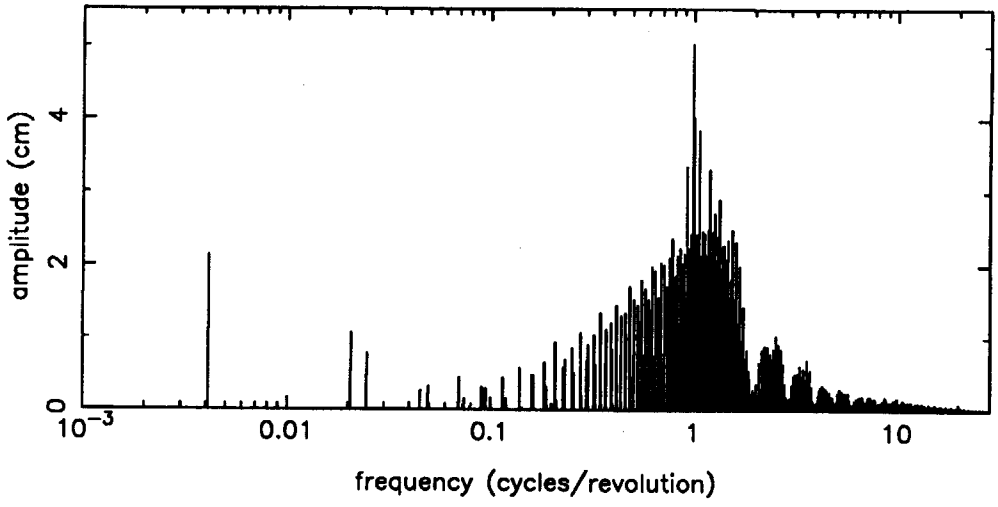

Figure 6.6 GEOSAT radial orbit error frequency spectrum with the GEM–T2 calibrated covariance matrix

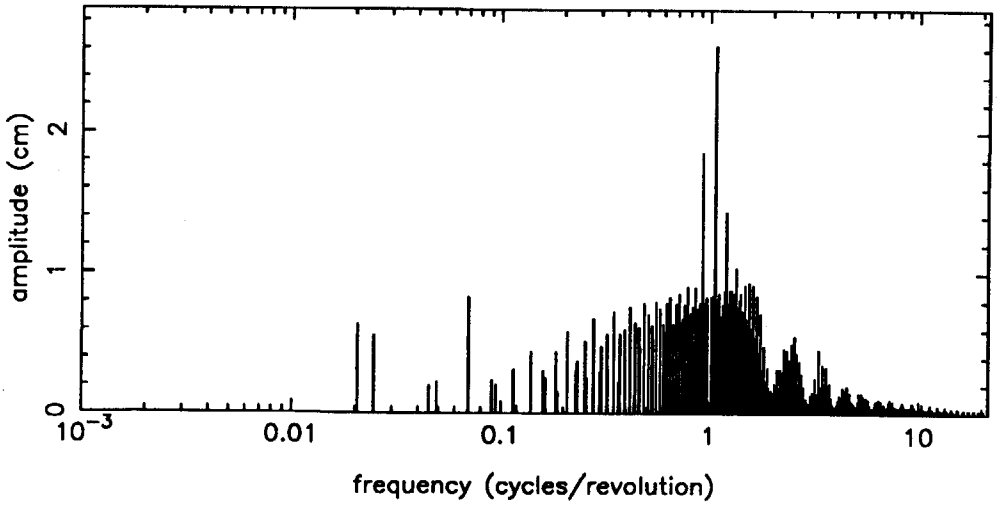

Figure 6.7 GEOSAT radial orbit error frequency spectrum with the covariance matrix of the integrated approach

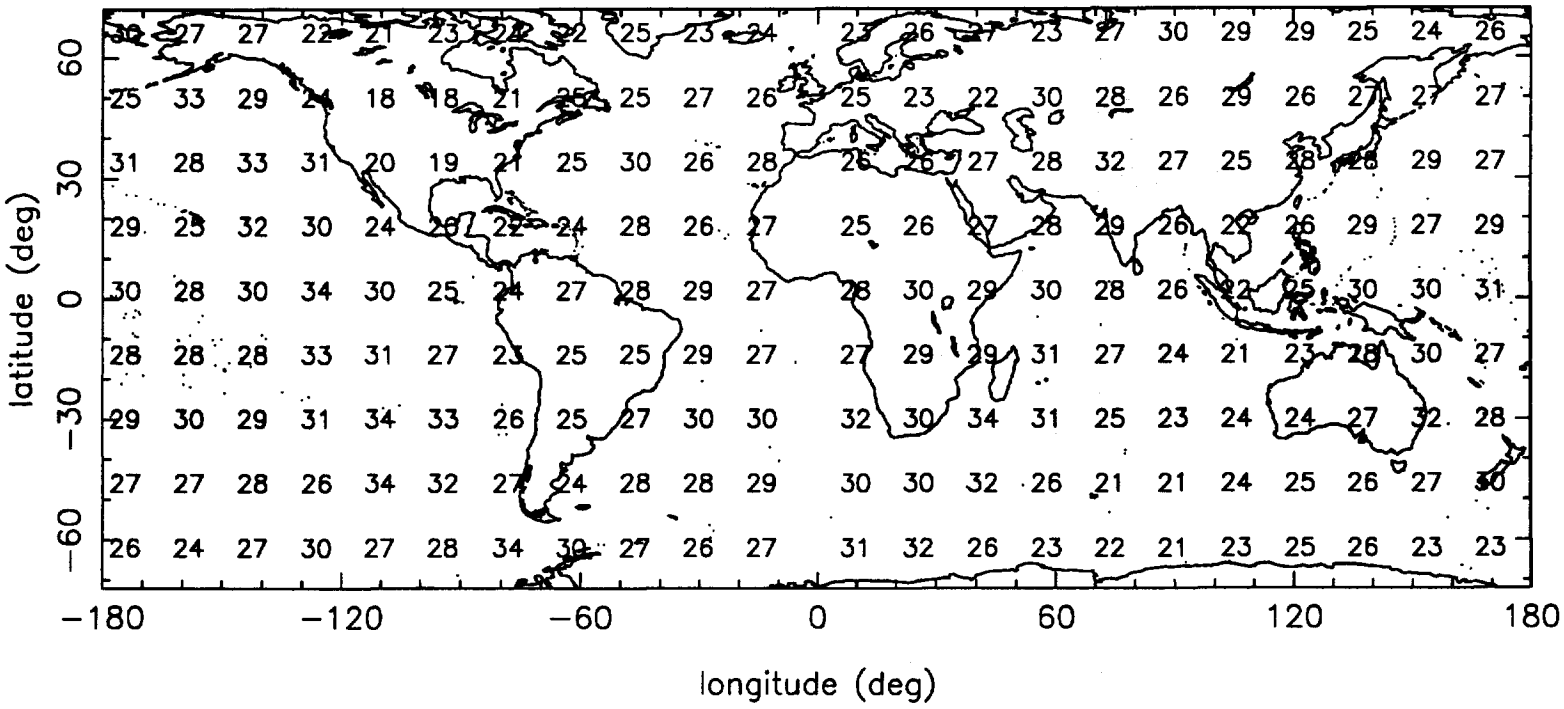

Figure 6.8 Distribution of residual crossover differences (cm) according to the calibrated GEM–T2 covariance matrix

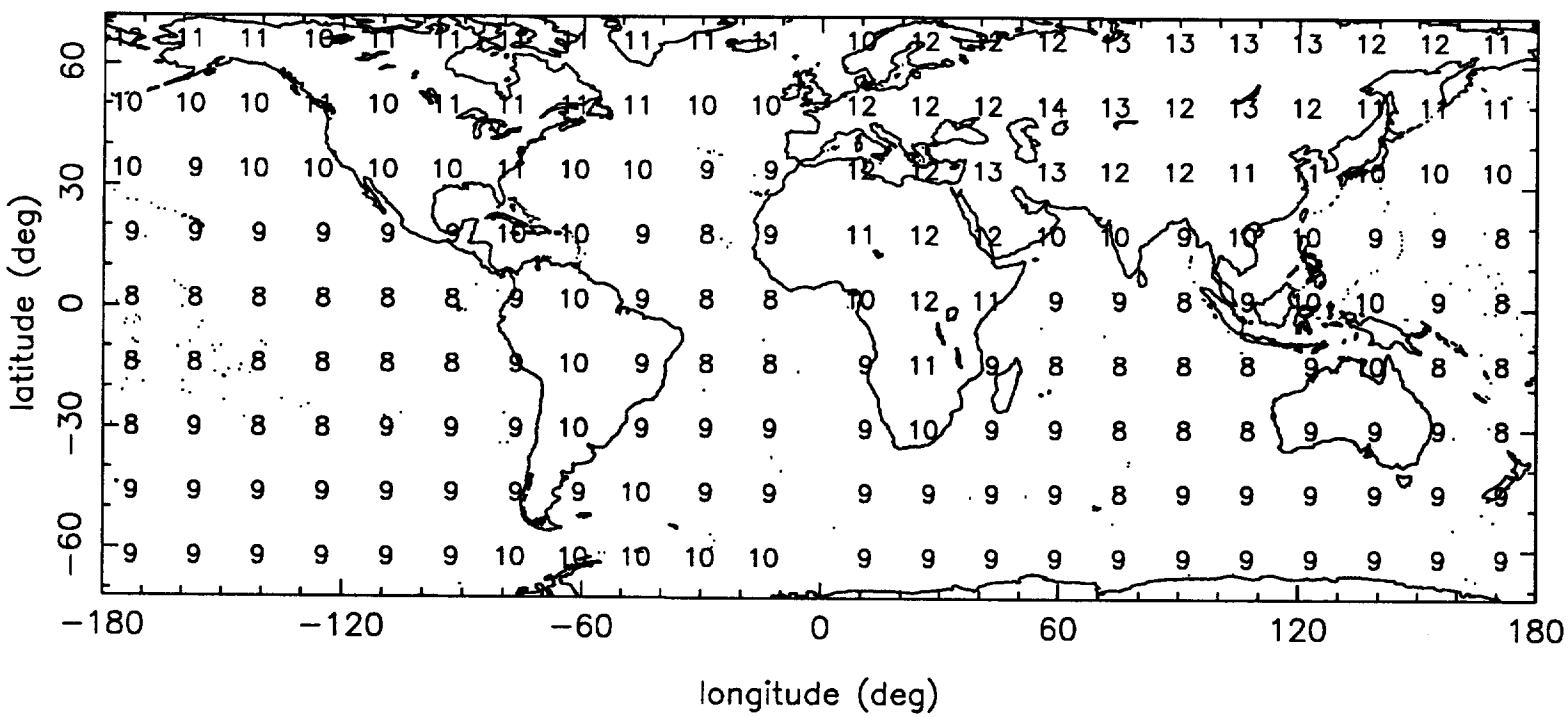

Figure 6.9 Distribution of residual crossover differences (cm) according to the covariance matrix of the integrated approach

the real rms-values (Figure 6.3), the latter are significantly larger. This may be explained by the fact that in addition to gravity field modeling errors, errors must be added due to mismodeling of non-conservative forces (e.g. atmospheric drag, solar radiation) and due to mismodeling of the altimeter observations (instrument correction errors, atmospheric delay correction errors, ocean surface variability, tide modeling errors, etc.).

Graphical representations of the new model for the dynamic sea surface topography can be found in the Figures 6.10 and 6.11, displaying contour levels of the dynamic sea heights and velocity vectors according to the geostrophic relations (see also: color plate I). The geostrophic relations read (Marsh et al., 1990):

$$u_g = -\frac{\gamma}{f_c}\frac{\partial h_{SST}}{\partial y} \tag{6.21a}$$

$$v_g = \frac{\gamma}{f_c}\frac{\partial h_{SST}}{\partial x} \tag{6.21b}$$

where γ is the local gravitational acceleration, f_c is the Coriolis parameter, u_g and v_g are the east-west and north-south geostrophic currents, and x and y are the local east-west and north-south coordinates. So, the gradients in the dynamic sea surface topography are a measure of the ocean current velocity in a direction perpendicular to the gradient. The Figures and the Color Plate I clearly reveal the circumpolar current at the Antarctic, the Agulhas current at South-Africa, the Gulf-Stream from Mexico to Western-Europe, and the Kuro-Shio current at Japan. The new topography model proves to be capable of modeling these known large-scale ocean currents very well. Graphical representations of the standard deviations of the adjusted GEM-T2 geoid and dynamic sea heights as a function of the geocentrical position are displayed in the color plates III and IV. As expected, the standard deviations are the largest over the land areas where no altimeter observations are available.

6.7 Analysis of two years of GEOSAT data with the adjusted gravity field model and the new model for the dynamic sea surface topography

The adjusted gravity field model and new model for the dynamic sea surface topography were used to analyze 43 17-day repeat periods (ERM's) of GEOSAT altimeter observations. These 43 periods range from November 8, 1986, to November 7, 1988, i.e. a period of exactly two years. Sea height residuals and residual crossover differences were computed and corrected by the procedures described in Section 6.5.

A number of additional corrections were applied to these sea height residuals and residual crossover differences. Firstly, orbit error corrections implied by the GEM-T2 coefficient adjustments obtained in the integrated approach were subtracted from the residual crossover differences and the sea height residuals. In addition, geoid corrections and dynamic sea heights computed with the new model for the dynamic sea

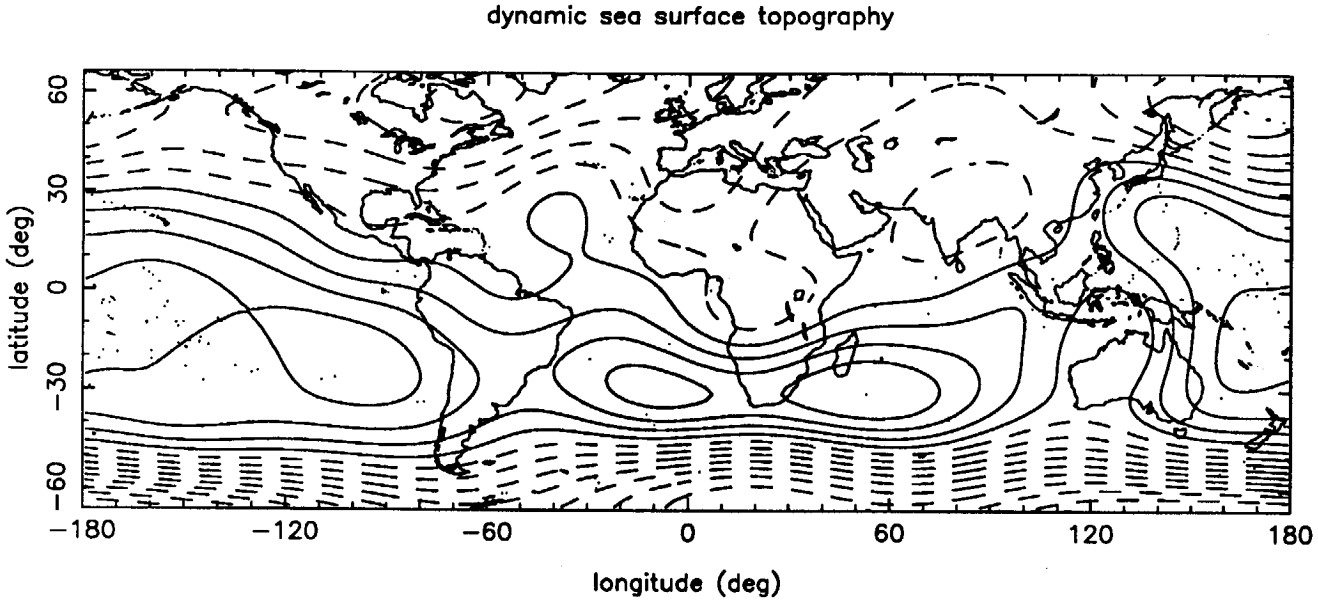

dashed contours <0 solid contours > 0
$-178.400\ (cm) < h_{SST} <\ 88.300\ (cm)$

Figure 6.10 Dynamic sea heights with the new SST−model

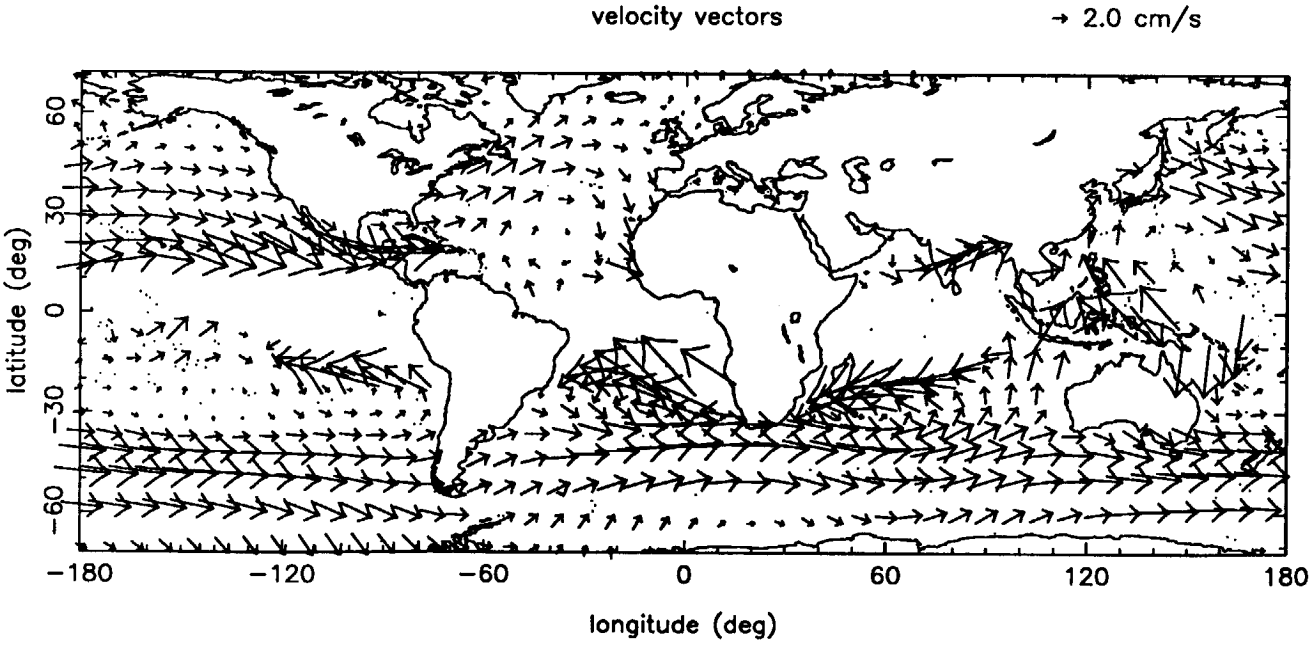

Figure 6.11 Ocean currents with the new SST−model

surface topography, also obtained in the integrated approach, were subtracted. Of course, the latter was only necessary for the sea height residuals. After this and finally, state-vector errors were estimated and also subtracted from the remaining sea height residuals and residual crossover differences. In this way, 43 17-day periods of fully corrected sea height residuals and residual crossover differences were obtained. The statistics of these sea height residuals and residual crossover differences are listed in the last columns of the Tables 6.3 and 6.4. As shown in these Tables, the rms of the a priori sea height residuals was reduced from about 140 cm to about 40-45 cm and the rms of the residual crossover differences from about 50-60 cm to about 35-40 cm. The a posteriori rms-values for the last three 17-day periods are relatively high, but this is probably caused by a deteriorated quality of the GEM-T2 orbits computed for these periods. Also the a priori rms-values for these three periods are relatively high. Especially, the rms-value of the a priori residual crossover differences of the last 17-day period, which is equal to 145 cm, is very high, indicating a poor orbit determination for this period. In general, it is concluded that the adjusted gravity field model and the new model for the dynamic sea surface topography behave very well for the 2-year period of GEOSAT observations.

The value of 40-45 cm for the rms of the a posteriori, or fully-corrected, sea height residuals represents for the greater part high-frequency geoid errors, altimeter measurement correction errors and ocean surface variability. By analyzing Table 6.3 in further detail, a 1-year cycle (about 21 17-day periods) can be distinguished for the rms-values, although the rms-values of the last 3 17-day periods are deviating. An interesting question that arises is whether part of this 1-year cycle can be attributed to variations in the long-wavelength ocean surface. In order to answer this question, the fully-corrected set of sea height residuals was used to determine variations in the long-wavelength ocean surface topography. This was done by applying a sort of long-wavelength filtering to this data set.

This filtering was performed in the following way: for each ERM normal equations were computed for a long-wavelength model, represented by a spherical harmonic expansion complete to degree and order 10. These models will be referred to as residual ocean surface topography solutions. Similar to the integrated approach, sea height residuals with an absolute value greater than 450 cm, residual sea heights in trench areas and residual sea heights in polar regions above 70° North or below 70° South were edited out.

It was possible to add and to solve any combination of normal equations of the 17-day periods. For example, normal equations could be combined and solved per 17-day period, per month (approximately 2 ERM's), per season (5-6 ERM's) or per year (21-22 ERM's). Constraints were added to keep the power of the residual sea surface topography within reasonable limits: the power of the solution must match the reduction of the a priori rms of the fully-corrected sea height residuals. Constraints were applied by adding degree variances of the ocean surface topography coefficients to the corresponding diagonal elements of the normal matrix (equation (6.14)). The power of the residual ocean surface topography solution was defined as:

Table 6.3 Statistics of two years of sea height residuals.

ERM-nr	nobs	a priori rms (cm)	-grav (cm)	-SST (cm)	-grav-SST (cm)	-all (cm)
1	30521	140.89	96.19	134.97	85.43	37.60
2	32109	144.54	101.55	136.32	87.20	35.20
3	32586	148.50	107.36	136.33	87.49	35.37
4	33269	151.03	111.10	135.42	86.63	38.67
5	33564	153.69	114.88	135.66	87.38	40.33
6	32966	156.00	116.60	136.30	87.67	42.15
7	33005	159.12	121.25	137.46	89.60	43.86
8	32390	155.49	116.51	134.93	86.06	53.98
9	31646	155.65	115.50	137.10	87.72	43.18
10	30618	151.06	109.21	135.88	85.48	42.16
11	30983	148.75	105.70	135.40	84.26	43.52
12	29017	147.56	102.91	135.69	83.46	44.41
13	29448	146.25	100.79	135.71	83.46	43.93
14	29050	144.42	98.47	135.11	82.99	43.19
15	25678	142.87	97.61	133.76	82.57	41.04
16	29272	141.50	95.04	133.80	82.23	45.29
17	31066	136.96	91.17	132.19	79.26	44.10
18	29375	138.51	91.66	132.18	80.68	45.42
19	28968	138.40	92.34	133.56	83.16	45.20
20	29306	139.18	92.34	134.73	84.07	40.71
21	28538	137.43	89.95	132.83	81.56	37.34
22	30473	140.47	94.11	135.67	85.47	36.54
23	16556	143.48	98.80	137.03	87.25	37.44
24	30104	143.66	99.51	135.73	85.99	37.77
25	32394	149.18	106.97	137.30	88.20	40.89
26	30877	152.96	112.43	136.61	88.04	45.29
27	29298	158.77	120.77	140.39	93.60	46.10
28	31136	157.54	119.66	137.38	90.04	45.54
29	31738	158.33	120.00	138.45	90.64	44.72
30	30664	156.13	116.23	138.58	89.81	43.91
31	27266	151.96	114.28	136.24	89.95	46.15
32	30880	152.59	112.36	137.73	89.55	44.45
33	28285	150.66	110.41	136.97	89.00	47.06
34	25720	145.00	104.34	132.98	85.53	43.39
35	25159	141.81	100.25	130.33	81.88	43.60
36	24794	139.80	97.19	129.65	80.94	45.14
37	22958	139.31	95.70	129.28	80.60	48.62
38	23045	138.31	95.47	130.21	83.01	53.37
39	17737	138.83	92.25	132.26	80.88	48.23
40	27465	141.63	95.56	136.32	86.55	47.44
41	26790	145.29	102.57	140.82	95.13	59.66
42	26387	147.19	105.85	142.35	98.12	54.49
43	26771	157.87	119.53	152.88	112.36	62.45

Table 6.4 Statistics of two years of residual crossover differences.

ERM	nobs	a priori rms (cm)	-grav (cm)	-all (cm)
1	16121	54.46	45.68	29.40
2	17735	55.12	46.55	26.24
3	18172	47.45	37.28	23.42
4	19534	43.00	32.38	23.40
5	16964	43.59	33.19	25.57
6	18926	49.59	40.74	26.06
7	18230	41.45	32.22	28.60
8	18398	41.77	32.22	28.32
9	17788	36.81	25.87	26.03
10	16468	40.32	29.18	28.73
11	16514	41.72	29.88	28.66
12	14418	48.65	37.20	35.92
13	14835	49.56	40.07	36.44
14	14641	50.78	41.10	32.34
15	11916	43.68	31.85	28.82
16	15531	48.57	38.48	38.61
17	17007	44.61	35.42	35.31
18	15381	55.26	48.55	40.10
19	14616	62.12	54.80	41.03
20	14630	61.77	54.89	25.92
21	13930	60.07	52.02	26.30
22	15864	63.13	55.62	25.58
23	4761	60.28	51.23	23.43
24	15417	51.64	42.56	23.57
25	18262	44.53	34.26	26.95
26	16349	50.33	41.81	39.80
27	14961	50.57	43.32	38.41
28	16452	41.04	31.80	31.92
29	18152	38.59	27.72	26.87
30	16297	40.32	29.37	28.71
31	12900	51.04	42.17	34.05
32	16562	53.74	45.71	30.12
33	13868	52.29	44.18	37.40
34	11705	44.71	33.94	33.34
35	11602	46.36	35.95	35.87
36	11673	53.02	44.19	44.05
37	10151	58.20	50.29	48.85
38	10320	63.59	57.42	53.39
39	5833	65.91	59.66	43.00
40	13438	84.25	79.97	45.14
41	12799	104.30	100.69	65.53
42	11858	118.79	114.34	56.78
43	12163	145.56	142.50	69.31

Table 6.5 Statistics of 17-day residual ocean surface topography solutions.

ERM	nobs	power SST (cm)	a priori rms sea heights (cm)	a posteriori rms sea heights (cm)
1	30308	18.096	35.04	32.40
2	32002	18.186	33.69	31.10
3	32387	16.233	33.16	30.04
4	32886	17.876	34.33	30.84
5	33081	17.931	35.68	32.05
6	32494	22.548	36.95	32.77
7	32449	21.241	38.39	34.31
8	31773	23.599	38.07	33.88
9	31185	26.230	36.73	32.46
10	30275	23.561	36.94	32.98
11	30575	21.543	36.92	33.18
12	28737	21.548	39.93	36.42
13	29123	19.705	39.45	36.19
14	28697	18.957	38.17	34.38
15	25343	19.513	36.28	32.11
16	28865	24.450	39.81	36.27
17	30678	23.565	39.58	36.54
18	29033	22.388	41.82	38.80
19	28655	24.414	42.25	39.61
20	29006	23.012	38.00	35.49
21	28227	20.666	34.23	31.03
22	30246	20.005	33.78	30.63
23	16411	18.160	33.74	30.05
24	29837	18.221	33.66	30.33
25	32043	19.417	35.41	31.93
26	30543	20.641	40.53	37.25
27	28928	22.017	41.12	37.72
28	30683	23.092	40.25	36.14
29	31231	26.874	38.09	33.58
30	30238	23.117	38.08	33.86
31	26912	23.079	40.35	36.09
32	30525	21.319	38.23	34.52
33	27922	22.508	40.97	37.07
34	25407	16.610	38.12	34.84
35	24814	18.654	38.04	34.61
36	24575	19.079	41.39	38.23
37	22717	20.434	45.85	42.90
38	22823	24.326	50.89	47.66
39	17514	22.938	44.30	40.69
40	27256	18.546	45.36	42.64
41	26619	19.693	57.98	55.49
42	26132	21.450	51.31	48.21
43	26469	22.288	59.25	56.81

$$power\ (SST) = a_e \left[\sum_{l=1}^{10} \sum_{m=0}^{l} \left[\bar{C}^{\xi}_{lm} \right]^2 + \left[\bar{S}^{\xi}_{lm} \right]^2 \right]^{1/2} . \qquad (6.22)$$

The normal equations were solved per ERM: the statistics of the obtained residual ocean surface topography solutions are listed in Table 6.5. As can be seen, the rms-values of the sea height residuals were not reduced dramatically (absolutely 3-4 cm, about 18 cm rms-wise). This can be explained by the long-wavelength filtering technique applied: only long-wavelength variations were estimated, which did not absorb the high-frequency geoid errors (although of course aliasing may occur but with a good global coverage of the oceans with observations and by the application of constraints this is not expected to be a serious problem).

After the determination of the residual ocean surface topography solutions, variations in these solutions were computed. This was performed by first computing for each period the sea heights (h_{SST}) over the oceans from the residual ocean surface topography solution of that period. Afterwards, in each point over the oceans the mean was computed. Finally, these mean values were subtracted from the sea heights for each period to obtain the variations. For the solutions listed in Table 6.5, the long-wavelength variability over the oceans has an rms-value of about 7 cm. A comparable value can be found in (Koblinsky et al., 1989), in which this variability was in good agreement with seasonal variations in the long-wavelength ocean currents determined from climatological data.

In addition, the correlations between the variations of Δh_{SST} with respect to the mean of all solutions were computed. The correlation ρ_{12} of the variations of two solutions 1 and 2 was defined as:

$$correlation_{12} = \frac{\sum_{oceans} \Delta h_{SST,1} \sum_{oceans} \Delta h_{SST,2}}{\left[\sum_{oceans} \Delta h_{SST,1}^2 \sum_{oceans} \Delta h_{SST,2}^2 \right]^{1/2}} . \qquad (6.23)$$

A correlation of 1 means that two solutions are equivalent (apart from a possible scale factor).

The correlations between all 17-day solutions are shown in Figure 6.12. Analyzing this Figure, it can be seen that bands of positive and negative correlations occur. These bands have a period of approximately 21 17-day periods, i.e. 1 year. In other words, the variations in the individual 17-day long-wavelength models exhibit a clear annual cycle.

The question now arises if this annual cycle can be attributed to seasonal ocean height variations or by other phenomena. For example, it is known that errors in the modeling of the ocean tides may exhibit an annual cycle. Another possibility is an annual cycle in the atmospheric delay corrections, e.g. the tropospheric and ionospheric corrections. With respect to the ocean-tides modeling, it is known that the M2-ocean tide causes an almost yearly variation in the sea heights at a fixed geographical position under the GEOSAT ground track (Cartwright and Ray, 1990). This variation can be written as:

Figure 6.12 Correlations, multiplied by 10, between variations of 17-day solutions for the long-wavelength ocean surface topography

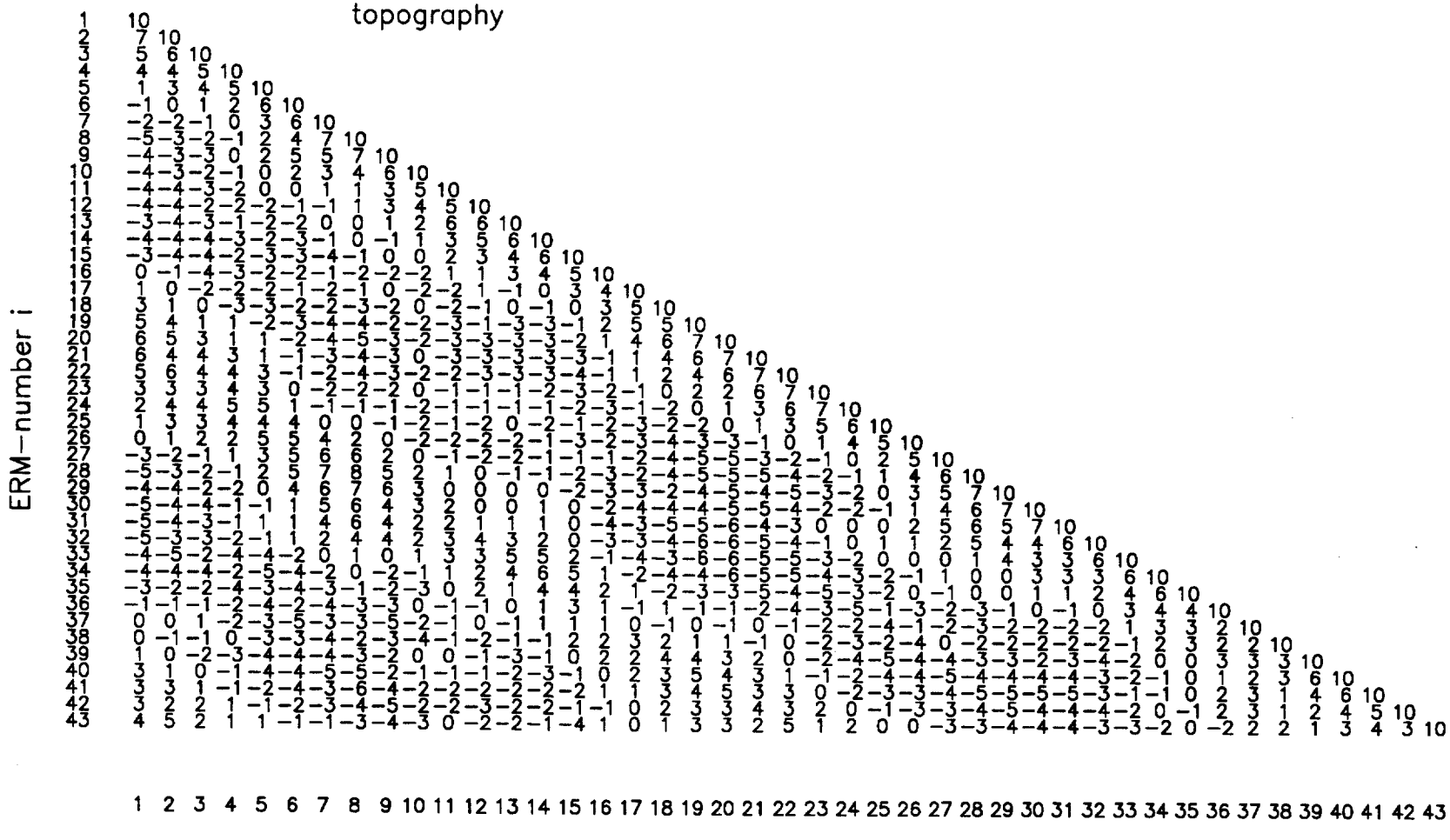

$$height\ (M2\text{–}tide) = A^* \cos([2^* \pi^* time\ (\text{days})/16.18]+\phi) \qquad (6.24)$$

where A and ϕ are constants. The GEOSAT repeat period is equal to 17.05 days. After about 19 repeat periods (close to 1 year), the satellite is at the same geographical position and the M2-tide height indicated by equation (6.24) has the same value. However, it can be shown that only a very small aliasing of the heights indicated by equation (6.24) occurs in the long-wavelength model solution, because geographically the tides-induced sea height indicated by this equation behaves as a short-wavelength function in each 17-day period. This wavelength is equal to 7.6° and the smallest wavelength in the residual ocean sea surface topography solutions was equal to 36°. As has been shown before (Section 4.2), the estimated error of the ocean-tide modeling was on the order of 10 cm for the large ocean basins spread over all tidal constituents. A very small part of this 10 cm is aliased in the long-wavelength solutions, whereas the variations in the long-wavelength ocean surface solutions have been shown to be on the order of 7 cm. In addition, the errors of the atmospheric path length corrections are expected to be very small (Section 4.2). In summary, a clear annual cycle in the long-wavelength solutions was determined. The mechanism behind this annual periodicity may be an annual cycle in the ocean surface height.

The results presented in this Section are very promising for the concept of satellite altimetry in relation to oceanographic and climatological studies. It seems very interesting to compare the results presented in this Section with independent climatological and oceanographic data. However, this comparison is outside the scope of this thesis.

6.8 Conclusions

The GEM-T2 model was adjusted by applying an integrated approach to two 17-day repeat periods of GEOSAT altimeter observations. Together with this adjustment, a new model for the long-wavelength dynamic sea surface topography was determined.

From a comparison with results published earlier (Nerem et al., 1988; Marsh et al., 1989b and 1990; Denker and Rapp, 1990; Engelis and Knudsen, 1989) and by conducting the procedures described in Section 6.4, it is concluded that the geoid computed with the adjusted GEM-T2 gravity field model is significantly more accurate than the geoid computed with the a priori GEM-T2 model. Moreover, residual cross-over differences were reduced significantly: the gravity field induced radial orbit error was decreased by about 20 cm. In addition, the new model for the dynamic sea surface topography behaves quite well in comparison with earlier published models. The new model is in good agreement with other models computed from satellite altimetry or from hydrographical information. The error in the new model seems to be between 10 and 30 cm for the dynamic sea heights compared to an rms-value of about 65 cm over the oceans for these heights. Moreover, the new model displays clearly well-known long-wavelength oceanic features, like the circumpolar current, the Agulhas current,

the Gulf-Stream and the Kuro-Shio current. Therefore, it is concluded that the integrated approach leads to valuable results.

The integrated approach was applied to only two 17-day repeat periods of GEOSAT observations. However, the adjusted GEM-T2 model and the new model for the dynamic sea surface topography were used to analyze two years of GEOSAT altimeter data. This analysis showed the possibility to determine systematic variations in long-wavelength ocean surface topography models. The most appealing result of this analysis was the determination of a clear annual cycle in the long-wavelength solutions.

The analysis in this Chapter has clearly shown the possibility of gravity field improvement and determination of the dynamic sea surface topography from satellite altimetry. In addition, also the possibility to study seasonal oceanographic or climatological phenomena has been indicated. With the altimeter missions ERS-1, which was launched in 1991, and TOPEX/Poseidon, which will be launched in 1992, the integrated approach is a very promising tool in gravity field related and oceanographic studies.

Part III. Gravity field recovery and adjustment from satellite-to-satellite tracking and gradiometry

7. Covariance analysis to a local gravity field recovery from satellite-to-satellite tracking and gradiometry

7.1 Introduction

With the advent and the ongoing deployment of the Global Positioning System (GPS), it becomes more and more interesting to implement GPS receivers on board of low Earth orbiting (LEO) satellites. This is especially true since these GPS receivers will be capable of delivering measurements of the range and/or range-rates between the LEO satellites and the GPS satellites. With these measurements, the orbits of the LEO satellites can be determined with great precision. In conjunction with this orbit reconstitution, it is also possible to improve our knowledge of the Earth's gravity field significantly. As already mentioned before, the altitude of the LEO satellite must be as low as possible to be able to determine a gravity field model with a fine resolution: only very low Earth satellite orbits are sensitive to high-frequency gravity field variations, because these variations are attenuated very quickly with increasing altitude. A dedicated satellite mission to improve our knowledge of the Earth's gravity field will be the ARISTOTELES mission, which is scheduled to be flown in 1997 (Rummel, 1989a). The primary objective of the ARISTOTELES mission is to determine a high-accuracy gravity field model with a resolution of about 100 km, which is equivalent to a spherical harmonic expansion complete to degree and order 180. For this resolution, the accuracy strived for is 5 mgal for gravity anomalies and 10 cm for geoid undulations. As shown in the previous Chapter, a high-accuracy gravity field model is a very important prerequisite for the correction of the altimeter measurements and opens the possibility to separate oceanographic features from gravity. Although already gravity field models complete to degree and order 360 exist (Rapp and Cruz, 1986; Rapp and Pavlis, 1990), these models are not very accurate for the shorter wavelengths and give for these shorter wavelengths merely a good representation of the mean sea surface, rather than of the gravity field (see section 1.3). If all mission objectives of ARISTOTELES are fulfilled, a gravity field model will be obtained that will not only behave nicely for the very long wavelengths (longer than 1000 km) but also for the shorter wavelengths (100 km - 1000 km). In that case, the ARISTOTELES mission will also facilitate the detection of oceanic features with shorter wavelengths than the long-wavelength dynamic sea surface topography that can be distinguished from satellite altimetry (see also: Figure 1.1).

The primary measurement device to be implemented on board of the ARISTOTELES satellite, will be a gravity gradiometer "sensing" the gravity tensor of the Earth at the satellite altitude. This gradiometer will consist of electrostatically suspended proof-masses which are separated by a distance on the order of 1 m. The differences between the accelerations of these proof-masses will be measured. These differential measurements will have an accuracy on the order of 0.01 EU (CIGAR, 1990) for gravity tensor components in the so-called sensitive axes, i.e. axes in a direction perpendicular to the satellite flight direction. Measurements in the flight direction are expected to be less accurate, because these measurement channels must have a greater dynamic range in order to accommodate atmospheric drag, compromising their sensitivity. The gradiometer will be implemented on a satellite which will fly in a low orbit and therefore the effect of atmospheric drag will be significant. Because of the limited bandwidth of the gradiometer, i.e. the gradiometer can only observe signals with a frequency between 0.005 and 5 Hz, the gradiometer is unable to deliver information about the low-frequency part of the gravity field, i.e. until degree 20-27, and about particular medium and high-degree gravity field spherical harmonics, i.e. from degree 28 to 180. The reason for this is that, especially for a polar orbit, also high-degree sectorial gravity field constituents cause for a significant part low-frequency orbit perturbations. This will be shown in Chapter 9. In that Chapter, also problems associated with the gradiometer bandwidth will be investigated.

A supplementary and complementary device to obtain gravity field information will be an on-board GPS receiver, yielding SST pseudo-range and carrier phase measurements. A pseudo-range measurement is obtained by measuring the transit time of coded radio-frequency signals transmitted by the GPS satellites and recorded by the GPS receiver, and by multiplying this transit time with the speed of light (Ambrosius et al., 1990). There are two types of pseudo-random noise codes modulated on carrier signals at the L-band frequencies (L1=1.575 and L2=1.227 GHz). The first code is the so-called "civilian access" (C/A) code, which is primarily intended to ease the acquisition of the second, more precise, P-code. The first code is the only code officially available to "civilian" users. This code has a "chip-rate" of about 1 MHz, and in conjunction with this, the highest accuracy of these measurements that can be achieved nowadays is on the order of 5 m. The P-code has a "chip-rate" of about 10 MHz, and therefore the accuracy of these measurements can be on the order of 1 m nowadays. Moreover, if P-code measurements are available in addition to C/A-code measurements, the so-called first order ionospheric propagation delay can be modeled (Gurtner, 1985). Apart from the C/A-code and P-code signals, the carrier itself may also be used for ranging. Although the system was not designed for this application, it was soon realized that the highly stable oscillators on board of the GPS satellites would allow very precise range measurements on this signal. The precision of these measurements can be as high as 0.5 cm.

The most important functions of the GPS receiver could be the support of a precise orbit determination of ARISTOTELES and the contribution of additional information about the low- and medium-degree part of the gravity field of the Earth. This could help to improve the accuracy of current (low-degree) spherical harmonic expansions of the gravity field to a higher level, so that low-degree errors will not obscure the

modeling of the higher degree field by the gradiometer measurements.

The capability of GPS to achieve this complementary objective has been shown extensively in several studies, especially the studies related to the Gravity Probe B and TOPEX/Poseidon mission (Wu and Yunk, 1986a and 1986b; Smith et al., 1988). In the study described in Part III, it will be investigated whether a GPS receiver has the capability to also provide information of the high-degree part of the gravity field of the Earth, thus serving as a supplementary device to the gradiometer. The expected accuracy of carrier phase measurements by future space-borne GPS receivers seems to open the possibility to achieve this objective (Ambrosius et al., 1990).

Because of the expected abundance of gradiometer measurements and GPS SST measurements from the full 21 (including 3 spares, proposed configuration as of 1988, the final configuration will include 3 more satellites making a total of 24) satellite configuration and a sampling rate of the order of a few seconds, and the huge amount of unknowns if a high-degree and -order spherical harmonic expansion of the gravity field is solved for, it was decided to first investigate the possibility of a local gravity field recovery. This means that the possibility of using GPS SST measurements to the ARISTOTELES satellite and ARISTOTELES gradiometer measurements for gravity anomaly/geoid undulation recovery with a resolution of 1° in longitude and latitude will be investigated for a restricted geographical area. The selected area extends from 0° to 20° longitude and from 40° to 60° northern latitude, thereby covering a large part of Western-Europe. Figure 7.1 gives an overview of the selected area. This Figure also displays the ground track pattern of a 30-day, 200 km altitude, ARISTOTELES orbital arc (CIGAR, 1989). In addition to the local gravity field recovery study, global gravity field recovery error analyses will be discussed in Chapter 9.

The study to a local gravity field recovery from satellite-to-satellite tracking (GPS) and gradiometry described in this thesis, can be divided into two parts. In this Chapter, a local gravity field recovery covariance analysis, based on the concept of least-squares collocation (Heiskanen and Moritz, 1967; Moritz, 1980; Rummel et al., 1976) is presented. This covariance analysis will give an insight in the requirements for the GPS receiver and gradiometer on board of ARISTOTELES to enable a high-precision, high-resolution gravity field recovery. The results of the covariance analysis can be compared with the results of the study described in Chapter 8. In that Chapter, a deterministic study to the possibility of a local gravity field recovery from ARISTOTELES GPS measurements is described. In the first part of this Chapter, the concept of least-squares collocation will be introduced. This will be followed by a description of the models used in the covariance analysis and the assumptions made in that analysis. Finally, results will be presented of the local gravity field recovery covariance analysis.

7.2 Least-squares collocation

The collocation formula for gravity anomaly (Δg) or geoid undulation (Δh) recovery from measurements at satellite altitude can be written in the following form (Moritz,

Figure 7.1 ARISTOTELES groundtracks over test area for a 30-days period

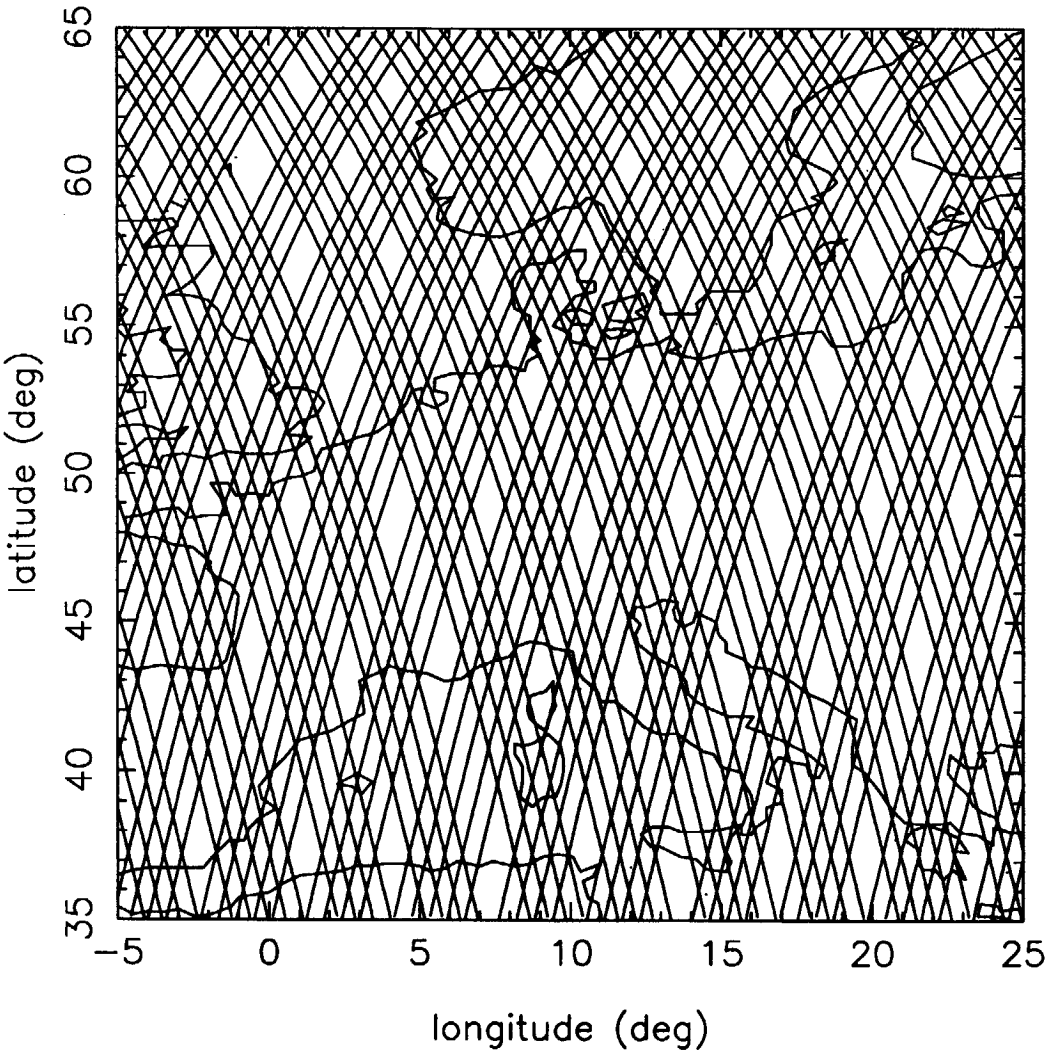

1980):

$$\Delta g/\Delta h = C_{\Delta g/\Delta h,t}(C_{tt}+D)^{-1}t \tag{7.1}$$

where $C_{\Delta g/\Delta h,t}$ is the row of correlations between the gravity anomaly/geoid undulation solved for and the column of measurements t, C_{tt} is the covariance matrix of the measurements t, and D is the noise variance matrix of these measurements. In the local gravity field recovery covariance analysis, the matrix D will be represented by a diagonal matrix. The elements of this matrix are equal to the variance of the noise. This means that the measurements are assumed to be corrupted by uncorrelated measurement errors. The measurements that will be considered, include gradiometer measurements for the sensitive axes, and ARISTOTELES satellite accelerations. The gradiometer measurements are represented by the tensor components Γ_{zz}, Γ_{zy} and Γ_{yy}, where the subscripts z and y denote components in the satellite radial and cross-track directions, respectively. For the ARISTOTELES orbit, which will be almost polar, the latter direction is almost equivalent with the West-East direction. In the local gravity field recovery covariance analysis described in this Chapter, the ARISTOTELES orbit was assumed to be polar. The tensor components of a disturbing potential T are defined by:

$$\Gamma_{zz} = \frac{\partial^2 T}{\partial z^2} \tag{7.2a}$$

$$\Gamma_{zy} = \frac{\partial^2 T}{\partial z\,\partial y} \tag{7.2b}$$

$$\Gamma_{yy} = \frac{\partial^2 T}{\partial y^2} \tag{7.2c}$$

The GPS range measurements contain the information from which accelerations of the ARISTOTELES satellite can be derived in the radial, along-track and cross-track directions. This will be discussed in Chapter 8.

The covariances, elements of the covariance row $C_{\Delta g/\Delta h,t}$ and the matrix C_{tt}, can be derived if the covariance functions for the gravity field functionals investigated, i.e. the gradiometer measurements, satellite accelerations, and gravity anomalies and geoid undulations, are known. Let *U(P)* and *U(Q)* be the potential from degree *lmin* to *lmax* of two points P and Q in space, with radii r_P and r_Q; then the covariance function *K(U(P),U(Q))* for this potential can be modeled by a spherical harmonic expansion from degree *lmin* to *lmax* (Moritz, 1980):

$$K(U(P),U(Q)) = \left[\frac{\mu}{a_e}\right]^2 \sum_{l=lmin}^{lmax} \left[\frac{a_e^2}{r_P r_Q}\right]^{(l+1)} k_l P_l(\cos\psi) \tag{7.3}$$

where ψ is the spherical distance between the points P and Q, and k_l the degree variance defined as:

$$k_l = \sum_{m=0}^{l} \left\{ \bar{C}_{lm}^{\,2} + \bar{S}_{lm}^{\,2} \right\}. \tag{7.4}$$

The covariance function of functionals L^1 and L^2 (e.g. gravity anomalies, geoid undulations, gradiometer measurements or satellite accelerations) of the potential U follows from the relation:

$$K(L^1U(P), L^2U(Q)) = L^1L^2K(U(P), U(Q)) \,. \tag{7.5}$$

As an example, the Rapp '79 anomaly degree variance model reads (Rapp, 1979):

$$\sigma^2(\Delta g_l) = (l-1)\left\{ \frac{3.405}{l+1} 0.998006^{l+2} + \frac{140.03}{(l-2)(l+2)} 0.914232^{l+2} \right\} \text{mgal}^2 \,. \tag{7.6}$$

where $\sigma^2(\Delta g_l)$ is the anomaly variance for degree l. From this model, the degree variances k_l can be computed by combining the equations (1.6), (7.3) and (7.5).

An important aspect of the method of collocation is that it can also provide accuracy estimates of recovered gravity anomalies/geoid undulations. For gravity anomalies, for example, the error estimate $\sigma_{err}^{\,2}(\Delta g)$ reads:

$$\sigma_{err}^{\,2}(\Delta g) = C(0)_{\Delta g} - C_{\Delta g,t}(C_{tt}+D)^{-1}C^T_{\Delta g,t} \tag{7.7}$$

where $C(0)_{\Delta g}$ is the variance, or square of the power, of the a priori gravity anomalies. This variance is found by inserting $\psi=0$ in the covariance function of the gravity anomalies.

The importance of the last formula lies in the possibility to estimate the accuracy of recovered gravity anomalies/geoid undulations, given a certain set of measurements t with a specified accuracy from which these gravity anomalies/geoid undulations are estimated. Equation (7.7) holds for accuracy estimates of point gravity anomalies. A similar equation can be derived for point geoid undulations. In addition to these accuracy estimates, also accuracy estimates for mean 1° x 1° gravity anomalies and geoid undulations will be computed, because the resolution of the gravity field recovery strived for is 1.0°. In the local gravity field recovery study described in this thesis, mean 1° x 1° values were computed by taking the mean of a large number of point values in a 1° x 1° block. The principles for the estimation of the accuracy of these mean values are described in Appendix E.

The computation of the covariance functions, the core of the collocation process, requires some special attention. The optimum (isotropic and homogeneous) covariance functions are obtained by using the same coefficients of the spherical harmonic expansions of the gravity field used to compute the accelerations, gradiometer measurements and gravity anomalies/geoid undulations for the degree variances (equation (7.4)). A covariance function value for certain gravity field induced signals is obtained by a summation of Legendre polynomials (equations (7.3) and (7.5)). A very efficient way

to perform these summations is the recursive method known as Horner's procedure (Tscherning, 1972), which starts with the smallest terms in the summation and is stable for computer applications.

7.3 Simulation set-up for the covariance analysis

Both in the local gravity field recovery covariance analysis and the deterministic gravity field recovery study (Chapter 8), the "real-world" gravity field was simulated by an existing high-degree and -order gravity field model: the OSU86F gravity field model complete to degree and order 360 (Rapp and Cruz, 1986). The resolution of this model is 0.5°, whereas the resolution of the gravity field strived for is 1.0° for the ARISTOTELES mission. A resolution of 1.0° is equivalent to a gravity field model complete to degree and order 180. Therefore, to study the effect of gravity field terms above degree 180, a gravity field model has been chosen with a maximum degree deliberately above 180 to represent the "real-world". Of course, even gravity field terms with a degree above 360 exist, but it will be shown that it can be expected that these terms will have a minor effect in the recovery of gravity field terms with a degree below 180.

It was assumed that the gravity anomalies and geoid undulations have to be estimated on the surface of the Earth from a regular grid of satellite accelerations and gradiometer measurements at the ARISTOTELES satellite altitude (Figure 7.2), i.e. the measurements at satellite altitude have to be continued downward to gravity anomalies and geoid undulations on the Earth's surface. This downward continuation is an instable process in which small errors in the measurements may lead to large errors in the recovered gravity anomalies and geoid undulations (Tikhonov, 1963). This will be shown in the covariance analysis described in this Chapter. The gravity anomaly or geoid undulation to be recovered is positioned at the projection of the center of the regular grid on the Earth's surface. This surface was represented by a sphere with a radius a_e equal to 6,378,137 m. All measurements were assumed to be made at a satellite altitude of 200 km. This will be the average altitude above the Earth's surface of the ARISTOTELES orbit (CIGAR, 1989). In addition, also an altitude of 160 will be considered briefly to study the effect of the measurement altitude. More attention to this will be paid in the next Chapter. The measurements were assumed to be distributed in a regular grid with a resolution (grid maze, Figure 7.2) of 1.0 degree both in the latitude and longitude directions, comparable to the resolution of the gravity field strived for. The size of this grid could be be varied.

In the covariance analysis, it was assumed that the low-degree part of the gravity field was subtracted from the measurements. Two cases were investigated. In the first case (in the following referred to as case 1), it was assumed that the gravity field part complete to degree and order 36 could be modeled exactly. In that case, this part of the gravity field was subtracted from the "real-world" gravity field. This means that the OSU86F gravity field model from degree 37 complete to degree and order 360 was

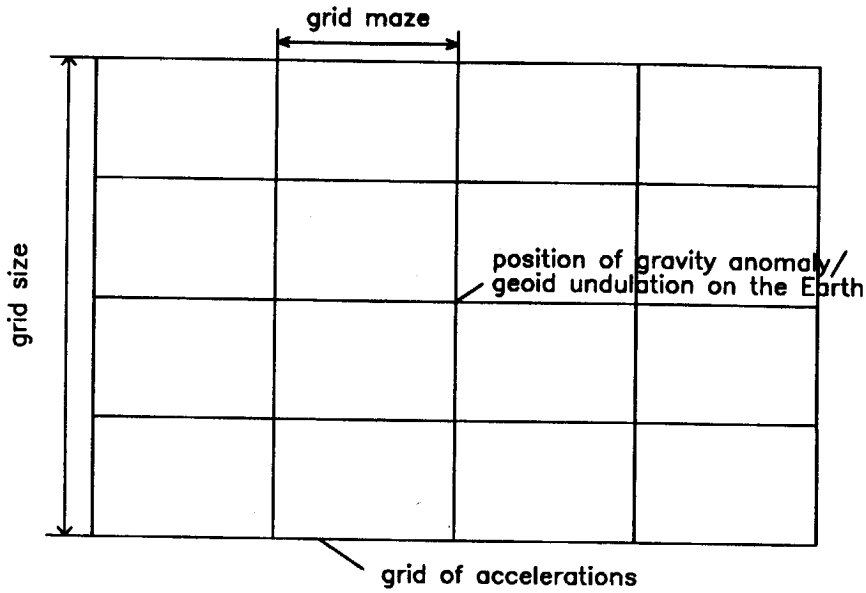

Figure 7.2 Configuration for downward continuation by least-squares collocation

used to model the degree variances (equation (7.4)). In the second case (in the following referred to as case 2), the low-degree part of the gravity field was modeled by the GEM-T1 model. The differences between OSU86F and GEM-T1 for low degrees and orders may be considered to reflect the accuracy of current gravity field models for low degrees and orders, and were used to simulate low-degree gravity field modeling error. This was done to study the effect of low-degree terms in a local gravity field recovery. In case 2, the OSU86F model, complete to degree and order 360, minus the GEM-T1 model, complete to degree and order 36, was used to compute the degree variances (equation (7.4)). In other words, in case 1, all measurements were assumed to be caused by the OSU86F gravity field above degree 36, and in case 2, by OSU86F minus GEM-T1.

Accuracy estimates for gravity anomalies and geoid undulations were computed for several combinations of measurements. Firstly, accuracy estimates were computed for different combinations of satellite accelerations. Secondly, this was done for different combinations of gradiometer measurements. Finally, accuracy estimates were computed for combinations of satellite accelerations and gradiometer measurements, and a few additional computations were performed to study the effect of the satellite altitude and to study the effect of the gravity field omission error, which is caused by truncating the "real-world" gravity field to degree 360.

As indicated in the previous Section, a distinction was made between point gravity anomalies/geoid undulations and mean gravity anomalies/geoid undulations, where mean gravity anomalies/geoid undulations were defined as the mean of a large number of point gravity anomalies/geoid undulations, which were distributed regularly in a 1° x 1° block, i.e. 1° in latitude and 1° in longitude, on the Earth's surface. It was found that a number of 25 was sufficient; taking the mean of more than 25 point values did not change the mean values significantly. The selected block was located at 50° northern latitude, i.e. in the middle of the selected area (Figure 7.1). In all cases investigated, both accuracy estimates for point values and mean values were computed. Accuracy estimates for mean gravity anomalies/geoid undulations for a 1° x 1° block area were computed to filter out the effect of gravity field terms with a resolution smaller than 1.0°.

In Table 7.1 power estimates of gravity anomalies, geoid undulations, satellite accelerations and gradiometer measurements are listed for case 1 and case 2. It can be seen that the power estimates for mean 1° x 1° gravity anomalies and geoid undulations are smaller than these estimates for point gravity anomalies and geoid undulations. As indicated above, this could be expected, because gravity field terms with a resolution smaller than 1.0° were filtered out. By analyzing Table 7.1, it is also concluded that the low-degree gravity field modeling errors have a significant effect on the power of the geoid undulations: the power estimate increases from 1.56 m (case 1) to 2.36 m (case 2) for point geoid undulations. The power estimate for point gravity anomalies only increases from 19.0 mgal to 19.9 mgal. The latter can be explained by considering the degree variances for gravity anomalies ($\sigma^2(\Delta g_l)$) and geoid undulations ($\sigma^2(\Delta h_l)$). These degree variances are obtained by combining equations (1.6)-(1.7) and (7.3)-(7.5). The degree variances read, if the Earth is approximated by a sphere with radius a_e:

Table 7.1 Power estimates for gravity anomalies, geoid undulations, satellite accelerations, and gradiometer measurements. The power estimates for the satellite accelerations and gradiometer measurements hold for a satellite altitude of 200 km.

	power	
	case 1	case 2
point anomalies (mgal)	19.0	19.9
mean 1° x 1° anomalies (mgal)	16.3	17.4
geoid undulations (m)	1.56	2.36
mean 1° x 1° undulations (m)	1.49	2.31
radial accelerations (mgal)	2.11	3.52
latitudinal/ longitudinal acc. (mgal)	1.48	2.44
Γ_{zz} (EU)	0.18	0.21
Γ_{zy} (EU)	0.12	0.15
Γ_{yy} (EU)	0.12	0.14

case 1: OSU86F above degree 36;
case 2: OSU86F minus GEM-T1.

$$\sigma^2(\Delta g_l) = \left[\frac{(l-1)\mu}{a^2_e}\right]^2 k_l \qquad (7.8a)$$

$$\sigma^2(\Delta h_l) = a_e{}^2 k_l \ . \qquad (7.8b)$$

The most important difference between the gravity anomaly and geoid undulation degree variances is the term $(l\text{-}1)^2$, which indicates that relatively a greater part of the gravity anomaly spectrum is concentrated at higher degrees compared to the geoid undulation spectrum. Therefore, the inclusion of low-degree gravity field modeling errors causes relatively a greater increase of the power estimate of the geoid undulations. Finally, it can be concluded from Table 7.1 that the power of measurements with all components in the radial accelerations, respectively radial satellite accelerations and the gravity tensor component Γ_{zz}, is relatively high, about 40-45 % higher than the power of respectively satellite accelerations and gradiometer measurements with components in non-radial directions.

7.4 Accuracy estimates for gravity field recovery from accelerations

Accuracy estimates for gravity anomalies and geoid undulations were computed assuming grids of satellite accelerations at the mean ARISTOTELES satellite altitude. The mean ARISTOTELES satellite altitude is defined as the average altitude of the ARISTOTELES satellite above the Earth's surface for the selected geographical area. As indicated in Section 7.3 two cases have been investigated. In the first case (case 1), it was assumed that the gravity field can be modeled exactly to degree and order 36. In the second case (case 2), low-degree gravity field modeling errors were introduced by taking the differences between the OSU86F and GEM-T1 gravity field models. For both cases, two different combinations of satellite accelerations were studied. The first combination consisted of radial satellite accelerations alone, and in the second combination, satellite accelerations in the West-East and Nort-South directions were added.

In Chapter 8, it will be shown that ARISTOTELES satellite accelerations can be computed from very precise GPS range measurements with an accuracy of about 1.0 mgal and a resolution of 1.0° in latitude and longitude. Therefore, accuracy estimates of gravity anomalies and geoid undulations, that have to be determined from these accelerations, were computed for the case that the satellite accelerations have an accuracy of 1.0 mgal. In that case, the satellite accelerations were assumed to be corrupted with uncorrelated measurement errors with a standard deviation of 1.0 mgal and an expectancy of 0.0 mgal. This case was compared with the "ideal" case, in which the satellite accelerations can be determined exactly, i.e. with an accuracy of 0.0 mgal.

The accuracy estimates for gravity anomalies and geoid undulations are listed in the Tables 7.2 and 7.3. As to be expected, the accuracy of recovered gravity anomalies and geoid undulations improves if the grid size increases, but it can also be concluded that it is not necessary to keep expanding this grid size. Taking more than 49 grid positions (i.e. a 7° x 7° area at satellite altitude) does not decrease the value of the

Table 7.2 Gravity anomaly recovery from satellite accelerations.

grid size ° x °	case	noise (mgal)	accuracy (mgal) radial direction	3 directions
1 x 1	1	0.0/1.0	14.4 / 15.3	14.4 / 15.3
1 x 1 mean	1	0.0/1.0	11.3 / 12.4	11.3 / 12.4
3 x 3	1	0.0/1.0	9.1 / 14.9	7.4 / 14.1
3 x 3 mean	1	0.0/1.0	5.7 / 12.0	4.2 / 11.1
5 x 5	1	0.0/1.0	6.6 / 14.1	3.5 / 13.3
5 x 5 mean	1	0.0/1.0	3.5 / 11.1	1.4 / 10.2
7 x 7	1	0.0/1.0	5.6 / 13.8	2.0 / 13.1
7 x 7 mean	1	0.0/1.0	2.5 / 10.7	0.6 / 10.0
9 x 9	1	0.0/1.0	5.1 / 13.7	1.2 / 13.1
1 x 1	2	0.0/1.0	15.8 / 16.1	15.8 / 16.1
1 x 1 mean	2	0.0/1.0	12.9 / 13.3	12.9 / 13.3
3 x 3	2	0.0/1.0	9.2 / 15.6	7.8 / 14.2
3 x 3 mean	2	0.0/1.0	5.9 / 12.7	4.6 / 11.1
5 x 5	2	0.0/1.0	6.8 / 14.1	3.9 / 13.4
5 x 5 mean	2	0.0/1.0	3.6 / 11.1	1.7 / 10.3
7 x 7	2	0.0/1.0	5.6 / 13.8	2.3 / 13.1
7 x 7 mean	2	0.0/1.0	2.6 / 10.7	0.7 / 10.0

mean: mean of 25 point values in a 1° x 1° block.

Table 7.3 Geoid undulation recovery from satellite accelerations.

grid size ° x °	case	noise (mgal)	accuracy (cm) radial direction	3 directions
1 x 1	1	0.0/1.0	56 / 84	56 / 84
1 x 1 mean	1	0.0/1.0	46 / 76	46 / 76
3 x 3	1	0.0/1.0	27 / 72	19 / 64
3 x 3 mean	1	0.0/1.0	18 / 63	11 / 55
5 x 5	1	0.0/1.0	16 / 68	7 / 59
5 x 5 mean	1	0.0/1.0	9 / 59	3 / 50
7 x 7	1	0.0/1.0	13 / 65	4 / 58
7 x 7 mean	1	0.0/1.0	6 / 56	1 / 49
9 x 9	1	0.0/1.0	12 / 65	3 / 58
1 x 1	1	0.0/1.0	63 / 89	63 / 89
1 x 1 mean	1	0.0/1.0	54 / 82	54 / 82
3 x 3	1	0.0/1.0	45 / 77	23 / 73
3 x 3 mean	1	0.0/1.0	39 / 68	18 / 64
5 x 5	1	0.0/1.0	28 / 75	10 / 69
5 x 5 mean	1	0.0/1.0	25 / 66	8 / 60
7 x 7	1	0.0/1.0	26 / 71	6 / 63
7 x 7 mean	1	0.0/1.0	23 / 63	5 / 55

accuracy estimates significantly. In all cases, the values of the accuracy estimates for mean gravity anomalies and geoid undulations are smaller than these values for point gravity anomalies and geoid undulations. As indicated before, this can be explained by the fact that by taking the mean of a large number (i.e. 25) of point values, high-frequency errors, in this case errors with wavelengths smaller than 2°, i.e. with a resolution of 1°, are filtered out. With faultless accelerations in 3 directions, mean 1° x 1° gravity anomalies and geoid undulations can be recovered with an accuracy of 0.6 mgal (Table 7.2) and 1 cm (Table 7.3) for case 1, respectively. For case 2, these values are 0.7 mgal and 5 cm, respectively. From the Tables 7.2 and 7.3, it can be seen that the inclusion of low-degree gravity field modeling errors (case 2) is not expected to be a severe problem: the accuracy estimates for both case 1 and case 2 are almost identical. This is especially true for a grid size equal to 7° x 7°: the accuracy estimates for point gravity anomalies and geoid anomalies, which are to be determined from faultless accelerations in three directions, are 2.0 mgal and 4 cm for case 1, and 2.3 mgal and 6 cm for case 2. The effect of the inclusion of low-degree gravity field modeling errors on the accuracy estimates of the gravity anomalies is relatively smaller than on the accuracy estimates of the geoid undulations. As indicated before, this may be explained by the fact that relatively a greater part of the gravity anomaly spectrum is concentrated at the higher degrees compared to the spectrum of geoid undulations (equations (7.8a)-(7.8b)). With an accuracy of 1.0 mgal of the accelerations, which are expected to be recovered from GPS measurements to ARISTOTELES (Chapter 8), the ARISTOTELES mission objectives (5 mgal and 10 cm accuracy for mean 1° x 1° gravity anomalies and geoid undulations, respectively) can not be reached. With an accuracy of 1.0 mgal of accelerations in 3 directions and a grid size of 7° x 7°, the accuracy estimates are 10.0 mgal (case 1 and case 2) for mean 1° x 1° gravity anomalies, and 49 cm (case 1) and 55 cm (case 2) for mean 1° x 1° geoid undulations, respectively. For point values these estimates were 13.1 mgal (case 1 and case 2) and 58 cm (case 1) and 63 cm (case 2). Thus, a noise of 1.0 mgal on the satellite accelerations is expected to cause errors in recovered gravity anomalies that are an order of magnitude larger. This phenomenon is characteristic for the concept of downward continuation, in which small errors of measurements, which are made at satellite altitude, may lead to large errors in the recovered gravity field on the Earth's surface (Tikhonov, 1963). The values of the accuracy estimates are significantly smaller than the power estimates for point and mean gravity anomalies (Table 7.1), respectively 19.0/19.9 mgal (case 1/case 2) and 16.3/17.4 mgal (case 1/case 2), and the power estimates for point and mean geoid undulations, respectively 156/149 cm mgal (case 1/case 2) and 236/231 cm (case 1/case 2). This indicates that a large part of the (residual) gravity field can be recovered.

The estimates obtained by assuming the availability of accelerations in 3 directions are comparable to the accuracy estimates for which it was assumed that only radial accelerations are available, for the case where the noise of the accelerations is 1.0 mgal. For example, for case 2 and a grid size of 7° x 7°, the accuracy estimates of mean 1° x 1° gravity anomalies and geoid undulations are 10.0 mgal and 55 cm, if accelerations in 3 directions are available, and 10.7 mgal and 63 cm, if only radial accelerations are available. This can be explained by considering the power estimates

in Table 7.1 for radial accelerations and accelerations in directions perpendicular to the radial. As indicated before, the power estimates of radial accelerations are about 40-45 % higher (for case 1 and case 2). This means that the power of the radial accelerations is about equal to the power of the combination of accelerations in the West-East and North-South directions.

7.5 Accuracy estimates for gravity field recovery from gradiometry

The same configurations as used in Section 7.4 were used for the estimation of accuracy estimates for gravity anomalies and geoid undulations from satellite gradiometry. These estimates are listed in the Tables 7.4 and 7.5. With faultless observations, the accuracy estimates for mean 1° x 1° gravity anomalies and geoid undulations for case 1 are respectively 0.8 mgal and 3 cm, for a grid size equal to 7° x 7° and when using all three components Γ_{zz}, Γ_{zy} and Γ_{yy}. For case 2 these estimates are equal to 0.8 mgal and 39 cm, respectively. For point gravity anomalies and geoid undulations, these estimates are respectively 2.0 mgal and 5 cm for case 1, and 2.1 mgal and 40 cm for case 2. By comparing the results of case 1 and case 2, it can be concluded that low-degree modeling errors have a small effect on the recovery of gravity anomalies, but a significant effect on the recovery of geoid undulations. This can be explained by the fact that a relatively great part of the signal content of gradiometer measurements is concentrated at the high degrees (this will be shown in Chapter 9 in the global gravity field recovery error analyses), even in comparison with satellite accelerations. Therefore, a relatively large error will be made in the low-degree part of geoid undulations, that are recovered from gradiometer measurements. However, in the preceding Section, it was shown that this problem can be reduced by using satellite accelerations in the estimation process. The concept of combining satellite accelerations and gradiometer measurements in the local gravity field covariance analysis will be discussed in the next Section.

With the projected accuracy of 0.01 EU of gradiometer measurements for components in the sensitive directions (perpendicular to the ARISTOTELES flight direction), the mission objectives can almost be reached for case 1: mean 1° x 1° anomalies and undulations can be recovered from all three gradiometer components, with an estimated accuracy of respectively 4.4 mgal and 14 cm. For point gravity anomalies and geoid undulations, these estimates are 7.6 mgal and 22 cm. If only Γ_{zz} is used, these values are respectively 8.0 mgal and 24 cm for case 1. If also low-degree gravity field modeling errors are included (case 2), the mission objectives can only partly be reached: for mean 1° x 1° gravity anomalies, the predicted accuracy is 4.5 mgal, but for mean 1° x 1° geoid undulations, the predicted accuracy is 52 cm. However, as indicated before, the larger part of the geoid undulation error will be concentrated at the low degrees. It will be shown that the low-degree gravity field modeling errors will be reduced significantly and will become much smaller than the differences between OSU86F and GEM-T1, if future GPS observations to ARISTOTELES are used to

Table 7.4 Gravity anomaly recovery from Γ_{zz}, Γ_{zy}, Γ_{yy}.

grid size ° x °	case	noise (0.01 EU)	accuracy (mgal) Γ_{zz}	3 components
1 x 1	1	0.0/1.0	12.0 / 12.1	12.0 / 12.1
1 x 1 mean	1	0.0 /1.0	8.7 / 8.8	8.7 / 8.8
3 x 3	1	0.0/1.0	7.7 / 9.1	5.2 / 8.6
3 x 3 mean	1	0.0/1.0	4.4 / 5.8	2.6 / 5.3
5 x 5	1	0.0/1.0	5.8 / 8.4	3.0 / 7.8
5 x 5 mean	1	0.0/1.0	2.7 / 5.3	1.3 / 4.6
7 x 7	1	0.0/1.0	5.1 / 8.0	2.0 / 7.6
7 x 7 mean	1	0.0/1.0	2.1 / 4.9	0.8 / 4.4
1 x 1	2	0.0/1.0	12.4 / 12.4	12.4 / 12.4
1 x 1 mean	2	0.0/1.0	9.1 / 9.1	9.1 / 9.1
3 x 3	2	0.0/1.0	7.9 / 9.3	5.4 / 8.7
3 x 3 mean	2	0.0/1.0	4.6 / 6.0	2.8 / 5.4
5 x 5	2	0.0/1.0	5.8 / 8.4	3.1 / 7.8
5 x 5 mean	2	0.0/1.0	2.7 / 5.4	1.4 / 4.6
7 x 7	2	0.0/1.0	5.1 / 8.0	2.1 / 7.6
7 x 7 mean	2	0.0/1.0	2.2 / 4.9	0.8 / 4.5

Table 7.5 Geoid undulation recovery from Γ_{zz}, Γ_{zy}, Γ_{yy}.

grid size ° x °	case	noise (0.01 EU)	accuracy (cm) Γ_{zz}	3 components
1 x 1	1	0.0/1.0	33 / 34	33 / 34
1 x 1 mean	1	0.0/1.0	24 / 25	24 / 25
3 x 3	1	0.0/1.0	26 / 32	15 / 29
3 x 3 mean	1	0.0/1.0	19 / 24	10 / 21
5 x 5	1	0.0/1.0	14 / 27	7 / 22
5 x 5 mean	1	0.0/1.0	7 / 20	3 / 15
7 x 7	1	0.0/1.0	13 / 24	5 / 22
7 x 7 mean	1	0.0/1.0	7 / 16	3 / 14
1 x 1	1	0.0/1.0	97 / 97	97 / 97
1 x 1 mean	1	0.0/1.0	95 / 96	95 / 96
3 x 3	1	0.0/1.0	90 / 93	69 / 81
3 x 3 mean	1	0.0/1.0	87 / 90	68 / 79
5 x 5	1	0.0/1.0	71 / 78	50 / 63
5 x 5 mean	1	0.0/1.0	71 / 76	50 / 62
7 x 7	1	0.0/1.0	64 / 68	40 / 55
7 x 7 mean	1	0.0/1.0	63 / 65	39 / 52

determine this low-degree gravity field part (Chapters 8 and 9).

With only the radial gradiometer component Γ_{zz}, it is expected that already the gravity field can be recovered on a local basis with high accuracy: the inclusion of the components Γ_{zy} and Γ_{yy} leads to comparable accuracy estimates for the 0.01 EU noise case. Again, this can be explained by considering the power estimates for these measurements (Table 7.1). The component Γ_{zz} has an estimated power of 0.18/0.21 EU (case 1/case 2) compared to an estimated power of 0.12-0.12/0.14-0.15 EU (case 1/case 2) for the other two components. Finally, it must be noted that the values of the accuracy estimates for mean gravity anomalies and geoid undulations are smaller than these values for point gravity anomalies and geoid undulations for all cases, which is in agreement with the discussions of Section 7.4.

7.6 Accuracy estimates for gravity field recovery from combinations of accelerations and gradiometry

It is also possible to compute accuracy estimates for gravity anomalies and geoid undulations from combinations of accelerations and gradiometer measurements. Accuracy estimates were computed for the combination of radial accelerations and Γ_{zz}, and the combination of accelerations in three directions and all three gradiometer components. These computations led to the values listed in the Tables 7.6 and 7.7.

With faultless observations and a grid size of only 3° x 3° and using all measurements (Table 7.7), the accuracy estimates for mean 1° x 1° gravity anomalies and geoid undulations are respectively 1.0 mgal and 2 cm, for case 1. For case 2, these values are 1.1 mgal and 9 cm. For point values these estimates are 2.8 mgal and 5 cm for case 1 and 2.9 mgal and 10 cm for case 2. With the projected accuracy of 0.01 EU of Γ_{zz} and 1.0 mgal of radial satellite accelerations, mean 1° x 1° anomalies and undulations can be determined with an accuracy of respectively 4.9/4.9 mgal (case 1/case 2) and 16/26 cm (case 1/case 2), respectively (Table 7.6). The results indicate that in the computations described in this Section, the inclusion of residual ARISTOTELES accelerations only yield marginally improved gravity field recovery covariance results for the high-degree part (case 1) compared to the computations where only gradiometer measurements are available (compare Tables 7.4 and 7.5 with Tables 7.6 and 7.7), but the inclusion of these measurements will be necessary to overcome the problem of low-degree gravity field modeling errors (included in case 2).

7.7 Additional tests

A few additional gravity field recovery covariance analysis computations were performed to answer the question of the effect of the satellite altitude and the question of

Table 7.6 Gravity field recovery from Γ_{zz} and radial accelerations.

grid size ° x °	noise Γ_{zz} (0.01 EU)	noise radial acc. (mgal)	accuracy anomalies (mgal) case 1	(mgal) case 2	accuracy geoid (cm) case 1	(cm) case 2
1 x 1	0	0	10.2	11.7	33	58
1 x 1 mean	0	0	6.9	8.3	24	50
1 x 1	1	1	11.7	11.9	34	72
1 x 1 mean	1	1	8.4	8.6	25	67
7 x 7	0	0	2.0	2.5	4	8
7 x 7 mean	0	0	0.6	0.7	1	5
7 x 7	1	1	8.0	8.0	24	31
7 x 7 mean	1	1	4.9	4.9	16	26

Table 7.7 Gravity field recovery from accelerations and Γ_{zz}, Γ_{zy}, Γ_{yy}.

grid size ° x °	noise grad. (0.01 EU)	noise acc. acc. (mgal)	accuracy anomalies (mgal) case 1	(mgal) case 2	accuracy geoid (cm) case 1	(cm) case 2
1 x 1	0	0	10.2	11.6	33	58
1 x 1 mean	0	0	6.9	8.3	23	50
1 x 1	1	1	11.7	11.9	34	72
1 x 1 mean	1	1	8.4	8.6	25	67
3 x 3	0	0	2.8	2.9	5	10
3 x 3 mean	0	0	1.0	1.1	2	9
3 x 3	1	1	8.5	8.6	27	39
3 x 3 mean	1	1	5.2	5.3	20	35

the omission error, caused by considering that the gravity field of the Earth can be represented by a gravity field model complete to degree and order 360. Accuracy estimates were computed for gravity anomaly and geoid undulation recovery from satellite accelerations and gradiometer measurements at an altitude of 160 km, for the case were low-degree gravity field modeling errors were included (case 2). These estimates are listed in Table 7.8. Comparing these estimates with the estimates listed in the Tables 7.2-7.5, which hold for an altitude of 200 km, it is concluded that a satellite orbit must be selected with an altitude as low as possible. For example, mean 1° x 1° gravity anomalies and geoid undulations can be recovered from accelerations in 3 directions, which are made at 160 km altitude and which have an accuracy of 1.0 mgal, with an estimated accuracy of 8.4 mgal and 45 cm (Table 7.8), compared to 10.3 mgal (Table 7.2) and 60 cm (Table 7.3) for a satellite altitude of 200 km, if the grid size is 5° x 5°. If mean 1° x 1° gravity anomalies are determined from the 3 gradiometer components, which have an accuracy of 0.01 EU, these estimates are equal to 2.9 mgal and 56 cm (Table 7.8) compared to 4.6 mgal (Table 7.4) and 62 cm (Table 7.5).

The omission error due to the truncation of the "real-world" gravity field to degree and order 360, was estimated by using the Rapp'79 anomaly degree variance model (equation (7.6)) to represent the "real-world". Firstly, accuracy estimates for gravity anomaly and geoid undulation recovery from radial satellite accelerations were computed by assuming that the "real-world" could be represented by this model from degree 37 to 360 (case A). Secondly, these estimates were computed by assuming that the "real-world" could be represented by the Rapp'79 model from degree 37 to infinity (case B, in this case the maximum degree was taken equal to 5000, taking a higher value did not alter the results). The accuracy estimates are listed in Table 7.9. The values listed in this Table show that the gravity field part above degree 360 has a significant effect on the accuracy estimates for point gravity anomalies and point geoid undulations. For faultless radial satellite accelerations, the accuracy estimates for these point gravity anomalies and geoid undulations change from 15.4 mgal (case A) to 32.0 mgal (case B), and from 35 cm (case A) to 46 cm (case B), respectively. However, for mean 1° x 1° gravity anomalies and geoid undulations, the accuracy estimates are almost the same for case A and case B. For faultless radial satellite accelerations, the accuracy estimates for mean 1° x 1° gravity anomalies and geoid undulations are 7.1 mgal (case A) and 8.2 mgal (case B), and 16 cm (case A) and 17 cm (case B), respectively. If the noise of the radial accelerations is equal to 1.0 mgal, the differences between accuracy estimates for mean 1° x 1° gravity anomalies and geoid undulations are even smaller. As mentioned before, the resolution strived for of the gravity field, which has to be determined from ARISTOTELES observations, is equal to 1.0°. Therefore, the choice for a gravity field model complete to degree and order 360 to represent the "real-world" (OSU86F) is justified by this analysis.

Table 7.8 Gravity field recovery from satellite accelerations and gradiometer measurements. The accuracy estimates hold for a satellite altitude of 160 km and low-degree gravity field modeling errors are included.

grid size ° x °	case	noise (mgal)	accuracy Δg (mgal)	accuracy Δh (cm)
5 x 5	(a)	0.0/1.0	1.8 / 11.6	7 / 52
5 x 5 mean	(a)	0.0/1.0	0.5 / 8.4	7 / 45
5 x 5	(b)	0.0/1.0	1.8 / 5.8	46 / 57
5 x 5 mean	(b)	0.0/1.0	0.7 / 2.9	46 / 56

case (a): from accelerations in three directions;
case (b): from Γ_{zz}, Γ_{zy}, and Γ_{yy}.

Table 7.9 Gravity field recovery from radial accelerations. The accuracy estimates hold for a satellite altitude of 200 km and are based on the Rapp'79 anomaly degree variance model.

grid size ° x °	case	noise (mgal)	accuracy Δg (mgal)	accuracy Δh (cm)
5 x 5	A	0.0/1.0	15.4 / 23.5	35 / 88
5 x 5	B	0.0/1.0	32.0 / 36.7	46 / 93
5 x 5 mean	A	0.0/1.0	7.1 / 15.7	16 / 70
5 x 5 mean	B	0.0/1.0	8.2 / 16.3	17 / 71

case A: Rapp'79 from degree 37 to 360.
case B: Rapp'79 above degree 36.

7.8 Conclusions

It has been shown that with satellite accelerations with an accuracy of 1.0 mgal, the ARISTOTELES gravity mission objectives can not be reached, but that an important part of the gravity field above degree 36 can be recovered, and that low-degree gravity field modeling errors can be reduced. With gradiometer measurements with an accuracy of 0.01 EU, the mission objectives can partly be reached. For the gravity field part above degree 36, mean 1° x 1° gravity anomalies and geoid undulations can be recovered with an accuracy of about 5 mgal and 10 cm, respectively. However, significant errors in the low-degree gravity field recovery will be made. A great part of this problem can be overcome by combining satellite accelerations and gradiometer measurements. This combination has been investigated and has shown to be very powerful.

8. Deterministic study to a local gravity field recovery from satellite-to-satellite tracking

8.1 Introduction

In the previous Chapter, a covariance analysis was performed to investigate the possibility of a local gravity field recovery from ARISTOTELES satellite accelerations and gradiometer measurements. It was indicated, that the GPS range measurements were assumed to contain the information from which accelerations of the ARISTOTELES satellite can be derived. Already extensive deterministic studies to a local gravity field recovery from gradiometer measurements have been performed (Arabelos and Tscherning, 1990; CIGAR, 1990). In (Arabelos and Tscherning, 1990; CIGAR, 1990), simulations are described in which gravity gradient measurements along a simulated ARISTOTELES orbit were continued downward by least-squares collocation to gravity anomalies and geoid undulations. These gravity anomalies and geoid undulations were compared with a priori values computed with the same gravity field model used to compute the ARISTOTELES orbit and gradiometer measurements. This model was the OSU86F gravity field model, which was also used in the analysis described in Chapter 7. The results presented in (Arabelos and Tscherning, 1990; CIGAR, 1990) were in good agreement with the results of the covariance analysis described in the previous Chapter. Therefore, the deterministic study, which is described in this Chapter, concentrated on a local gravity field recovery from GPS satellite-to-satellite tracking measurements to ARISTOTELES (Visser et al., 1990; Visser et al., 1991).

As indicated in the previous Chapter, one of the problems encountered is the problem of downward continuation: the mapping of the observed accelerations at the ARISTOTELES altitude to the Earth's surface (Tikhonov, 1963). This will be the first problem investigated in this study. Two techniques have been considered, both minimum-norm techniques:

- Using the equations as derived by Stokes (Heiskanen and Moritz, 1967), i.e. the observed ARISTOTELES accelerations are modeled by gravity anomalies at the Earth's surface using these equations, and the so obtained set of measurement equations is solved by the method of least-squares;
- Least-squares collocation (Moritz, 1980), this concept was introduced in the preceding Chapter. In this Chapter, this concept will be used to recover gravity anomalies and geoid undulations from simulated GPS measurements to ARISTOTELES.

Although the downward continuation of ARISTOTELES accelerations is actually the last step in the gravity field recovery from GPS SST measurements to ARISTOTELES, this step was investigated first. In other words, first local gravity field recovery experiments were performed, in which gravity anomalies and geoid undulations were

recovered from simulated ARISTOTELES accelerations. This approach prevented unnecessary, and costly, simulations of GPS SST measurements and ARISTOTELES orbits. These results gave, together with the results of the local gravity field recovery covariance analysis, a first indication of the accuracy of the GPS SST measurements to the ARISTOTELES satellite required to recover gravity anomalies/geoid undulations with sufficient precision. As indicated before, the mission objective is to recover mean 1° x 1° gravity anomalies with an accuracy of 5 mgal and geoid undulations with an accuracy of 10 cm.

The investigation of the downward continuation techniques was followed by the computation of GPS and ARISTOTELES orbits using available high-degree and -order spherical harmonic expansions of the Earth's gravity field (although truncated for the high-altitude GPS satellites) to simulate GPS SST range measurements. The ARISTOTELES accelerations were recovered from these measurements along the ARISTOTELES orbit. Only those parts of the ARISTOTELES orbits that passed over a restricted geographical area were selected (Figure 7.1), and the accelerations along these tracks were transformed to a regular grid suitable for downward continuation. This implied the investigation of gridding techniques, i.e. the transformation of an irregular grid of observed ARISTOTELES accelerations to a regular grid of accelerations at a mean ARISTOTELES satellite altitude. This gridding was performed by the method of least-squares collocation.

The effect of two error sources affecting the GPS SST measurements on the gravity anomaly/geoid undulation recovery was investigated. These are uncorrelated measurement noise with a normal distribution and the first-order ionospheric effect. This Chapter will be concluded by a discussion of the results and some recommendations.

8.2 Minimum-norm techniques

The purpose of this Section is to establish the measurement equations and solution techniques for downward continuation of observed accelerations at a specified altitude to gravity anomalies and geoid undulations on the surface of the Earth. Two minimum-norm techniques will be discussed:

- least-squares solution of measurement equations using the equations as derived by Stokes (Heiskanen and Moritz, 1967);
- the method of least-squares collocation (Rummel et al., 1976).

8.2.1 Minimum-norm technique using the equations of Stokes

The accelerations of a satellite orbiting in a circular orbit in the radial, East-West (longitude) and North-South (latitude) direction, can be deduced from gravity anomalies on the Earth's surface (which is represented by a sphere with radius a_e)

using the equations derived by Stokes (Heiskanen and Moritz, 1967):

$$\ddot{r}(\lambda,\phi) = \frac{a_e}{4\pi}\iint \Delta g \frac{\partial S(r,\psi)}{\partial r} ds \tag{8.1a}$$

$$\ddot{NS}\ (\lambda,\phi) = \frac{a_e}{4\pi r}\iint \Delta g \frac{\partial S(r,\psi)}{\partial \psi}\frac{\partial \psi}{\partial \phi} ds \tag{8.1b}$$

$$\ddot{EW}\ (\lambda,\phi) = \frac{a_e}{4\pi r\cos\phi}\iint \Delta g \frac{\partial S(r,\psi)}{\partial \psi}\frac{\partial \psi}{\partial \lambda} ds \tag{8.1c}$$

$$S(r,\psi) = \frac{2a_e}{l}+\frac{a_e}{r}-\frac{3a_e l}{r^2}-\frac{a_e^2}{r^2}\cos\psi\left[5+3\ln\left(\frac{r-a_e\cos\psi+l}{2r}\right)\right] \tag{8.1d}$$

$$l = \left\{r^2+a_e^2-2ra_e\cos\psi\right\}^{\frac{1}{2}} \tag{8.1e}$$

$$\cos\psi = \sin\phi\sin\phi'+\cos\phi\cos\phi'\cos(\lambda-\lambda') \tag{8.1f}$$

where S, $(\partial S/\partial r)$ and $(\partial S/\partial \psi)$ are the Stokes kernel functions; $\ddot{r}$, $\ddot{NS}$ and $\ddot{EW}$ denote the satellite accelerations in the radial, latitude and longitude directions, respectively; r, λ and ϕ denote the geocentrical coordinates of the satellite; and λ' and ϕ' denote the geocentrical position of the gravity anomaly Δg on the Earth's surface.

In principle, the integration in the preceding formulae should encompass the surface of the entire Earth. However, in this study the observed satellite accelerations were considered to be residual satellite accelerations, i.e. they were formed after subtracting a low-degree reference gravity field model. Thus, the observed accelerations were considered to be caused by the high-frequency part of the gravity field, and possibly by small errors in the low-degree part. Therefore, it was expected that with the anomalies in the selected geographical area, it is possible to model an acceleration above this area with satisfactory accuracy. This is also justified by the quick damping of the Stokes kernel functions. The latter implies that the perturbations on a satellite orbit that are caused by a gravity anomaly, decrease very rapidly with increasing distance between that anomaly and the satellite. Because mean 1° x 1° gravity anomalies were to be determined, the integration in the above formulae transforms to a summation of block anomalies:

$$\ddot{r}(\lambda,\phi) = \sum\frac{a_e}{4\pi}\Delta g(\lambda',\phi')\frac{\partial S(r,\psi)}{\partial r}\Delta s \tag{8.2a}$$

$$\ddot{NS}(\lambda,\phi) = \sum\frac{a_e}{4\pi r}\Delta g(\lambda',\phi')\frac{\partial S(r,\psi)}{\partial \psi}\frac{\partial \psi}{\partial \phi}\Delta s \tag{8.2b}$$

$$\ddot{EW}(\lambda,\phi) = \sum \frac{a_e}{4\pi r \cos\phi} \Delta g(\lambda',\phi') \frac{\partial S(r,\psi)}{\partial \psi} \frac{\partial \psi}{\partial \lambda} \Delta s \qquad (8.2c)$$

where Δs denotes a 1° x 1° block area. These formulae form the observation equations for the gravity anomalies in a selected local area, and these equations are solved by the method of least-squares.

Unfortunately, as mentioned before, it can be shown that this downward continuation process is an ill-posed problem, i.e. small fluctuations in the accelerations at satellite altitude may lead to large fluctuations in recovered anomalies (Tikhonov, 1963). This is reflected in the least-squares solution, which is based on an ill-conditioned normal matrix, leading to high correlations between recovered adjacent gravity anomalies. A possibility to overcome this problem is the method of regularization. The principle of regularization is equal to the addition of a priori information in the form of measurements with expectancy zero. The method of regularization requires the minimization of the following formula (compare with the minimum-variance solution with a priori information, as expressed in equation (5.12)):

$$||Ax - R||^2 + \alpha x^T V_A^{-1} x \qquad (8.3)$$

where x denotes the vector of unknowns (in this case gravity anomalies), R the measurements (satellite accelerations), α the regularization parameter, and V_A an a priori covariance matrix for the unknowns. The most rudimentary form of regularization is the addition of a diagonal matrix V_A reflecting the variances of the parameters to be determined (gravity anomalies) to the left-hand side of the normal equations (see also: Chapter 5). The solution of the preceding equation is:

$$x = (A^T A + \alpha V_A^{-1})^{-1} A^T R. \qquad (8.4)$$

The second minimum-norm technique that will be used in the downward continuation of satellite accelerations, is the concept of least-squares collocation. This concept was introduced in Chapter 7 (equation (7.1)).

8.2.2 Comparison of the two minimum-norm techniques

Important characteristics of the method using the equations of Stokes, are:

- truncation errors arise due to the limited geographical area used in the fitting of satellite accelerations;
- errors arise due to the block averaging in the integration;
- instability of the normal equations (ill-posed problem);
- the size of the normal equations is equal to the number of gravity anomalies to be solved for;

• the matrix is full.

The first characteristic is not considered to be a severe problem, especially for the higher-frequency part of a spherical harmonic expansion of the Earth's gravity field. Because high-frequency gravity field induced signals attenuate very quickly with increasing altitude, also the second characteristic is not considered to be a problem. Studies have indicated (Smith et al., 1988) that the finest resolution of a gravity field that can be solved for is equal to about half the altitude of the satellite. In this thesis, this altitude is of the order of 200 km. Thus, the finest resolution achievable is equal to 100 km. This is equal to 1° at the equator and compares to the 1° resolution in longitude and latitude of 1° x 1° gravity anomalies to be solved for. Regularization is a tool to overcome the instability of the normal equations. The problem is to find optimal regularization parameters α, but several studies (DGFI-TUM-TH Delft, 1987) have shown, and also this thesis will show, that the solution of the normal equations is not very sensitive to a change of these parameters around the optimal value for α. The last two characteristics have as a consequence that when a larger area of block anomalies is taken, this leads to a quadratic increase in the volume of computations to set up and solve the normal equations.

A few characteristics of the method of least-squares collocation are:

- a priori information can be implemented in the solution in the form of degree variance models of the gravity field;
- each gravity anomaly/geoid undulation can be determined separately;
- the possibility exists to obtain accuracy estimates, which was shown extensively in Chapter 7.

Possible degree variance models are the already mentioned Rapp '79 anomaly degree variance model (equation (7.6)), or current spherical harmonic expansion models of the Earth's gravity field, like the OSU86F gravity field model. A quick method to compute covariance functions up to high-degree terms is Horner's procedure (Section 7.2). With this method, a grid of covariance functions for the gravity field induced signals to be investigated was computed. The grid had such a resolution (0.01° in spherical distance, approximately equal to 1 km on the Earth's surface) that linear interpolation can be assumed to be of sufficient accuracy. When the method of collocation was applied in this thesis, each gravity anomaly/geoid undulation, using the method of collocation was estimated from a small area of observed satellite accelerations above that particular gravity anomaly/geoid undulation (see also: Figure 7.2). It is therefore easy to expand to a larger area because of the separate recovery of each gravity anomaly/geoid undulation.

The comparison of both methods leads to the conclusion that the method of collocation offers more possibilities. Accuracy estimates can be easily obtained (Chapter 7) and the geoid undulation can be recovered directly. Because of the instability of the first method and the necessity to perform regularization, it is difficult to interpret and calibrate the normal equations for an accuracy estimate of the recovered mean 1° x 1° gravity anomalies. In principle, it is possible to compute geoid undulations in a second step from recovered gravity anomalies using the equations of Stokes. However, this method leads to an accumulation of errors. Errors arise during the recovery of gravity anomalies to which are added the integration and truncation errors in the integration of

these gravity anomalies to obtain geoid undulations. A disadvantage of the method of least-squares collocation is that an extra effort is required to obtain averaged block values of gravity anomalies/geoid undulations. Mean 1° x 1° gravity anomalies/geoid undulations are determined by recovering for each 1° x 1° block a grid of point gravity anomalies/undulations and by taking the average of this grid.

8.3 Simulation set-up of gravity anomaly/geoid undulation recovery from acceleration data at a certain satellite altitude

This Section will give a short description of the following subjects:

- computation of gravity field derived quantities, e.g. gravity anomalies, using high-degree and -order spherical harmonic expansions;
- simulation set-up for the method using the equations of Stokes;
- simulation set-up for the least-squares collocation method.

8.3.1 Computation of high-degree and -order spherical harmonics

The expected resolution of the gravity field to be solved for from the GPS SST data is 1° both in latitude and longitude, which is equivalent to a spherical harmonic expansion to degree and order 180. In the simulations described in this Chapter, use was made of a spherical expansion of the Earth's gravity field up to degree and order 360, the already mentioned OSU86F gravity field model. It was shown in the local gravity field recovery covariance analysis that in a gravity field recovery from satellite accelerations, the part of the gravity field above degree 360 is expected to be aliased only for a very small part in gravity field terms below degree 180. Therefore, the results in this thesis for mean 1° x 1° gravity anomalies are considered to give a realistic estimate of the possibilities of the ARISTOTELES mission to recover the gravity field with a resolution of 1.0°.

The choice for a gravity field model complete to degree and order 360, requires the computation of spherical harmonics up to this degree and order 360. To prevent numerical problems due to computer round-off (VAX 3100 work station/CONVEX 240), use was made of normalized recurrence relations of the Legendre polynomials (Schrama, 1986b). It must be noted that also Horner's procedure can be applied. In that case it is not necessary to determine the spherical harmonics explicitly (Tscherning et al., 1983). Appropriate software was provided by the Faculty of Geodesy, Delft University of Technology, and this software is capable of manipulating high-degree and -order spherical harmonics. It has been modified to adapt it for the investigations described in this study. This software is capable of computing geoid undulations, gravity anomalies and accelerations at an arbitrary geographical location, either given in

geocentric or geodetic coordinates.

8.3.2 Simulation set-up for downward continuation using Stokes' equations

The starting point of the simulations was a rectangular grid of accelerations in the radial, East-West and North-South directions at a specific altitude. These accelerations were computed with the mentioned OSU86F gravity field model, complete to degree and order 360. The selected geographical test area extends from 0° to 20° in longitude and from 40° to 60° in latitude (covering a great part of Western-Europe, Figure 7.1). Because the main interest is in the high-frequency part of the gravity field, a low-degree and -order spherical expansion was subtracted from the full OSU86F gravity field. The same approach was followed in the local gravity field recovery covariance analysis (Chapter 7). The low-degree gravity field model was either the OSU86F gravity field itself up to degree and order 36 or a different model, GEM-T1, which is an expansion complete up to degree and order 36. As indicated before, the differences between OSU86F and GEM-T1 for low degrees and orders may be considered to reflect the accuracy of current gravity field models for low degrees and orders, and were used to simulate the low-degree gravity field modeling error.

The resolution of the grid of accelerations was chosen to be consistent with the expected real data coverage. In North-South direction, the grid-spacing is equal to 0.2°, based on a GPS receiver measurement interval of 2.5 s and an orbital velocity of the ARISTOTELES satellite of about 8 km/s. The selected resolution in the East-West direction is equal to 0.33 degree. The maximum width of the holes in the ground track pattern of the 91-days ARISTOTELES is about 0.25°, so that this number is a bit conservative.

Using the same spherical harmonic expansions of the gravity field, also point anomalies at the Earth's surface within the test area were computed. Mean 1° x 1° gravity anomalies were subsequently computed by taking the arithmetic mean of a grid of point anomalies in each 1° x 1° block. These anomalies are the a priori values that represent the "real-world" and should be recovered from the acceleration data.

From the grid of simulated accelerations, normal equations for the mean 1° x 1° gravity anomalies were formed using Stokes' formulae (equations (8.2a)-(8.2c)). With such a regular data set the existence of several symmetries can be exploited and the normal equations can be built up very efficiently. If the test area is divided in longitude in 20 geographical subareas, each 1° wide (equal to the resolution in this direction of the gravity anomalies to be solved for), and the overall data set is divided in 20 subsets corresponding to these subareas, then the contribution of the k-th subset to the normal submatrix of the correlations between the anomalies in the areas i and j (20 x 20 matrix) will be denoted by $N_{ij}(k)$. These submatrices satisfy the following symmetry relations:

$$N_{i,j}(k) = N_{j,i}(k) \qquad (8.5a)$$

1)j=i :

a)k≥i : $N_{i,i}(k)=N_{1,1}(1+k-i)$ (8.5b)

b)k<i : $N_{i,i}(k)=N_{1,1}(1+i-k)$ (8.5c)

2)j>i :

a)k>j : $N_{i,j}(k)=N_{1,1+j-i}(1+k-i)$ (8.5d)

b)i≤k≤j:

k-i≤j-k : $N_{i,j}(k)=N_{1,1+j-i}(1+k-i)$ (8.5e)

k-i>j-k : $N_{i,j}(k)=N^{T}_{1,1+j-i}(1+j-k)$ (8.5f)

c)k<i : $N_{i,j}(k)=N^{T}_{1,1+j-i}(1+j-k)$ (8.5g)

These symmetry relations led to a reduction in the number of computations of approximately a factor 27 (about 20*4/3). The normal equations were solved using the Cholesky decomposition method.

To reduce the numerical instability of the normal equations obtained in this way, regularization can be applied in the form of adding a diagonal matrix with variable weight to the normal equations. This will particularly be necessary when the accelerations are corrupted with noise. This was simulated by adding uncorrelated measurement noise, with a power that can be selected, to the accelerations. The possibility existed to use the accelerations in all three directions (radial, East-West and North-South) independently. The normal equations could be built up separately for each direction, and then combined afterwards. The solution of the normal equations was of course compared with the a priori values to give an estimate of the accuracy of the recovered anomalies.

8.3.3 Simulation set-up for downward continuation using least-squares collocation

For these simulations the same spherical harmonic expansions of the gravity field and the same test area as described in the previous Section were used. In addition to accelerations at a specific altitude and gravity anomalies, also the geoid undulations were now computed. This is because the method of collocation is capable of recovering geoid undulations in a similar way as gravity anomalies.

Each gravity anomaly/geoid undulation was recovered separately (which does not mean that they were not correlated) from a regular grid of accelerations at a selected

satellite altitude. The size of this grid in latitude and longitude direction and the density of the accelerations in this grid (grid maze) could be varied (Figure 7.2). However, it will be obvious that the grid maze must compare with the expected resolution of the observed accelerations, which was also indicated in the previous Section, and the resolution of the gravity field to be solved for. From Figure 7.2, it follows that for adjacent gravity anomalies/geoid undulations a certain overlap exists in the accelerations used to estimate them. It will also be obvious that the geographical area of satellite acceleration observations must be slightly larger than the area of gravity anomalies/geoid undulations to be solved for.

Also in the method of collocation the existence of symmetry can be exploited, provided that a regular grid of accelerations is available. In that case, for each parallel (i.e. constant latitude) only one single covariance matrix must be constructed and inverted (equations (7.1)). It is stressed that the use of symmetry was possible because of the isotropy and homogeneity of the applied covariance functions.

Also in the case of collocation the possibility existed to use the accelerations in the three directions independently or in combinations. Uncorrelated measurement noise could be added to the accelerations and the collocation process could be "regularized" by adding a "noise-variance (diagonal) matrix" to the covariance matrix of accelerations (i.e. the matrix D in equation (7.1)).

8.4 Results of the downward continuation simulations

This Section contains a description of the computations of gravity anomalies/geoid undulations from a grid of accelerations at a mean satellite altitude by the two minimum-norm techniques discussed in Section 8.2 and according to the simulation set-ups described in Section 8.3. Firstly, a short summary is given of the configurations tested and the characteristics of the gravity field induced signals. Subsequent Sections contain results of the tests.

8.4.1 Test configurations

The primary objective of this study was to investigate the possibility of using GPS for high-resolution gravity field recovery from the ARISTOTELES mission. Therefore, the tests that have been performed concentrated on the higher-degree part of the OSU86F gravity field. As indicated before, in reality, the GPS SST range measurements to ARISTOTELES will also contain information of the low-degree terms of the gravity field and hence will be affected by errors in these terms. Therefore, also the effect of errors in this part of the spherical harmonic expansion of the gravity field was simulated, as has been shown by taking the differences between the OSU86F and

GEM-T1 gravity field models.

An important parameter in the downward continuation process was the satellite altitude: the higher the satellite altitude, the more difficult it will be to recover the gravity field, especially the high-frequency part. To study this effect, simulations were performed for different altitudes.

The following cases have been investigated:

- case 1: accelerations at 160 km altitude using OSU86F above degree 36;
- case 2: accelerations at 200 km altitude using OSU86F above degree 36;
- case 3: accelerations at 160 km altitude using OSU86F minus GEM-T1.

In Table 8.1 (see also: Table 7.1), the magnitude of gravity field induced signals for these cases are listed. These results were computed in two ways:

- by taking the rms of the grid values in the selected geographical area for a certain gravity field induced signal;
- by computing the covariance function for that gravity induced signal using the same spherical harmonic expansion that was used to compute the regular grid (mean 1° x 1° values of the covariance functions were computed using the method described in Appendix E).

Included in Table 8.1 are power estimates computed with the Rapp '79 anomaly degree variance model for a satellite altitude of 160 km (denoted by case 4). Studying Table 8.1, the following conclusions can be drawn:

- The power estimates from the covariance functions appear to agree with the rms of the simulated signals, showing the consistency of the applied algorithms;
- The rms of the geoid undulations increases from 1.60 m to 2.29 m if low-degree gravity field modeling errors are included. For gravity anomalies, this increase is much less pronounced. This is in agreement with the statements made in the local gravity field recovery covariance analysis (Chapter 7);
- The mean of all gravity field induced signals are very small compared to the rms of these signals, except the mean of geoid undulations for case 3 has a relatively large value (0.47 cm compared to an rms-value of 2.29 m), which is caused by low-degree gravity field error terms that do not average out over the selected area; in all computations to be described in this Chapter, it was found that the mean of the differences between a priori and recovered gravity anomalies and geoid undulations was below 1 mgal and 5 cm, respectively;
- The empirical model of Rapp' 79 gives relatively high powers for the gravity field induced signals; the Rapp '79 model probably gives too high estimates for the high-degree gravity field part (Rapp, 1979);
- The gravity field induced signals rapidly attenuate when going from a satellite altitude of 160 km to 200 km; for example, the rms-value for radial satellite accelerations is 3.29 mgal for case 1 and 2.37 mgal for case 2.

Table 8.1 Characteristics of gravity field induced signals over a 20° x 20° test area.

	case	mean of grid values	rms of grid values	power estimate from covariance function
point anomalies (mgal)	1	-0.04	18.33	18.96
	3	1.15	19.04	19.89
	4	-	-	27.23
mean anomalies (mgal)	1	-0.05	15.90	16.30
	3	1.13	16.72	17.35
	4	-	-	20.28
geoid undulations (m)	1	0.01	1.60	1.56
	3	0.47	2.29	2.36
	4	-	-	1.73
radial acc. (mgal)	1	0.16	3.29	2.95
	2	0.12	2.37	2.11
	3	0.22	4.87	4.42
	4	-	-	3.09
longitudinal acc. (mgal)	1	0.05	2.51	2.06
	2	0.03	1.83	1.48
	3	0.40	3.84	3.07
	4	-	-	2.17
latitudinal acc. (mgal)	1	0.08	2.17	2.06
	2	0.06	1.54	1.48
	3	0.09	2.90	3.07
	4	-	-	2.17

case 1: OSU86F above degree 36, 160 km satellite altitude;
case 2: OSU86F above degree 36, 200 km satellite altitude;
case 3: OSU86F minus GEM-T1, 160 km satellite altitude;
case 4: Rapp'79 from degree 37 to 360, 160 km satellite altitude.

8.4.2 Gravity anomaly recovery by the method using the equations of Stokes

The simulation set-up as described in Section 8.3.2 was used to form the normal equations for the 400 mean 1° x 1° gravity anomalies in the test area from the simulated satellite accelerations above this area. These normal equations were solved using the Cholesky decomposition method and regularization was applied with different weight factors.

During the tests, it was discovered that the accelerations in the directions perpendicular to the radial direction hardly improved the solutions of the gravity anomalies, and did not help to stabilize the normal equations. This can be explained by the structure of the equations of Stokes: gravity anomalies that are located close to the projection of satellite accelerations on the Earth's surface are correlated most with accelerations in the radial direction and hardly with accelerations in a direction perpendicular to this. Therefore, in this Section only results from radial satellite accelerations are displayed and discussed.

In the top of Table 8.2, the results are listed when the OSU86F gravity field model above degree 36 for a satellite at 160 km altitude was used. What strikes first is that even with "perfect" accelerations, the difference between the a priori model and the solution is quite large. This is apparently due to the instability of the set of normal equations, since the recovered anomalies compare much better with their a priori values when regularization is applied. Still, the rms of differences does not become close to zero, because of the errors mentioned in Section 8.2.2. However, an rms of differences of mean 1° x 1° gravity anomalies close to 5 mgal seems possible if the noise of the observed satellite accelerations is below 1 mgal. Because it is likely that the recovered gravity anomalies in the central area (i.e. 5°-15° longitude, 45°-55° latitude) will be of better quality, due to truncation effects at the border of the area, some tests were performed where only these recovered anomalies were compared with their a priori values. The top of Table 8.3 (case 1) shows the results that seem to confirm the previous assumption. Recovered anomalies close to the border are less accurate because only a partial grid of accelerations is surrounding these anomalies, yielding a significant smaller amount of information.

In the middle of the Tables 8.2 and 8.3, the results for case 2, i.e. using a different satellite altitude of 200 km, are listed. The rms of differences of the recovered anomalies with their a priori values for this case is worse than for the 160 km satellite altitude. The rms of differences deteriorates from 6.84 mgal for the first case to 8.02 mgal for the second, assuming a noise of 1 mgal in both simulations.

In the bottom of the Table 8.2 and 8.3, the results are listed for the case of a satellite at 160 km altitude where the low-degree effects are also included (case 3). In case of a 1 mgal noise on the satellite accelerations the rms of differences of the recovered anomalies with their a priori values is equal to 7.95 mgal. This value is comparable to the value of the rms of differences for case 1, which is 6.84 mgal. Thus, the addition of low-degree gravity field modeling errors is not considered to be a severe problem.

As already mentioned above, the rms of differences for inner subareas is smaller than for the entire area. For example, the rms of differences for the first case becomes

Table 8.2 Gravity anomaly recovery for the test area (400 anomalies), using the equations of Stokes.

noise (mgal)	case	sig. mag. (mgal)	rms of dif. (mgal)	corr.	add.
0.0	1	22.92	14.44	0.78	0.000
0.0	1	16.18	6.14	0.93	0.008
1.0	1	16.51	6.84	0.91	0.008
2.0	1	17.48	8.83	0.86	0.008
2.0	1	14.86	7.22	0.89	0.023
2.0	1	12.98	7.48	0.89	0.052
0.0	2	46.62	43.14	0.38	0.000
0.0	2	14.44	7.64	0.88	0.008
0.0	2	13.22	7.99	0.87	0.016
1.0	2	14.63	8.02	0.87	0.008
1.0	2	13.29	8.17	0.86	0.016
2.0	2	15.29	9.18	0.83	0.008
2.0	2	13.61	8.73	0.84	0.016
0.0	3	40.31	35.30	0.49	0.000
0.0	3	18.45	8.35	0.89	0.008
0.0	3	16.21	7.79	0.89	0.028
1.0	3	16.90	7.95	0.89	0.020
2.0	3	19.55	10.39	0.85	0.008
2.0	3	17.20	8.57	0.87	0.020
2.0	3	16.47	8.31	0.87	0.028

noise = uncorrelated measurement noise added to the satellite accelerations
sig. mag. = signal magnitude of recovered anomalies (rms-wise)
rms of dif. = root-mean-square of differences between recovered and a priori mean gravity anomalies
corr. = correlation between recovered and a priori mean gravity anomalies
add. = constant added to the diagonal of the normal equations (regularization)

Table 8.3 Gravity anomaly recovery for the central part of the selected geographical area (100 gravity anomalies), using the conditions of Table 8.2.

noise (mgal)	case	sig. mag. (mgal)	rms of dif. (mgal)	corr.	add.
0.0	1	11.36	4.49	0.94	0.008
1.0	1	11.70	4.91	0.92	0.008
2.0	1	12.46	6.73	0.86	0.008
2.0	1	10.44	6.48	0.86	0.023
2.0	1	9.19	7.42	0.82	0.052
0.0	2	10.00	6.71	0.85	0.008
0.0	2	9.27	7.64	0.80	0.016
1.0	2	10.00	7.14	0.83	0.008
1.0	2	9.24	7.93	0.78	0.016
2.0	2	10.53	8.23	0.73	0.008
2.0	2	9.51	8.55	0.74	0.016
0.0	3	11.52	4.26	0.94	0.008
0.0	3	9.94	6.01	0.89	0.028
1.0	3	10.36	5.72	0.90	0.020
2.0	3	10.62	6.39	0.87	0.020

4.91 mgal for the inner 100 gravity anomalies compared to 6.84 mgal for the whole area if the noise on the satellite accelerations is equal to 1 mgal (Tables 8.2 and 8.3). The results seem to suggest that in order to obtain gravity anomalies with high accuracy, one must solve for an area of gravity anomalies and take only the results of the central part of this area. However, for the first case, the ratio of the rms of differences and the rms of the recovered anomalies is 6.84/16.51 = 0.41 for the whole area (top of Table 8.2) and 4.91/11.70 = 0.42 for the "inner" area (Table 8.3), assuming a noise equal to 1 mgal. Thus this ratio remains approximately the same. But the noise of 1 mgal of the accelerations is equal for both the whole area and the "inner" area, thus the ratio of the rms of the accelerations and this noise (the signal to noise ratio) is smaller for the "inner" area, whereas this does not lead to a higher relative error in the recovery (about 0.4 for both areas). It is therefore conclude that for the "inner" area the gravity anomaly recovery is indeed better.

All the Tables show that it is not trivial to find the optimal regularization parameters, but that the solution is not very sensitive to (small) deviations from the (imaginary) optimal value. All results discussed in this Section indicate that it is difficult to recover mean 1° x 1° gravity anomalies with an accuracy of 5 mgal for the simulated cases, using the equations of Stokes. However, for the central part of the test area and for the first test case with a satellite altitude of 160 km, it is possible to reach an rms of differences smaller than 5 mgal, if the noise on the accelerations is below 1.0 mgal. If the satellite altitude is increased to 200 km, this accuracy does not seem to be achievable. Also the inclusion of errors in the low-degree part of the gravity field deteriorates the rms of differences. However, the results indicate that this effect is not a severe problem. Moreover, as indicated before (Chapter 7), especially the GPS system is considered to have the ability to improve the low-degree part of current gravity field models to a precision far better than the differences in the low-degree coefficients of OSU86F and GEM-T1 (Wu and Yunk, 1986a and 1986b; Smith et al., 1988).

8.4.3 Gravity anomaly/geoid undulation recovery by least-squares collocation

This Section contains the results of point gravity anomaly/geoid undulation recovery using collocation for the cases described in Section 8.4.1, and applying two types of degree variance models in the computation of the covariance functions. The first type is determined by the models that were used to compute the satellite accelerations and the a priori point gravity anomalies/geoid undulations, and the other uses the empirical Rapp '79 anomaly degree variance model (equation (7.6)). The choice for the grid size and grid maze of the grid of accelerations from which a gravity anomaly/geoid undulation is estimated by least-squares collocation, (Figure 7.2) was discussed in Chapter 7.

Results of the first case are displayed at the top of the Tables 8.4-8.7. The OSU86F gravity field above degree 36 was used both for simulating the satellite accelerations at 160 km altitude and for simulating the a priori point gravity anomalies/geoid undulations. Moreover, the OSU86F gravity field was used in the computation of the

Table 8.4 Point gravity anomaly recovery from radial accelerations, using least-squares collocation.

step °	case	noise (mgal)	noise col. (mgal)	grid size ° x °	sig. mag. (mgal)	rms of dif. (mgal)	corr.
1.0	1	0.0	0.0	5x5	17.83	4.16	0.97
1.0	1	1.0	1.0	5x5	13.62	11.18	0.79
1.0	1	0.0	0.0	7x7	18.20	4.34	0.97
1.0	1	1.0	1.0	7x7	13.95	10.77	0.81
1.0	2	0.0	0.0	5x5	17.58	4.98	0.96
1.0	2	1.0	1.0	5x5	11.96	12.81	0.72
1.0	2	0.0	0.0	7x7	24.96	16.76	0.74
1.0	2	0.0	0.25	7x7	14.74	8.14	0.90
1.0	2	1.0	1.0	7x7	12.15	12.45	0.74
0.5	3	0.0	0.0	5x5	19.20	4.05	0.98
1.0	3	0.0	0.0	5x5	18.43	4.32	0.97
0.5	3	1.0	1.0	5x5	15.28	11.03	0.82
1.0	3	1.0	1.0	5x5	14.59	11.20	0.81
0.5	3	0.0	0.0	7x7	65.90	62.22	0.33
1.0	3	0.0	0.0	7x7	18.74	3.77	0.98
0.5	3	1.0	1.0	7x7	15.64	10.08	0.85
1.0	3	1.0	1.0	7x7	15.13	10.76	0.83
1.0	4	0.0	0.0	5x5	18.01	4.21	0.97
1.0	4	1.0	1.0	5x5	13.87	11.23	0.79
1.0	4	0.0	0.0	7x7	19.62	8.00	0.91
1.0	4	1.0	1.0	7x7	14.23	10.80	0.81

step = grid maze

noise col. = input parameter for the collocation process

case 4: OSU86F above degree 36, 160 km satellite altitude; the Rapp'79 model was used in the computation of the covariance functions.

Table 8.5 Point gravity anomaly recovery from accelerations in three directions, using least-squares collocation.

step °	case	noise (mgal)	noise col. (mgal)	grid size ° x °	sig. mag. (mgal)	rms of dif. (mgal)	corr.
1.0	1	0.0	0.0	3x3	17.86	4.36	0.97
1.0	1	1.0	1.0	3x3	14.25	10.79	0.81
1.0	1	0.0	0.0	5x5	21.30	11.69	0.84
1.0	1	0.0	0.25	5x5	16.19	5.92	0.95
1.0	1	1.0	1.0	5x5	14.49	10.03	0.84
1.0	2	0.0	0.0	3x3	17.53	5.25	0.96
1.0	2	1.0	1.0	3x3	12.60	12.71	0.72
1.0	2	0.0	0.0	5x5	18.00	4.63	0.97
1.0	2	1.0	1.0	5x5	13.06	11.81	0.77
1.0	3	0.0	0.0	3x3	18.39	4.79	0.97
1.0	3	1.0	1.0	3x3	15.17	10.89	0.82
1.0	3	0.0	0.0	5x5	20.00	8.12	0.91
1.0	3	0.0	0.25	5x5	16.88	6.01	0.95
1.0	3	1.0	1.0	5x5	15.64	10.05	0.85
1.0	4	0.0	0.0	3x3	18.08	4.41	0.97
1.0	4	1.0	1.0	3x3	14.40	10.86	0.81
1.0	4	0.0	0.0	5x5	22.66	14.26	0.78
1.0	4	0.0	0.25	5x5	16.36	5.71	0.95
1.0	4	1.0	1.0	5x5	14.69	10.08	0.84

Table 8.6 Geoid undulation recovery from radial accelerations, using least-squares collocation.

step °	case	noise (mgal)	noise col. (mgal)	grid size ° x °	sig. mag. (m)	rms of dif. (m)	corr.
1.0	1	0.0	0.0	3x3	1.56	0.18	0.99
1.0	1	0.0	0.0	5x5	1.60	0.10	1.00
1.0	1	0.0	0.0	7x7	1.60	0.10	1.00
1.0	1	0.5	0.0	5x5	3.22	2.82	0.48
1.0	1	0.5	0.5	5x5	1.50	0.39	0.97
1.0	1	1.0	0.0	5x5	5.84	5.64	0.26
1.0	1	1.0	1.0	5x5	1.44	0.51	0.95
1.0	2	0.0	0.0	5x5	1.60	0.13	1.00
1.0	2	0.5	0.5	5x5	1.44	0.52	0.95
1.0	2	1.0	1.0	5x5	1.37	0.64	0.92
1.0	3	0.0	0.0	3x3	2.24	0.33	0.99
1.0	3	0.0	0.0	5x5	2.29	0.18	1.00
1.0	3	0.0	0.0	7x7	2.29	0.17	1.00
1.0	3	0.5	0.5	5x5	2.25	0.44	0.98
1.0	3	1.0	1.0	5x5	2.20	0.54	0.97
1.0	4	0.0	0.0	5x5	1.60	0.10	1.00
1.0	4	0.0	0.0	7x7	1.61	0.18	1.00
1.0	4	0.5	0.5	5x5	1.52	0.39	0.97
1.0	4	1.0	1.0	5x5	1.45	0.51	0.95

Table 8.7 Geoid undulation recovery from accelerations in three directions, using least-squares collocation.

step °	case	noise (mgal)	noise col. (mgal)	grid size ° x °	sig. mag. (m)	rms of dif. (m)	corr.
1.0	1	0.0	0.00	5x5	1.61	0.24	0.99
1.0	1	0.0	0.25	5x5	1.56	0.17	0.99
1.0	1	0.0	0.50	5x5	1.53	0.24	0.99
2.0	1	0.0	0.0	5x5	1.59	0.13	1.00
2.0	1	1.0	1.0	5x5	1.43	0.56	0.94
1.0	2	0.0	0.0	5x5	1.60	0.11	1.00
1.0	2	0.0	0.25	5x5	1.53	0.27	0.99
2.0	2	0.0	0.0	5x5	1.59	0.14	1.00
2.0	2	1.0	1.0	5x5	1.36	0.70	0.90
1.0	3	0.0	0.0	5x5	2.29	0.24	0.99
1.0	3	0.0	0.25	5x5	2.26	0.20	1.00
2.0	3	0.0	0.0	5x5	2.26	0.14	1.00
2.0	3	1.0	1.0	5x5	2.22	0.59	0.97
1.0	4	0.0	0.0	5x5	1.62	0.31	0.98
1.0	4	0.0	0.25	5x5	1.56	0.17	0.99
2.0	4	0.0	0.0	5x5	1.59	0.13	1.00
2.0	4	1.0	1.0	5x5	1.46	0.56	0.94

covariance functions. The rms of differences for point gravity anomalies deteriorates from about 4 mgal to about 10 mgal, if the magnitude of the uncorrelated measurement noise on the satellite accelerations increases from 0.0 mgal to 1.0 mgal. For geoid undulations these numbers are respectively about 10 cm and 51 cm. From the results displayed in the top of the Tables 8.4-8.7 (case 1), it can be concluded that the addition of accelerations in directions perpendicular to the radial one does not really contribute to an improved gravity field recovery. Improvements are only made for noise values unequal to zero mgal. This indicates that the addition of these accelerations to the radial leads to an instable C_{tt}-matrix (equation (7.1)). This instability shows the ill-conditioning of the downward continuation process and explains why the addition of a diagonal matrix D, whose elements are equal to the variance of the noise, to this matrix improves the recovery ("regularization"). For example, for faultless radial satellite accelerations and a grid size of 7° x 7°, the rms of differences reduces from 16.76 mgal, if the elements of the matrix D are equal to 0.0 mgal^2, to 8.14 mgal, if the elements of the matrix D are equal to 0.25^2 mgal^2 (case 2, Table 8.4). The accuracy of recovered point gravity anomalies/geoid undulations deteriorates quickly with increasing magnitude of the uncorrelated measurement noise.

Similar results are shown at the bottom of the Tables 8.4-8.7 for the same case, but now the empirical Rapp '79 anomaly degree variance model was used in the computation of the covariance functions (denoted by case 4). Comparing these results with those of case 1, it may be concluded that the method of collocation has some flexibility in the choice of degree variance models in the computation of covariance functions, because the values for the rms of differences are almost identical with those listed at the top of these Tables.

In the middle of the Tables 8.4-8.7, results are displayed for the second case, again using OSU86F above degree 36, but for a different satellite altitude of 200 km. The rms of differences for point gravity anomalies ranges from about 5 mgal to about 13 mgal and for geoid undulations from about 12 cm to about 65 cm, if the magnitude of the uncorrelated measurement noise on the accelerations grows from 0.0 mgal to 1.0 mgal. Finally, Tables 8.4-8.7 show the results for case 3, using the OSU86F gravity field model minus the GEM-T1 gravity field model, both for computing the gravity field induced signals and the covariance functions, and for a satellite altitude of 160 km. Compared to the first case, there is a slight deterioration in the rms of differences of geoid undulations, but for gravity anomalies there is hardly any difference. Thus, the part of the gravity anomaly signal caused by the differences in the low-degree terms of the OSU86F and GEM-T1 gravity field models seems to be recoverable for the larger part.

The results indicate that the rms of differences for point gravity anomalies/geoid undulations grows quickly with increasing noise on the satellite accelerations. The results show that for a noise of 1 mgal on the satellite accelerations a value of 12 mgal for the rms of differences between a priori and recovered point gravity anomalies is reached for a satellite altitude of 200 km, and this value is almost reached for a satellite altitude of 160 km. This is significantly above the 5.0 mgal accuracy strived for, although the latter value refers to mean 1° x 1° gravity anomalies. The question that now arises is how the value of 12 mgal for the accuracy of point gravity anomalies

relates to the accuracy of mean 1° x 1° gravity anomalies. From Table 8.1, it can be seen that the OSU86F gravity field model above degree 36 has a power of 18.96 mgal for point gravity anomalies and 16.30 mgal for mean 1° x 1° gravity anomalies. The difference between these two values can be considered to represent the power of the point gravity anomalies due to gravity field terms with a resolution smaller than 1.0°, and is equal to 9.68 mgal in rms sense. If this term is subtracted rms-wise from 12 mgal, a new estimate for the accuracy of mean 1° x 1° can be found equal to 7 mgal. This is still above the 5.0 mgal strived for. Moreover, also the rms of differences for geoid undulations is above the 0.10 m strived for, if this noise is equal to 1.0 mgal. Thus, it seems that, in order to meet the mission objectives, the satellite accelerations should have an accuracy on the order of 1.0 mgal or better.

The results also indicate that the radial accelerations have the largest contribution in the gravity field/geoid undulation recovery for the configurations discussed in this Section. Besides the remarks made in Chapter 7, this can be explained with the help of the Figures 8.1-8.4. These Figures show the small correlations for accelerations in directions perpendicular to the radial direction with gravity anomalies/geoid undulations, which is why they add little information for their recovery.

The conclusions from Section 8.4.2 are corroborated by the results of the least-squares collocation technique. An altitude of 200 km seems the maximum satellite altitude to recover the gravity field with the desired accuracy and resolution, on the condition that the satellite accelerations have an accuracy of 1.0 mgal or better. Errors in the low-degree part of the gravity field do not seem to hamper the recovery of the higher degree part. It must be mentioned that in all simulations, the results are in good agreement with the results of the local gravity field recovery covariance analysis (Chapter 7), showing the consistency of all the computations.

Looking at all Tables, it seems strange that "perfect" accelerations do not yield perfect recovered point anomalies/geoid undulations. An explanation is the limited grid size of satellite accelerations used for downward continuation to a point gravity anomaly/geoid undulation. For a grid size of 5° x 5° and a grid maze of 1.0° this effect is below 5 mgal, and it is even less for mean 1° x 1° gravity anomalies (this has been shown in Chapter 7).

8.4.4 Additional tests

A question that arises when using collocation is what is the effect of the limit of the maximum degree of the harmonic expansion used in the computation of the covariance functions. A possible answer to this question might be to use as a criterion the magnitude of the noise in the observations used to estimate the gravity field. It seems reasonable to truncate the expansion if the power of the omitted part is less than the noise of the observed accelerations. To investigate this, the following test was performed. This test consisted of a rerun of the second case (OSU86F above degree 36 and 200 km satellite altitude), but now the covariance functions were computed with the model

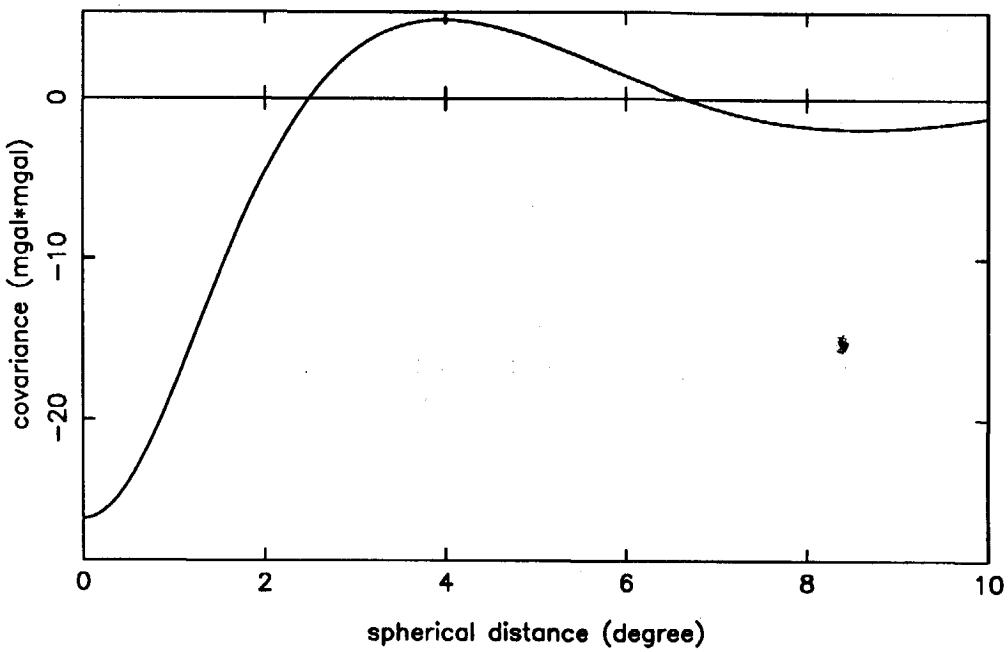

Figure 8.1 Covariance function for gravity anomalies and radial accelerations using OSU86F above degree 36 (200 km altitude)

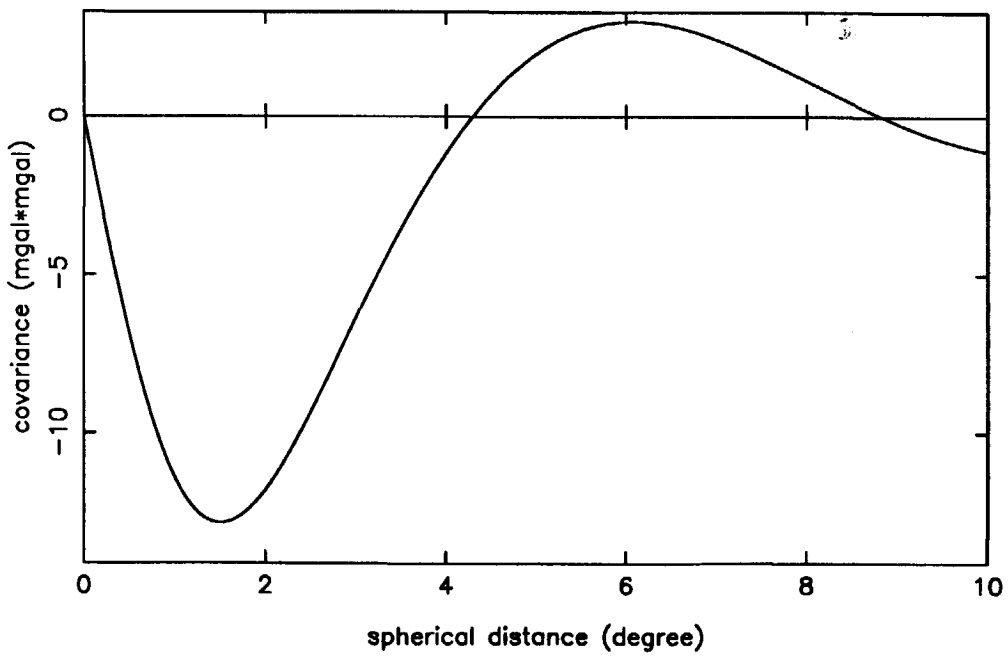

Figure 8.2 Covariance function for gravity anomalies and accelerations perpendicular to the radial direction using OSU86F above degree 36 (200 km altitude)

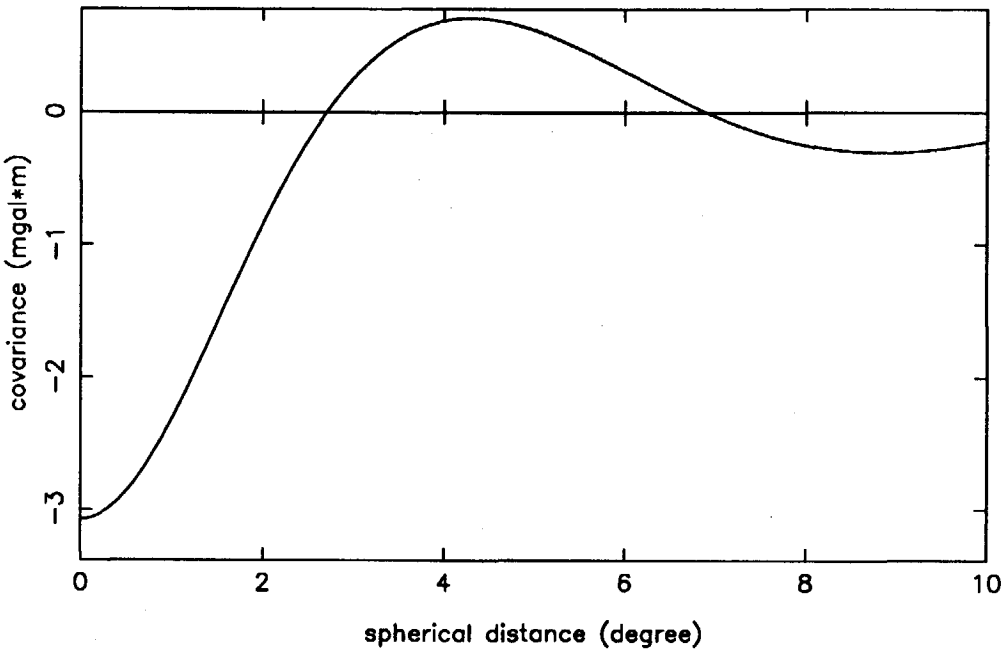

Figure 8.3 Covariance function for geoid heights and radial accelerations using OSU86F above degree 36 (200 km altitude)

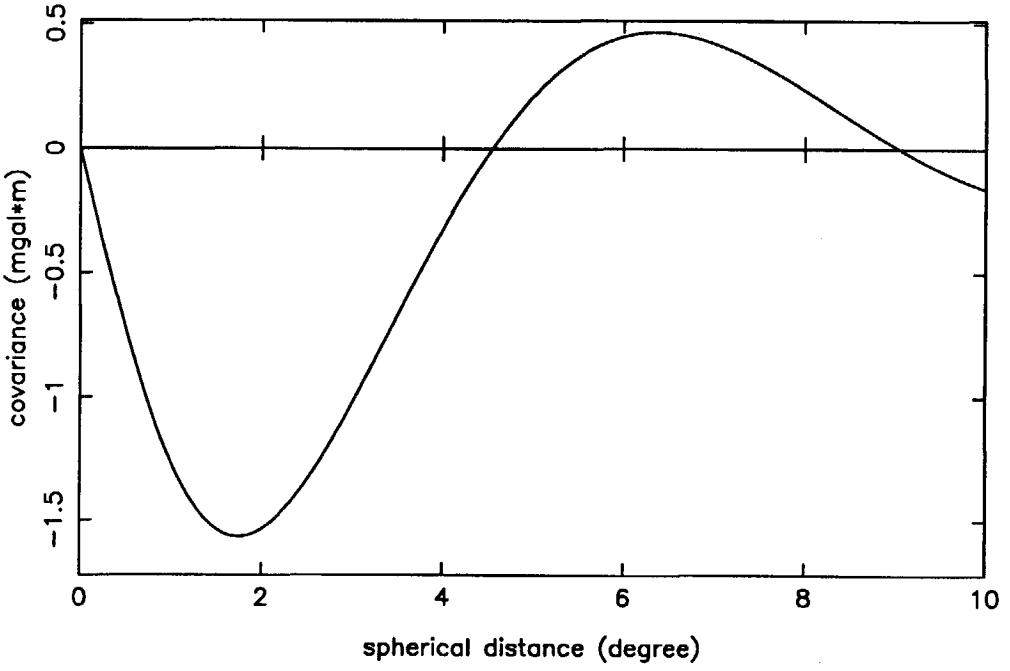

Figure 8.4 Covariance function for geoid heights and accelerations perpendicular to the radial direction using OSU86F above degree 36 (200 km altitude)

Table 8.8 Point gravity anomaly/geoid undulation recovery from radial accelerations, using least-squares collocation and applying the OSU86F gravity field model above degree 36. The results hold for a satellite altitude of 200 km. In the computation of covariances, only use is made of the OSU86F gravity field from degree 37 to 180. The grid maze is equal to 1.0°. The values between brackets denote the original values.

Gravity anomalies

noise (mgal)	noise col. (mgal)	grid size °x°	sig. mag. (mgal)	rms of dif. (mgal)	corr.
0.0	0.0	5x5	17.38	5.15(4.98)	0.96(0.96)
1.0	1.0	5x5	11.96	12.80(12.81)	0.72(0.72)
0.0	0.0	7x7	18.02	7.09(8.14)	0.92(0.90)
1.0	1.0	7x7	12.15	12.44(12.45)	0.74(0.74)

Geoid undulations

noise (mgal)	noise col. (mgal)	grid size °x°	sig. mag. (m)	rms of dif. (m)	corr.
0.0	0.0	5x5	1.60	0.14(0.13)	1.00(1.00)
1.0	1.0	5x5	1.37	0.64(0.64)	0.92(0.92)

truncated at degree and order 180 instead of 360. The power of satellite accelerations of the OSU86F gravity field above degree 180 is less than 1 mgal. The results of this test are listed in Table 8.8. In case of zero noise the recovery compares well with the "original" solution, i.e. using the full OSU86F gravity field model above degree 36 in the covariance computation. If uncorrelated measurement noise with a magnitude of 1 mgal is applied on the accelerations, the results are almost identical, giving support to the assumption that it is not necessary to apply an infinite number of terms in the computation of the covariance functions.

A second important question to be answered is for which domain of the gravity field, the recovery gives the worst results. In order to give an answer to this question, additional tests were performed where only a certain domain of the OSU86F minus GEM-T1 gravity fields was used in the simulation of gravity anomalies/geoid undulations and satellite accelerations at 200 km altitude. The gravity anomalies/geoid undulations were recovered from these accelerations by means of collocation and using the OSU86F minus GEM-T1 gravity fields in the computation of the covariance functionals. The results are listed in Table 8.9. The error in the recovery of the gravity field above degree 200 for a noise-level of 1 mgal on the accelerations is exceeding the magnitude of the recovered signal, in this case point gravity anomalies. The part of the gravity field until degree 100 seems very well recoverable, even if the noise on the satellite accelerations is equal to 1.0 mgal. In all cases listed in Table 8.9, the noise was concentrated in the domain to be solved for, thus yielding pessimistic results. When solving for a complete gravity field up to degree 360, the noise will be spread over the entire range of degrees to be solved for.

8.4.5 Summary

The two minimum-norm techniques investigated here, both indicate that it is possible to recover high-resolution and high-accuracy gravity field information from satellite accelerations with a precision of 1 mgal. It was also found that errors in the low-degree part of the gravity field (below degree 37) are not a severe problem. Moreover, it is expected that these errors will be reduced for the larger part from global analysis of the same GPS SST tracking data that are the subject of the study described in this Chapter. Several studies on this subject have demonstrated the enormous potential of GPS SST for reducing the low-degree gravity field errors of current gravity field models by orders of magnitude (Schrama, 1990; Wu and Yunk, 1986a and 1986b; Smith et al., 1988). This will also be shown in Chapter 9.

The least-squares collocation technique seems to be the most attractive one of the two minimum-norm techniques analyzed. Three reasons for this are that it has the capability of providing accuracy estimates, it can handle gravity anomalies as well as geoid undulations, and it provides a "constant quality" over the recovery area when a regular grid of observed accelerations is available. The other technique has the problem that the recovered anomalies close to the border of the test area seem to be of

Table 8.9 Gravity field recovery for different domains of the gravity field. The results hold for a satellite altitude of 200 km and a grid size of 5°x5°. Use was made of the full OSU86F model minus GEM-T1 in the computation of the covariance functions.

a) noise=0.0 mgal

domain of the gravity field spectrum		sig. mag.	rms of dif.	corr.	sig. mag.	rms of dif.	corr.
upper degree	lower degree	anomaly (mgal)	anomaly (mgal)	anomaly	geoid (m)	geoid (m)	geoid
36	5	6.07	0.44	0.998	1.75	0.10	0.998
50	37	6.01	0.83	0.995	1.06	0.04	1.000
100	51	11.02	1.52	0.992	0.91	0.06	0.998
200	101	11.71	3.31	0.960	0.64	0.11	0.986
360	201	2.49	4.35	0.685	0.09	0.11	0.731

b) noise=1.0 mgal

domain of the gravity field spectrum		sig. mag.	rms of dif.	corr.	sig. mag.	rms of dif.	corr.
upper degree	lower degree	anomaly (mgal)	anomaly (mgal)	anomaly	geoid (m)	geoid (m)	geoid
36	5	7.50	4.81	0.77	1.80	0.32	0.98
50	37	8.09	4.80	0.81	1.11	0.31	0.96
100	51	9.21	5.66	0.84	0.78	0.41	0.90
200	101	5.21	11.22	0.29	0.34	0.59	0.31
360	201	4.76	7.37	0.01	0.31	0.35	0.01

c) a priori magnitudes

domain of the gravity field spectrum		sig. mag.	sig. mag.
upper degree	lower degree	anomaly (mgal)	geoid (m)
36	5	5.85	1.73
50	37	6.59	1.05
100	51	10.43	0.93
200	101	11.53	0.60
360	201	5.65	0.15

anomaly = point gravity anomalies, geoid = point geoid undulations

inferior quality. Another problem using this method is the determination of the optimal regularization parameter and in combination with this the difficulty in the interpretation of results.

In the next Sections, an investigation will be described to establish the required characteristics of GPS SST measurements to ARISTOTELES in order to be able to compute ARISTOTELES accelerations with a 1-mgal accuracy.

8.5 Computation of GPS and ARISTOTELES orbits and SST measurements

In the previous Section, only the last step in the gravity field recovery process has been discussed: the downward continuation of (residual) satellite accelerations at a mean satellite altitude to the Earth's surface in the form of gravity anomalies/geoid undulations. In reality, the accelerations will be derived from very precise GPS range measurements, which will actually consist of phase measurements of the carrier signals broadcast by the GPS satellites. To simulate these measurements, the orbits of the GPS satellites and ARISTOTELES have to be integrated with a very high accuracy, using a spherical harmonic expansion of the Earth's gravity field to high degree and order. Also, it must be shown that it is possible to extract sufficiently accurate acceleration observations (better than 1 mgal for a 1° resolution in latitude and longitude) from the range measurements. These subjects will be discussed in the Sections 8.5.1 and 8.5.2.

8.5.1 Orbit integration

For the very accurate integration of orbits of the GPS satellites and ARISTOTELES, an Adams-Moulton integrator was used (Appendix F) with a Runge-Kutta initialization. This integrator was also used in the orbit computations described in Chapter 3. The order of the integration could be chosen freely and the possibility existed to integrate relative to a Keplerian reference ellipse. In that case only the perturbations relative to this Keplerian ellipse are integrated. For this study, the order of the integration was taken equal to 11. A higher value for this order did not change the computed orbits significantly.

For ARISTOTELES, only orbit segments covering a selected geographical area, extending from -5° to 25° longitude and from 35° to 65° latitude (thus overlapping the area solved for in the downward continuation), were integrated for a 30-days period. The only force model used in the orbit integration was the OSU86F gravity field, which represents the "real-world". Although in reality the ARISTOTELES orbit will also be perturbed by other forces, for example luni-solar attraction, non-conservative forces like atmospheric drag (which will be significant for the low-altitude ARISTOTELES satellite) and solar radiation, these forces can either be modeled very

accurately or will be measured. For example, the atmospheric drag can be reconstituted very accurately from measurements of accelerations of the gradiometer in the "less-sensitive" flight direction. The interest of the simulations described in this thesis lies in the determination of the gravity field of the Earth, and it was assumed that the perturbations caused by this gravity field can be separated from other orbit perturbations. The initial state-vector of each orbit segment was taken from the 30-days orbit computed in the CIGAR Phase I study (CIGAR, 1989). GPS orbits were generated only for the periods of the ARISTOTELES orbit segments, starting from state-vectors listed in the CIGAR Phase I study for the 18-satellite configuration. The initial state-vector of each GPS satellite orbit segment was obtained by a simple Keplerian propagation of the state-vector from CIGAR Phase I.

Since the GPS orbits are, because of their high altitude, not expected to be affected by terms of spherical harmonic expansions of the gravity field above degree 36 significantly, all GPS orbits were computed with the OSU86F gravity field model truncated at degree and order 36. The simulated "real-world" ARISTOTELES orbit was obtained using the full 360 x 360 OSU86F gravity field model. In addition, two different ARISTOTELES reference orbits were computed, the first with the GEM-T1 gravity field model and the second with the OSU86F gravity field model up to degree and order 36. These reference orbits were assumed to represent the outcome of a precise orbit determination using low-degree (until degree 36) state-of-the-art gravity field models during the first part of the ARISTOTELES mission.

An important variable in the simulations is the data rate of the GPS receiver. In this study it was taken equal to the time step of the integration of the ARISTOTELES orbit, which was 2.5 s. This 2.5 s integration step is also small enough to "follow" the variations of the 360 x 360 OSU86F gravity field. A gravity field of this size has a resolution of about 50 km, whereas 2.5 s amounts to an ARISTOTELES orbital arc of about 20 km. Future GPS receivers are expected to have the possibility to provide 1 observation per second, so that the number used in this study is conservative.

The GPS SST range measurements were obtained by subtracting the ARISTOTELES positions from the GPS positions, but only if the elevation angle of a GPS satellite as seen from ARISTOTELES was greater than 0°. The GPS measurements to the "real-world" ARISTOTELES orbit were considered to represent the "real-world" GPS observations. The GPS measurements to the ARISTOTELES reference orbits then represent the "computed" observations derived from a priori models. The differences between the "real-world" and "computed" observations are the residuals, which may be considered to be caused by the "unknown" gravity anomalies that are to be recovered. However, in these simulations, they are known and caused by the difference between the full OSU86F model and that model truncated at degree and order 36, or they are caused by the difference between the full OSU86F model and GEM-T1. For the case of the truncated OSU86F ARISTOTELES reference orbit, only the high-frequency part of the gravity field represented the source of the GPS SST range residuals, whereas in the case of the GEM-T1 ARISTOTELES reference orbit also low-degree effects were included.

8.5.2 Results

From the GPS SST range residuals, the residual accelerations of the ARISTOTELES satellite can be obtained in the following way. Firstly, a second-order polynomial is fitted through successive range residuals of one GPS satellite. The second derivative of this polynomial is closely related to the residual acceleration of ARISTOTELES in the direction of that satellite. If three or more GPS satellites are in view at the same time, which will always be the case after the full GPS-configuration has been established, ARISTOTELES residual accelerations in the radial, East-West and North-South direction are computed geometrically from these residual accelerations by a least-squares fit. An advantage of this method of fitting a polynomial and taking the second derivative to obtain the accelerations is that the effect of biases and linear drifts in the ranges or errors which vary slowly with time are filtered out. Examples are GPS clock drift and ephemeris errors, but in particular the ambiguities associated with carrier phase measurements drop out as a problem.

In the next Section, it will be discussed how the irregular grid of ARISTOTELES residual accelerations obtained this way is transformed to a regular grid at a mean satellite altitude. This simplifies the downward continuation and makes it possible to use the software and algorithms described in Section 8.3.

An important question with the second-order polynomial fit of the GPS SST residuals is how many points should be used. This choice is a trade-off between two effects. Increasing the number of points will help to reduce the noise in the data due to averaging. On the other hand, the variations in the residuals will become more difficult to fit by a second-order polynomial which leads to discretization errors. To investigate this problem, experiments with different numbers of points were performed.

Table 8.10 summarizes the results of various experiments to fit a second-order polynomial through successive GPS SST measurement residuals to obtain residual accelerations and velocities. What is displayed in this Table, is the rms of differences between the accelerations obtained by discretization and the accelerations by subtracting the accelerations along the ARISTOTELES "reference" orbit computed with the "reference" gravity field ($\bar{a}_{ref}$ at r_{ref}, Figure 8.5) from the "real-world" accelerations computed with the "real-world" gravity field ($\bar{a}_{rw}$ at r_{rw}, Figure 8.5). The difference between these two accelerations can be linearly approximated by:

$$\bar{a}_{rw} - \bar{a}_{ref} = a_1 - a_2 + G(T)\Delta\rho \; . \tag{8.6}$$

where a_1 is the acceleration at r_{rw} computed with the "real-world" gravity field, a_2 is the acceleration at the same position computed with the "reference" gravity field, $\Delta\rho$ is the orbit error and $G(T)$ is the gravity tensor at that position. The listed errors will be referred to as the "discretization effect" and were obtained for noise-free GPS SST range residuals. Part of these errors are caused by the fact that each batch of 9 GPS SST range residuals is modeled as a second-order polynomial and this second-order polynomial can not follow these residuals exactly. To these errors must be added centrifugal and Coriolis terms caused by the orbit differences $\Delta\rho$ (Figure 8.5) between the "reference" and "real-world" orbits and its time derivative $d\Delta\rho/dt$. These orbit differences reflect the errors due to integrating with a reference gravity field model

Table 8.10 Rms of differences between the accelerations obtained by discretization of the GPS SST range residuals and the accelerations obtained directly from the gravity field.

nr. of points in discretization	case	position (μm)	velocity (mm/s)	acceleration (mgal)
3	a	0.01	0.07	0.08
5	a	0.01	0.07	0.08
7	a	0.01	0.07	0.08
9	a	0.01	0.07	0.09
3	b	0.06	0.18	0.19
9	b	0.06	0.18	0.20
9-3	b	0.00	0.02	0.06

case a: OSU86F above degree 36;
case b: OSU86F minus GEM-T1.

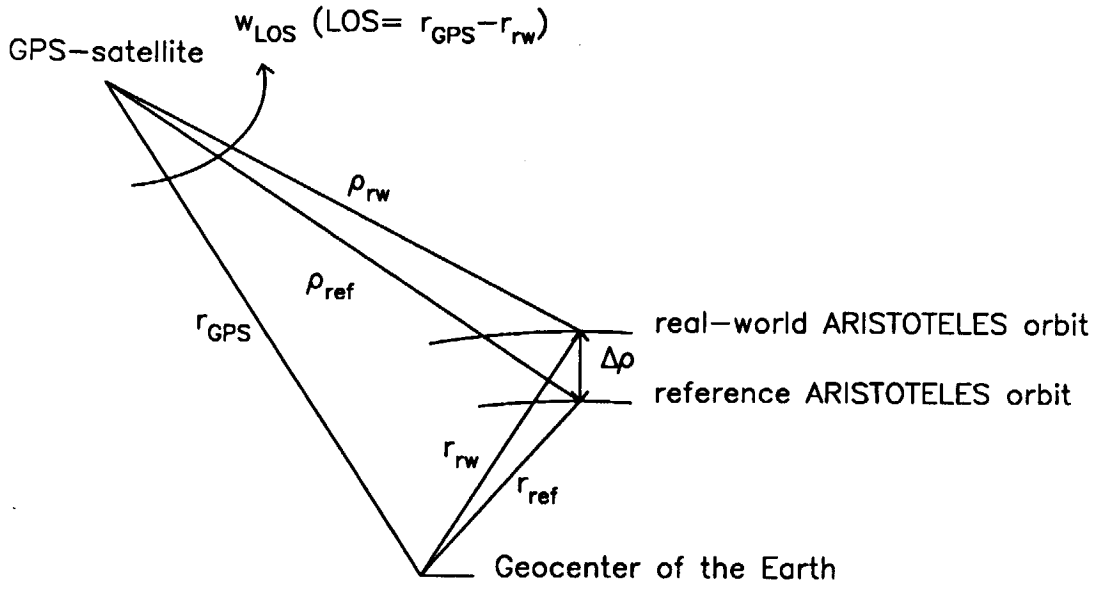

Figure 8.5 GPS–ARISTOTELES tracking geometry

instead of with the "real-world" gravity field. It can be shown that the centrifugal and Coriolis terms are smaller than 0.05 mgal. These terms are part of the errors displayed in Table 8.10.

In the downward continuation, a second acceleration error is included due to the position offset $\Delta\rho$. The residual acceleration obtained should reflect the residual gravity field along the "real-world" ARISTOTELES orbit (a_1-a_2). However, this acceleration value is positioned along the "reference" orbit. Thus an error equal to $G(T)\Delta\rho$ is made (equation (8.6)). For example, if it is assumed that the only acceleration of the ARISTOTELES orbit is produced by the central term of the Earth's gravity field, the error in modeling the radial acceleration due to a satellite radial position error $\Delta\rho$ (m) is equal to:

$$\frac{2\mu}{r_3}\Delta\rho \sim 0.3\Delta\rho \text{ mgal} . \qquad (8.7)$$

This equation indicates that for a 1 mgal radial acceleration accuracy, the ARISTOTELES orbit must be determined with a radial accuracy of better than 3 m.

The maximum number of points used in the polynomial fit was nine, which corresponds to a distance covered by ARISTOTELES of approximately 150 km at a data rate of 1 observation per 2.5 s. This is of the same order of magnitude as the block size of the anomalies that are to be recovered from the data. Because of this, it may be argued that when further increasing the number of points, the polynomial fit would absorb the effects of more than one anomaly. This may degrade the accuracy of the fit, since the signal will become more complex and therefore harder to fit by a second-order polynomial. From Table 8.10 it can be seen that the discretization error for the accelerations is always much smaller than 1 mgal, so that it will cause only minor errors in the gravity field recovery.

To obtain some insight in the effect of measurement noise and different discretization strategies on the accuracy of the derived accelerations, the following approach was adopted:

- uncorrelated measurement noise was generated in the radial direction at an altitude of 200 km above the selected test area;
- residual radial accelerations were computed by discretization of this noise using different numbers of points; the standard deviation of the noise was chosen such, that the residual accelerations that were computed from this noise had a standard deviation of 1.0 mgal; it was assumed that in each 1° x 1° block only one such acceleration can be determined;
- from these radial accelerations gravity anomalies/geoid undulations were recovered by means of least-squares collocation, in which the matrix D (equation (7.1)) was represented by a diagonal matrix; the elements of this matrix were equal to 1.0 mgal^2.

The results are displayed in Table 8.11. From this Table, it may be concluded that the accuracy of the GPS SST measurements must be at the millimeter level for a maximum of 9 points in the polynomial fit, because the magnitudes of the recovered anomalies and geoid undulations were about 5.0 mgal and 25 cm, respectively. If only

Table 8.11 Point gravity anomaly and geoid undulation recovery from the radial component of GPS SST range measurements. These measurements consisted of uncorrelated measurement noise. From these observations, radial satellite accelerations were estimated and continued downward to gravity anomalies and geoid undulations on the Earth's surface. The results hold for a satellite altitude of 200 km, and the Rapp'79 anomaly degree variance model was used to compute the covariance functions.

grid maze = 1.0°
grid size = 5°x5°
sampling rate = 2.5 s

noise (mm)	nr. of points in discretization	noise col. (mgal)	rms of Δg (mgal)	rms of h_g (m)
0.0255	3	1.0	6.16	0.38
0.1169	5	1.0	4.18	0.24
0.2864	7	1.0	4.81	0.27
0.5484	9	1.0	5.29	0.30

Table 8.12 Effect of different domains of the OSU86F gravity field on the position and velocity perturbations along the short arcs over the selected local area.

domain of the gravity field spectrum		rms of position (cm)	rms of velocity (mm/s)
upper degree	lower degree		
20	10	63.73	3.86
36	20	38.76	2.02
50	36	27.56	1.56
100	50	21.46	0.97
360	100	1.94	0.11
36	10	80.64	4.59
50	10	88.91	4.89
100	36	35.54	1.86
360	36	35.91	1.87

one acceleration in a 1° x 1° block can be determined by the second-order polynomial fit, an accuracy of even 0.5 mm would be required. However, in reality, many more satellite observations will be available in such an area so that the demand of a 0.5 mm GPS SST measurement accuracy may be relaxed; this will be shown in Section 8.6. Another indication for the requirement of millimeter accuracy of GPS SST measurements is shown in Table 8.12, which lists the effect of different domains of the OSU86F gravity field on the position and velocity of the ARISTOTELES satellite along the short arcs. The values listed in this Table were obtained by integrating the ARISTOTELES orbit with the OSU86F gravity field model truncated at different degrees, and by computing the rms of differences of the position and velocity between the orbits computed with the different truncated OSU86F gravity field models. Above degree 100 the effect in orbital position is below 2.0 cm for the orbit segments.

8.5.3 Summary

The concept of discretization, where a second-order polynomial fit is applied to GPS SST range residuals to obtain satellite acceleration observations in the desired directions, was shown to be applicable to recover gravity field information from ARISTOTELES orbit perturbations. To achieve an acceleration-accuracy-level of 1 mgal along the ARISTOTELES orbit segments, at least 9 residuals should be used for the polynomial fit when a sampling rate of 2.5 s and a GPS SST carrier phase measurement accuracy at the millimeter level are assumed. Using less data points increases the error due to measurement noise; using more points jeopardizes a high-resolution gravity field recovery. Any bias/linear drift and/or carrier phase cycle ambiguity cancel in the approach of fitting a second-order polynomial and taking the second derivative.

8.6 Gridding

After having processed the GPS SST measurements as described in the previous Sections, an irregular grid of accelerations along the ARISTOTELES orbit segments has been obtained. The downward continuation techniques, as developed and proposed in this study, make use of a regular grid of accelerations at a mean satellite altitude. This constant satellite altitude yields the opportunity to make use of several symmetry considerations. Therefore, a technique has been developed to transform the irregular grid of accelerations into a regular grid at a mean satellite altitude. The first part of this Section gives a description of this gridding technique, while in the second part some results will be presented.

8.6.1 Gridding technique

The algorithms described in Section 8.2 and the software that has been developed make use of a regular grid of accelerations at a constant altitude from which gravity anomalies/geoid undulations are computed. The resolution of this grid of accelerations was taken equal to 1° if the method of least-squares collocation was applied and equal to 0.33°/0.2° (longitude/latitude) if the equations of Stokes were used. Therefore, the irregular grids of satellite accelerations obtained by discretization of the GPS SST residuals, had to be transformed to regular grids with the specified resolutions. This transformation consisted of the following steps:

- Assigning recovered ARISTOTELES accelerations along the ARISTOTELES orbits within a "block of influence" to a grid point at the center of that block. This implies that one observed ARISTOTELES acceleration may be assigned to more than one grid point;
- The value of the grid point at the center of the block is predicted by means of least-squares collocation from the accelerations assigned to that grid point at a selected mean ARISTOTELES altitude.

In case of downward continuation by the method of least-squares collocation, the "block of influence" was chosen such that each recovered ARISTOTELES acceleration was assigned to only one grid point. This means that the obtained regular grids consisted of grid points which were determined independently. Using the equations of Stokes for downward continuation, a block of influence of 1° x 1° in spherical distance was applied.

The covariance function for the ARISTOTELES accelerations, necessary to build up the covariance matrix in the least-squares collocation process, was tabulated in a data set on the VAX3100/CONVEX 240 for several altitudes with a resolution of 1 km and for several spherical distances with a resolution of 0.01° (approximately 1 km). The reason for this is that the ARISTOTELES accelerations were scattered in altitude and also in longitude and latitude, so that it must be possible to interpolate both in the radial and longitude/latitude directions. The covariance functions were computed using the same spherical harmonic expansions of the orbit integration. It was found that the altitude variations of the ARISTOTELES orbits in the selected geographical area had a range of 21 km, thus all recovered ARISTOTELES accelerations were situated in a shell of 21 km around a mean altitude of 191 km, thus the measurements were made at altitudes ranging from about 180 to 200 km. This variation can be explained by the adopted orbit parameters of the ARISTOTELES orbit (CIGAR, 1989). At the epoch of the 30-days period, a semi-major axis equal to 6577.05 km, an eccentricity equal to 0.001, an inclination equal to 96.3° and an argument of perigee equal to 0.0° were selected. It was found that the (osculating) eccentricity varied from $2*10^{-5}$ to $3*10^{-3}$ and together with the variation of the (osculating) argument of perigee the variation of 21 km in altitude can be explained.

Taking as gravity field signal to be recovered the difference between the OSU86F

and GEM-T1 gravity field models and adopting a nominal 191 km satellite altitude, a change in altitude of 1 km means a change in satellite residual acceleration on the order of 0.02 mgal. When this value is compared with the 1 mgal accuracy requirement, the resolution of the covariance function of 1 km indeed seems to be sufficient.

8.6.2 Results

Results of the gridding process, both for simulations including and for simulations excluding errors in the low-degree and -order terms of the gravity field, are listed in Table 8.13. The accelerations that were obtained in the gridding process, were compared with the accelerations that were computed directly from the gravity field models. For a resolution of the regular grid equal to 1°, the accuracy of these accelerations drops from 0.22-0.36 mgal to 0.89-0.96 mgal, if the noise on the GPS SST measurements increases from 0.0 mm to 2.0 mm. The lower limits of these numbers hold for the simulations excluding low-degree effects and the higher limit for the simulations including low-degree effects. When the measurement noise is equal to 5.0 mm, the error in the recovered residual accelerations is significantly larger than 1.0 mgal (top of Table 8.13). For a resolution of 0.33/0.2° (longitude/latitude), the accuracy of the radial accelerations dropped from 1.02-1.41 mgal to 1.41-1.70 mgal. Further attention to this deterioration will be paid in Section 8.7.1.1. It is concluded that, if a resolution of 1° of the grid of accelerations is strived for, equal to the resolution of the gravity field recovery, an accuracy of the satellite accelerations of 1 mgal seems possible for a noise on the GPS carrier phase measurements at the millimeter-level, provided a data rate of one observation per 2.5 s.

8.6.3 Summary

The least-squares collocation process is an appropriate method for the transformation of an irregular grid of satellite accelerations at varying altitudes to a regular grid at a mean satellite altitude. With a GPS SST range measurement accuracy of 2 mm, a 1 mgal precision of the accelerations in the regular grid with a resolution of 1° is possible. This conclusion is strongly supported by the fact that in the analysis only a 30-days period has been simulated, i.e. 1/3 of a full ARISTOTELES repeat period. Thus, the coverage of the ARISTOTELES orbits above the selected geographical area is far from ideal considering the resolution of the gravity field to be determined. Due to computer limitations no simulations for a full repeat period have been performed.

Table 8.13 Accuracy of recovered radial ARISTOTELES accelerations in a regular grid at a mean satellite altitude of 191 km. The accelerations in this regular grid are derived from radial accelerations along the ARISTOTELES orbit by means of collocation. These values are subsequently compared with the accelerations in a regular grid which are computed directly from the gravity field models.

I: resolution of grid is equal to 1° in latitude and longitude direction.

a) OSU86F gravity field above degree 36.

noise GPS SST (mm)	noise in collocation (mgal)	precision estimate (mgal)	rms of difference (mgal)
0.0	0.5	0.20	0.22
1.0	2.0	0.58	0.49
2.0	4.0	1.01	0.89
5.0	8.0	1.57	1.63

b) OSU86F minus GEM-T1 gravity fields.

noise GPS SST (mm)	noise in collocation (mgal)	precision estimate (mgal)	rms of difference (mgal)
0.0	0.5	0.21	0.36
1.0	2.0	0.59	0.56
2.0	4.0	1.09	0.96

II: resolution of grid is equal to 0.2° in latitude and 0.33° in longitude direction.

a) OSU86F gravity field above degree 36.

noise GPS SST (mm)	noise in collocation (mgal)	precision estimate (mgal)	rms of difference (mgal)
0.0	0.5	0.48	1.02
1.0	2.0	0.85	1.20
2.0	4.0	1.24	1.41

b) OSU86F minus GEM-T1 gravity fields.

noise GPS SST (mm)	noise in collocation (mgal)	precision estimate (mgal)	rms of difference (mgal)
0.0	0.5	0.58	1.41
1.0	2.0	0.95	1.48
2.0	4.0	1.44	1.70

8.7 Gravity field recovery from GPS SST range measurements

The final step in the processing of the GPS SST range measurements consisted of the downward continuation of the regular grid of accelerations computed from the simulated GPS SST range measurements. In the major part of the simulations only radial satellite accelerations were recovered, because it was proven that accelerations in directions perpendicular to the radial do not add much information for the recovery of gravity anomalies/geoid undulations. However, in Section 8.7.1.4 a few results will be displayed where, besides radial, also accelerations in two directions perpendicular to the radial were recovered from the simulated GPS SST range measurements and used in the downward continuation. This in order to support the preceding reflections and to support the discussions in Section 8.4.3. In the last Part of this Section a short discussion of possible error sources on the GPS SST measurements and their effect on the gravity field recovery is presented.

8.7.1 Downward continuation results

The two minimum-norm techniques proposed in this study will be investigated and compared for the downward continuation of the regular grids of radial accelerations. The regular grids used in this Section satisfy the requirements on the resolution of the grids as specified in Section 8.3 (see also Section 8.6). Thus, the resolutions were accommodated to the simulation set-ups as described in that Section.

8.7.1.1 Downward continuation using the equations of Stokes

Tests were performed using the GPS SST range measurements as computed and described in Section 8.5. These tests hold for the cases where errors in the low-degree part of the gravity field were included or excluded. In the simulations of Section 8.3, a regular grid of accelerations with a resolution of 0.2° in latitude and 0.33° in longitude was applied. Therefore, the irregular grid of recovered radial accelerations along the ARISTOTELES orbits was first transformed to a regular grid with this resolution by means of least-squares collocation. As shown in Table 8.13, this led to a somewhat deteriorated quality of the accelerations in the obtained regular grid when compared to the accelerations in the regular grid with a resolution of 1° in both directions, which grid maze size will be used in the next Section. This deterioration can be explained by analyzing the ground track pattern of the 30-day ARISTOTELES orbit over the selected area (Figure 7.1). This ground track pattern shows some "holes", and if a resolution of 0.2°/0.33° is selected, relatively many accelerations of the regular grids

Table 8.14 Mean 1° x 1° gravity anomaly recovery from GPS SST range measurement residuals.

residuals caused by OSU86F gravity field model above degree 36

noise GPS SST (mm)	sig. mag. (mgal)	rms of dif. (mgal)	corr.	add.
0.0	10.18	10.66	0.75	0.040
0.0	10.91	10.70	0.74	0.028
1.0	9.04	11.20	0.73	0.040
1.0	9.78	11.28	0.71	0.028
2.0	7.69	11.86	0.70	0.040
2.0	8.41	11.93	0.68	0.028

residuals caused by OSU86F minus GEM-T1 gravity fields

noise GPS SST (mm)	sig. mag. (mgal)	rms of dif. (mgal)	corr.	add.
0.0	15.20	12.87	0.68	0.016
0.0	13.07	11.63	0.72	0.040
0.0	12.14	11.51	0.72	0.063
1.0	12.36	11.76	0.71	0.040
1.0	11.44	11.66	0.72	0.063
2.0	12.17	12.38	0.67	0.028
2.0	12.94	12.83	0.65	0.020

- 9 point second-order polynomial fit through residuals;
- transformation of all the radial accelerations to a regular grid at a mean satellite altitude of 191 km;
- downward continuation by means of the Stokes' equations.

with this resolution are located in such "holes". These accelerations will be less accurate. However, per 1° x 1° block 15 accelerations were estimated instead of 1, so the effect of the deteriorated quality will be filtered out using this greater amount of accelerations in the mean 1° x 1° gravity anomaly recovery.

The top-half of Table 8.14 shows the results for the case where only the OSU86F gravity field was used both in the computation of the "real-world" ARISTOTELES orbit segments (full field) and the reference orbits (truncated field). In this case, it is expected that the recovered residual ARISTOTELES accelerations will not be affected by the errors in the low-degree part of the gravity field. The rms of differences of recovered mean 1° x 1° gravity anomalies with their a priori values deteriorates from 10.66 mgal to 11.86 mgal for an increase of the noise on the GPS measurements from 0.0 to 2.0 mm. The accuracy of the radial accelerations used in the downward continuation was in the range of 1.0 to 1.5 mgal (Table 8.13). For a noise-level of the radial accelerations below 2.0 mgal the results listed in Table 8.2 (case 2) indicate that an rms of differences equal to about 8.5 mgal seems possible.

Similar results are listed in the bottom-half of Table 8.14 for the case where also errors in the low-degree part of the gravity field were simulated, i.e. the GEM-T1 gravity field model was used in the computation of the ARISTOTELES reference orbits. The rms of differences deteriorates slightly compared to the rms of differences of the previous case (top-half of Table 8.14). For example, if a noise of 2.0 mm is applied to the GPS measurements, the rms of differences becomes 12.38 instead of 11.86 mgal.

In summary, the results listed in Table 8.14 indicate that the larger part of the high-frequency gravity field can be recovered using the equations of Stokes, but the results are not very satisfactory compared to the results of Section 8.4. An explanation for the deterioration of e.g. the 8.5 mgal value of Table 8.2 to 10.66-11.86 mgal of Table 8.14 may be the non-perfect coverage of the selected geographical test area by the 30-days ARISTOTELES orbital arc analyzed. For some gravity anomalies there is hardly any information in the 30-days ARISTOTELES arc (approximately 1/3 of a full repeat period, (CIGAR, 1989)). This can also be seen by studying Figure 7.1. More attention to this phenomenon will be paid in the next Section.

The results indicate again that the inclusion of errors in the low-degree part of the gravity field does not seem to be a severe problem. The minimum-norm technique that was used in this Section, shows that the rms of differences in the recovered mean 1° x 1° gravity anomalies exceeds the rms of the recovered anomalies themselves, if the noise on the GPS SST measurements is above 2.0 mm (Table 8.14).

8.7.1.2 Downward continuation by least-squares collocation

The same tests were performed as in Section 8.7.1.1, but now also geoid undulation recovery was investigated. Table 8.15 shows the results for the gravity anomaly/geoid undulation recovery, both for tests including and tests excluding errors in the low-

Table 8.15 Point gravity anomaly/geoid undulation recovery from GPS SST range measurement residuals.

residuals caused by OSU86F gravity field model above degree 36

noise (mm)	noise col. (mgal)	sig. mag. anomaly (mgal)	rms of dif. anomaly (mgal)	corr. anomaly	sig. mag. geoid (m)	rms of dif. geoid (m)	corr. geoid
0.0	0.20	13.89	9.11	0.88	1.48	0.37	0.97
1.0	0.58	11.78	11.28	0.80	1.35	0.52	0.95
1.0	0.49	12.21	11.15	0.81	1.37	0.51	0.95
2.0	1.01	9.42	12.71	0.76	1.14	0.68	0.93
2.0	0.89	9.71	12.57	0.77	1.15	0.66	0.94
5.0	1.57	5.97	14.67	0.71	0.72	0.98	0.92
5.0	1.63	5.90	14.71	0.71	0.71	0.99	0.92

residuals caused by OSU86F minus GEM-T1 gravity fields;

noise (mm)	noise col. (mgal)	sig. mag. anomaly (mgal)	rms of dif. anomaly (mgal)	corr. anomaly	sig. mag. geoid (m)	rms of dif. geoid (m)	corr. geoid
0.0	0.21	15.13	9.54	0.87	2.31	0.47	0.98
0.0	0.36	14.19	10.18	0.85	2.28	0.50	0.98
0.0mn	0.21	14.25	7.04	0.91	-	-	-
1.0	0.59	13.34	11.42	0.81	2.21	0.59	0.97
1.0	0.56	13.48	11.38	0.81	2.22	0.58	0.97
2.0	1.09	11.45	12.58	0.77	2.05	0.67	0.96
2.0	0.96	11.78	12.44	0.77	2.06	0.66	0.96
2.0mn	1.09	11.05	9.94	0.82	-	-	-

- 9 point second-order polynomial fit through residuals;
- transformation of all the radial accelerations to a regular grid at a mean satellite altitude of 191 km;
- downward continuation by means of least-squares collocation.
- grid maze = 1.0°;
- grid size = 5x5 points;
- mn = mean 1° x 1°.

degree part of the gravity field. If the errors in the low-degree part of the gravity field are not included, an increase of the noise on the GPS SST measurements from 0 to 2 mm results in a deterioration of the accuracy of the recovered point gravity anomalies from 9.11 to 12.57 mgal. For geoid undulations this decrease in accuracy is from 0.37 to 0.66 m. For comparison, also results are listed in Table 8.15 for the case that a noise of 5.0 mm was added to the GPS range measurements. For that case, the rms of differences for gravity anomalies is equal to 14.67 mgal, much above the rms of the a posteriori (recovered) gravity anomalies, which is equal to 5.97 mgal. Results of the case where the GEM-T1 model was used to compute the ARISTOTELES reference orbit are displayed in the bottom-half of Table 8.15. Thus, this case refers to a situation where errors are present in the low-degree part of the gravity field. For a GPS SST measurement noise of 0-2 mm, the point gravity anomaly accuracy ranges from 9.54 to 12.44 mgal and the geoid undulation accuracy from 0.47 to 0.66 m. These results show the minor change in accuracy of recovered point gravity anomalies and geoid undulations if errors in the low-degree part of the gravity field are also simulated.

One of the mission objectives is to recover mean 1° x 1° gravity anomalies with an accuracy of 5.0 mgal. To verify the discussions on the relation between the accuracy of point gravity anomalies and of mean 1° x 1° gravity anomalies (Section 8.4), additional tests were performed. A finer grid of point gravity anomalies was determined, from which mean 1° x 1° gravity anomalies were derived. The resolution of this grid was such that 16 point gravity anomalies in each 1° x 1° block were recovered and averaged to be compared with the a priori mean 1° x 1° gravity anomalies (taking more than 16 points did not alter the results significantly). The results are shown in the bottom-half of Table 8.15. The rms of differences improves from 12.44 mgal for point gravity anomalies to 9.94 mgal for mean 1° x 1° gravity anomalies. Thus a signal with an rms value of 7.5 mgal (rms-wise) was filtered out. What may seem strange in the results is the rms of differences of approximately 9 mgal for point gravity anomalies, if there is no noise on the GPS SST range measurements. Why not approximately 5 mgal as in the simulations of Section 8.4 where a regular grid of perfect accelerations was used ? At least three effects are important that may clearify the deterioration in the rms of differences. Firstly, the errors made due to discretization of the GPS SST range residuals in determining the residual accelerations. Secondly, errors caused by the differences between the "real-world" and reference orbits (equations (8.6) and (8.7)). Finally, the inappropriate coverage: only 1/3 of a repeat period was simulated, meaning that certain 1° x 1° gravity anomaly blocks were not yet covered by ARISTOTELES orbits (Figure 7.1).

For GPS SST observations with zero noise, the rms of differences is on the order of 9 mgal, whereas for accelerations with zero noise and perfect coverage, the results of Section 8.4 indicate that a value of 5 mgal is possible. This is probably for the greater part due to the non-perfect coverage for only a 1/3 repeat period. For higher noise-levels of the GPS SST observations, the "noise-effect" exceeds the "non-perfect-coverage-effect", and the results compare well to those of Section 8.4. This result can be explained by the fact that for certain noise-levels of observed accelerations the resolution of the solved-for gravity field is limited and this resolution will approach the

resolution of the ground track pattern of even the 1/3 repeat period.

The first effect, that is the discretization effect, has been shown to be small and of the order of 0.1 mgal in the determination of radial ARISTOTELES accelerations. The magnitude of the second effect can be estimated by inserting the value of the orbit differences in equations (8.7). The rms for these differences is on the order of 35 cm (Table 8.12), yielding an acceleration error of about 0.1 mgal. However, the third effect may be substantial. Tests have been performed where, instead of the accelerations obtained by discretization of the GPS SST measurements, the real accelerations along the ARISTOTELES orbits as computed from the spherical harmonic expansions of the gravity field were used. This irregular grid of perfect accelerations was subsequently transformed to a regular grid as used in Section 8.4 by means of least-squares collocation. Point gravity anomalies were recovered with this grid and were compared with the results of Section 8.4. The results have shown that the effect due to the coverage limitation has an rms level on the order of 7 mgal, i.e. the rms of these additional errors in the point gravity anomalies recovered is equal to about 7 mgal. Subtracting this rms-level from the 9.11 mgal rms of differences of Table 8.15 leads to a value for the rms equal to 5.8 mgal, for the case where errors in the low-degree part of the gravity field were excluded. This is in good agreement with the results discussed in Section 8.4.

8.7.1.3 Possibilities for improvement

An important part of the errors in the recovered gravity anomalies/geoid undulations was shown to be caused by a non-perfect coverage of the selected geographical area by the 30-days ARISTOTELES orbital arc. Without any doubt a simulation for the full repeat ARISTOTELES orbital arc of 91 days would have led to better results. Moreover, the entire ARISTOTELES gravity mission will have a period of at least 6 months, i.e. 2 repeat periods, so that the gravity field recovery will improve further. Also, the gridding can be improved. In the gridding applied in this thesis, a constant uncorrelated measurement noise on the recovered ARISTOTELES accelerations along the orbit segments was assumed in the least-squares collocation approach. A better technique is probably to scale the noise value in the collocation process (not the actual measurement noise but the noise value as input parameter for the least-squares collocation) with a geometric quantity determined by the actual instantaneous GPS-ARISTOTELES configuration. For example, this parameter may be the PDOP-factor (Position-Dilution-of-Precision). This PDOP-factor is a measure of the spatial distribution and the number of GPS satellites in view of the ARISTOTELES satellite. The PDOP-factors may be computed in the transformation of the ARISTOTELES accelerations in the direction of a GPS satellite to the accelerations in the appropriate coordinate frame. In addition, in the gridding process no account has been taken of the fact that subsequent observed accelerations along the orbit segments are correlated because they partly use the same GPS observations. It is recalled that each observed

acceleration was determined from batches of 9 subsequent GPS observations. Taking into account these correlations may lead to better results. The same argument holds for the downward continuation. Again, a constant uncorrelated measurement noise for the radial accelerations in the regular grid was applied, whereas, in principle, the gridding technique has the possibility to give a precision estimate of each radial acceleration in the regular grid separately. However, implementation of these precision estimates in the downward continuation will significantly slow down the downward continuation computation process, because no use of symmetry can be made anymore. In that case, for each gravity anomaly/geoid undulation to be recovered, a new inversion of the covariance matrix of accelerations has to be performed, using the algorithms described in Sections 7.2 and 8.3. Nevertheless, the results from all simulations presented in this thesis show that, even without the implementation of these more refined methods, the major part of the high-frequency gravity field can be recovered if the GPS SST measurements have a noise-level below 2 mm.

It will be shown in the next Section that only small improvements in the gravity field recovery can be realized if residual ARISTOTELES accelerations are recovered also in the South-North and West-East directions, perpendicular to the radial direction.

8.7.1.4 Extension to three directions

A few tests have been performed, where besides residual ARISTOTELES accelerations in the radial direction, also accelerations in the South-North and West-East directions were recovered. This was done to support the discussion in Section 8.4.3. The accelerations in the South-North and West-East directions were determined using the same procedure as for the radial accelerations. Thus a second-order polynomial was fitted through successive GPS SST range residuals and the second derivative represents the residual acceleration in the direction of that GPS satellite, and these accelerations were transformed geometrically to accelerations in the radial and the two other directions. Hereafter, a regular grid of accelerations at a mean satellite altitude was determined by means of least-squares collocation for each direction separately. Thus, the regular grids of radial accelerations were identical to the grids used in Section 8.7.1.2, regular grids of residual ARISTOTELES accelerations in the other two directions were simply added to the regular grid of radial accelerations. Only the method of least-squares collocation was applied in the downward continuation of these grids.

Table 8.16 shows the quality of the recovered accelerations for all three directions, the radial, longitude (West-East) and latitude (South-North), for an uncorrelated measurement noise of 0.0, 2.0 and 5.0 mm, excluding and including low-degree effects. It may be concluded that it is possible to recover residual ARISTOTELES accelerations in any direction with an accuracy of better than 1.0 mgal at 191 km altitude for a measurement noise of 2.0 mm or less on the GPS SST range measurements. For a measurement noise above 2.0 mm, the recovery of satellite accelerations deteriorates quickly. It may also be concluded that the grids of accelerations for all three directions

Table 8.16 Accuracy of recovered ARISTOTELES accelerations, for three directions, in a regular grid at a mean satellite altitude of 191 km. The accelerations in this regular grid are derived from accelerations along the ARISTOTELES orbit by means of collocation. These values are subsequently compared with the accelerations in a regular grid which are computed directly from the gravity field models. The differences from this comparison are listed in the last column. The resolution of grid is equal to 1° in latitude and longitude directions.

a) OSU86F gravity field above degree 36.

direction	noise GPS SST (mm)	noise in collocation (mgal)	precision estimate (mgal)	rms of dif. (mgal)
radial	0.0	0.5	0.20	0.22
long.	0.0	0.5	0.17	0.15
lat.	0.0	0.5	0.18	0.20
radial	2.0	4.0	1.01	0.89
long.	2.0	4.0	0.90	0.91
lat.	2.0	4.0	0.91	0.90
radial	5.0	8.0	1.57	1.63
long.	5.0	8.0	1.27	1.44
lat.	5.0	8.0	1.28	1.31

b) OSU86F minus GEM-T1 gravity fields.

direction	noise GPS SST (mm)	noise in collocation (mgal)	precision estimate (mgal)	rms of dif. (mgal)
radial	0.0	0.5	0.21	0.36
long.	0.0	0.5	0.18	0.23
lat.	0.0	0.5	0.19	0.27
radial	2.0	4.0	1.09	0.96
long.	2.0	4.0	1.02	0.96
lat.	2.0	4.0	1.03	0.92

Table 8.17 Point gravity anomaly/geoid undulation recovery from the regular grids of Table 8.16. The accelerations in all three directions were weighted equally in the least-squares collocation downward continuation.

a) OSU86F gravity field above degree 36.

noise (mm)	noise col. (mgal)	sig. mag. anomaly (mgal)	rms of dif. anomaly (mgal)	corr. ano	sig. mag. geoid (m)	rms of dif. geoid (m)	corr. geoid
0.0	0.20	14.28	8.16	0.90	1.49	0.32	0.98
2.0	0.95	9.41	12.41	0.78	1.08	0.68	0.94
5.0	1.40	5.46	14.70	0.75	0.63	1.04	0.93

b) OSU86F minus GEM-T1 gravity fields.

noise (mm)	noise col. (mgal)	sig. mag. anomaly (mgal)	rms of dif. anomaly (mgal)	corr. ano	sig. mag. geoid (m)	rms of dif. geoid (m)	corr. geoid
0.0	0.30	14.71	8.90	0.89	2.33	0.45	0.98
2.0	1.00	12.40	12.03	0.79	2.12	0.63	0.96

have approximately the same quality. Therefore, the accelerations in all three directions have been assigned equal weights in the downward continuation. The results of this downward continuation are listed in Table 8.17. Comparison with the results listed in Tables 8.15 fully supports the idea that the accelerations in the longitude and latitude directions do not contribute much extra information for the gravity anomaly/geoid undulation recovery: the improvements are less than 1.0 mgal for gravity anomalies and only a few centimeters for geoid undulations.

8.7.2 Error sources of GPS SST measurements

In the simulations performed so far, the only error source that has been accounted for is uncorrelated measurement noise on the GPS SST range measurements plus errors caused by the difference in position of the "real-world" and reference orbits. The latter represents a part of the orbit error that will be made when computing the reference orbits. The method of simulation assumes that the epoch-vector of each orbit segment is correct, but that due to errors in and truncation of the reference gravity field models applied to compute the reference orbits, orbit errors will arise. This error is on the 1-m level and was assumed to be realistic. In reality, an epoch-vector will be determined that results in a best fit of the orbit through the tracking data, using a certain reference gravity field model. Thus, in reality orbit errors due to gravity field modeling errors and epoch-vector uncertainties will arise. But these two error sources will produce orbit errors that are partly of opposite sign, so that the net effect is limited. In this study, the epoch-vector errors for each orbit segment are zero, and for a long integration period this may result in very large orbit errors, using a reference gravity field model and not adjusting the epoch-vector to obtain a best orbit compared to the "real-world" orbit. However, the orbit segments are short (of the order of a few minutes in time) and the orbit errors of approximately 1 m (rms-wise over the orbit segments) were assumed to be realistic, as stated before. Because it was assumed that carrier phase measurements are available, a measurement noise at the millimeter level was adopted.

Other significant error sources are: GPS orbit errors, ARISTOTELES orbit errors due to modeling errors of non-gravitational perturbing forces, such as drag and solar radiation, perturbations caused by solid-Earth tides and ocean tides, the effect of the ionosphere on GPS signals, linear drifts and biases of the GPS measurements, multipath, etc.

The orbit errors caused by epoch-vector uncertainties are not considered to be a severe constraint in the gravity field recovery: these errors are for the major part of a long-wavelength nature. As an example, an error of 2 m with a frequency of one cycle per revolution leads to an ARISTOTELES radial acceleration error of approximately 0.2 mgal ($w^2\Delta r$). The non-gravitational perturbing forces are expected to be measured by the accelerometers of the gradiometer. In this approach, measured accelerations are used when processing the GPS SST and gradiometer measurements. As shown in the

POPSAT/GRM-study (DGFI-TUM-TH Delft, 1987), the perturbations caused by solid-Earth and ocean tides are of a long-wavelength nature with small power. Linear drifts and biases of the GPS SST range measurements are effectively eliminated by the processing method adopted in this study, in which the second derivative of a second-order polynomial, fitted through successive range residuals, is computed.

Therefore, the major problem in the high-frequency gravity field recovery is expected to be caused by multipath and the ionosphere. The multipath effect is very dependent on the antenna configuration and with a proper configuration this effect can be limited to a few mm (private comm., European Space Technology Center, Noordwijk). A few small tests have been performed, in which the ionospheric error contribution is modeled as 5 % of the first-order ionospheric effect on the GPS SST carrier phase measurements. The first order ionospheric propagation delay was modeled by the following equation (Gurtner, 1985):

$$delay = \Delta\rho = \frac{41}{f^2\cos\phi}\left\{e_0+e_1\cos((t_{loc}-14)\pi/12)\right\} \quad (m) \tag{8.8a}$$

where,

$$\cos\phi = \sqrt{1-\sin^2\phi} \tag{8.8b}$$

$$\sin\phi = \frac{r_{st}}{a_e+h_0}\sin z \ . \tag{8.8c}$$

Equation (8.8a) is valid for 8 a.m.$<t_{loc}<$ 8 p.m., otherwise:

$$\Delta\rho = \frac{41e_0}{f^2\cos\phi} \tag{8.8d}$$

In these equations, t_{loc} is the local solar time, r_{st} is the geocentric distance of the GPS receiver, in this case equal to the radius of the ARISTOTELES satellite orbit, h_0 is the height of the ionospheric layer (350.0 km), e_0 is the total night-time electron content (10^{17} electrons/m^2), e_0+e_1 the maximum electron content at 2 p.m. ($50*10^{16}$ electrons/m^2), f the frequency of the carrier of the GPS measurements (1227.60 Hz) and z is equal to 90° minus the elevation of the GPS satellite as seen from ARISTOTELES.

The error level of 5 % holds for a situation where a two-frequency GPS receiver is on board of ARISTOTELES, and the measurements received on both frequencies are used to eliminate the first-order propagation effect. Only the method of least-squares collocation was applied in the downward continuation of the satellite accelerations to analyze the effects of this error source on the recovered gravity anomalies/geoid undulations.

The results of these tests are listed in Table 8.18. In all simulations, a 30-days ARISTOTELES orbital arc was taken into consideration. Only radial accelerations were used in the downward continuation. As can be seen from the equations (8.8a)-(8.8d), the ionospheric delay has its greatest effect on measurements when the GPS satellite is low above the ARISTOTELES horizon and the signal path through the ionosphere is relatively long. Therefore, the accuracy of accelerations in the longitude

Table 8.18 Effect of measurement noise and ionospheric propagation on the gravity field recovery (OSU86F minus GEM-T1 gravity field).

noise range measurements (mm)	percentage of first-order ion. (%)	elevation cut-off angle (deg.)	rms of dif. radial acc. (mgal)	rms of dif. recovered ano./geoid (mgal)/(m)
0.0	0	0	0.36	9.54/0.47
1.0	0	0	0.59	11.42/0.59
2.0	0	0	0.96	12.58/0.67
0.0	5	10	0.38	10.29/0.51
2.0	5	10	1.14	13.14/0.72
2.0mn	5	10	1.14	10.53/--

and latitude directions will be deteriorated more than the accuracy of radial accelerations. Thus, the effect of including the accelerations in the longitude and latitude directions on the gravity field recovery will even be more reduced. For the worst case simulation, the rms of differences between point gravity anomalies and their a priori values is equal to 13.14 mgal, compared to a power of the a priori point anomalies of 19.89 mgal (Table 8.1). For 16-point mean 1° x 1° gravity anomalies the rms of differences of the recovered anomalies with the a priori values is equal to 10.53 mgal, compared to a signal magnitude of the a priori values of 17.35 mgal. If the SST GPS measurements have a noise level of 2.0 mm, the rms of differences for geoid undulations increases from 67 cm to 72 cm, if first-order ionospheric delay errors are included, whereas the power of the a priori geoid undulations is equal to 2.36 m. Thus, still a large part of the gravity field above degree 36 may be recovered in the regional approach. As stated before, improvements can be made if GPS SST measurements during a full ARISTOTELES repeat period can be used.

8.8 Conclusions

In the downward continuation of satellite accelerations measured at an altitude of 160-200 km to gravity anomalies/geoid undulations on the Earth's surface, three parameters play an important role: the resolution of the distribution of the accelerations, their altitude above the Earth's surface and their accuracy. The simulations show that the resolution must be at least equal to the required resolution of the gravity anomalies/geoid undulations on the Earth's surface. With an altitude range of 160 to 200 km above the Earth, the accuracy of the measured satellite accelerations must be of the order of 1 mgal, if mean 1° x 1° gravity anomalies are to be recovered with an accuracy of 5 mgal and point geoid undulations with an accuracy of 0.5 m. The 200 km altitude seems to be the maximum allowable altitude, if a resolution of gravity anomalies/geoid undulations of 1° in both the longitude and latitude directions on the Earth's surface is strived for.

The simulations performed in this study demonstrate the capability of a GPS receiver on board of the ARISTOTELES satellite to recover regional information about the high-frequency gravity field (above degree 36) of the Earth. The simulations have demonstrated that through SST valuable information can be determined up to degree and order 100 of a spherical harmonic expansion of the gravity field of the Earth. Two very important parameters used in the simulations are the sampling rate of 2.5 s and a measurement noise of 0-2 mm for the GPS SST range measurements. Current ground-based GPS receivers have shown the ability to perform GPS carrier phase measurements with a 1 s sampling rate and a precision of better than 0.5 cm. If this precision can be represented by uncorrelated measurement noise with a standard deviation of 0.5 cm, it can be shown that this is equivalent to a sampling rate of 2.5 s with a noise of 3.2 mm. If future space-borne GPS receivers can achieve a comparable accuracy, the assumptions made about these parameters seem to be realistic. However, to achieve the

precision of 0.5 cm in the carrier phase measurements, a two-frequency receiver is required on board of ARISTOTELES.

Using only GPS, it seems difficult to meet the mission objectives of ARISTOTELES: a 5 mgal mean 1° x 1° gravity anomaly accuracy and a 0.10 m geoid undulation accuracy. However, this study does show the ability of a GPS receiver on board of ARISTOTELES to significantly support the gradiometer mission. In this context it is recalled that in this study only 1/3 of a repeat period of the ARISTOTELES orbit has been simulated, leading to a far from perfect coverage of the investigated geographical area. A GPS receiver can definitely contribute to the improvement of our knowledge of the low-degree part of the gravity field, and by that in higher quality ARISTOTELES orbits.

9. Global gravity field recovery error analyses from satellite-to-satellite tracking and gradiometry

9.1 Introduction

In the previous Chapters, local gravity field recovery from gradiometry and GPS SST tracking of ARISTOTELES was investigated. This Chapter describes a method to estimate the formal error of the global gravity field harmonic coefficients from data acquired on board of the Low Earth Orbiter ARISTOTELES. These data were assumed to consist of gradiometer data or precise GPS SST range measurements. It must be noted that in the local gravity field recovery, first satellite accelerations were determined from the GPS SST measurements, and these accelerations were continued downward to gravity anomalies/geoid undulations on the Earth's surface. However, in the global gravity field recovery error analyses, the GPS SST measurements were assumed to deliver precise information of the ARISTOTELES position perturbations in the radial, along-track and cross-track perturbations. These perturbations can be connected with the (global) gravity field harmonic coefficients by the linear perturbation theory, which was introduced in Chapter 2.

One of the ARISTOTELES mission goals is to solve for the gravity field with a resolution of 100 km. For a global gravity field recovery, this implies the set up of normal equations for more than 30,000 harmonic coefficients. With the expected abundance of gradiometer and GPS SST range measurements, it will be obvious that it is an immense task to compute and solve the normal equations for this number of unknown harmonic coefficients in a straightforward manner.

Therefore, various simplifying assumptions are usually introduced. The starting point in all simulations of formal error estimates was a circular reference repeat orbit. For the GPS SST range measurements, it was assumed in this study that the measurements to each GPS satellite in view of ARISTOTELES (with the full GPS configuration always at least 5 GPS satellites will be in view of the ARISTOTELES satellite) will be transformed to measurements in the satellite along-track, cross-track and radial direction (the x, y and z directions of the satellite local-horizontal, local-vertical triad). Also the gradiometer measurements were assumed to be available in this local triad. The time interval between successive measurements was taken constant during a complete repeat period.

With the preceding assumptions it can be shown that the normal matrix has a special structure (Colombo, 1984; Schrama, 1990; see also: Section 6.3 and Appendix D). Attention to this phenomenon will be paid in the first part of this Chapter, together with an investigation of the signal contents of ARISTOTELES orbit perturbations and gradiometer measurements. After this, the concept of global gravity field recovery error analyses will be described.

In addition, attention will be paid to the required specifications of the

ARISTOTELES GPS receiver in order to satisfy the mission objectives. In the first place, this GPS receiver must deliver the information for a precise orbit computation and in the second place for an accurate modeling of the gravity field for the low degrees. In the third place, a GPS receiver will be necessary to deliver the low-frequency gravity field information that will be missing in the gradiometer measurements due to the bandwidth limitation of the gradiometer instrument. As indicated before, the bandwidth limitation of the gradiometer hinders this gradiometer to observe signals with a frequency below 0.005 Hz. Thus, with gradiometer measurements alone, the low-frequency gravity field can not be determined. Therefore, gravity field recovery error analyses were performed for several combinations of ARISTOTELES orbit perturbations (derived from the GPS SST range measurements) and gradiometer measurements. The effect of the gradiometer bandwidth limitation was included in the investigations.

In the analyses described in this Chapter, it was assumed that the ARISTOTELES satellite will fly in a polar orbit at about 200 km altitude. However, in reality, this altitude will be slightly non-polar (the inclination will be 96.3°, (CIGAR, 1989)). In that case, no ARISTOTELES measurements will be available for the polar caps. To analyze the effect of a non-polar ARISTOTELES orbit, also a few gravity field recovery error analyses were performed, in which the inclination of the ARISTOTELES orbit was unequal to 90°.

9.2 Modeling of the ARISTOTELES measurements

If the gravity field potential is described by a spherical harmonic expansion, the unknown part of the gravity field potential may be expressed by equation (1.8). From this equation, any other gravity field induced signal along a near-circular satellite orbit, in this Chapter the gravity tensor $\Delta\Gamma_{ij}$ or orbit perturbations Δr_i, can be derived, where the indices i and j denote the radial, along-track or cross-track direction. In order to find these relations, equation (1.8) can be transformed into an equation using orbital elements (equation (2.2a)). The chosen ARISTOTELES orbit is a circular repeat orbit, i.e. the eccentricity e is equal to zero. For such an orbit, the combination of the equations (2.2a)-(2.2c) and (2.4a)-(2.4c), and the fact that the functions G_{lpq} are of order $O(e^{|q|})$, yields:

$$T = \sum_{l=2}^{\infty}\sum_{m=0}^{l}\sum_{p=0}^{l}\sum_{q=-\infty}^{\infty}\frac{\mu a_e^{\,l}}{r^{l+1}}F_{lmp}G_{lpq}S_{lmpq}(\omega,M,\Omega,\theta) =$$

$$\frac{\mu}{a_e}\sum_{l=2}^{nmax}\left[\frac{a_e}{r}\right]^{l+1}\sum_{m=0}^{l}\sum_{p=0}^{l}F_{lmp}S_{lmp}(\omega+M,\Omega-\theta) \qquad (9.1a)$$

where

$$S_{lmp}(\omega+M,\Omega-\theta) = \begin{bmatrix} \Delta\bar{C}_{lm} \\ -\Delta\bar{S}_{lm} \end{bmatrix} \begin{matrix} l-m \text{ even} \\ l-m \text{ odd} \end{matrix} \cos((l-2p)(\omega+M)+m(\Omega-\theta)) +$$

$$\begin{bmatrix} \Delta\bar{S}_{lm} \\ \Delta\bar{C}_{lm} \end{bmatrix} \begin{matrix} l-m \text{ even} \\ l-m \text{ odd} \end{matrix} \sin((l-2p)(\omega+M)+m(\Omega-\theta)) \; . \qquad (9.1b)$$

In the following two parts of this Section linear relations will be discussed that connect the unknown gravity field harmonic coefficients with the orbit perturbations or the gradiometer measurements. In the last part of this Section, the structure of the normal matrix is discussed that is obtained if gravity field harmonic coefficients are estimated from a global set of gradiometer and orbit perturbations, which are derived from GPS SST range measurements.

9.2.1 Orbit perturbations

The Hill equations describe the linearized equations of motion along a circular reference orbit (Dunning, 1973). If T (equations (9.1a)-(9.1b)) is used as the disturbing potential, the equations are the ones already derived in Chapter 2, i.e. the equations (2.6a)-(2.6c). These equations establish the relation between the disturbing potential T and the orbit perturbations in the radial, along-track and cross-track directions. These perturbations were assumed to be recovered with great precision from the GPS-measurements. Use will be made of the characteristic that for an exact repeat orbit, these equations become true Fourier series (Colombo, 1984).

9.2.2 Gradiometer measurements

In this Section, the linear relations connecting the unknown $\bar{C}_{lm}$, $\bar{S}_{lm}$ and the gravity tensor components Γ_{ij} are established for a circular reference orbit. Because it is expected that no precise gradiometer measurements with a component in the along-track (the so-called less-sensitive axis) direction are obtained, because this is the direction of the relatively large and fluctuating drag, only relations have to be established for Γ_{zz}, Γ_{zy} and Γ_{yy}. In (Schrama, 1990; Rummel, 1990) the following relations were derived:

$$\Gamma_{zz} = \frac{\partial^2 T}{\partial r^2} \qquad (9.2a)$$

$$\Gamma_{zy} = \frac{\cos(\omega+M)}{\sin i}\left[-\frac{1}{r}\frac{\partial^2 T}{\partial r \partial \Omega}+\frac{1}{r^2}\frac{\partial T}{\partial \Omega}+\right.$$

$$\cos i\left\{\frac{1}{r}\frac{\partial^2 T}{\partial r\,\partial(\omega+M)}-\frac{1}{r^2}\frac{\partial T}{\partial(\omega+M)}\right\}\Bigg] + \sin(\omega+M)\left[\frac{1}{r}\frac{\partial^2 T}{\partial r\,\partial i}-\frac{1}{r^2}\frac{\partial T}{\partial i}\right] \qquad (9.2b)$$

$$\Gamma_{yy} = -\frac{\partial^2 T}{\partial r^2} - \frac{1}{r^2}\frac{\partial^2 T}{\partial(\omega+M)^2} - \frac{1}{r}\frac{\partial T}{\partial r} \qquad (9.2c)$$

Combining the equations (9.1a)-(9.1b) and (9.2a)-(9.2c) yields:

$$\Gamma_{zz} = \frac{\mu}{a_e}\frac{(l+1)(l+2)}{a^2}\left[\frac{a_e}{a}\right]^{l+1} F_{lmp} S_{lmp} \qquad (9.3a)$$

$$\Gamma_{zy,lmp} = -\frac{\mu}{a_e}\frac{(l+2)}{2a^2}\left[\frac{a_e}{a}\right]^{l+1}\left\{\left[\frac{(m-(l-2p)\cos i)F_{lmp}}{\sin i} - F'_{lmp}\right]S^*_{(l+1)mp} + \left[\frac{(m-(l-2p)\cos i)F_{lmp}}{\sin i} + F'_{lmp}\right]S^*_{(l-1)mp}\right\} \qquad (9.3b)$$

$$\Gamma_{yy,lmp} = \frac{\mu}{a_e}\frac{1}{a^2}\left[\frac{a_e}{a}\right]^{l+1} F_{lmp}\left[(l-2p)^2 - (l+1)^2\right]S_{lmp} \qquad (9.3c)$$

where

$$S^*_{lmp}(\omega+M,\Omega-\theta) = \begin{bmatrix}\Delta\bar{C}_{lm}\\ -\Delta\bar{S}_{lm}\end{bmatrix}\begin{matrix}l-m\ even\\ l-m\ odd\end{matrix} \sin((l-2p)(\omega+M)+m(\Omega-\theta)) - \begin{bmatrix}\Delta\bar{S}_{lm}\\ \Delta\bar{C}_{lm}\end{bmatrix}\begin{matrix}l-m\ even\\ l-m\ odd\end{matrix} \cos((l-2p)(\omega+M)+m(\Omega-\theta)) \; . \qquad (9.3d)$$

In addition to the equations (2.6a)-(2.6c) for the orbit perturbations, also the equations (9.3a)-(9.3c) become true Fourier series for an exact repeat orbit.

9.2.3 Structure of the normal matrix

It has been stated that for a circular repeat orbit, the linear relations connecting the unknown harmonic coefficients with the gradiometer and GPS observations (or orbit perturbations) can be represented by Fourier series. If many observations are made during a complete repeat period and a constant sampling-rate is applied, it can be shown that the normal matrix becomes block-diagonal if organized per order (Colombo, 1984; Schrama, 1990; Rummel, 1990; see also: Appendix D). The measurements behave as true Fourier series, and for different orders m of the gravity field coefficients, the frequencies of the orbit perturbations or gradiometer signal caused by

such coefficients become decorrelated (provided a perfect coverage). The greatest dimension of these blocks is equal to approximately half the maximum degree of the gravity field harmonic expansion that is to be determined (Appendix D). The inversion of the total normal matrix transforms to an inversion of block-matrices with dimensions much smaller than the total number of unknowns for harmonic expansions up to high degree and order. This prevents very costly computer runs and, in addition, only a small part of the total normal matrix (only the blocks on the diagonal) has to be stored.

9.3 Orbit perturbations and tensor signal

A quantitative analysis was performed showing the information content of orbit perturbations in the satellite orbit frame (radial, along-track and cross-track directions) and of the gradiometric signal along the circular reference repeat orbit. Use was made of the equations (9.3a)-(9.3d) and (2.6a)-(2.6c), giving the relations between orbit perturbations and gradiometer components and a certain gravity field harmonic coefficient.

The OSU86F gravity field model truncated at degree 180 was used to compute the Fourier series of the orbit perturbations and of the gradiometric signal along the satellite orbit. The cut-off at degree 180 is justified by considering the resolution of 100 km of the gravity field strived for with the ARISTOTELES mission.

The effect of the gradiometer bandwidth, i.e. certain frequencies are not observable, on the signal content was also investigated. The ARISTOTELES satellite was assumed to be in a 200 km altitude polar orbit (i = 90°). The repeat period was taken equal to 91 days, in which the satellite completes 1479 revolutions.

9.3.1 Orbit perturbations

The frequency spectrum of the orbit perturbations as described by the linear perturbation theory (LPT) was computed using the OSU86F gravity field model from degree 37 to 180. The part of the OSU86F gravity field below degree 37 was neglected, because it has been shown extensively in other studies that the GPS measurements acquired on board of ARISTOTELES can be used to solve this part of the gravity field to great precision (Smith et al., 1988; Wu and Yunk, 1986a and 1986b; Colombo, 1990). Attention to low-degree gravity field recovery from orbit perturbations will be paid in Section 9.4.1. Another important question that will be addressed is whether it is possible to recover the gravity field for degrees above degree 36 from GPS SST measurements to ARISTOTELES.

In the Figures 9.1-9.3, the frequency spectra of the orbit perturbations for this part of the gravity field are displayed. The rss of the amplitudes of these spectra are listed

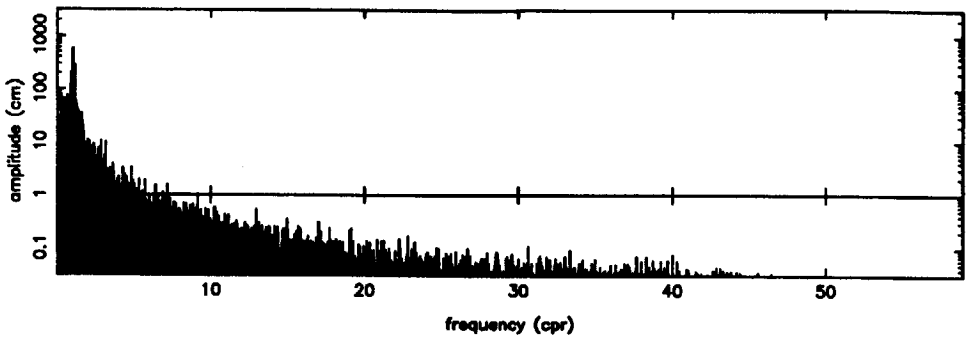

Figure 9.1 Spectrum of ARISTOTELES radial orbit perturbations using the OSU86F model from degree 37 to 180

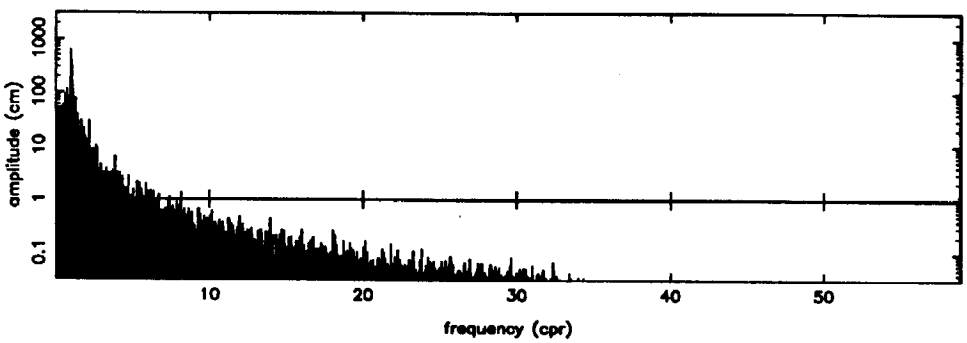

Figure 9.2 Spectrum of ARISTOTELES cross-track orbit perturbations using the OSU86F model from degree 37 to 180

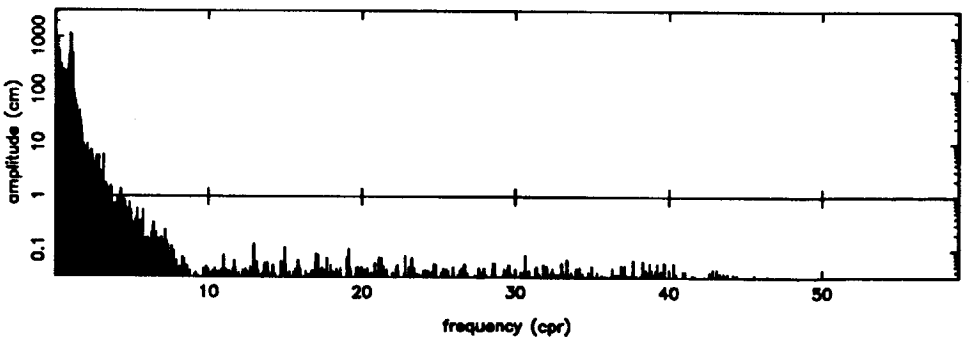

Figure 9.3 Spectrum of ARISTOTELES along-track orbit perturbations using the OSU86F model from degree 37 to 180

in Table 9.1. The rss-value for the cross-track perturbations is 12.16 m compared to 14.28 m and 778.07 m for the radial and along-track perturbations. The high value for the along-track perturbations is caused by very high peaks close to 0 cpr, with amplitudes up to 766.42 m. As can be seen in the Figures 9.1-9.3, the frequency spectrum of the radial orbit perturbations is more spread over the higher frequencies compared to the frequency spectra of the along-track and cross-track perturbations. Above about 30 cpr, the amplitudes of the cross-track perturbations (Figure 9.2) are smaller than those of the radial perturbations (Figure 9.1), and amplitudes of the along-track perturbations drop very quickly for frequencies above 10 cpr (Figure 9.3). Therefore, it is expected that if a gravity field is recovered from radial orbit perturbations, the errors of this recovered gravity field, especially of the high-degree part, will be smaller than the errors of gravity fields that have to be recovered from either along-track or cross-track perturbations.

9.3.2 Gradiometer measurements

The Fourier series for Γ_{zz}, Γ_{zy} and Γ_{yy} were computed using the OSU86F gravity field model to degree and order 180. The frequency spectra are displayed in the Figures 9.4-9.6. Studying these Figures, it is directly obvious that, compared to orbit perturbations, the larger part of the power of the gradiometric signal can be found at higher orbital frequencies (note that the vertical scale of the Figures 9.1-9.3 is logarithmic and of the Figures 9.4-9.6 linear). This concentration at the higher frequencies becomes even more pronounced if, as in the computation of the frequency spectra of the ARISTOTELES orbit perturbations, only the part of the OSU86F gravity field above degree 36 is used in the computation of the gradiometer frequency spectra. Thus, the gradiometric signal is expected to deliver more information about the high-degree terms of the gravity field than the orbit perturbations of the ARISTOTELES satellite. Comparing the Figures 9.4-9.6, it can be seen that the amplitudes of the gradiometer component Γ_{zz} are higher than those of the other displayed in these Figures. In reality, the gradiometer can not observe signals with a frequency below about 27 cpr due to the limited gradiometer bandwidth (0.005-5 Hz). Because gravity field terms with a degree below 28 almost only cause gradiometer signals with a frequency below 28 cpr (equations (9.3a)-(9.3d) and (2.2d)), the part of the gravity field below degree 28 is unobservable using the gradiometer measurements. To study the effect of the limited gradiometer bandwidth, the rss of the amplitudes of the frequency spectrum was computed both for excluding and including the part of the OSU86F gravity field model below degree 28. However, not only the part of the gravity field below degree 28 is unobservable, also a part of the gravity field above degree 28 is unobservable, because gravity field terms with a degree above 28 also produce gradiometer signals with a frequency below 27 cpr. This effect was studied by applying a frequency cut-off equal to 27 cpr, i.e. in the computation of the rss-values of the amplitudes of the gradiometer spectra, those amplitudes that belong to a frequency below 27 cpr were

Table 9.1 Frequency analysis of ARISTOTELES orbit perturbations using OSU86F from degree 37 to 180.

	radial (cm)	along-track (m)	cross-track (m)
rss	14.28	778.07	12.16

Table 9.2 Frequency analysis of gravity tensor components measured at the ARISTOTELES altitude.

OSU86F from degree 1 to 180

	cof (cpr)	Γ_{zz} (EU)	Γ_{zy} (EU)	Γ_{yy} (EU)
rss	0.0	0.40	0.28	0.24
rss	27.0	0.21	0.11	0.08

OSU86F from degree 28 to 180

	cof (cpr)	Γ_{zz} (EU)	Γ_{zy} (EU)	Γ_{yy} (EU)
rss	0.0	0.27	0.20	0.17
rss	27.0	0.21	0.11	0.08

cof = frequency cut-off.

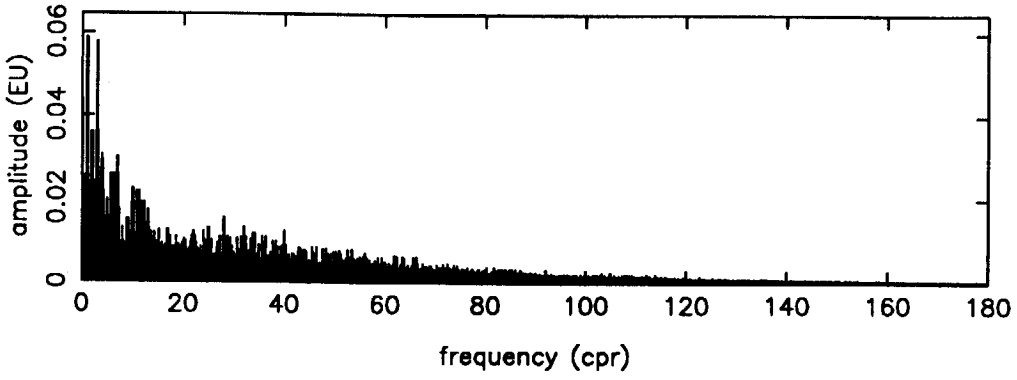

Figure 9.4 Spectrum of the Γzz gradiometer component for the ARISTOTELES satellite using the OSU86f model complete to degree and order 180

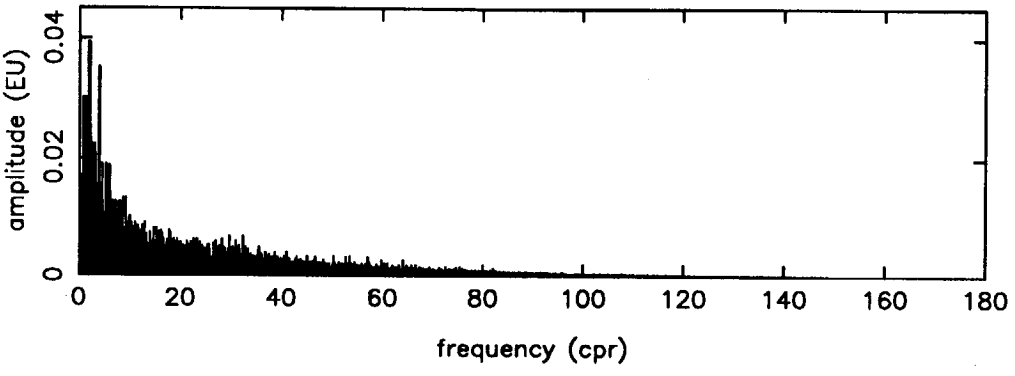

Figure 9.5 Spectrum of the Γzy gradiometer component for the ARISTOTELES satellite using the OSU86f model complete to degree and order 180

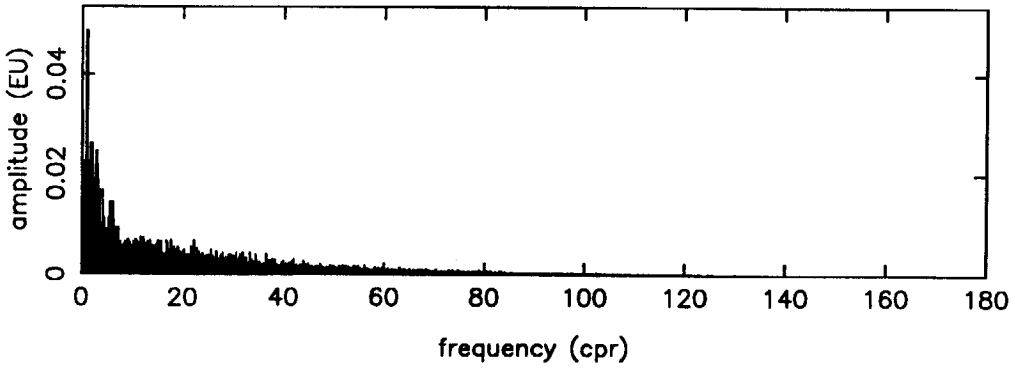

Figure 9.6 Spectrum of the Γyy gradiometer component for the ARISTOTELES satellite using the OSU86f model complete to degree and order 180

not included.

For example, sectorial coefficients almost only cause a gradiometric signal in the very low frequency band (at least below 27 cpr) for a polar orbit. Figure 9.7 supports this conclusion. In this Figure the average ratio of the gradiometric signal above 27 cpr and the complete signal caused by harmonic coefficients is displayed as a function of the degree minus order (*l-m*). It is concluded that for coefficients close to the sectorial band the largest part of the gradiometric signal content is below 27 cpr.

The rss-values for the several cases are listed in Table 9.2. The exclusion of the gravity field part below degree 28 reduces the rss-values by about 30 %, if the cut-off frequency is not applied. For example, the rss-value for Γ_{zz} reduces from 0.40 EU to 0.27 EU. If also the frequency cut-off is applied, the rss-values drop an extra 30 to 50 %, from 0.27 EU to 0.21 EU for Γ_{zz}, from 0.20 EU to 0.11 EU for Γ_{zy}, and from 0.17 EU to 0.08 EU for Γ_{yy}. If the frequency cut-off is applied, the rss-values of the case where the part of the gravity field below degree 28 is included are equal to the rss-values where this part of the gravity field is excluded. This is in agreement with the assumption that the gravity field part below degree 28 almost does not produce signals with a frequency above 27 cpr. Therefore, it is concluded that the GPS SST range measurements will be necessary to improve our knowledge of the low-degree gravity field and to deliver the low-frequency information of the higher degree, especially sectorial, gravity field terms.

9.4 Global gravity field recovery error analyses

In this Section, results of global gravity field recovery error analyses will be discussed. In the first part of this Section, attention will be paid to gravity field recovery error analyses from orbit perturbations which are assumed to be determined from GPS SST range measurements. In the analyses described in the second part, gradiometer measurements were the input of the gravity field recovery error analyses and the effect of the gradiometer bandwidth limitation will be studied. It will be shown that this limitation will prevent a stable gravity field solution. In addition, the orbit inclination will be varied. In the last part, recovery experiments from combinations of orbit perturbations and gradiometer measurements are described. It will be shown that the latter combination is a very powerful concept that seems capable of solving bandwidth-related problems.

In the simulations, it was assumed that the ARISTOTELES satellite was in a circular orbit at 200 km altitude and a nominal inclination equal to 90°, unless if another value for the inclination is specified. As indicated before, this orbit has a repeat period of 91 days, in which the satellite completes 1479 orbital revolutions. It was assumed that one complete repeat period of observations will be available.

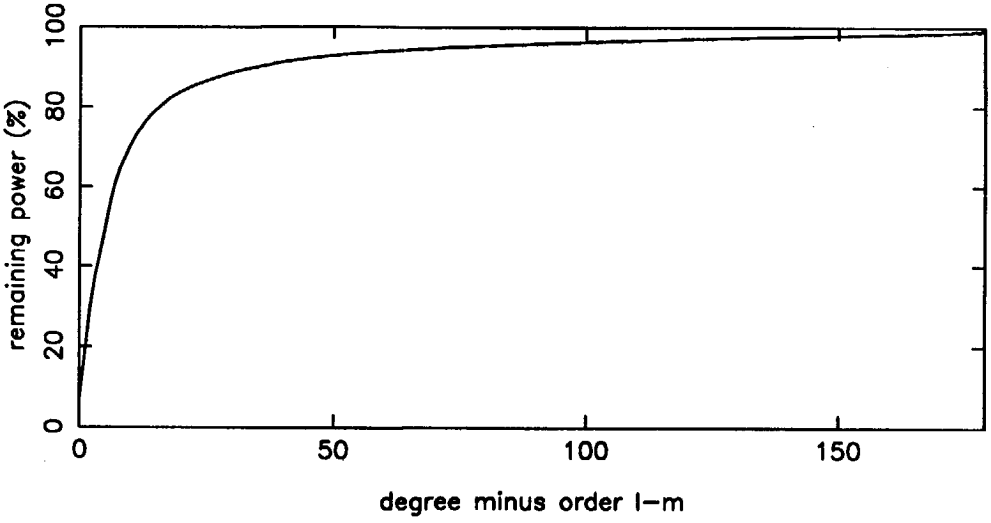

Figure 9.7 Effect of gradiometer bandwidth on the power of the Γzz gradiometer term, per harmonic coefficient

9.4.1 Orbit perturbations

In the first place, the question is addressed whether it is possible to determine high-accuracy low-degree gravity field models from GPS SST range measurements. Four cases will be investigated. These four cases show the effect of the accuracy of recovered orbit perturbations and the addition of a priori information on the gravity field recovery. The accuracy of the recovered orbit perturbations will depend on the availability of the several GPS SST measurement types. For example the precision of C/A-code measurements is on the order of 5-10 m (Ambrosius et al., 1990). However, if also P-code measurements will be available to the scientific community, this community will have GPS SST measurements with a precision on the order of 1 m. The precision of carrier phase measurements may be on the millimeter-level (see also: Section 7.1).

Case 1. It was assumed that future GPS receivers can deliver P-code/CA-code measurements from which it is possible to determine the ARISTOTELES orbit with an accuracy of 3 m in both the radial, along-track and cross-track directions. It was assumed that this accuracy-level holds for all state-vectors which are separated each 60 s during a complete repeat period. From this data set of orbit perturbations, a gravity field model complete to degree and order 36 is to be recovered. For this configuration, the rms of the formal harmonic coefficient error estimates per degree are displayed in Figure 9.8. Studying this Figure, it is obvious that an accuracy of 3 m for the orbit perturbations is not sufficient to determine a high-accuracy low-degree gravity field model if no additional information is available. Already for degrees above 20, the estimated errors of the gravity field harmonic coefficients become greater than their magnitude as predicted by Kaula's rule of thumb (equation (1.3)).

Case 2. To show the current status of gravity field modeling, the normal equations were used that led to the GEM-T2 gravity field model (Marsh et al., 1989a). This is the inverse of the calibrated GEM-T2 covariance matrix that was also used in computations of Chapter 6. The part of this matrix that holds for the gravity field complete to degree and order 36 was used to compute the formal error estimates of the gravity field harmonic coefficients. As shown in Figure 9.8, these error estimates are well below the error estimates of case 1.

Case 3. The question now arises whether the data set of case 1 can improve the current status of gravity field modeling. To give an answer to this question, this data set was added to the GEM-T2 normal matrix and new error estimates for the gravity field harmonic coefficients were computed. These error estimates are only a little bit smaller than those of case 2, i.e. with an accuracy of 3 m of the ARISTOTELES orbit perturbations the accuracy of current gravity field models can not be improved dramatically. With C/A-code measurements it will be difficult to determine an ARISTOTELES orbit with a precision of 3 m, and therefore the availability of P-code measurements is highly desirable.

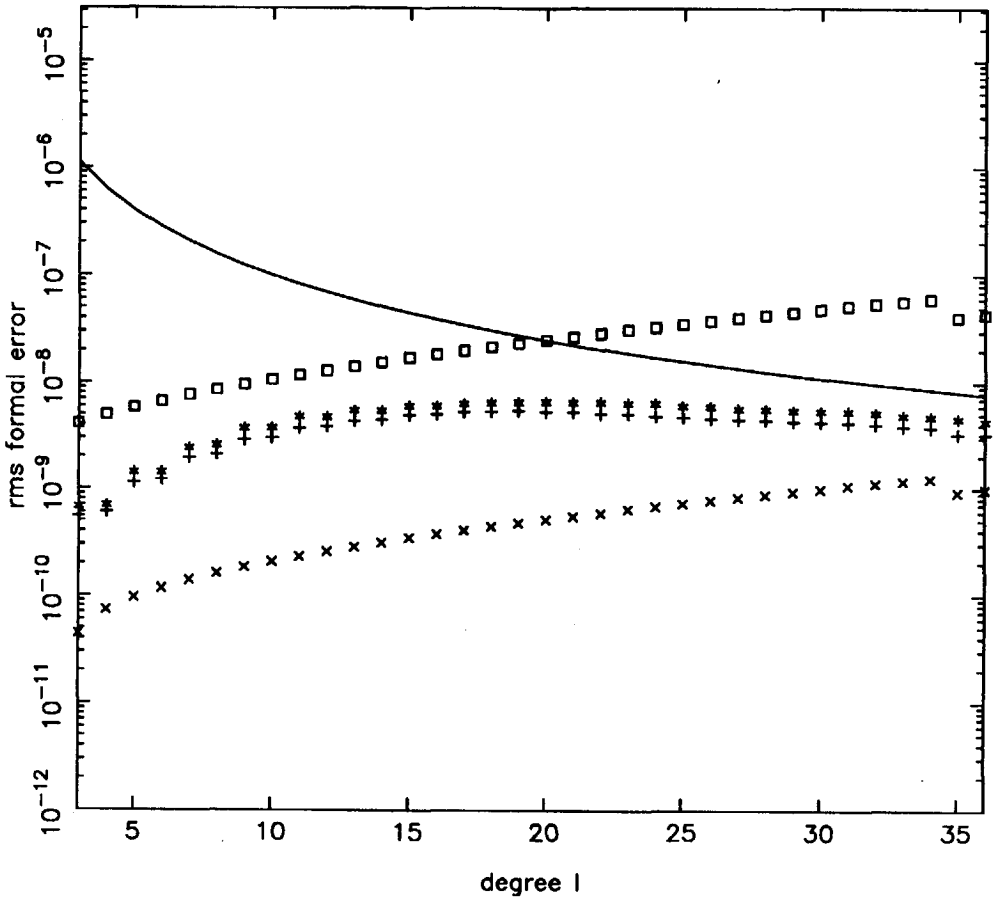

□ case 1: only ARISTOTELES GPS SST observations with 3 m accuracy and 1 min measurement interval

* case 2: error estimates from GEM–T2 normal normal matrix to degree and order 36

\+ case 3: the cases 1 and 2 in a combined solution

× case 4: only ARISTOTELES GPS SST observations with 10 cm accuracy and 1 min measurement interval

solid line: Kaula's rule of thumb

Figure 9.8 RMS of formal errors of low–degree harmonic coefficients

Case 4. The state of the art in gravity field modeling can improve dramatically if also accurate carrier phase measurements will be available that can deliver information from which it is possible to compute ARISTOTELES orbit perturbations with an accuracy of 10 cm, with intervals of 1 min (this accuracy and time interval is anticipated for the TOPEX/Poseidon mission, (Wu and Yunk, 1986a)). With only such a data set of 10-cm accurate ARISTOTELES orbit perturbations (i.e. no a priori information), the accuracy of current gravity field models can be improved by an order of magnitude (Figure 9.8). It is therefore concluded that if the entire spectrum of GPS SST measurements will be available, current low-degree gravity field models can be improved significantly.

The question that arises now is whether it is possible to recover a gravity field model for degrees above 36 if really accurate GPS SST range measurements become available, for example carrier phase measurements with an accuracy of 1 cm. For that purpose, gravity field recovery error analyses were performed in which it was assumed that a gravity field model complete from degree 3 to degree and order 180 has to be recovered. In these analyses, it was assumed that it will be possible to determine ARISTOTELES orbit perturbations with an accuracy of 1 cm and with a state-vector interval of 1 s. Comparable values were used in (Colombo, 1990; Schrama, 1990). It was also assumed that high-accuracy orbit perturbations with a frequency below 2 cpr will not be observable because of the basic low-frequency orbit errors. This was implemented by assigning zero weight to orbit perturbations with a frequency below 2 cpr. These major orbit errors are known to be for the greater part of a low frequency nature (Chapter 3).

Formal error estimates of gravity field harmonic coefficients were computed using orbit perturbations in the radial, along-track and cross-track directions separately, or all together. Of course, the smallest error estimates are expected to be made if orbit perturbations in all three directions are combined. The result of the computations is displayed in Figure 9.9. The decreasing line denotes the spectrum of the gravity field as predicted by Kaula's rule of thumb (equation (1.3)). The other four lines denote, from above to below, the formal error estimates using only cross-track, along-track or radial perturbations, or perturbations in all three directions in a combined solution. As predicted in Section 9.3.1, indeed the error estimates are smaller for the case where radial perturbations are used separately, compared to the cases where along-track or cross-track perturbations are used separately. As indicated before, the combined solution will be the best one, but for higher degrees the results are close to the solution using only the radial or along-track perturbations. For the combined solution, it seems possible to obtain significant harmonic coefficient values for degrees up to 120, if the previously described conditions are fulfilled.

The results displayed in Figure 9.9 hold for a measurement interval of 1 s and an accuracy of the orbit perturbations equal to 1 cm. However, it may be interesting to know how the error estimates change if these parameters are varied. It can be shown that the following relation exists between the error estimates of the gravity field harmonic coefficients $\bar{C}_{lm}$, $\bar{S}_{lm}$ and the sampling-rate and accuracy of the orbit perturbations:

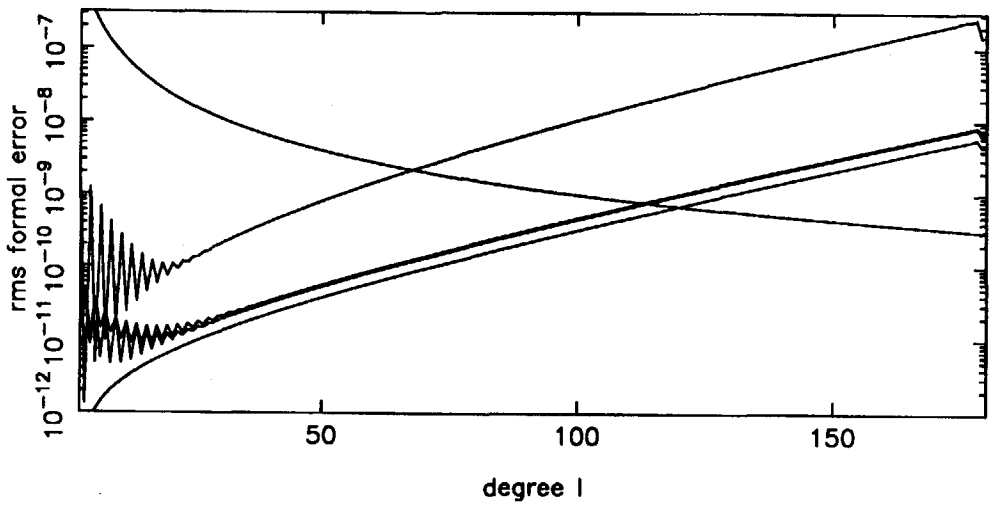

Figure 9.9 Propagated error spectrum with σ=1 cm and Δt=1 s of a gravity field recovery error analysis from ARISTOTELES orbit perturbations in the cross-track, along-track, radial and all three directions (from above to below). The decreasing line denotes the spectrum predicted by Kaula's rule of thumb. The orbit inclination is 90° (polar orbit)

$$\frac{\sigma^2(orbit)\Delta t}{\sigma^2(\bar{C}_{lm},\bar{S}_{lm})} = \text{constant} \qquad (9.4)$$

where $\sigma(orbit)$ is the orbit accuracy, Δt the measurement interval, and $\sigma(\bar{C}_{lm}, \bar{S}_{lm})$ the formal error estimate for the gravity field harmonic coefficients. Gravity field error analyses were performed for several values of $\sigma^2\Delta t$ and the results are displayed in Figure 9.10. For example, if the orbit accuracy is 100 cm and the measurement interval 100 s ($\sigma^2\Delta t = 10^6$ cm^{2}s), the most upper line intersects the line of Kaula's rule of thumb at a degree equal to about 30. The lowest line is valid for $\sigma^2\Delta t = 1$ cm^{2}s. This line is identical to the lowest line of Figure 9.9.

9.4.2 Gradiometer measurements

Gravity field error analyses from gradiometer measurements for models complete to degree and order 180 were performed. In the simulations related to the gradiometer measurements, it was assumed first that frequencies below 2 cpr are not observable, just as in the experiments of the Section 9.4.1. Gravity field recovery from gradiometer measurements will also be corrupted by orbit errors. For example, if an orbit error Δr (m) in the radial direction is made, the interaction of this error with the central term of the Earth's gravity field leads to a gradiometer Γ_{zz}-error equal to (compare with equation (8.7)):

$$\Delta\Gamma_{zz} = \frac{6\mu}{r^4}\Delta r \sim 10^{-3}\Delta r \ (\text{EU}) . \qquad (9.5)$$

For a 0.01 EU measurement accuracy, the consequence of equation (9.5) is that the orbit must be reconstituted with an accuracy of 10 m, which is much above the 3 m (Section 8.5.2) accuracy constraint necessary to fully exploit the GPS-carrier phase information content.

With a measurement noise of 0.01 EU and a measurement interval of 4 s the simulations led to results as displayed in Figure 9.11. The monotonously decreasing line again shows the spectrum of the gravity field as predicted by Kaula. The other four lines denote, from above to below, the formal error estimates using respectively Γ_{yy}, Γ_{zy}, Γ_{zz} and these three components in a combined solution. The fluctuations at the low degrees are caused by the frequency truncation at 2 cpr. This truncation causes an ill-conditioning of the normal matrix, especially for coefficients close to the sectorial band. As expected, the use of Γ_{zz} yields the lowest formal error estimates compared to the use of Γ_{zy} or Γ_{yy}. The solution in which all the three gradiometer components are combined led, of course, to the smallest error estimates. It can be concluded that with this simulation set-up the gravity field can be solved to at least degree 180.

Additional simulations (with a frequency cut-off of 2 cpr) were performed for inclinations of 92°, 93° and 94°. For inclinations of 92° and 93°, the formal error estimates are almost identical to the formal error estimates for an inclination of 90°, with the exception of formal error estimates in the "saw-tooth" area. The saw-tooth pattern has

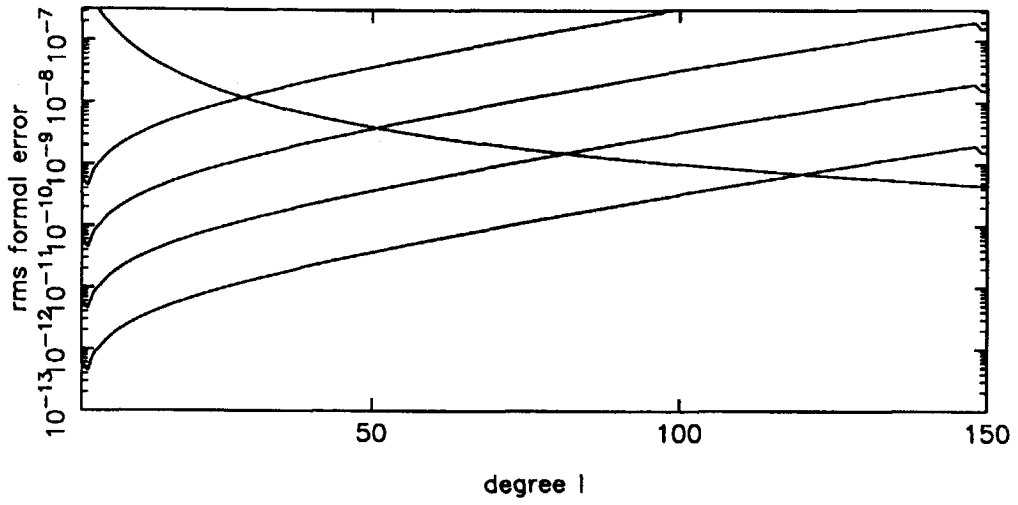

Figure 9.10. Propagated error spectrum of gravity field recovery error analysis from ARISTOTELES orbit (i=90°) perturbations in all three directions. The decreasing line denotes the spectrum predicted by Kaula's rule of thumb. The other four lines hold, from below to above, for $\sigma^2\Delta t$ equal to respectively 1, 10^2, 10^4 and 10^6 cm^2s

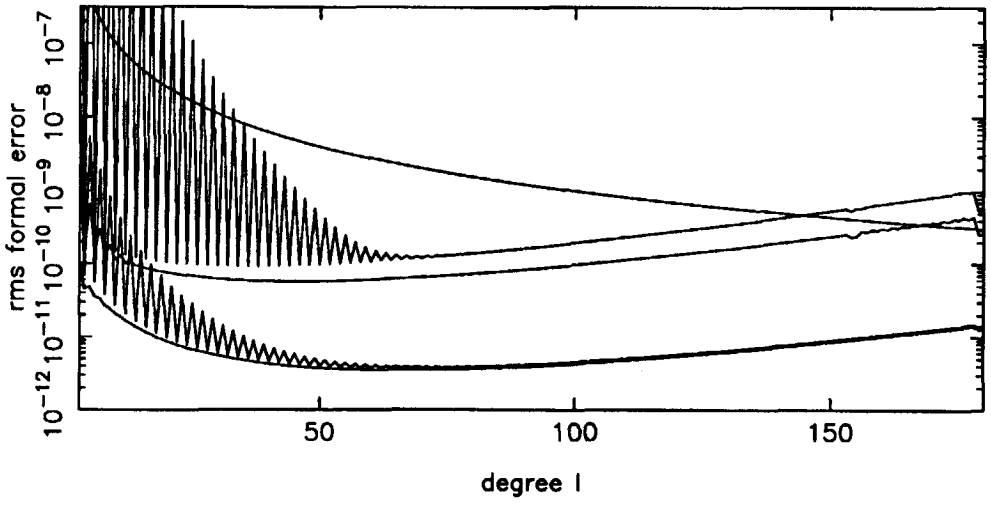

Figure 9.11 Propagated error spectrum with σ=0.01 EU and Δt=4 s of a gravity field recovery analysis from the ARISTOTELES gradiometer components Γyy, Γzy, Γzz and from all these three components (from above to below). The decreasing line denotes the spectrum predicted by Kaula's rule of thumb. The orbit inclination is 90° (polar orbit)

almost disappeared (Figures 9.12 and 9.13). This is caused by the better sampling of fluctuations caused by coefficients close to the sectorial band for the low degrees, which results in a better conditioning of the normal equations. This also leads to smaller fluctuations in the rms error spectrum for the low degrees. For an inclination of 94°, the normal equations blew up and no significant results were obtained. This may be explained by the fact that it is tried to solve for harmonic coefficients up to degree 180, i.e. a resolution of 1°, whereas a polar cap of 4° is not covered by the ground track of the ARISTOTELES orbit. Although in reality the ARISTOTELES satellite will be in an orbit with an inclination of approximately 96°, the problem of an instable normal matrix may and will be overcome by including additional information in the normal equations. For example, the spectrum of the magnitude of gravity field coefficients as a function of the degree l as predicted by Kaula's rule of thumb (equation (1.3)) may be added (regularization, (Schrama, 1990)), or separate observations over the polar cap or even simulated polar observations with a value equal to zero may be added to the normal equations. In these cases, the gravity field model obtained will be accurate over the entire globe covered by ARISTOTELES orbits, but with a deterioration of the accuracy over the polar caps.

As indicated before, gradiometer signals with a frequency below 27 cpr will be unobservable. If a frequency cut-off of 27 cpr was applied, the normal equations, in this case for a gravity field from degree 37 to 180, blew up and no significant error estimates were obtained. This result indicates that even with the normal matrix of a high-accuracy gravity field model complete to degree and order 36 added to the normal matrix of the gradiometer measurements, the bandwidth-limitation related problems can not be solved. In the next Section, attention will be paid to the question whether the addition of normal equations computed from precise ARISTOTELES orbit perturbations can help to solve this problem.

9.4.3 Combination of orbit perturbations and gradiometer measurements

As stated in the previous Section, problems arise in the gravity field recovery from gradiometer measurements, if frequencies below 27 cpr are not observable. The addition of normal equations computed from precise orbit perturbations might help to overcome these problems. To investigate this, first a simulation was performed in which the normal equations, computed from orbit perturbations in all three directions with a 1 cm accuracy and 1 s measurement interval (i.e. the configuration that led to Figure 9.9) were added to the normal equations from the gradiometer measurements (all three components) with a frequency truncation at 27 cpr. This led to a stable solution and a highly-accurate gravity field model can be determined (lowest line in Figure 9.14). Also cases in which the accuracy of the orbit perturbations is equal to 10 cm (second line from below in Figure 9.14) and equal to 3 m (third line from below in Figure 9.14) with measurement intervals equal to 60 s were included in the investigations. In the latter two cases it was assumed that also the orbit perturbations below 2 cpr could

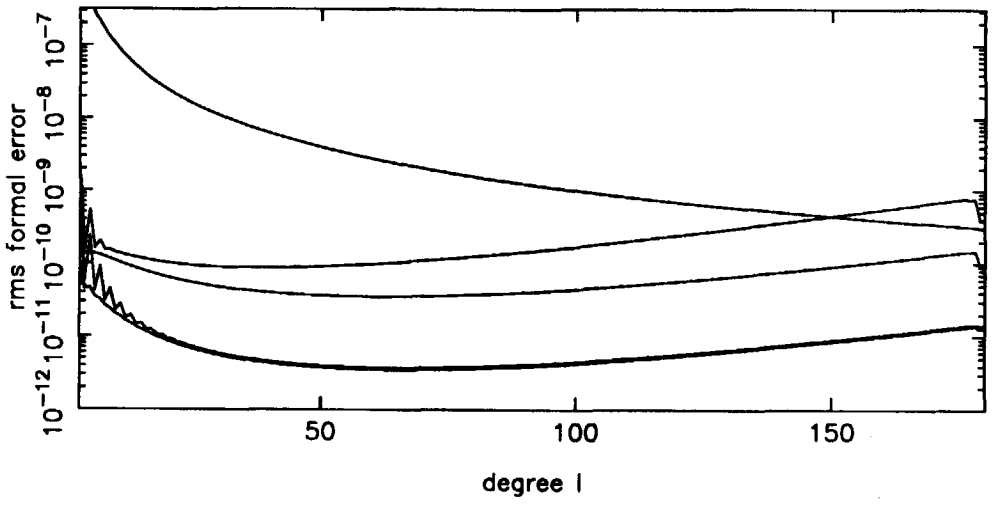

Figure 9.12 Propagated error spectrum from gradiometer measurements if the orbit inclination is equal to 92° (compare with Figure 9.11)

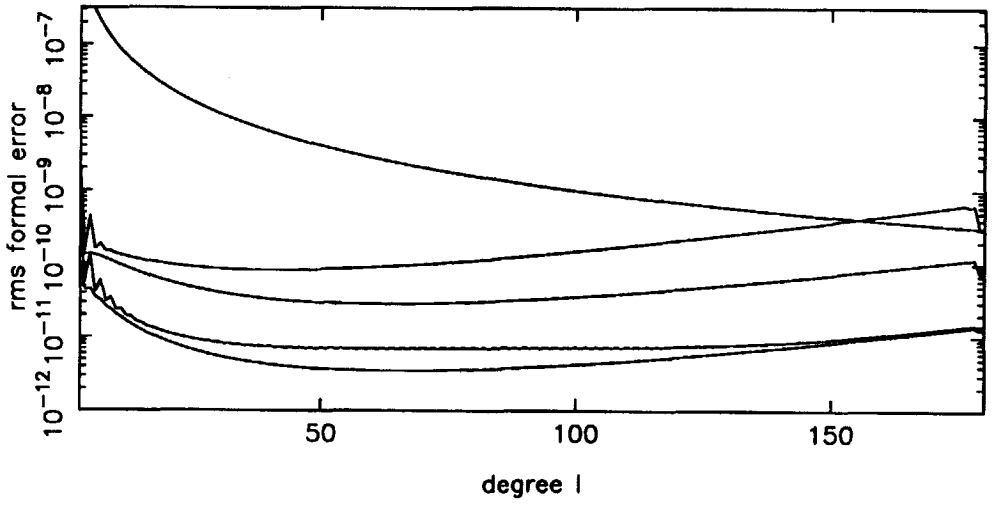

Figure 9.13 Propagated error spectrum from gradiometer measurements if the orbit inclination is equal to 93° (compare with Figure 9.11)

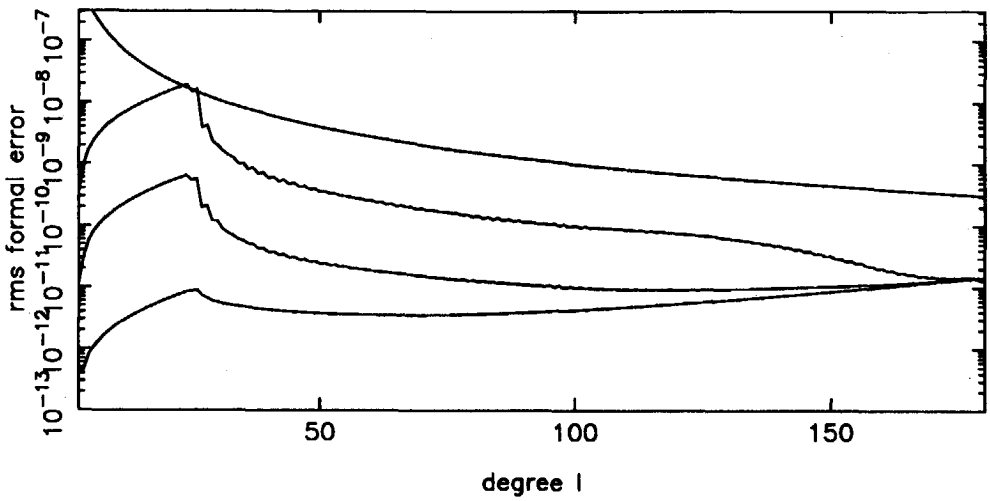

Figure 9.14 Propagated error spectrum of gravity field recovery from the combination of all three gradiometer components and all three directions of orbit perturbations for three cases. In all cases $\sigma(\Gamma ij)$=0.01 EU, Δt=4 s and all frequencies below 27 cpr were assumed to be unobservable. From above to below, the σ(orbit) is respectively 3 m, 10 cm and 1 cm and the Δt 60 s, 60 s and 1 s.

be determined with this accuracy. For the higher degrees, all the three solutions converge to each other, and the gradiometer signal contents determines the quality of the solution. However, for the lower degrees great differences in gravity field accuracy may be distinguished. The quality of the low-degree gravity field recovery is for the greater part determined by the accuracy of the orbit perturbations. It is obvious that a high-quality GPS receiver will be necessary to fully exploit the information content of the gradiometer measurements and to facilitate a high-accuracy low- to medium-degree gravity field recovery. It may be concluded that the gradiometer really needs an additional measurement device in the form of a GPS receiver, which can deliver precise information of the ARISTOTELES orbit perturbations, especially in the low-frequency band. Similar conclusions were also drawn in (Schrama, 1990).

9.5 Comparison with local gravity field recovery

The formal error estimates for the gravity field harmonic coefficients can be used to determine the accuracy of gravity anomalies and geoid undulations on the Earth's surface. Variances can be computed as a function of the harmonic degree and these values can be used as input for the covariance function computing algorithms described in Chapter 7. In this way the results of the global gravity field recovery error analyses with the GPS-ARISTOTELES configuration can be compared with those of the local recovery. In the local recovery, the measurement time interval was equal to 2.5 s and the nominal noise equal to 2.0 mm, while in the global error analyses values of respectively 1.0 s and 1.0 cm were used. However, with equation (9.4), it can be shown that in the global gravity field recovery error analyses a measurement interval equal to 2.5 s and a noise of 6 mm leads to equivalent results. This equation indicates that in the global gravity field recovery error analyses, the formal harmonic coefficient error estimates are obtained by multiplying the inverse of the normal matrix with a factor equal to $\sigma^2(orbit)\Delta t$. Thus the degree variances computed from the formal error estimates are based on less accurate measurements than the measurements used in the deterministic local gravity field recovery simulations. However, this is partially compensated by the fact that in the global gravity field recovery error analyses it was assumed that measurements will be available for a complete repeat period, i.e. 3 times as long as the simulated 30-days period in the local gravity field recovery simulations.

The standard deviations for the gravity anomalies and geoid undulations computed from the formal error estimates of the global gravity field error analyses become as specified in Table 9.3. With the GPS-ARISTOTELES configuration, the gravity field can be recovered complete to degree and order 120 with an accuracy of 4.15 mgal for gravity anomalies and 24.8 cm for geoid undulations (commission errors of the gravity field part complete to degree and order 120). Above degree 120, the degree variances become greater than Kaula's rule of thumb. In the local recovery, the rms of differences between the a priori and recovered gravity anomalies and geoid undulations

Table 9.3 Standard deviation of (point) gravity anomalies and geoid undulations with the formal harmonic coefficient error estimates.

Figure	minimum degree	maximum degree	Δg (mgal)	N (cm)
9.9	1	120	4.15	24.8
9.9	1	180	70.16	274.4
9.11	1	180	0.21	1.5
9.11	28	180	0.21	0.9
9.12	1	180	0.21	1.4
9.13	1	180	0.21	1.4
9.14	1	180	0.21	0.9

were respectively about 12 mgal and about 65 cm (Table 8.15). However, in the local gravity field recovery, the a priori values were computed with a gravity field model complete to degree and order 360. If the (omission) effect of the gravity field from degree 121 to 360 is added, the standard deviations of the gravity anomalies and the geoid undulations for the global recovery become 12.9 mgal and 53.5 cm. These values compare very well with those of the local recovery. The geoid undulations seem to be better recoverable on a global basis. This can be explained by the fact that these undulations have a more pronounced long-wavelength nature than gravity anomalies. In a global gravity field recovery, the "missing information" for the long-wavelength terms will be available.

As was to be expected, the addition of gradiometer measurements improves the accuracy of the gravity field drastically, especially for the higher degrees. The commission errors for gravity anomalies and geoid undulations for a gravity field solution complete to degree and order 180 are 0.21 mgal and 0.9 cm, respectively, if gradiometry and GPS SST are combined (best solution, lowest line in Figure 9.14). However, these numbers are based only on pure formal error estimates, i.e. the gravity field model complete to degree and order 180 describes the "real-world". In reality, omission errors and errors due to mismodeling of e.g. non-conservative forces, errors in modeling the gradiometer measurements due to uncertainties in the ARISTOTELES attitude, orbit errors (equation (9.5)), etc., must be added.

9.6 Conclusions

Although a number of simplifications was applied in the theory of formal error estimates, this theory is a valuable tool to gain insight in the gravity field recovery from ARISTOTELES gradiometer measurements and satellite orbit perturbations derived from GPS SST range measurements. In addition, the global gravity field recovery simulation results are in agreement with the results of the local gravity field recovery simulation results (Chapters 7 and 8).

It was shown that with the implementation of a high-quality GPS receiver on board of ARISTOTELES it is possible to improve current low-degree gravity field models drastically, if such a receiver is capable of delivering information from which it is possible to determine ARISTOTELES orbit perturbations with an accuracy on the order of 10 cm at measurement intervals of 60 s. If this accuracy is 1 cm and the measurement interval 1 s, even valuable information of the gravity field can be obtained up to degree and order 120. The effect of several parameters has been studied, including the inclination of the satellite orbit and the limited gradiometer bandwidth. An inclination of the satellite orbit close to 90° (polar orbit) leads to the best monitoring of the Earth's global gravity field. If the inclination differs too much from 90°, extra information of the gravity field above the polar caps is necessary to stabilize the normal equations for a high-degree gravity field recovery. It was found that a deviation of 4° from

the true polar inclination already resulted in a very instable set of normal equations.

The gradiometer bandwidth limitation, i.e. the fact that the low-frequency band (<27 cpr) of the gravity tensor is not observable, requires additional information of some gravity field induced signal in the low-frequency band. A GPS receiver seems capable of delivering this information in the form of precise SST range measurements to the ARISTOTELES satellite, from which precise orbit perturbations can be derived. The combination of a high-quality GPS receiver and a gradiometer on board of ARISTOTELES seems to be the optimum solution to achieve a gravity field recovery with the resolution and accuracy strived for.

Part IV. Conclusions, bibliography, appendices

10. Conclusions

In the time period 1988-1992, the author of this thesis has performed various studies on the application of tracking data to compute precise satellite orbits and on the application of satellite observations to determine the gravity field, the marine geoid and the dynamic sea surface topography. These studies have demonstrated the feasibility to use existing satellite data sets to further improve the gravity field modeling, satellite precise orbit determination and the modeling of oceanic phenomena. Moreover, the possibilities in these fields of new satellite altimeter missions, satellite-to-satellite tracking and gradiometry have been addressed.

This Chapter will present a summary of the techniques developed and applied in the first three parts of this thesis and the results obtained. Conclusions will be made based on the results obtained in each part separately.

In the first part of this thesis, an analytical theory for the modeling of satellite orbit perturbations and orbit errors was presented: the Linear Perturbation Theory (LPT). Orbit perturbations computed with this theory were compared with perturbations obtained from a numerical orbit integration process for an ERS-1-like satellite orbit. It was shown that these perturbations were in very good agreement with each other: 90% of the orbit perturbations found from the numerical integration could be modeled with the analytical theory, both for the radial, along-track and cross-track directions. Moreover, it was shown that the remaining analytical modeling errors were for the greater part concentrated at the zero and one cycle-per-orbital-revolution (cpr) frequency (resonance). In a real precise orbit determination process, these errors will be absorbed for the larger part by the adjustment of the satellite epoch state-vector. Therefore, it was concluded that the LPT is an appropriate tool for modeling orbit errors. Advantages of the LPT in comparison to numerical orbit integration are that the LPT is computationally very efficient and can predict and explain the effect of individual gravity field terms very easily.

In the second part of this thesis, the application of the LPT to satellite altimeter measurements led to very promising results in the field of orbit error modeling, gravity field model adjustment and modeling of the long-wavelength semi-permanent dynamic sea surface topography.

In Chapter 5 it was described how the LPT was applied to SEASAT laser range measurement residuals and residual altimeter crossover differences. These residuals were reduced from initial rms-values of 56 and 62 cm for the GEM-T1 gravity field model, to 50 and 40 cm with the LPT. These improvements were obtained by adjusting only a limited set of gravity field coefficients (120 unknowns) and were

comparable to the improvements obtained by the numerical orbit integration and parameter estimation program GEODYN. This again demonstrated the strength of the LPT and also justified the use of the LPT in gravity field parameter estimation. Moreover, the implementation of the LPT in this estimation process was computationally more efficient than the parameter estimation process of GEODYN.

In Chapter 6, a so-called integrated approach was formulated to achieve simultaneously a gravity field model adjustment and a solution for the long-wavelength dynamic sea surface topography from satellite altimetry. Also in this approach the LPT was implemented successfully to model radial orbit errors and gravity field induced geoid errors. The approach led to very promising results in the fields of orbit error modeling, gravity field improvement and the modeling of the dynamic sea surface topography and the large-scale ocean circulation. For the GEOSAT satellite, the rms of the radial orbit errors was reduced from an initial level of about 35 cm for GEM-T2 orbits to about 16 cm. Moreover, differences between the GEM-T2 geoid and the OSU89b geoid were reduced by about 100 cm. The differences between the dynamic sea heights computed with the "new" model and other published models were on the order of 30 cm, within the range of the predicted standard deviation of the "new" model.

It was found that an important parameter for the success of the integrated approach, i.e. the successful separation of ocean and gravity field signals from altimetry, was the weight assigned to the a priori information about the input gravity field model. By using the known accuracy of the GEM-T2 model (available calibrated covariance matrix), which was the a priori gravity field model in the integrated approach, the long-wavelength terms of this model could be constrained and separated from the long-wavelength dynamic sea surface topography terms. Moreover, this separation was strengthened by the addition of residual crossover differences, which added in principle only information about radial orbit errors. Also, a priori information about the magnitude of long-wavelength dynamic sea surface topography terms was implemented successfully. Finally, it was found that the last problem encountered in the integrated approach, i.e. the high correlations between the 1 cpr state-vector error and the term of the dynamic sea surface topography with $l=1$ and $m=0$, could be solved by assigning constraints with a magnitude comparable to the known radial orbit modeling accuracy to these state-vector terms.

All these procedures led to a separation of the gravity field and dynamic sea surface topography solutions of better than 80 % (the correlation between the two solutions was equal to -0.18). The rms of the standard deviation of the dynamic sea heights was equal to 10 cm for the oceans, and of the geoid computed with the adjusted GEM-T2 model equal to 20 cm. The rms of these dynamic sea heights was equal to 65 cm, about 7 times the rms of their standard deviations. Further tests with the covariance matrix of the adjusted GEM-T2 model showed the consistency of the approach. In the first place, the calibrated GEM-T2 radial orbit error decreased from 20 cm to 10 cm, consistent with the decrease of the rms-values of the a priori residual crossover differences to the rms-values of the a posteriori residual crossover differences. Secondly, the standard deviation of the geoid undulations of the new model was equal to 54 cm, comparing very well with the rms of differences of 65 cm between the OSU89b (truncated at degree and order 36) and adjusted GEM-T2 geoid (complete to

degree and order 36). Finally, it was found that the magnitudes of both the dynamic sea surface topography coefficients and gravity field model adjustments were consistent with the reduction of the rms-values of the residual crossover differences and sea height residuals when subtracting corrections using these coefficients and adjustments.

In addition, variations in the long-wavelength models fitted through successive 17-day periods (ERM's) of two years of fully-corrected GEOSAT sea height residuals (using the adjusted gravity field model and the "new" dynamic sea surface topography model) were determined. This analysis led to 43 17-day long-wavelength residual ocean surface topography solutions. The variability of these solutions was equal to 7 cm. The variations of these solutions exhibited a clear annual cycle, demonstrating the enormous potential of satellite altimetry to study oceanographic and climatological phenomena. With ERS-1, launched in July 1991, and TOPEX/Poseidon, to be launched in mid 1992, and the ongoing development in gravity field modeling and orbit determination, the impact of altimetry in geodesy, geophysics, oceanography and related subjects, such as climatology, will grow and grow. Especially the ERS-1 will deliver a wide variety of observations, e.g. altimeter height observations, wind-speed measurements and sea surface temperature measurements. These measurements can be used in the development of ocean circulation models and climatological models. The variety of measurements will enable the answering of the basic question of what mechanism is behind the observed cycles in the sea height residuals obtained from the GEOSAT altimeter measurements.

In the third part of this thesis, simulation studies have shown the enormous potential of the concepts of satellite-to-satellite tracking (SST) and satellite gradiometry in extending our knowledge of the gravity field of the Earth, both on a local and global scale. Especially the combination of these two concepts will undoubtedly lead to very promising results in this field. The first mentioned concept will be very important for improving the modeling of low- and medium-degree gravity field terms, i.e. to degree and order 80-120, and the second concept will be essential for improving medium- and high-degree terms, i.e. from degree 30 up to greater than 180. This would mean that gravity on Earth can be modeled with a resolution better than 100 km.

Local gravity field recovery using satellite-to-satellite tracking of ARISTOTELES with the GPS system was investigated in the Chapters 7 and 8. This concept was assumed to be capable of delivering carrier phase measurements with a sampling rate of 2.5 s and an accuracy on the order of a few millimeters. It is expected that this precision level will be achieved with future high-quality space-borne GPS receivers. With these values it seems possible to determine the ARISTOTELES orbital accelerations with an accuracy of 1.0 mgal. That accuracy will allow the modeling of gravity anomalies and geoid undulations on the Earth's surface with a precision of respectively about 10 mgal and 65 cm, with a resolution on the order of 100 km. This means that the objectives of the ARISTOTELES mission can not be achieved with measurements from a GPS receiver alone, but that a great part of the high-degree gravity field up to degree 100 can be recovered with highly-accurate GPS measurements to ARISTOTELES. Moreover, it was indicated in the local gravity field recovery covariance analysis described in Chapter 7, that with the combination of precise ARISTOTELES

satellite accelerations determined from GPS measurements and gradiometer measurements, the ARISTOTELES objectives can be achieved. With gradiometer measurements alone this will be very difficult, if not impossible. As will be concluded later, the picture will even improve if a global data set of GPS measurements of the ARISTOTELES orbit is available.

The determination of gravity anomalies and geoid undulations from the GPS-ARISTOTELES range measurements consisted of a number of consecutive processing steps. The first step was the computation of so-called "reference ARISTOTELES orbits" and "computed" GPS SST range measurements with a low-degree and -order gravity field model. The differences between the reference orbits and "real-world" ARISTOTELES orbits, simulated with a high-degree and -order gravity field model, were on the order of 1 m. The "computed" range measurements were subtracted from the "real-world" measurements to obtain range residuals. These residuals were also on the order of 1 m.

The second step consisted of fitting a second-order polynomial through a number of successive range residuals. The second-derivative of this polynomial was the so-called residual acceleration. With a sampling rate of 2.5 s, the accuracy of this concept was found to be equal to 0.08-0.20 mgal. Therefore, the concept using the second-order polynomial was found to be appropriate. The residual accelerations were transformed successfully to residual accelerations in the satellite radial, along-track and cross-track direction by means of a geometrical method.

These residual accelerations were irregularly distributed over the selected local geographical area. A gridding procedure was developed that converted in the third step this irregular grid of accelerations to a regular grid. This procedure was based on the concept of least-squares collocation, a concept that has the capability of reducing the effect of measurement noise and of estimating the accuracy of the accelerations in the regular grid. With a measurement noise of 2.0 mm for the GPS SST range measurements, it was possible to obtain regular grids of accelerations with an accuracy of 1.0 mgal for a resolution of 1° in the longitude and latitude directions. The altitude of this grid was approximately 200 km and the resolution approximately 70 km at 50° latitude. If the resolution was made smaller, the accuracy deteriorated.

In the fourth and final step, the regular grid of accelerations was continued downward to gravity anomalies and geoid undulations by using the equations of Stokes or by using the method of least-squares collocation. In this downward continuation of satellite accelerations measured at an altitude of 160-200 km to gravity anomalies/geoid heights on the Earth's surface, three parameters were found to play an important role: the resolution of the distribution of accelerations, their altitude above the Earth's surface and their accuracy. The simulations showed that the resolution must be at least equal to the required resolution of the gravity anomalies/geoid heights on the Earth's surface. With an altitude range of 160 to 200 km above the Earth, the accuracy of the measured satellite accelerations had to be on the order of 1 mgal, if mean 1° x 1° gravity anomalies were to be recovered with an accuracy of 5 mgal, and point geoid heights with an accuracy of 50 cm. The 200 km altitude seems to be the maximum allowable altitude, if a resolution of gravity anomalies/geoid heights of 1° in both the longitude and latitude directions on the Earth's surface is strived for.

The simulations performed showed the capability of a GPS receiver on board of the ARISTOTELES satellite to recover information about the high-frequency gravity field (above degree 36) of the Earth on a regional basis. The simulations demonstrated that through SST valuable information can be obtained up to about degree 100 of a spherical harmonic expansion of the gravity field of the Earth. Two very important parameters used in the simulations were the sampling rate of 2.5 s and a measurement noise of 0-2 mm for the GPS SST range measurements. Current ground-based GPS receivers have shown the ability to measure the GPS carrier phase with a 1 s sampling rate and a precision of better than 0.5 cm. If future space-borne GPS receivers have comparable capabilities, the assumptions made about these parameters seem to be realistic. However, to achieve the precision of 0.5 cm in the 1 s carrier phase measurements, a two-frequency high-quality receiver is required on board of ARISTOTELES, in order to be able to eliminate the first-order ionospheric propagation effect on the GPS measurements.

Using only GPS on a regional basis, it seems difficult to meet the mission objectives of ARISTOTELES: a 5 mgal mean 1° x 1° gravity anomaly accuracy and a 10 cm geoid height accuracy. However, in the deterministic local gravity field recovery experiments only 1/3 of a repeat period of the ARISTOTELES orbit was simulated, leading to a far from perfect coverage of the investigated geographical area. The results obtained in the deterministic local gravity field recovery experiments were found to be in agreement with the results of a local gravity field recovery covariance analysis.

The concept of formal harmonic coefficient error estimation was applied to a global satellite-to-satellite tracking and gradiometry numerical experiment. For the case that the GPS receiver and gradiometer on board of ARISTOTELES deliver a data set of observations with global coverage, it was possible to compute and invert normal equations for gravity field harmonic coefficients very efficiently. The simulations using this concept indicated the possibility to determine a gravity field model with a high accuracy and a small resolution (<100 km), if a high-quality GPS receiver and gradiometer are implemented on board of the ARISTOTELES satellite. Moreover, the combination of GPS measurements with gradiometer measurements offers the possibility to overcome problems associated with the gradiometer bandwidth limitation. It was also shown that a high-quality GPS receiver is necessary to improve the current state-of-the-art in low-degree gravity field modeling (i.e. up to degree and order 36).

The effect of several parameters was studied. These parameters included the orbital inclination of ARISTOTELES and the gradiometer bandwidth. As to be expected, a polar orbit leads to the best monitoring of the Earth's global gravity field. If the inclination differs too much from 90° (polar orbit), additional information of the gravity field at the polar caps is necessary to stabilize the normal equations for a high-degree gravity field recovery. Already for an inclination of 94°, the normal equations for a gravity field recovery complete to degree and order 180 become singular without this additional information.

The gradiometer bandwidth, i.e. the low-frequency band (<27 cpr) of the gravity tensor is not observable, leads to singular normal equations if no additional

information is added. However, a GPS receiver on board of ARISTOTELES seems to be capable of delivering this information. Combining these two data types, a very accurate and high-resolution gravity field recovery seems possibly, up to at least degree and order 180. Using only GPS observations, a maximum degree and order equal to 120 is the ultimate achievable. The assumptions made in the simulations were a measurement noise of 1.0 cm and 0.01 EU for GPS and gradiometer measurements, respectively, and a measurement time interval of 1.0 and 4.0 s, respectively. The global gravity field recovery error analyses were in good agreement with the local gravity field recovery simulation results.

In summary, the analyses described in this thesis have shown the tremendous possibilities of altimetry (both past, SEASAT and GEOSAT, today, ERS-1, and future missions, TOPEX/Poseidon) and gradiometry/GPS-tracking (ARISTOTELES, Gravity Probe B) in the field of geophysics, geodesy, oceanography and even climatology. Especially the combination of altimetry and gravity field products from the ARISTOTELES mission seem to be very promising, because of the possibility to separate gravity from oceanographic signals.

Bibliography

The following bibliography gives an overview of literature that has been used by the author in the research described in this thesis. This overview consists of literature referred to in the main text and additional literature that has served as valuable background information.

Ambrosius, B.A.C., Visser, P.N.A.M., and Wakker, K.F. (1990) On the use of GPS for the ARISTOTELES mission, contribution to the Dornier/ESA ARISTOTELES Additional Study.

Anderle, R.J. (1978) The ocean geoid deduced from GEOS-3 satellite radar altimetry data, NSWC, Dahlgren, Virginia.

Arabelos, D., and Tscherning, C.C. (1990) Simulation of regional gravity field recovery from satellite gravity gradiometer data using collocation and FFT, Bull. Geod. 64, pp. 363-382.

Balmino, G. (1985) A satellite gradient (SGG) project for the geosciences, CSTG Bulletin, no. 8, Future missions, systems and projects.

Bertiger, W., Lichten, S., Wu, S., and Yunk, T. (1986) Tracking Landsat-5 by a differential GPS technique, paper no. AIAA-86-2215-CP, AIAA/AAS Astrodynamics Conference, Williamsburg, Virginia.

Bosch, W., and Schwintzer, P. (1986) Accuracy of geoid undulations derived by error propagation using the full variance-covariance matrix of the harmonic coefficients of a global Earth's gravity model, International symposium on the definition of the geoid, Florence.

Boyce, W.E., and DiPrima, R.C. (1986) Elementary differential equations and boundary value problems, 4th edition, Wiley, New-York.

Breakwell, J.V., Parkinson, B.W., Everitt, C.W., and Tapley, M.B. (1989) Impact of Gravity Probe B mission on satellite navigation and geodesy.

Cartwright, D.E., and Ray, R.D. (1990) Oceanic tides from GEOSAT altimetry, JGR, vol. 95, no. c3, pp. 3069-3090

Casotto, S., and Dow, J.M. (1990) Use of GPS in support of ARISTOTELES orbit maintenance, ESA/ESOC, Darmstadt, Germany.

CIGAR (1989) Study on precise gravity field determination and mission requirements, final report CIGAR Phase I prepared by CISI, ESA Contract 7521/87/F/FL, January 1989.

CIGAR (1990) Study on precise gravity field determination and mission requirements, final report CIGAR Phase II prepared by CISI, ESA Contract 8153/88/F/FL, February 1990.

Colombo, O.L. (1984) The global mapping of gravity with two satellites, Netherlands Geodetic Commission, vol. 7, no. 3.

Colombo, O.L. (1990) Mapping the gravity field with orbiting GPS receivers, Presented at the general meeting of the I.A.G. in Edinburgh.

Denker, H., Rapp, R.H. (1990) Geodetic and oceanographic results from the analysis of 1 year of GEOSAT data, JGR, vol. 95, no. c8, pp. 13,151-13,168.

DGFI-TUM-TH Delft (1987) Study of a satellite-to-satellite tracking gravity mission, final report, ESTEC/Contract no. 6557/85/NL/PP(SC), Munich.

Dunning, R.S. (1973) The orbital mechanics of flight mechanics, NASA, Langley research center, and scientific and technical information office, NTIS, Springfield.

Engelis, T. (1987) Spherical harmonic expansion of the Levitus sea surface topography, Report no. 385, Department of geodetic science and surveying, OSU, Columbus, Ohio.

Engelis, T. and Knudsen, P. (1989) Orbit improvement and determination of the ocean geoid and topography from 17 days of SEASAT data, Department of geodetic science and surveying, OSU, Columbus, Ohio.

Gravity Workshop (1987) Geophysical and geodetic requirements for global gravity field measurements 1987-2000, report of a gravity workshop Colorado Springs February 1987, Geodynamics branch, Division of Earth science and applications, NASA.

Gulick, L.J. (1970) A comparison of methods for computing gravitational potential derivatives, ESSA TR C&GS 40.

Gurtner, W. (1985) GPS-papers presented by the astronomical institute of the university of Berne in the year 1985, Mitteilungen der satelliten-beobachtungssation Zimmerwald, no. 18.

Haines, B.J., Born, G.H., Rosborough, G.W., Marsh, J.G., and Williamson, R.G. (1990) Precise orbit computation for the GEOSAT exact repeat mission, JGR, vol. 95, no. C3, pp. 2871-2885, March 15.

Hedin, A.E., Salah, J.E., Evans, J.V., Reber, C.A., Newton, G.P., Spencer, N.W., Kayser, D.C., Alcayde, D., Bauer, P., Cogger, L., and McClure, J.P. (1977) A global thermospheric model based on mass spectrometer and incoherent scatter data, JGR, vol. 82, no 16, pp. 2139-2147.

Heiskanen, W.A., and Moritz, H. (1967) Physical geodesy, Freeman&Co, San Fransisco.

Hwang, C. (1991) Orthogonal functions over the oceans and applications to the determination of orbit error, geoid and sea surface topography from satellite altimetry, Report no. 414, Department of geodetic science and surveying, OSU, Columbus, Ohio.

Kaula, W.M. (1966) Theory of satellite geodesy, Blaisdell Publishing Co.

Kaula, W.M. (1983) Inference of variations in the gravity field from satellite-to-satellite range rate, JGR, vol. 88, no. B10, pp. 8345-8349.

Kahn, W.D. (1986) Gravity field fine structure mapping, using a spaceborne gravity gradiometer, NSFC, Presentation at the 14th gravity gradiometry conference, USAF Academy, Colorado Springs, Colorado, Feb. 11,12, 1986.

Kendal, M.G., and Stewart A. (1961) The advanced theory of statistics, vol. II, London.

Klokocnik, J. (1985) Further comparisons of Earth gravity models by means of lumped coefficients, Bull. Astron. Inst. Czechosl. 36, 27-43.

Klosko, S.M., and Wagner, C.A. (1982) Spherical harmonic presentation of the gravity field from dynamic satellite data, Planet. Space Sci., vol. 30, no. 1, pp. 5-28.

Koblinsky, C.J., Marsh, J., Lerch, F., Klosko, S.M., Williamson, R.G., and Engelis, T. (1989) Ocean topography mapping, improvement of the marine geoid, and global permanent ocean circulation studies from TOPEX altimeter data, Presentation for the TOPEX science working team

Knudsen, P. (1989) Simultaneous estimation of the gravity field and sea surface topography from satellite altimeter data by least squares collocation, Submitted to Geophysical Journal International.

Koop, R., and Stelpstra, D. (1989a) On the computation of the gravitational potential and its first and second derivatives, Manuscripta Geodaetica, 14:373-382.

Koop, R., and Schrama, E.J.O. (1989b) Gravity field recovery performance, ARISTOTELES add-on study Part 1, Work package no. 2420/1.

Lambeck, K. (1990) ARISTOTELES: an ESA mission to study the Earth's gravity field, ESA Journal 1990, vol. 14, pp. 1-21.

Lerch, F.J., Marsh, J.G., Klosko, S.M., Pavlis, E.C., Patel, G.B., Chinn, D.S., and Wagner C.A. (1988) An improved error assessment for the GEM-T1 gravitational model, Nasa technical memorandum 100713, Greenbelt, Maryland.

Lerch, F.J. (1989) Optimum data weighting and error calibration for estimation of gravitational parameters, NASA technical memorandum 100737, Greenbelt, Maryland.

Marsh, J.G., Lerch, F.J., Putney, B.H., Christodoulidis, D.C., Felsentreger, T.L., Sanchez, B.V., Smith, D.E., Klosko, S.M., Martin, T.V., Pavlis, E.C., Robbins, J.W., Williamson, R.G., Colombo, O.L., Chandler, N.L., Rachlin, K.E., Patel, G.B., Bhati, S., and Chinn, D. (1986) An improved model of the Earth's gravitational field: GEM-T1, Geodynamics branch GSFC, EG&G/Washington analytical services center, and Science applications and research corp.

Marsh, J.G. (1988) Status of GSFC gravity field and altimeter analysis: GEM-T1, T2 and T3, Presentation at DUT/FAE 1988.

Marsh, J.G., Lerch, F.J., Putney, B.H., Felsentreger, T.L., Sanchez, B.V., Klosko, S.M., Patel, G.B., Robbins, J.W., Williamson, R.G., Engelis, T.E., Eddy, W.F., Chandler N.L., Chinn, D.S., Kapoor, S., Rachlin, K.E., Braatz, L.E., and Pavlis, E.C. (1989a) GSFC e.a., The GEM-T2 gravitational model, NASA technical memorandum 100746, Greenbelt, Maryland.

Marsh, J.G., Lerch, F., Koblinsky, C.J., Klosko, S.M., Robbins, J.W., Williamson, R.G., and Patel, G.B. (1989b) Dynamic sea surface topography, gravity, and improved orbit accuracies from the direct evaluation of SEASAT altimeter data, NASA technical memorandum 1000735, Greenbelt, Maryland.

Marsh, J.G., Koblinsky, C.J., Lerch, F., Klosko, S.M., Robbins, J.W., Williamson, R.G., and Patel, G.B. (1990) Dynamic sea surface topography, gravity, and improved orbit accuracies from the direct evaluation of SEASAT altimeter data, JGR, vol. 95, no. C8, pp. 13,129-12,150.

Martin, T.V., Eddy, W.F., Rosen, B., Brenner, A., and McCarthy, J. (1980) GEODYN System description, vol. I and II, EG&G/Washington Analytical Services Center, Riverdale, Maryland

Moritz, H. (1980) Advanced physical geodesy, Herbert Wichmann Verlag, ISBN 3-87907-106-3, Abacus Press 0-85626-195-5.

Nerem, R.S., Tapley, B.D., Shum C.K., and Yuan D.N. (1988) A model for the general ocean circulation determined from a joint solution for the Earth's gravity field, Presented at the Chapman conference on progress in the determination of the Earth's gravity field, Ft. Lauderdale, Florida, September 13-16, 1988.

Rapp, R.H. (1979) Potential coefficient and anomaly degree variance modeling revisited, Report no. 292, Department of geodetic science, OSU, Columbus, Ohio.

Rapp, R.H., and Cruz, J.Y. (1986) Spherical harmonic expansions of the Earth's gravitational potential to degree 360 using 30 minute mean anomalies, Report no. 376, 22 pp., Department of geodetic science and surveying, OSU, Columbus, Ohio.

Rapp, R.H., and Pavlis, N.K. (1990) The development of geopotential coefficient models to spherical harmonic degree 360, JGR, vol. 95, no. B13, pp. 21,885-21,911, December 10.

Rosborough, G.W. (1986) Satellite orbit perturbations due to the geopotential, CSR, University of Texas.

Rosborough, G.W., Tapley, B.D. (1987a) Radial, transverse and normal satellite position perturbations due to the geopotential, Celestial Mechanics 40, pp. 409-421.

Rosborough, G.W. (1987b) Orbit error due to gravity model error, University of Colorado, AAS/AIAA Astrodynamics Specialist Conference, Kalispell, Montana.

Rosborough, G.W. (1988) Geographically correlated orbit error, Progress in the determination of the Earth's gravity field, University of Colorado.

Rummel, R., Hajela, D.D., and Rapp, R.H. (1976) Recovery of mean gravity anomalies from satellite-to-satellite range-rate data using least-squares collocation, Report no. 248, Department of geodetic science, OSU, Columbus.

Rummel, R. (1986a) Satellite Gradiometry, DUT Faculty of Geodesy, Lecture note in Earth sciences, vol. 7.

Rummel, R. (1986b) Satellite altimetry as part of a geodetic model, I Hotine-Marussi symposium on mathematical geodesy, Rome, 3-6 June 1985, IAG, vol. 2, Milan.

Rummel, R. (1989a) ARISTOTELES: surface gravity from space geometry, Proceedings of the Italian Workshop on the European solid-Earth mission ARISTOTELES, May 30-31, Trevi, Italy.

Rummel, R. (1989b) ARISTOTELES and the long-wavelength part of the gravitational field spectrum, Delft.

Rummel, R., Teunissen, P., and Gelderen, M. van (1989c) Uniquely and overdetermined geodetic boundary value problem by least squares, Bull. Geod. 63, pp. 1-33.

Rummel, R. (1990) A method of global recovery of harmonic coefficient from SGG data with peculiar geometry, CIGAR Phase II: Work Package 510 A, Contribution to final report of "Study on Precise Gravity Field Determination Methods and Mission Requirements (Phase 2)", ESA Contract No. 8153/88/F/FL

Schrama, E.J.O. (1986a) A study of a satellite-to-satellite tracking configuration by application of linear perturbation theory, DUT Faculty of Geodesy.

Schrama, E.J.O. (1986b) Estimability of potential coefficients from orbit perturbations, DUT Faculty of Geodesy.

Schrama, E.J.O. (1989) The role of orbit errors in processing of satellite altimeter data, Thesis, DUT, Faculty of Geodesy.

Schrama, E.J.O. (1990) Gravity field error analysis: applications of GPS receivers and gradiometers on low orbiting platforms, NASA technical memorandum 100679, GSFC, Greenbelt, Maryland.

Schmid, P.E., Trudell, B.J., and Vonbun, F.O. (1975) ATS-6 satellite-to-satellite tracking and data relay experiments, IEEE Transactions on aerospace and electronic systems, vol. AES-11, no. 6, pp. 1048-1058.

Smith, D.E., Lerch, F.J., Colombo, O.L., and Everitt, C.W.F. (1988) Gravity field information from Gravity Probe B, Proceedings of the Chapman conference on progress in the determination of the Earth's gravity field, pp. 159-163, Ft. Lauderdale, Florida, September 13-16, 1988.

Sneeuw, N.J. (1991) Inclination functions: group theoretical background and a recursive algorithm, Reports of the DUT Faculty of Geodesy/ Department of mathematical and physical geodesy, The Netherlands

Tai, C.-K. (1988) Estimating the basin-scale ocean circulation from satellite altimetry. Part I: straightforward spherical harmonic expansion, Journal of physical oceanography, vol. 18, no. 10.

Tapley, B.D., Born, G.H., and Parke, M.E. (1982) The SEASAT altimeter data and its accuracy assessment, JGR, vol. 87, no. C5, pp. 3179-3188, April 10.

Tapley, B.D., and Rosborough, G.W. (1985) Geographically correlated orbit error and its effect on satellite altimetry missions, JGR, vol. 90, no. C6, pp. 11,817-11,831, November 20.

Tapley, B.D., Shum, C.K., Yuan, D.N., Ries, J.C., and Schutz, B.E. (1988) An improved model of the Earth's gravity field, TEG-1, Presented at the Chapman conference on progress in the determination of the Earth's gravity field, Ft. Lauderdale, Florida, September 13-16, 1988.

Tikhonov, A.N. (1963) Regularization of incorrectly posed problems, Soviet Math. Dokl., 4, 1624-1627.

Tscherning, C.C. (1972) Representation of covariance functions related to the anomalous potential of the Earth using reproducing kernels, The Danish Geodetic Institute, Internal Report no. 3, Kopenhagen.

Tscherning, C.C., and Rapp, R.H. (1974) Closed covariance expressions for gravity anomalies, geoid undulations, and deflections of the vertical implied by anomaly degree variance models, Report no. 208, Department of geodetic science, OSU, Columbus, Ohio.

Tscherning, C.C., Rapp, R.H., and Goad, C.C. (1983) A comparison of methods for computing gravimetric quantities from high degree spherical harmonic expansions, Manuscripta Geodaetica, vol. 8, pp. 249-272.

Vassiliou, A.A., and Schwartz, K.P. (1987) Study of the high-frequency spectrum of the anomalous gravity potential, JGR, vol. 92, no. B1, pp. 609-617.

Vermeer, M. (1989) FGI studies on satellite gravity gradiometry, 1. Experiments with a 5-degree buried masses grid representation, Reports of the Finnish Geodetic Institute, Helsinki.

Visser, P.N.A.M., Wakker, K.F., and Ambrosius, B.A.C. (1990) Recovery of mean 1 deg x 1 deg gravity anomalies and geoid heights in a local area from GPS tracking of ARISTOTELES, CIGAR Phase II: Work Package 420, Contribution to final report of "Study on Precise Gravity Field Determination Methods and Mission Requirements (Phase 2)", ESA Contract No. 8153/88/F/FL

Visser, P.N.A.M., Wakker, K.F., and Ambrosius B.A.C. (1991) Determination of the regional geoid from simulated GPS measurements by the ARISTOTELES solid-Earth satellite, International association of geodesy symposia, Symposium no. 106, Determination of the geoid, present and future, Milan, June 11-13, 1990.

Vonbun, F.O., Kahn, W.D., Wells, W.T., and Conrad, T.D. (1980) Determination of 5 deg x 5 deg gravity anomalies using satellite-to-satellite tracking between ATS-6 and Apollo, Geophys. J.R. and Soc., no. 61, pp. 645-657.

Wagner, C.A., and Douglas, B.C. (1969) Perturbations of existing resonant satellites, Planet. Space Sci., vol. 17, pp. 1505-1517.

Wagner, C.A. (1983) Direct determination of gravitational harmonics from low-low GRAVSAT Data, JGR, vol. 88, no. B12, pp. 10309-10321.

Wagner, C.A., and McAdoo, D.C. (1986) Time variations in the Earth's gravity field detectable with GRM intersatellite tracking, JGR, vol. 91, no. B8, pp. 8373-8386.

Wagner, C.A. (1987a) Geopotential orbit variations: applications to error analysis, JGR, vol. 92, no. B8, pp. 8136-8146.

Wagner, C.A. (1987b) Improved gravitational recovery for a geopotential research mission satellite pair flying en echelon, JGR, vol. 92, no. B8, pp. 8147-8155.

Wakker, K.F., Ambrosius, B.A.C., Zandbergen, R.C.A, and van Geldorp, G.H.M. (1987a) Precise orbit computation, gravity model adjustment and altimeter data processing for the ERS-1 altimetry mission, DUT/FAE/SOM.

Wakker, K.F., Zandbergen R.C.A., Ambrosius B.A.C. (1987b) SEASAT orbit determination experiments in preparation for the ERS-1 altimetry mission, AAS/AIAA Astrodynamics Specialist Conference, Kalispell, Montana.

Wakker, K.F., Zandbergen, R.C.A., Naeije, M.C., and Ambrosius, B.A.C. (1990a) GEOSAT altimeter data analysis for the oceans around South Africa, JGR, vol. 95, no. C3, pp. 2991-3006.

Wakker, K.F., Naeije, M.C., Scharroo, R., and Ambrosius, B.A.C. (1990b) Extraction of mesoscale ocean currents information from GEOSAT altimeter data, Delft.

Wolff, M. (1969) Direct measurement of the Earth's gravitational potential using a satellite pair, JGR, vol. 74, no. 22.

Wu, J.-T., and Yunk, T.P. (1986a) Topex orbit determination and gravity recovery using GPS data from repeat orbits, AIAA-86-0575, JPL, California.

Wu, S.C., and Yunk, T.P. (1986b) Non-dynamic decimeter tracking of Earth satellites using the global positioning system, AIAA-86-0404, JPL, California.

Yuan D.N., Shum, C.K., and Tapley, B.D. (1988) Gravity field determination and error assessment techniques, Presented at the Chapman conference on progress in the determination of the Earth's gravity field, Ft. Lauderdale, Florida, September 13-16, 1988.

Zandbergen, R.C.A., Wakker, K.F., and Ambrosius, B.A.C. (1988) Application of satellite altimeter data to orbit error correction and gravity model adjustment, DUT/FAE/SOM, 27th COSPAR Meeting, Finland.

Zandbergen, R.C.A. (1990) Satellite Altimeter Data Processing, From Theory To Practice, Thesis, Delft University Press, Delft, The Netherlands.

Appendix A. Short description of satellite missions

The most important satellite missions referenced in this thesis are the SEASAT, GEOSAT and ERS-1 satellites and the future TOPEX/Poseidon and ARISTOTELES satellites. In this Appendix, some characteristics of these satellites will be presented. In addition, a short description will be given of the GPS navigation satellite system.

SEASAT. The US SEASAT satellite was launched in June 1978. One of the objectives of this mission was to map the oceans with a radar altimeter. The noise level of this instrument was claimed to be less than 10 cm. Unfortunately, this instrument has delivered only three months of observations, but already with this data set very encouraging results were obtained in the field of orbit determination, oceanography and gravity field modeling. The SEASAT orbit had an average altitude of 800 km and an inclination of 108°. The latter means that no altimeter measurements could be made above 72° North latitude or below 72° South latitude. SEASAT has flown two orbits with different ground track patterns. The data set used in this thesis, refers to an orbit for which the ground track repeated itself after 3 days, in which the satellite completed 43 orbital revolutions.

GEOSAT. The US Navy satellite GEOSAT, a dedicated altimetry satellite, was launched in 1985 and has delivered accurate altimeter observations for a period of almost 5 years, until the satellite failed in January 1990. The first two years of this mission were classified. After these two years, the satellite was maneuvered into a 17-day repeat orbit and three years of altimeter observations have been made available to the scientific community. The GEOSAT satellite was in an orbit comparable to the SEASAT orbit: 800 km altitude and with an orbital inclination of 108°. For the GEOSAT altimeter measurements used in this thesis, the repeat period was equal to 17 days, in which the satellite completed 244 orbital revolutions.

ERS-1. The European Remote-Sensing satellite ERS-1 was launched in July 1991 and is equipped with a wide spectrum of Earth-observing instruments, one of them being a radar altimeter. The Section Orbital Mechanics of the Delft University of Technology (DUT/SOM) has been and still is involved in this mission. The ERS-1 satellite is in a sun-synchronous orbit with an average altitude of 780 km an an inclination of 98°. The ERS-1 satellite will be maneuvered into several repeat orbits, respectively a 3-day, 35-day and 176-day repeat orbit. The selection of these repeat orbits was a trade-off between temporal and spatial resolution of ocean phenomena.

TOPEX/Poseidon. The TOPEX/Poseidon satellite is a dedicated US/French altimeter satellite, scheduled to be launched in June 1992. Preparations have been made for an extremely precise orbit determination (the satellite will be equipped with a GPS receiver) to be able to fully exploit the information content of the precise altimeter observations, and to meet the ambitious objectives in the field of oceanography. The

TOPEX/Poseidon satellite will be injected into a 1300 km altitude orbit with an inclination of 63°. The satellite's ground track will repeat itself after 10 days or 127 orbital revolutions.

ARISTOTELES. The European/US solid Earth satellite ARISTOTELES is scheduled to be launched in 1997. The objectives of this satellite are the determination of the geomagnetic and gravity fields of the planet Earth to a high accuracy and spatial resolution. The ARISTOTELES satellite orbit is scheduled to be flown in a 200 km altitude, 96° inclined orbit for the gravity field part of the mission.

GPS. The Global Positioning System was developed to be a global, all-purpose satellite navigation system. The final configuration will consist of 24 satellites (3 active spares) at 20,000 km altitude (2 orbital revolutions per day) with inclinations of 55° and 63°. The satellites will be distributed over 6 orbital planes, each shifted 60° in their right ascension of ascending node. The final constellation is expected to reach its completion in 1993.

Appendix B. Partial derivatives of satellite laser range (SLR) measurements to gravity field harmonic coefficients

The computation of partial derivatives of satellite laser range (SLR) measurements to gravity field harmonic coefficients with the Linear Perturbation Theory (LPT) for a circular reference orbit consists of the following steps:

a- determination of the unit vectors pointing in the orbital radial, along-track and cross-track directions at all measurement times;
b- determination of the unit vector pointing in the direction from station to satellite at all measurement times;
c- computation of the derivatives of the radial, along-track and cross-track perturbations to the harmonic coefficients to be adjusted;
d- computation of the derivatives of the range between station and satellite to the radial, along-track and cross-track directions;
e- combination of the steps a-d to the desired derivatives of SLR measurements to harmonic coefficients to be adjusted.

Ad a. The unit vectors in radial, cross-track and along-track directions are determined using Figure B.1 and the following relations:

$$\cos(\omega+M) = \cos(\alpha-\Omega)\cos\delta \tag{B.1}$$

$$\sin(\omega+M)\cos\psi = \cos(\alpha-\Omega)\sin\delta \tag{B.2}$$

$$\sin(\omega+M)\cos i = \cos\delta\sin(\alpha-\Omega) \tag{B.3}$$

$$\sin(\alpha-\Omega) = \sin\psi\sin(\omega+M) \tag{B.4}$$

$$\sin\delta = \sin i \sin(\omega+M) \tag{B.5}$$

The desired directions, in the Earth-fixed reference system, are computed as follows:

$$\text{radial}: \bar{u}_r = \begin{bmatrix} \cos\delta\cos(\alpha-\theta_g) \\ \cos\delta\sin(\alpha-\theta_g) \\ \sin\delta \end{bmatrix} = \begin{bmatrix} u_r(x) \\ u_r(y) \\ u_r(z) \end{bmatrix} \tag{B.6}$$

$$\text{cross-track}: \bar{u}_c = \begin{bmatrix} \sin i \sin(\Omega-\theta_g) \\ -\sin i \cos(\Omega-\theta_g) \\ \cos i \end{bmatrix} = \begin{bmatrix} u_c(x) \\ u_c(y) \\ u_c(z) \end{bmatrix} \tag{B.7}$$

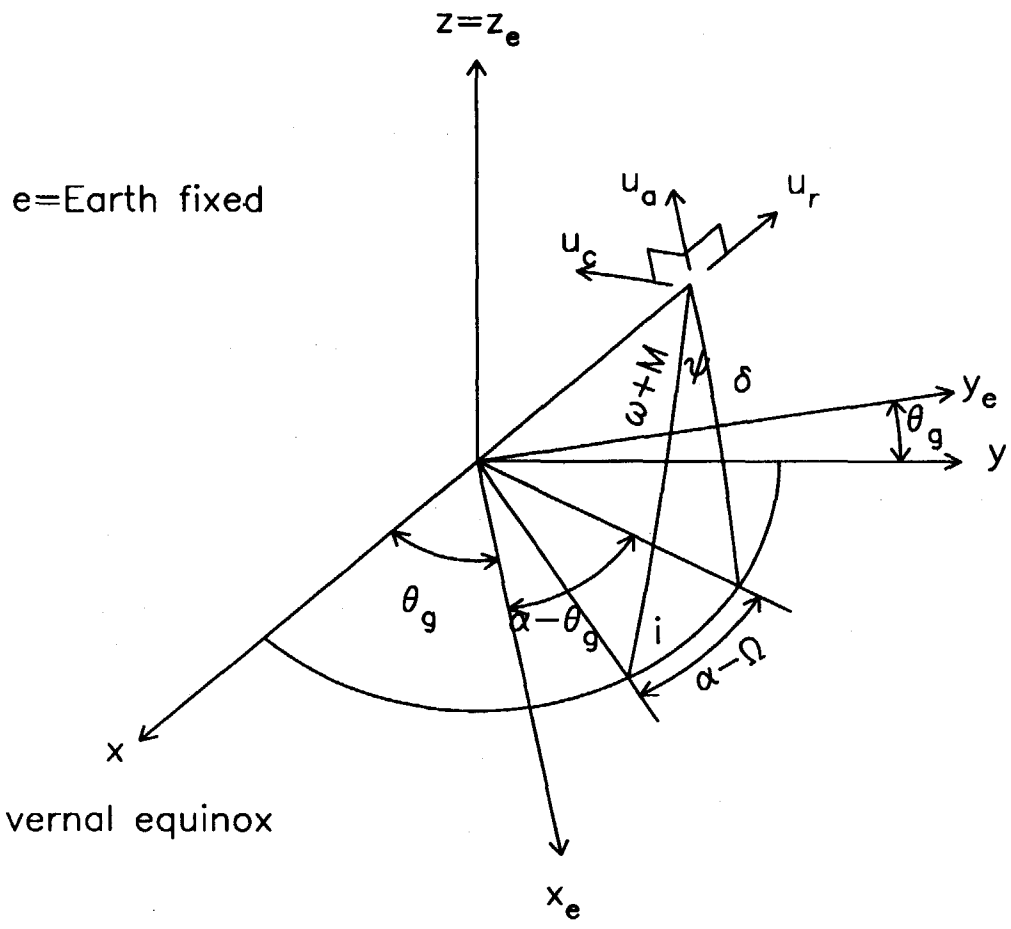

Figure B.1

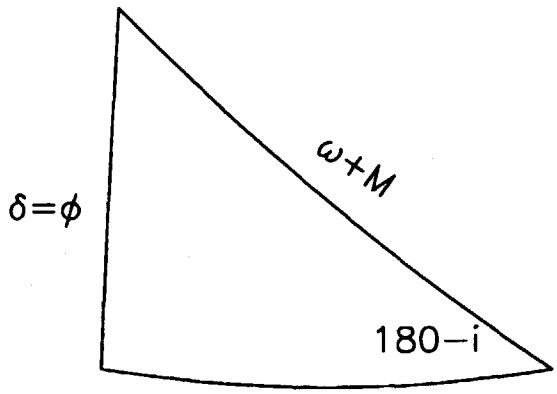

Figure B.2

$$\text{along-track}: \bar{u}_a = \begin{bmatrix} -\sin(\omega+M)\cos(\Omega-\theta_g)-\cos(\omega+M)\cos i\sin(\Omega-\theta_g) \\ -\sin(\omega+M)\sin(\Omega-\theta_g)+\cos(\omega+M)\cos i\cos(\Omega-\theta_g) \\ \cos(\omega+M)\sin i \end{bmatrix}$$

$$= \begin{bmatrix} u_a(x) \\ u_a(y) \\ u_a(z) \end{bmatrix} \tag{B.8}$$

It can easily be shown that an orthonormal system is obtained:

$$\bar{u}_r \bullet \bar{u}_c = \bar{u}_r \bullet \bar{u}_a = \bar{u}_c \bullet \bar{u}_a = 0 \tag{B.9a}$$

and

$$||\bar{u}_r|| = ||\bar{u}_a|| = ||\bar{u}_c|| = 1 \ . \tag{B.9b}$$

Suppose that $(\Omega\text{-}\theta)_p$ is the ascending node passage at the time t_p, and that the orbital angular velocity can be written as:

$$n = \frac{d(\omega+M)}{dt} \ . \tag{B.10}$$

With (B.10) and (B.1)-(B.5) the unit vectors in the radial, along-track and cross-track directions (equations (B.6)-(B.8)) at arbitrary time t can be computed:

$$\sin\delta = \sin i \sin n(t-t_p) \tag{B.11}$$

$$\cos\delta = \sqrt{1-\sin^2\delta} \tag{B.12}$$

$$\cos(\alpha-\Omega) = \frac{\cos n(t-t_p)}{\cos\delta} \tag{B.13}$$

$$\sin(\alpha-\Omega) = \frac{\sin n(t-t_p)\cos i}{\cos\delta} \tag{B.14}$$

$$\Omega-\theta = (\Omega-\theta)_p + \frac{d(\Omega-\theta)}{dt}(t-t_p) = B \tag{B.15}$$

$$\cos(\alpha-\theta_g) = \cos(\alpha-\Omega+\Omega-\theta_g) = \cos(\alpha-\Omega)\cos B - \sin(\alpha-\Omega)\sin B \tag{B.16}$$

$$\sin(\alpha-\theta_g) = \sin(\alpha-\Omega)\cos B + \sin B\cos(\alpha-\Omega) \ . \tag{B.17}$$

Ad b. To determine the unit vector in the direction from station to satellite, the position of the satellite in the Earth-fixed reference system must be determined. It is assumed that the station coordinates in the Earth-fixed reference system are known:

$$\bar{r}_{sta} = \begin{bmatrix} x_{sta} \\ y_{sta} \\ z_{sta} \end{bmatrix} \tag{B.18}$$

At the ascending node passage the longitude is taken equal to λ_a and the latitude ϕ is equal to 0°. For an orbit inclination i greater than 90° (retrograde satellite orbit) the following relations can be derived (see also Figure B.2):

1- geocentric longitude :

$$\lambda = \lambda_a + \frac{d(\Omega-\theta)}{dt} * (t-t_p) - f \tag{B.19}$$

$$\cos(\omega+M) \geq 0 \rightarrow f = \arctan\left[\cos(180°-i)\tan(\omega+M)\right] \tag{B.20}$$

$$\cos(\omega+M) < 0 \rightarrow f = \arctan\left[\cos(180°-i)\tan(\omega+M)\right] + 180° \tag{B.21}$$

2- geocentric latitude :

$$\phi = \arcsin\left[\sin(180°-i)\sin(\omega+M)\right] . \tag{B.22}$$

The unit range vector can now be determined, with r the radius of the orbital trajectory:

$$\bar{u}_{range} = \frac{\begin{bmatrix} r\cos\phi\cos\lambda - x_{sta} \\ r\cos\phi\sin\lambda - y_{sta} \\ r\sin\phi - z_{sta} \end{bmatrix}}{\rho} \tag{B.23}$$

where,

$$\rho = \left[(r\cos\phi\cos\lambda - x_{sta})^2 + (r\cos\phi\sin\lambda - y_{sta})^2 + (r\sin\phi - z_{sta})^2\right]^{\frac{1}{2}} \tag{B.24}$$

With the above derived unit vectors in the radial, along-track, cross-track and range vector directions, a laser range residual with a value equal to *resid* can be split in components in radial, along-track and cross-track directions:

$$(resid)_{radial} = resid \bullet (\bar{u}_{range} \bullet \bar{u}_r) \tag{B.25}$$

$$(resid)_{along} = resid \bullet (\bar{u}_{range} \bullet \bar{u}_a) \tag{B.26}$$

$$(resid)_{cross} = resid \bullet (\bar{u}_{range} \bullet \bar{u}_c) \tag{B.27}$$

Ad c. With the LPT the partial derivatives of the radial, along-track and cross-track orbit perturbations to the harmonic coefficients to be adjusted can be computed. These derivatives can be found by taking the partial derivatives of the equations (2.6a)-(2.6c) to the harmonic coefficients.

Ad d. With the equations (B.6)-(B.8) the partial derivatives of the satellite vector $(x_{sat}, y_{sat}, z_{sat})$ in the Earth-fixed reference system to radial (r), along-track (τ) and cross-track (c) directions can be computed:

$$\frac{\partial x_{sat}}{\partial r} = u_r(x)\,,\ \frac{\partial y_{sat}}{\partial r} = u_r(y)\,,\ \frac{\partial z_{sat}}{\partial r} = u_r(z) \tag{B.28}$$

$$\frac{\partial x_{sat}}{\partial \tau} = u_a(x)\,,\ \frac{\partial y_{sat}}{\partial \tau} = u_a(y)\,,\ \frac{\partial z_{sat}}{\partial \tau} = u_a(z) \tag{B.29}$$

$$\frac{\partial x_{sat}}{\partial c} = u_c(x)\,,\ \frac{\partial y_{sat}}{\partial c} = u_c(y)\,,\ \frac{\partial z_{sat}}{\partial c} = u_c(z) \tag{B.30}$$

The SLR measurement can be modeled as:

$$\rho = \sqrt{(x_{sat}-x_{sta})^2+(y_{sat}-y_{sta})^2+(z_{sat}-z_{sta})^2} \tag{B.31}$$

With the equations (B.28)-(B.31) the partial derivatives of the SLR measurements to the radial, along-track and cross-track directions can be computed.

Ad e. If H is an harmonic coefficient $\bar{C}_{lm}$ or $\bar{S}_{lm}$ and ρ the range between the ground tracking station and the satellite, the derivative of this range to the harmonic H is:

$$\frac{\partial \rho}{\partial H} = \frac{1}{\rho}\left[(x_{sat}-x_{sta})\frac{\partial x_{sat}}{\partial H}+(y_{sat}-y_{sta})\frac{\partial y_{sat}}{\partial H}+(z_{sat}-z_{sta})\frac{\partial z_{sat}}{\partial H}\right] =$$

$$\bar{u}_{range}\bullet\begin{bmatrix}\dfrac{\partial x_{sat}}{\partial H}\\[2ex] \dfrac{\partial y_{sat}}{\partial H}\\[2ex] \dfrac{\partial z_{sat}}{\partial H}\end{bmatrix} =$$

$$\bar{u}_{range}\bullet\begin{bmatrix}\dfrac{\partial x_{sat}}{\partial r}\dfrac{\partial r}{\partial H}+\dfrac{\partial x_{sat}}{\partial \tau}\dfrac{\partial \tau}{\partial H}+\dfrac{\partial x_{sat}}{\partial c}\dfrac{\partial c}{\partial H}\\[2ex] \dfrac{\partial y_{sat}}{\partial r}\dfrac{\partial r}{\partial H}+\dfrac{\partial y_{sat}}{\partial \tau}\dfrac{\partial \tau}{\partial H}+\dfrac{\partial y_{sat}}{\partial c}\dfrac{\partial c}{\partial H}\\[2ex] \dfrac{\partial z_{sat}}{\partial r}\dfrac{\partial r}{\partial H}+\dfrac{\partial z_{sat}}{\partial \tau}\dfrac{\partial \tau}{\partial H}+\dfrac{\partial z_{sat}}{\partial c}\dfrac{\partial c}{\partial H}\end{bmatrix} \tag{B.32}$$

All elements of equation (B.32) can be computed with the equations (B.1)-(B.31) and (2.6a)-(2.6c). Equation (B.32) is used in the computation of the observation equations for SLR measurements in the gravity field tailoring experiments of Chapter 5.

Appendix C. Statistical considerations

In this Appendix, relations are derived for the standard deviations of and correlations between subset solutions of normal equations with a priori information. After this, relations are derived for standard deviations of certain phenomena, if a covariance matrix for a model describing these phenomena is available.

Suppose the following set of observation equations:

$$Ax = [\,A_1 \;\; A_2\,] \begin{bmatrix} x_1 \\ x_2 \end{bmatrix} = R \tag{C.1}$$

where x is the vector of unknowns divided in the subsets x_1 and x_2, and R is the vector of residuals. Further, the expectancy for each element of the vector x is assumed to be equal to zero.

In addition, suppose a priori information in the form of inverse covariance matrices G_1 and G_2 for the subsets x_1 and x_2 and weight factors w_1 and w_2. In this case, the minimum-variance solution with a priori information reads:

$$x = \begin{bmatrix} A_1{}^T A_1 + w_1 G_1 & A_2{}^T A_1 \\ A_1{}^T A_2 & A_2{}^T A_2 + w_2 G_2 \end{bmatrix}^{-1} A^T R \tag{C.2}$$

$$= \begin{bmatrix} C_{11} & C_{12} \\ C_{12}{}^T & C_{22} \end{bmatrix} A^T R = C A^T R$$

The matrix C represents the a posteriori covariance matrix for the unknowns x, provided a proper calibration for this matrix, which is supposed to be the case.

The correction of an observation at a certain time t_k by application of the subset solution x_1 is:

$$correction_k = \sum_{i=1}^{N} A_{1,ki} x_{1,i} \tag{C.3}$$

where x_1 is a vector with N elements and $A_{1,ki}$ is the element of row k and column i of the matrix A_1. The standard deviation for this correction is:

$$\sigma^2(correction_k) = \sigma^2\left\{\sum_{i=1}^{N} A_{1,ki} x_{1,i}\right\} = E\left\{\left[\sum_{i=1}^{N} A_{1,ki} x_{1,i}\right]^2\right\} \tag{C.4}$$

$$= E\left\{\sum_{i=1}^{N}\sum_{j=1}^{N} A_{1,ki} A_{1,kj} x_{1,i} x_{1,j}\right\} = \sum_{i=1}^{N}\sum_{j=1}^{N} A_{1,ki} A_{1,kj} \sigma^2(x_{1,i} x_{1,j})$$

In the derivation of equation (C.4) the zero expectancy of the elements of the vector x_1 was applied. The term $\sigma^2(x_{1,i}x_{1,j})$ is equal to the element of the *i'th* row and the *j'th* column of the matrix C_{11} in equation (C.2):

$$\sigma^2(correction_k) = \sum_{i=1}^{N}\sum_{j=1}^{N} A_{1,ki}A_{1,kj}C_{11,ij} \qquad (C.5)$$

Taking all the observations *nobs*, equation (C.5) becomes:

$$\sum_{k=1}^{nobs}\sigma^2(correction_k) = \sum_{k=1}^{nobs}\sum_{i=1}^{N}\sum_{j=1}^{N} A_{1,ki}A_{1,kj}C_{11,ij} = \sum_{i=1}^{N}\sum_{j=1}^{N}\left\{\sum_{k=1}^{nobs} A_{1,ki}A_{1,kj}\right\}C_{11,ij} \qquad (C.6)$$

The summation between brackets is equal to the element $(A_1{}^T A_1)_{ij}$; thus the rms of the standard deviations is:

$$\bar{\sigma}(correction) = \left\{\frac{1}{nobs}\sum_{i=1}^{N}\sum_{j=1}^{N}(A_1{}^T A_1)_{ij}C_{11,ij}\right\}^{\frac{1}{2}} \qquad (C.7)$$

In a similar way, equations for the standard deviation of the corrections with the solution for x_2 and the covariance of the corrections with the solutions for x_1 and x_2 can be derived. The covariance of the subsets x_1 and x_2 reads, if the vector x_2 has M elements:

$$\bar{\sigma}^2(x_1x_2) = \frac{1}{nobs}\sum_{i=1}^{M}\sum_{j=1}^{N}(A_1{}^T A_2)_{ij}C^T{}_{12,ij} \qquad (C.8)$$

$$= \frac{1}{nobs}\sum_{i=1}^{N}\sum_{j=1}^{M}(A_2{}^T A_1)_{ij}C_{12,ij} \; .$$

Suppose the availability of a calibrated covariance matrix C of a model with N parameters P_i describing the phenomenon f. It is assumed that f is modeled by a linear relation:

$$f = \sum_{i=1}^{N} f_i P_i \; . \qquad (C.9)$$

It is possible to derive in the same way as in the derivation of equation (C.5) that the variance of f is equal to:

$$\sigma^2(f) = \sum_{i=1}^{N}\sum_{j=1}^{N} f_i f_j C_{ij} \; . \qquad (C.10)$$

Examples of the matrix C may be calibrated gravity covariance matrices or covariance matrices of the dynamic sea surface topography; examples of f may be amplitudes of orbit perturbation frequencies, geoid heights or altimeter crossover differences at a certain geographical position, dynamic sea heights, etc.

Appendix D. Theory of formal error estimates from satellite observations with a special geometry

This Appendix describes the theory of formal harmonic coefficient error estimates when the LPT is applied to a data set of satellite observations with a special geometry. It will be shown that under certain conditions normal equations for the harmonic coefficients can be derived that are block-diagonal. Such a structure of the normal matrix facilitates a quick inversion of this matrix, leading to the formal error estimates of the harmonic coefficients.

In general, a gravity field induced signal or signal of the dynamic sea surface topography $f(g)$ along an almost circular satellite orbit can be described as a function of the gravity field harmonic coefficients and the orbit parameters:

$$f(g) = \sum_{l=2}^{lmax} \sum_{m=0}^{l} \sum_{p=0}^{l} Q(a)_{lmp} F_{lmp} S(\omega+M, \Omega-\theta)_{lmp} \ . \tag{D.1}$$

The factors $Q(a)_{lmp}$ and F_{lmp} are functions of respectively the semi-major axis and the inclination of the satellite orbit and are constants. Examples of $f(g)$ may be satellite orbit perturbations (Chapter 2) and gradiometer measurements (Chapter 9). The function $S(\omega+M,\Omega-\theta)_{lmp}$ can be written as:

$$S(\omega+M, \Omega-\theta)_{lmp} = J_{lm} \cos(f_{lmp} nt + m\lambda_a - \beta_{lm}^{\ *}) \tag{D.2}$$

where,

$$J_{lm} = \sqrt{C_{lm}^{\ 2} + S_{lm}^{\ 2}} \tag{D.3}$$

$$\beta_{lm}^{\ *} = \begin{cases} \arctan \dfrac{S_{lm}}{C_{lm}} & l-m \ even \\ \arctan \dfrac{S_{lm}}{C_{lm}} - \dfrac{\pi}{2} & l-m \ odd \end{cases} \tag{D.4}$$

$$f_{lmp} = l - 2p - \frac{m}{nr} \tag{D.5}$$

$$n = \sqrt{\frac{\mu}{a^3}} \tag{D.6}$$

where λ_a is the longitude at the ascending node passage, t the time after this passage and nr is the number of orbital revolutions per day.

It is assumed that the satellite is in an exact repeat orbit: the satellite makes *nrev* orbital revolutions in *nday* nodal days. For such an orbit, equation (D.1) takes the form of a Fourier series and nr is equal to *nrev/nday* . It is now supposed that in one repeat period, N_m observations are made with a constant sampling rate. If f_{lmp} is smaller than the so-called Nyquist-frequency, the following relation can be derived (Colombo, 1984):

$$\sum_{i=1}^{N_m} \cos(f_{lmp}\, ni\, \Delta t + \alpha)\cos(f_{l'm'p'}\, ni\, \Delta t + \alpha) = \begin{cases} 0 & m \neq m' \text{ or } l-2p \neq l'-2p' \\ \frac{1}{2}N_m & m = m' \; l-2p = l'-2p' \end{cases} \quad \text{(D.7)}$$

With the equations (D.1)-(D.7) it can be shown that for the N_m observations, the harmonic coefficients of a certain order m are uncorrelated with harmonic coefficients of any order m' unequal to m for $m,m' < nrev/2$. This means that if normal equations are computed for harmonic coefficients from satellite observations made by or to a satellite in a repeat orbit with a constant sampling-rate, the normal matrix has a block-diagonal structure, if this matrix is organized per order m (Figure D.1). The largest block has a dimension less than two plus the maximum degree used in the spherical harmonic expansion solved for (provided that this maximum degree is smaller than $nrev/2$). In fact, the maximum dimension is half of this number, because also coefficients for even and odd degree l are uncorrelated. The inverse of the normal matrix is easily obtained by taking the inverse of each block. This is a much smaller effort than computing the inverse of the full matrix for e.g. 120,000 unknowns, if a gravity field model complete to degree and order 360 is to be estimated.

Having computed the inverse, the formal error estimate of an harmonic coefficient is found by taking the square root of the diagonal elements of the inverse and multiplying this with the standard deviation or accuracy of the measurements.

The theory of formal error estimates may be applied to e.g. gravity field harmonic coefficient estimation or dynamic sea surface topography harmonic coefficient estimation or to a combination of the two from e.g. satellite altimeter measurements, gradiometer measurements or orbit perturbations. It must be noted that if two harmonic models describing two different phenomena (e.g. gravity field and dynamic sea surface topography, Chapter 6) are estimated together, the maximum dimension of a block may become equal to two plus half the sum of the maximum degrees of each model.

The theory of formal harmonic coefficient error estimates has been implemented in a computer program (FORTRAN-code). This software is capable of estimating formal error estimates of gravity field coefficients and/or coefficients for the dynamic sea surface topography from any combination of the following observations:

1- satellite orbit perturbations in the radial, along-track and cross-track directions (Chapters 6 and 9);
2- satellite altimeter observations (Chapter 6);
3- gradiometer components Γ_{zz}, Γ_{zy} and Γ_{yy} (Chapter 9);
4- range-rates between two satellites in the same circular orbit but with a different phase angle.

The parameters than can be manipulated in this software are the semi-major axis a, the orbit inclination i, the repeat period in nodal days $nday$, the number of revolutions in a repeat period $nrev$, the measurement interval Δt (or N_m), and the noise of the observations σ.

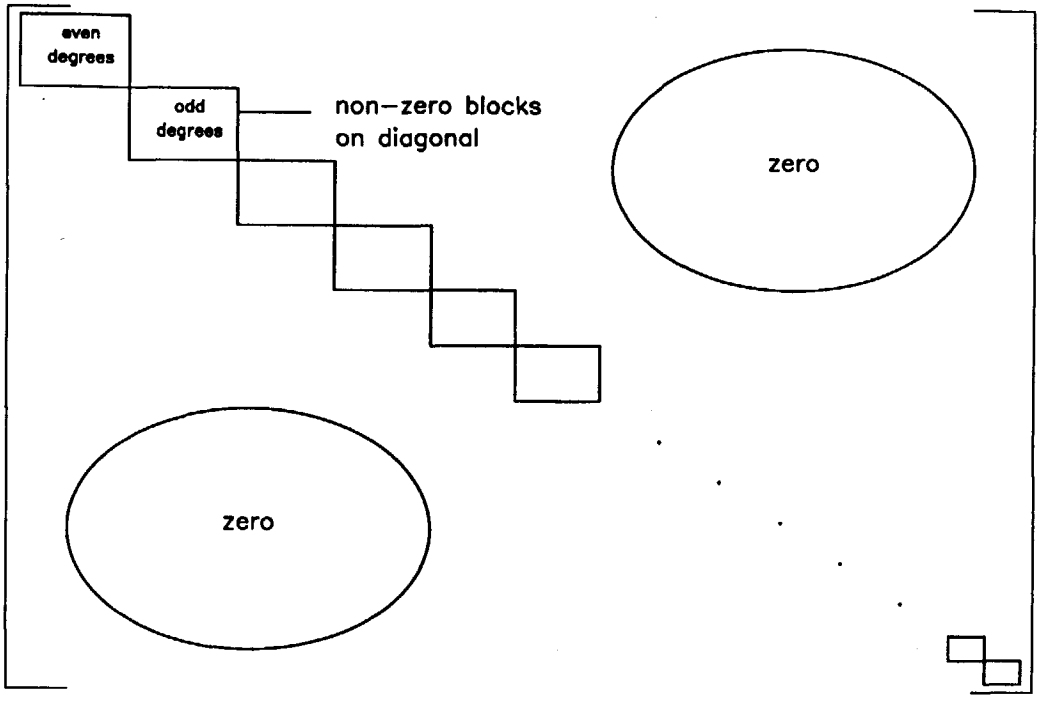

Figure D.1 Structure of the normal matrix

Appendix E. Least-squares collocation covariance analysis

The estimate by least-squares collocation of a certain gravity field induced signal s from gravity field induced observations t reads (Chapter 7):

$$s = C_{st}(C_{tt}+D)^{-1}t \tag{E.1}$$

where the diagonal elements of the matrix D consist of the square of the measurement accuracy (variance of the measurement noise) and the off-diagonal elements of the cross-correlations between the measurement accuracy of two observations (non-zero for "colored" noise). The estimate of the standard deviation of the estimate for s becomes (Moritz, 1980):

$$\sigma^2(s) = E\left\{(s-\bar{s})^2\right\} = C(0)-C_{st}(C_{tt}+D)^{-1}C_{st}^T \tag{E.2}$$

where $C(0)$ is equal to the value on the diagonal of the matrix C_{tt}. The estimate of the correlation between the estimates s_1 and s_2 can be written as:

$$\sigma(s_1 s_2) = E\left\{(s_1-\bar{s}_1)(s_2-\bar{s}_2)\right\} = C(0)_{12}-C_{s_1t}(C_{tt}+D)^{-1}C_{s_2t}^T \quad . \tag{E.3}$$

These equations are valid for point values of s. If the mean of a certain number N of point values is computed, e.g. the mean of a regular distribution of N point values in a 1°x1° area on the Earth's surface, the error estimate for this value can be found by:

$$\sigma^2(s_{mean}) = \frac{1}{N}\sum_{i=1}^{N}\sum_{j=1}^{N}\sigma(s_1 s_2) \tag{E.4}$$

where

$$s_{mean} = \frac{1}{N}\sum_{i=1}^{N}s_i \; . \tag{E.5}$$

Appendix F. Adams-Moulton integrator

In order to be able to integrate satellite orbits with a high-degree and -order spherical harmonic expansion, an Adams-Moulton integrator with a Runge-Kutta initialization was developed. The integration takes place in a right-handed, Cartesian, geocentric semi-inertial reference frame with the X-axis pointing in the direction of the Vernal Equinox and the Z-axis pointing to the North-pole. The Earth is assumed to be rotating with a constant angular velocity ω_e around the Z-axis.

The equations of motion that have to be integrated can be represented as:

$$\dot{\bar{x}} = \bar{f}(t,\bar{x}) \tag{F.1}$$

where $\bar{x}$ is the satellite state-vector that consists of the position vector x, y and z and the velocity vector, i.e. the time derivatives of x, y and z in the semi-inertial reference frame. The vector $\bar{f}(t,\bar{x})$ consists of the velocity vector and the gravity field force factor elements in the X-, Y- and Z-directions. The variable t denotes the time.

The Adams-Moulton integrator is a multi-step method, a so-called predictor-corrector method. The method as implemented in the software integrates with a constant time step Δt. The rationale behind the Adams-Moulton integrator is the expansion of the state-vector as a function of time in a Taylor-series. If the order is taken equal to n, the state-vector at time t_{i+1} is modeled as:

$$\bar{x}_{i+1} = \bar{x}_i + \bar{f}(t_i,\bar{x}_i)\Delta t + \dot{\bar{f}}(t_i,\bar{x}_i)\frac{\Delta t^2}{2!} + \ddot{\bar{f}}(t_i,\bar{x}_i)\frac{\Delta t^3}{3!} + \ldots + \bar{f}^{n-1}(t_i,\bar{x}_i)\frac{\Delta t^n}{n!} . \tag{F.2}$$

The (multiple) time-derivatives of the vector $\bar{f}(t_i,\bar{x}_i)$ are computed by using again a Taylor expansion with n-1 preceding values for this vector. In this way, a system of equations has to be solved that reads, in matrix notation:

$$A^p Y = F^p \tag{F.3}$$

where,

$$Y^T = (\bar{f}(t_i,\bar{x}_i), \dot{\bar{f}}(t_i,\bar{x}_i), \ddot{\bar{f}}(t_i,\bar{x}_i), \ldots, \bar{f}^{n-1}(t_i,\bar{x}_i)) \tag{F.4}$$

$$(F^p)^T = (\bar{f}(t_i,\bar{x}_i), \bar{f}(t_{i-1},\bar{x}_{i-1}), \bar{f}(t_{i-2},\bar{x}_{i-2}), \ldots, \bar{f}(t_{i-n+1},\bar{x}_{i-n+1})) . \tag{F.5}$$

The elements of the matrix A^p can be written as:

$$A^p{}_{ij} = \frac{[(1-i)\Delta t]^{(j-1)}}{(j-1)!} . \tag{F.6}$$

Solving the equations (F.3) and inserting this solution in equation (F.2), the predicted state-vector can be written as:

$$\bar{x}^p{}_{i+1} = \bar{x}_i + \sum_{j=1}^{n} p_j \bar{f}(t_{i+1-j},\bar{x}_{i+1-j}) . \tag{F.7}$$

Equation (F.7) represents the predictor step. For a certain integration step Δt, the coefficients p_j are constants. The predicted state-vector $\bar{x}^p{}_{i+1}$ is used to predict the

value $\bar{f}(t_{i+1},\bar{x}^p{}_{i+1})$. After this, a same procedure as used in the predictor step is used to compute the (multiple) time-derivatives of the vector $\bar{f}(t_i,\bar{x}_i)$ from n-2 preceding values for this vector and the value $\bar{f}(t_{i+1},\bar{x}^p{}_{i+1})$. Again a set of equations similar to equation (F.3) has to be solved:

$$A^c Y = F^c \ . \tag{F.8}$$

The vector of unknowns Y can be represented by equation (F.4). The vector F^c can be written as:

$$(F^c)^T = (\bar{f}(t_{i+1},\bar{x}^p{}_{i+1}),\bar{f}(t_i,\bar{x}_i),\bar{f}(t_{i-1},\bar{x}_{i-1}),.....,\bar{f}(t_{i-n+2},\bar{x}_{i-n+2})) \ . \tag{F.9}$$

The elements of the matrix A^c become:

$$A^c{}_{ij} = \frac{[(2-i)\Delta t]^{(j-1)}}{(j-1)!} \ . \tag{F.10}$$

Solving the equations (F.8) and inserting this solution in equation (F.2) delivers a relation comparable to equation (F.7):

$$\bar{x}^c{}_{i+1} = \bar{x}_i + c_1 \bar{f}(t_{i+1},\bar{x}^p{}_{i+1}) + \sum_{j=2}^{n} c_j \bar{f}(t_{i+2-j},\bar{x}_{i+2-j}) \ . \tag{F.11}$$

Equation (F.11) represents the corrector step. Also the coefficients c_j are constants for a constant time step Δt.

In order to be able to start the Adams-Moulton integrator, n values for the vector $\bar{f}(t,\bar{x})$ must be known. However, the state-vector $\bar{x}$ is only known at the epoch time t_0. This so-called initialization is performed with a fourth-order Runge-Kutta integrator:

$$\bar{x}_{i+1} = \bar{x}_i + \frac{1}{6}(\bar{k}_1 + \bar{k}_2 + \bar{k}_3 + \bar{k}_4) \tag{F.12}$$

where,

$$\bar{k}_1 = \Delta t \bullet \bar{f}(t_i,\bar{x}_i) \tag{F.13a}$$

$$\bar{k}_2 = \Delta t \bullet \bar{f}(t_i + \frac{1}{2}\Delta t, \bar{x}_i + \frac{1}{2}\Delta t \bullet \bar{k}_1) \tag{F.13b}$$

$$\bar{k}_3 = \Delta t \bullet \bar{f}(t_i + \frac{1}{2}\Delta t, \bar{x}_i + \frac{1}{2}\Delta t \bullet \bar{k}_2) \tag{F.13c}$$

$$\bar{k}_4 = \Delta t \bullet \bar{f}(t_i + \Delta t, \bar{x}_i + \Delta t \bullet \bar{k}_3) \ . \tag{F.13d}$$

The order of the Adams-Moulton integrator can be chosen much higher than the order of this Runge-Kutta initialization. Thus relatively large initialization errors can be made. Therefore, an advanced start-up procedure was developed. For an n-th order Adams-Moulton orbit integration, this start-up procedure consisted of the following steps:

1- integrate n-1 time steps Δt backwards with Runge-Kutta;
2- integrate n-1 time steps Δt forward with the Adams-Moulton integrator using the

values of the first step;

3- integrate again n-1 time steps Δt backwards but now with the Adams-Moulton integrator using the values of the second step or fourth step when available;
4- integrate again n-1 time steps Δt forward with the Adams-Moulton integrator using the values of the third step;
5- repeat the steps 3 and 4 (in the following referred to as an iteration) until convergence.

The start-up procedure was applied in the computation of the ERS-1 orbits used in the simulations described in Chapter 3. To show the convergence of the initialization procedure, the state-vector at a time equal to $t_0+\Delta t$ (i.e. the first point after epoch) was stored after the initialization step number 2 (1 state-vector) and after each iteration i (until convergence). The position and velocity differences between these successive state-vectors are displayed in Figure F.1. The values displayed are defined as:

$$\Delta position = \sqrt{(x_{i+1}-x_i)^2+(y_{i+1}-y_i)^2+(z_{i+1}-z_i)^2} \qquad \text{(F.14a)}$$

$$\Delta velocity = \sqrt{(\dot{x}_{i+1}-\dot{x}_i)^2+(\dot{y}_{i+1}-\dot{y}_i)^2+(\dot{z}_{i+1}-\dot{z}_i)^2}\,. \qquad \text{(F.14b)}$$

As can be seen from Figure F.1, the initialization converges logarithmically. After 7 iterations the differences have become negligible: the position differences have become less than 0.01 μm and the velocity differences equal to zero.

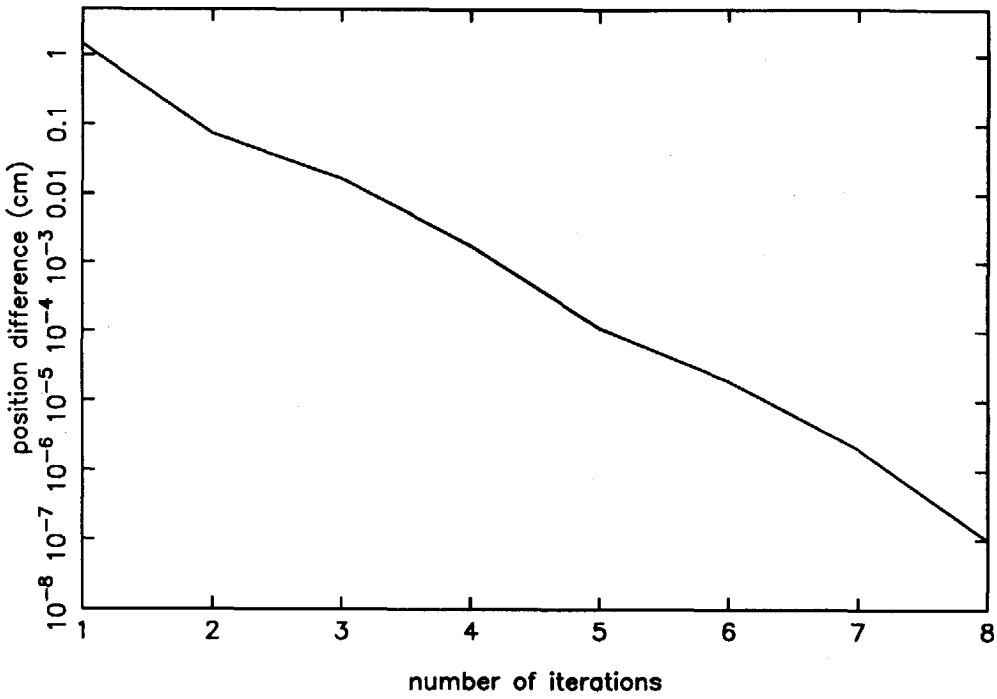

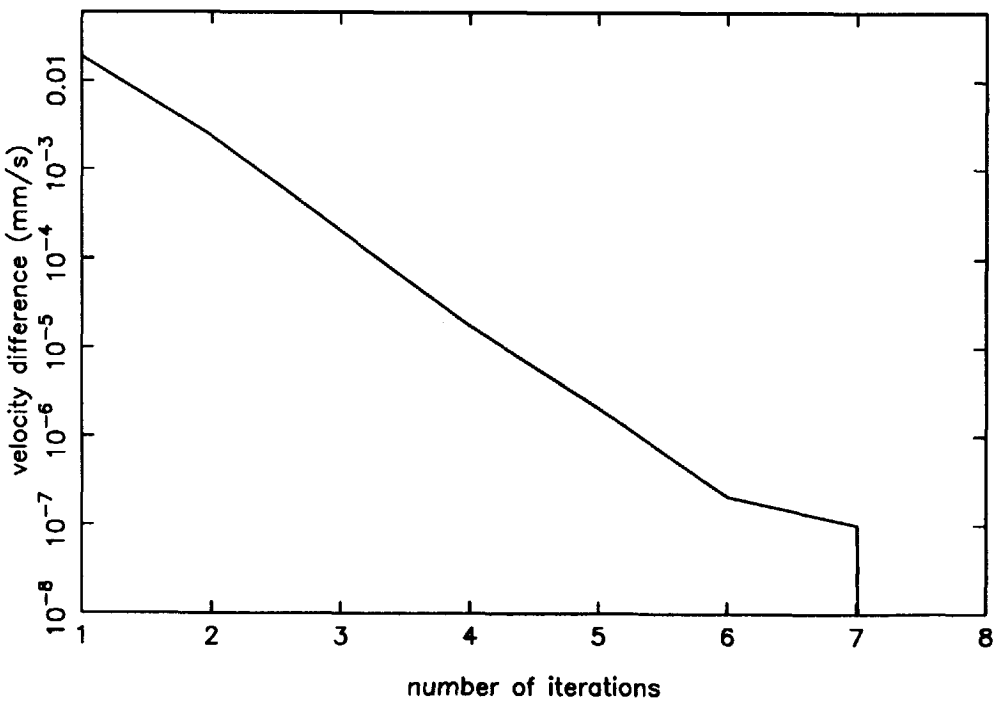

Figure F.1 Initialization of ERS−1 orbit integration

Plate I: Dynamic sea heights (m) from the new SST-model

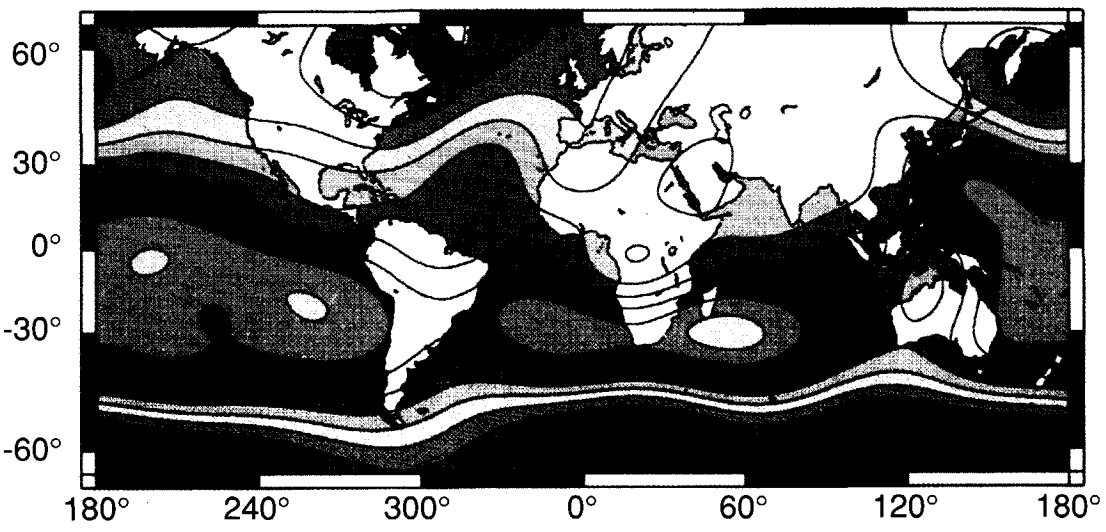

Plate II: Dynamic sea heights (m) from Marsh et al., 1989b

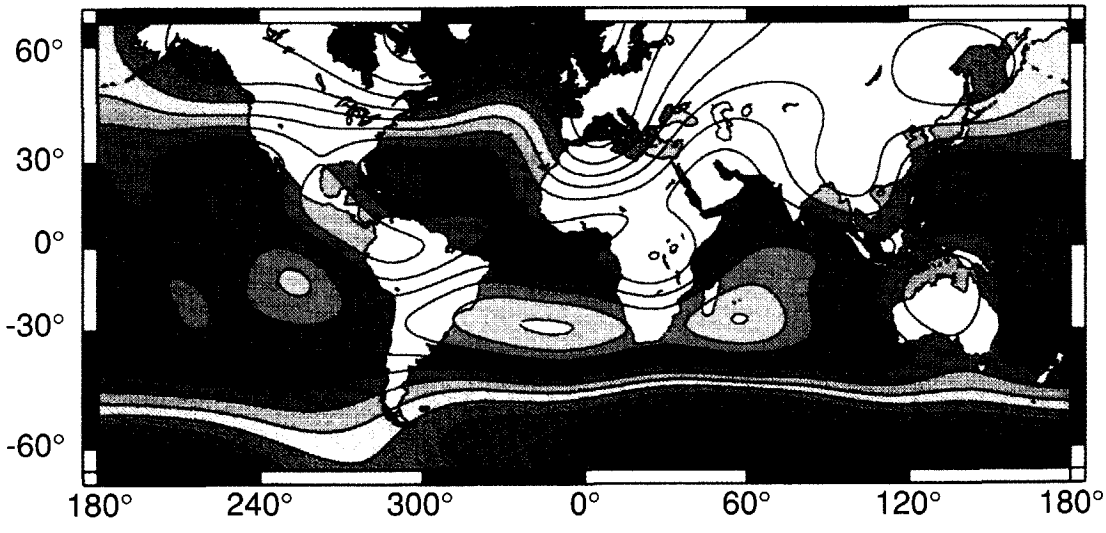

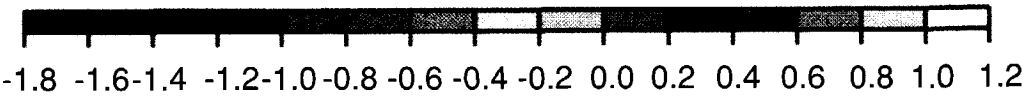

Plate III: Standard deviation (cm) of the adjusted geoid

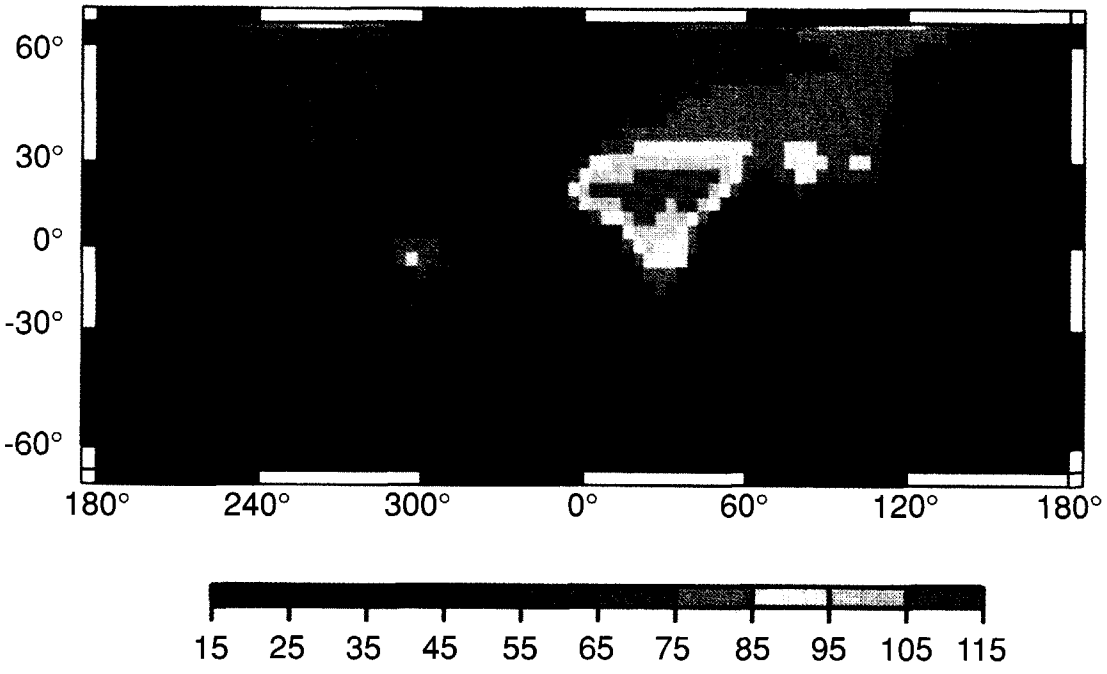

Plate IV: Standard deviation (cm) of the new SST-model